Tracing Redox Cycles during Microbe-Clay Interactions Using Stable Iron Isotopes

by

Bingjie Shi

A thesis
presented to the University of Waterloo
in fulfillment of the
thesis requirement for the degree of
Doctor of Philosophy
in
Earth Sciences

Waterloo, Ontario, Canada, 2018

Examination Committee Membership

The following served on the Examining Committee for this thesis.

External Examiner	Dr. Paul A. Schroeder Professor Department of Geology University of Georgia
Supervisor	Dr. Philippe Van Cappellen Professor and Canada Excellence Research Chair in Ecohydrology Department of Earth & Environmental Sciences University of Waterloo
Internal Member	Dr. David W. Blowes Professor and Canada Research Chair in Groundwater Remediation Department of Earth & Environmental Sciences University of Waterloo
Internal-External Member	Dr. Laura Hug Assistant Professor Canada Research Chair in Environmental Microbiology Department of Biology University of Waterloo
Other Member	Dr. Clark M. Johnson Vilas Distinguished Professor Department of Geoscience University of Wisconsin-Madison
Other Member	Dr. Eric E. Roden Albert and Alice Weeks Professor Department of Geoscience University of Wisconsin-Madison

AUTHOR'S DECLARATION

This thesis consists of material all of which I authored or co-authored: see Statement of Contributions included in the thesis. This is a true copy of the thesis, including any required final revisions, as accepted by my examiners.

I understand that my thesis may be made electronically available to the public.

Statement of Contributions

Chapter 2 is a co-authored paper. As the first author of this paper, I was primarily responsible for the study design and execution. The following summarizes the contributions of the co-authors:
Lingling Wu (LW) and I developed the research questions. Kai Liu (KL) and I conducted laboratory research with guidance from Weiqiang Li (WL) and Christina M. Smeaton (CMS). KL and I analyzed the data. LW and I interpreted data and wrote the paper, with input from KL, CMS and Philippe Van Cappellen. All other authors provided feedback on data interpretation or writing suggestions.

Abstract

Iron redox cycling, especially Fe(III) reduction, is mostly driven by microbial activity in the shallow subsurface. A wide range of bacteria, archaea, and fungi reduce Fe(III) to acquire energy with soil organic compounds as the electron donors. Iron isotope signatures in ancient rocks (3.1-2.4 Ga) associated with dissimilatory Fe reduction (DIR) have been interpreted in terms of global changes in oceanic redox condition. Iron isotopes have also been used as indicators of redox processes involving Fe minerals such as Fe(III) (oxyhydr)oxides and pyrite. Clay minerals, however, contain approximately the same amount of Fe as all other Fe minerals combined, thereby playing a key role in Fe redox cycling. There have been numerous studies focusing on the mineralogical changes of clays during microbially, chemically, and electrochemically mediated redox cycles, and linking these changes to the bioavailability and reversibility of clay, including processes such as layer collapse, structural Fe migration, and dehydroxylation and water fixation. I used Fe isotopes, for the first time, to trace the redox cycling of clay minerals. Model nontronite minerals NAu-1 and NAu-2 were purified prior to the experiments to exclude impurities such as Fe oxides, kaolinite, and quartz. The purity of NAu-1 and NAu-2 was checked with X-ray diffraction (XRD) and scanning electron microscopy (SEM) coupled to energy dispersive spectroscopy (EDS), and transmission electron microscopy (TEM).

In Chapter 2, I present Fe isotope fractionations measured during the microbial reduction, chemical reduction, and mixing experiment of nontronite NAu-1. Microbial (*Shewanella oneidensis* MR-1 and *Geobacter sulfurreducens* PCA) and chemical (dithionite) reduction of NAu-1 produced isotopically lighter aqueous Fe(II) during the early stage of the reduction, with maximum isotope fractionation factors between aqueous Fe(II) and structural Fe(III) from -1.2 to -0.8‰. Iron isotope fractionation was produced by the electron transfer coupled atom exchange (ETAE) between aqueous Fe(II) and structural Fe(III) via the adsorbed Fe(II) on edge sites. With microbial reduction proceeding to the extent at which structural Fe(II) fully covered the edge surface of NAu-1, isotope fractionation between aqueous Fe(II) and structural Fe(III) decreased to ~0‰ due to a lack of ETAE. Meanwhile, minor ETAE continued between edge-bound Fe(II) and structural Fe(III). The variation of Fe isotope fractionation was coupled to the reduction of bioavailable structural Fe(III), which represented ~10% of the total Fe in NAu-1, showing that Fe isotopes can be useful tracers of Fe redox changes in clay minerals.

On the basis of the results of Chapter 2, in Chapter 3 I exposed NAu-1 and *S. oneidensis* MR-1 to three successive redox cycles to assess the redox reversibility of bioavailable Fe in NAu-1. Each redox cycle consisted of a long biotic reduction period (RP) and a short abiotic oxidation period (OP), between which the dissolved Fe(II) was removed to minimize the formation of Fe(III) (oxyhydr)oxides. Secondary mineral formation was not detected during the redox cycles. The initial fraction of bioavailable Fe in the unaltered NAu-1 was ~10% as proposed in Chapter 2. The remaining bioavailable Fe decreased from RP1 to RP3 due to the removal of the dissolved bioavailable Fe during the preceding RP. The dissolution of bioavailable Fe was primarily generated by the reduction of the smallest NAu-1 particles, while bioavailable Fe in the larger particles remained within the solid upon reduction. Due to the consumption of the small particles, bioavailable edge surface where ETAE takes place decreased with successive RPs, as implied by the decreasing Fe isotope fractionation from RP1 to RP3. By extrapolating the linear relationship between the extent of Fe(III) reduction and the fraction of dissolved Fe(II), I predict that ~4.2% of the total Fe in NAu-1 is redox reversible upon continued redox cycling, while ~5.8% of the total Fe is removed into solution.

In Chapter 4 I examine the bioavailability of Fe in a tetrahedral Fe(III)-containing nontronite (NAu-2) via microbial (*S. oneidensis* MR-1) and chemical reduction (dithionite). The microbial reduction of NAu-2 exhibited three stages according to the change in isotope fractionation between different Fe pools [i.e., aqueous Fe(II), basal-sorbed Fe(II), edge-bound Fe, structural Fe]: 1) stage 1 was characterized by increasing isotope fractionation between aqueous Fe(II)/edge-bound Fe and structural Fe, indicating ETAE mainly occurred along the edge surface of NAu-1; 2) at medium to high reduction extent, stage 2 exhibited decreasing isotope fractionation between edge-bound Fe and structural Fe, while the fractionation between aqueous Fe(II)/basal-sorbed Fe(II) and structural Fe further increased, implying that the edge surface was blocked and prevented ETAE (that is, from then on ETAE mainly occurred on the basal plane surface); 3) Fe reduction reached its maximum extent during stage 3, while the isotope fractionation between aqueous Fe(II)/basal-sorbed Fe(II) and structural Fe decreased, indicating that the ETAE through the basal planes became inhibited. The observed iron isotope fractionations show that NAu-2 has increased exchangeable basal plane redox reactivity due to the presence of tetrahedral Fe(III). The reactive basal plane surface may be particularly important under acidic condition, because, under low pH, cation adsorption mainly takes place on the basal planes.

Overall, my results show that Fe isotopes are a useful tool to study the Fe redox reversibility of clay minerals during redox cycles. However, on the basis of my results, I propose that microbial reduction of Fe(III) in clay may not have contributed to the isotope signatures recorded in BIFs during the late Archean. In addition, the presence of tetrahedral Fe may enhance the reactivity of clay minerals towards redox-active contaminants.

Acknowledgments

I am grateful to my supervisor Dr. Philippe Van Cappellen who is always a model of a mature scientist for me to learn from. He is always supporting and encouraging me. I would like to thank my former supervisor Dr. Lingling Wu who has been closely working with me and put enormous effort into my projects. I thank them for broadening my sight by keep offering me new opportunities, which benefit not only my career but also my life.

I am indebted to Kai Liu – my coworker – who has selflessly provided laboratory effort for me. I appreciate Dr. Christina Smeaton, Yan Zhang, and Dr. Chris Parsons who have helped me countless times with work in the labs and on the research articles. Thanks to Dr. Shuhuan Li, Marianne Vandergriendt, Dr. Liyan Xing for their great guidance and assistant with my sample analyses.

Thanks to Elaine, Tatjana, Tariq, Bijen, Zahra, Gabriel, Stephanie, David for being friends since the early days when I became an international student. Thank Lu for the afternoon-tea talks. I appreciate the nice suggestions to my PhD defense by Kunfu and Peng. Thanks to our excellent Ecohydrology group providing such wonderful research and working atmosphere, which is the part I love the most.

Thank my host supervisor Dr. Eric Roden at the University of Wisconsin-Madison for providing working areas, introducing excellent colleagues, and discussing my work during the course of exchanging program. Thank Dr. Clark Johnson, Brian Beard, and Dr. Brian Kendall for offering isotope lab and working assistant. Thank Seungyeol Lee and Dr. Huifang Xu for helping with sample analyses and discussing on my work. Thank Dr. David Blowes and people from his group for experimental trials. Thank Dr. Laura Hug and Dr. Paul Schroeder for participating in my defense examination committee and reviewing my thesis. I am indebted to Dr. Anke Neumann and Dr. Michelle Scherer for providing a set of experimental data and insightful comments.

Lastly, I would like to thank funding provided for this work by the Canada Excellence Research Chair (CERC) program, as well as an Ontario Early Researcher Award and NSERC Discovery grant to Dr. Lingling Wu, and the NASA Astrobiology Institute. The NSERC-funded TERRE-CREATE program provided me with travel funds to visit the University of Wisconsin-Madison.

Dedication

This thesis is dedicated to

my dear parents

and

my beloved husband Chuan Liu

Table of Contents

List of Figures

List of Tables

Chapter 1
Introduction

The main goal of this thesis is to advance the current state of clay biogeochemistry research by elucidating the underlying mechanisms governing the bioavailability and reversibility of Fe in clays. This chapter provides a summary of the past and current Fe-biogeochemistry literature and is mainly focused on Fe redox cycling, the development and establishment of using Fe isotopes as a robust probe for examining redox chemistry, and redox-induced clay mineral transformations. Moreover, the knowledge gaps and accompanying hypotheses and research objectives are identified.

1.1 Biogeochemical Fe redox cycling

Iron is an essential element to nearly all living organisms on Earth (Melton *et al.*, 2014). For example, heme-bearing cytochromes participate in electron transfer during respiratory energy production (Castresana and Moreira, 1999). Despite its importance, dissolved Fe concentrations are typically low and thereby limited due to the formation of insoluble Fe(III) phases [e.g. ferrihydrite, goethite, lepidocrocite] in oxic surface environments. Even under anaerobic conditions, Fe(II) will also precipitate with anions such as sulfide, carbonate, and phosphate, thereby becoming less bioavailable. Thus, the generation of soluble Fe is a key driver in Fe biogeochemical cycling. Some organisms overcome this difficulty by producing siderophores that form strong bonds with Fe(III), which becomes soluble after complexation (Butler, 2005; Mawji *et al.*, 2008). In seawater, Fe(III)-siderophore complexes are either directly uptaken by certain bacteria or used as electron acceptors to produce photolytic Fe(II) (Barbeau *et al.*, 2001). Biogeochemical Fe redox cycling takes place in redox transition zones in surface to subsurface environments, such as streams & aquifer systems (meter to decameter scale) and groundwater iron-seep system (centimeter to millimeter scale) (Roden, 2012). Microorganisms utilize Fe by reducing Fe(III) organotrophically or oxidizing Fe(II) lithotrophically (Melton *et al.*, 2014).

1.1.1 Dissimilatory Fe(III) reduction

Dissimilatory Fe(III) reduction (DIR) is hypothesized to have occurred in the late Archean (~3 Ga), and may have been one of the earliest forms of respiration on Earth (Lovley, 1991; Johnson *et al.*, 2008b). DIR is a metabolism pathway through which microorganisms acquire energy by using extracellular Fe(III) as an electron acceptor (Lovley, 1991). However, DIR was not discovered to support microbe growth until the 1970s-80s (Balashova and Zavarzin, 1979; Lovley and Phillips,

1988). In anaerobic soils and sediments, a wide range of bacteria, fungi and archaea can facilitate DIR using various electron donors via different electron transfer strategies (Lovley *et al.*, 2004; Pentrakova *et al.*, 2013). Several bacterial species belonging to the genera *Geobacter* and *Shewanella* are used as model microorganisms to examine Fe(III) reduction mechanisms (Myers and Nealson, 1990; Lovley *et al.*, 2004).

1.1.1.1 Electron donors

Iron-reducing organisms can couple Fe(III) reduction with the oxidation of organic acids, such as lactate and acetate (Lovley *et al.*, 2004). Acetate, which can be oxidized by *Geobacter* spp., is ubiquitous and is one of the most important electron donors in soils and sediments (Lovley *et al.*, 2004). In contrast, *Shewanella* spp. use formate or lactate as electron donors to reduce Fe(III) (Myers and Nealson, 1990). The oxidation of lactate coupled to Fe(III) reduction during DIR is described using the following half reaction:

$$CH_3CH(OH)COO^- + 4Fe(III) + 2H_2O \rightarrow CH_3COO^- + HCO_3^- + 4Fe(II) + 5H^+ \quad (1.1)$$

Some *Geobacter* species and most *Shewanella* species can also oxidize hydrogen while reducing Fe(III) minerals (Lovley *et al.*, 2011). Iron reduction may also be coupled with the oxidation of elemental sulfur (Brock and Gustafson, 1976) and the fermentation of glucose (Roberts, 1947), therefore, DIR is linked to sulfur and carbon cycling in the redox transition zones. Aromatic compounds (e.g., toluene, benzene) may also serve as electron donors during DIR, which contributes to soil remediation (Kane *et al.*, 2002; Zhang *et al.*, 2013b). Iron-ammox bacteria facilitate DIR with ammonium as the electron donor (Melton *et al.*, 2014).

1.1.1.2 Electron transfer strategies

Electrons that are generated through intracellular catabolism are transferred by proteins or quinones from the inner membrane to the periplasm and are further carried by primarily *c*-type cytochromes to the outer membrane (Lovley *et al.*, 2004; Shi *et al.*, 2009). Depending on the strategies employed, electrons can be transferred for varied distances. Direct contact of bacteria outer membrane with Fe(III) minerals allows electron hopping within <2 nm (Hernandez and Newman, 2001; Gray and Winkler, 2009). *Shewanella* spp. can secrete electron shuttles (e.g. flavins) (Marsili *et al.*, 2008) and chelators (Nevin and Lovley, 2002a) to facilitate electron transfer over nanometer-to-micrometer scale (Melton *et al.*, 2014). Moreover, both *Shewanella* spp. and *Geobacter* spp. are able to produce

conductive nanowires which expand the distance of electron transfer to micrometer scale (Reguera *et al.*, 2005; Gorby *et al.*, 2006).

1.1.2 Microbially mediated Fe(II) oxidation

In freshwater and marine systems, microaerophiles use O_2 as an electron acceptor to oxidize Fe(II) under aerobic conditions (Emerson and Moyer, 1997). Photoferrotrophs oxidize Fe(II) using light energy and bicarbonate as an electron acceptor (Widdel *et al.*, 1993). Phototrophic Fe(II) oxidation may have significantly contributed to the sedimentary material of the Precambrian banded iron formations (BIF) (Widdel *et al.*, 1993; Kappler *et al.*, 2005). Nitrate-reducing bacteria are also known to couple Fe(II) oxidation with nitrate reduction (Straub *et al.*, 1996). Moreover, if the resulting nitrite persists, Fe(II) will be further abiotically oxidized (Carlson *et al.*, 2013; Scholz *et al.*, 2016).

1.2 Variation of iron isotopes during Fe redox cycling

1.2.1 Iron isotope in the ancient rocks

Iron isotope measurements began in the late 1990s and have led to several important scientific advances in the field of Fe biogeochemistry (Beard et al., 1998; Bullen, 1998; Beard and Johnson, 1999). For example, intriguing large Fe isotope variations ($\delta^{56}Fe$ = ~-4 to ~+2‰) were discovered in BIFs, sedimentary pyrites, black shales, and carbonates between ~3.1 and ~2.4 Ga whereas earlier and later Fe isotope rock records are closer to the bulk crust ($\delta^{56}Fe_{bulk\ crust}$ = ~0‰) (Johnson *et al.*, 2008b; Busigny *et al.*, 2014; McCoy *et al.*, 2017). Anoxygenic photosynthesis (Widdel *et al.*, 1993; Olson, 2006) and oxygenic photosynthesis (Goldblatt *et al.*, 2006; Planavsky *et al.*, 2014) were established prior to the Great Oxidation Event (~2.4 Ga) (Holland, 1984) and oxidized Fe^{2+} in the ferruginous ocean to Fe^{3+} (Poulton and Canfield, 2011). The product Fe^{3+} became the electron acceptor for DIR, during which isotopically negative Fe^{2+} was extensively produced (Johnson *et al.*, 2008b; McCoy *et al.*, 2017; Eickmann *et al.*, 2018). It was also shown that Fe isotope variation is also the result of partial oxidation of Fe^{2+} by the anoxygenic photosynthesis or by oxygen produced during oxygenic photosynthesis (Rouxel *et al.*, 2005; Busigny *et al.*, 2014). Moreover, some studies suggest that ~3‰ ($\Delta^{56}Fe$) of Fe isotope fractionation can be induced by partial pyrite precipitation from Fe(II) (Guilbaud *et al.*, 2011; Rolison *et al.*, 2018). However, this non-redox process might be less significant in alteration of Fe isotope composition of the late Archean ocean (Czaja *et al.*, 2012).

1.2.2 Iron isotope fractionation during abiotic and biotic redox processes

On modern earth, we also observe non-zero Fe isotope values of solid and water samples from terrestrial aquifers (groundwater and sediments) (Guo *et al.*, 2013), lakes (water and sediments) (Busigny *et al.*, 2014), rivers (dissolved and suspended Fe) (Chen *et al.*, 2014), estuaries (pore water and sediments) (Rouxel *et al.*, 2008), continental shelves (pore water) (Homoky *et al.*, 2009), and seawater (dissolved and particulate Fe) (Labatut *et al.*, 2014). These Fe isotope values are produced by a series of complicated abiotic and biotic processes.

1.2.2.1 Abiotic Fe isotope fractionation

Iron isotopes fractionate during redox reactions due to different bond strengths of light and heavy isotopes. Bond strengths of light isotopes are lower than those of heavy isotopes (Anbar and Rouxel, 2007). In other words, light isotopes tend to stay in the weak bonds while heavier isotopes prefer strong bonds. For example, in aqueous environments, Fe isotope fractionation between Fe(II) and Fe(III) is ~-3‰ in Δ^{56}Fe based on both theoretical calculations (Anbar *et al.*, 2005) and experiments (Johnson *et al.*, 2002). Under oxic conditions, partial oxidation of Fe(II) produces isotopically heavy Fe(III) precipitation (Bullen *et al.*, 2001). Under anoxic conditions, Fe(II) adsorption on the surface of Fe (oxyhydr)oxides is an important abiotic redox process that produces Fe isotope fractionation:

$$^{i}\mathrm{Fe(II)}_{\mathrm{aqueous}} \rightarrow {}^{i}\mathrm{Fe(II)}_{\mathrm{adsorb}} \quad (1.2)$$

$$^{i}\mathrm{Fe(II)}_{\mathrm{adsorb}} + {}^{j}\mathrm{Fe(III)}_{\mathrm{mineral}} \rightarrow {}^{i}\mathrm{Fe(III)}_{\mathrm{mineral}} + {}^{j}\mathrm{Fe(II)}_{\mathrm{adsorb}} \quad (1.3)$$

$$^{j}\mathrm{Fe(II)}_{\mathrm{adsorb}} \rightarrow {}^{j}\mathrm{Fe(II)}_{\mathrm{aqueous}} \quad (1.4)$$

where $\mathrm{Fe(II)}_{\mathrm{aqueous}}$, $\mathrm{Fe(II)}_{\mathrm{adsorb}}$, $\mathrm{Fe(III)}_{\mathrm{mineral}}$ are aqueous Fe(II), adsorbed Fe(II), and mineral Fe(III); superscripts *i* and *j* indicate atomic masses of Fe atoms. In this process, an aqueous ^{i}Fe(II) atom (atomic mass is *i*) adsorbs onto Fe (oxyhydr)oxides surface and reduces the mineral ^{j}Fe(III) (atomic mass is j). The newly formed ^{i}Fe(III) becomes a mineral atom, while the new ^{j}Fe(II) may be released into the aqueous phase. Note that the Fe isotope exchange occurs between aqueous and mineral Fe phases during this abiotic redox process [Eq. (1.3)]. Iron oxides become more crystalline (recrystallization) after "adsorption-atom exchange-desorption" (equations 1.2-1.4) and may release the trace elements (e.g. As) contained in the original mineral to outer circumstance (Thompson *et al.*, 2006; Tishchenko *et al.*, 2015; Joshi and Gorski, 2016; ThomasArrigo *et al.*, 2017). The extent of isotope exchange may be enhanced with increasing pH (Reddy *et al.*, 2015; Zarzycki and Rosso, 2017) and decreasing particle size (Handler *et al.*, 2014; Frierdich *et al.*, 2015). However, the

adsorption of Si (Wu *et al.*, 2012a) and organic matter (Swanner *et al.*, 2017; ThomasArrigo *et al.*, 2017) can block the surface site of Fe oxides and restrict Fe isotope exchange between aqueous Fe(II) and Fe(III) minerals. Iron atom exchange has also been observed during mixing dissolved Fe(II) and smectite (Neumann *et al.*, 2015). While extensive research has focused on isotope partitioning relating to Fe oxides, Fe isotope partitioning involving clay minerals has not been systematically studied.

1.2.2.2 Biotic Fe isotope fractionation

In a landmark study published nearly two decades ago, Beard *et al.* (1999) showed that microbial reduction of Fe oxides produced isotopically light dissolved Fe(II). The mechanism for equilibrium Fe isotope fractionation between aqueous Fe(II) and Fe(III) minerals during DIR was first reported in the mid-2000s (Crosby *et al.*, 2005; Crosby *et al.*, 2007). The author showed that continuous Fe (oxyhydr)oxide reduction produces dissolved Fe(II), which undergoes electron transfer coupled to atom exchange (ETAE) with structural Fe(III) in the mineral phase (Crosby *et al.*, 2005; Crosby *et al.*, 2007). The fractionation factors between aqueous Fe(II) and Fe (oxyhydr)oxides (hematite, goethite, ferrihydrite) are ~-3‰ (Crosby *et al.*, 2005; Crosby *et al.*, 2007; Percak‐Dennett *et al.*, 2011). Moreover, Fe isotope fractionation also occurs during the Fe(II) oxidation by photoferrotrophs (Swanner *et al.*, 2015) and oxygen produced by cyanobacteria (Swanner *et al.*, 2017). However, Fe isotope fractionation may be weakened because that biogenic organics (e.g. exopolysaccharides) sorption on Fe minerals can partially suppress ETAE processes (Swanner *et al.*, 2017).

1.3 Clay in Fe redox cycling

1.3.1 Clays: An introduction

Clays, a group of hydrous aluminum phyllosilicates pervasively found in soils, are closely connected to human life due to their wide applications in various fields, such as geological research (e.g., geological and mineral history, petroleum prospect), environmental engineering (e.g., hazardous waste storage and treatment), medicine (e.g., digestive tract treatment), and manufacture (e.g., cosmetics, paints, pottery) (Meunier, 2005; Dong, 2012). In the oceanic system, clay minerals form through the precipitation of hydrothermal fluids (Sun *et al.*, 2012) or continental material transported by rivers (Michalopoulos and Aller, 1995). As Fe/Mg-rich clay minerals have been discovered on Mars, it was proposed that the paleoenvironment of Mars may be comparable with that of Earth (e.g. water occurrence, temperature, redox conditions) (Ehlmann *et al.*, 2011; Gainey *et al.*, 2017). Among

all clay minerals, smectites, including montmorillonite, nontronite, beidellite, and trioctahedral smectites, provide more bioavailable Fe(III) to microorganisms due to their high expandability (Dong *et al.*, 2009; Dong, 2012). One smectite layer comprises two tetrahedral sheets and one octahedral sheet (Figure 1.1). Oxygen atoms and hydroxyl groups connect tetrahedral and octahedral cations. Tetrahedral cations are primarily Si(IV), which can be substituted by Al(III) and Fe(III). Octahedral sheets prefer trivalent cations such as Al(III) and Fe(III), although one also finds Mg(II) and Fe(II). As a result of the cation substitution, negative charge forms in the smectite layers and is compensated with interlayer cations. Two model nontronite (an end member of smectite) minerals NAu-1 and NAu-2 will be further introduced in section 1.3.3.1.

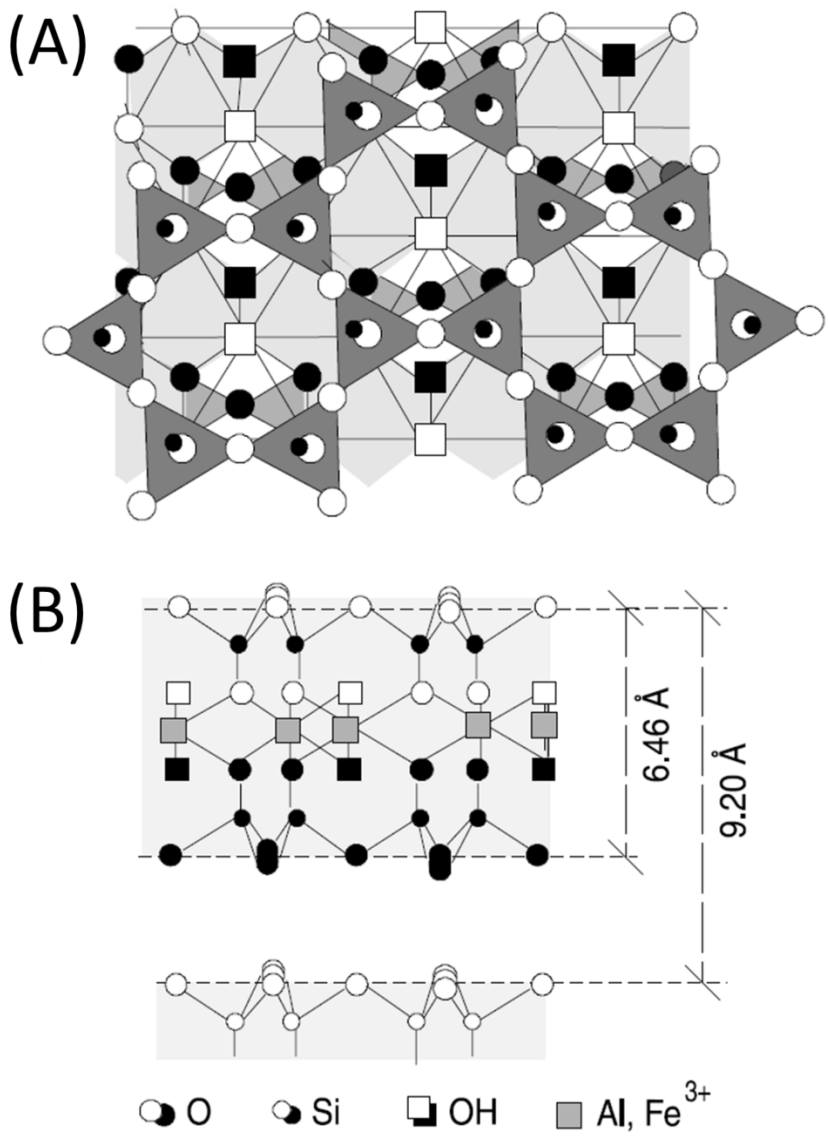

Figure 1.1. A) Top and B) side views of dioctahedral phyllosilicates (e.g., smectites) structure [modified from Meunier (2005)].

1.3.2 Clays and Fe cycling

In terms of global Fe cycling, continental Fe (oxyhydr)oxides and Fe sulfide in sea sediments have been considered the dominant source and sink for Fe in the modern ocean (Raiswell and Canfield, 1998; Raiswell, 2011; Raiswell and Canfield, 2012). Nevertheless, in the deep sea, Fe(II) sequestration by green clays is proposed to be several times higher than that by pyrite (Baldermann *et*

al., 2015). Microbially mediated clay dissolution, in turn, supplies Fe and Si to sediment pore water (Vorhies and Gaines, 2009). Persistent attention has been applied to clay minerals as they are proven to be an important player in biogeochemical Fe cycling (Kostka *et al.*, 1999a; Kim *et al.*, 2004; Stucki and Kostka, 2006; Dong, 2012; Pentrakova *et al.*, 2013).

Iron(III) in clay minerals is reducible by a wide range of microorganisms, including bacteria, archaea, and fungi (Dong *et al.*, 2009; Dong, 2012; Pentrakova *et al.*, 2013). The reduction of structural Fe(III) in clay can be coupled with the oxidation of organic compounds or H_2 by Fe- or sulfate- reducing bacteria (Li *et al.*, 2004; Lovley *et al.*, 2004; Jaisi *et al.*, 2005; Jaisi *et al.*, 2007; Liu *et al.*, 2012). Interestingly, methanogens are also capable of using H_2 or methanol as an electron donor to reduce Fe(III) in clays which in turn inhibits methanogenesis (Liu *et al.*, 2011; Zhang *et al.*, 2013a). Under anoxic conditions, structural Fe(II) in clay is oxidizable by Fe-oxidizing bacteria which use nitrate as the electron acceptor (Shelobolina *et al.*, 2003; Shelobolina *et al.*, 2012a; Shelobolina *et al.*, 2012b). While under oxidizing conditions, the oxidation of Fe(II) in clay induces the formation of hydroxyl radical (•OH), which is toxic to bacteria (Wang *et al.*, 2017; Yuan *et al.*, 2018). Consequently, Fe-clay cycling is closely linked to the redox conditions and the resulting carbon, sulfur, and nitrogen cycling in soils and sediments. (Liu *et al.*, 2011; Zhang *et al.*, 2012; Liu *et al.*, 2016).

The bioavailability of clay, which is equivalent to the fraction of microbially reducible Fe(III) or oxidizable Fe(II), is dependent on many factors including the clay's layer charge, particle size, total Fe content, Fe atom location, microorganism type, cell density, solution chemistry, electron donor type, byproduct accumulation, and temperature (Dong *et al.*, 2009; Dong, 2012). For example, expandable smectite is more reducible than other non-expandable clay minerals, such as illite, chlorite, palygorskite, and vermiculite (Dong *et al.*, 2009; Dong, 2012). Overall, the release of Fe(II) from clays into the aqueous phase following microbial Fe(III) reduction is less than that observed for Fe (oxyhydr)oxides (Kostka *et al.*, 1999a; Dong *et al.*, 2003). Consequently, the remaining structural Fe(II) in clays may serve as renewable Fe reservoirs during subsequent redox cycles (Ernstsen *et al.*, 1998; Chen *et al.*, 2018).

1.3.3 Mineralogical changes during clay redox cycling

1.3.3.1 Clay property changes

Iron predominantly located in the octahedral sheets of clay (Meunier, 2005). Microbial reduction of Fe(III) in clay starts from the edge surface (Ribeiro *et al.*, 2009; Stucki, 2011). Increasing reduction of structural Fe(III) leads to higher negative charge in clay layers, which in turn attracts interlayer cations (e.g. NH_4^+ and K^+) onto the basal planes (Dong, 2012). The addition of interlayer cations can be reversible, as expulsion of NH_4^+ and K^+ are induced upon oxidation of Fe(II) in clay minerals (Dong, 2012). Structural changes upon Fe(III) reduction have been observed, such as dehydroxylation, water molecules trapping in structural vacancies, and migration of Fe from *cis*- to *trans*- octahedral positions (Fialips *et al.*, 2002; Ribeiro *et al.*, 2009; Stucki, 2011).

A small fraction of Fe(III) may enter the tetrahedral sheets in some clay minerals which results in a decrease in the clay crystallinity (Baron *et al.*, 2017). The fraction of tetrahedral Fe(III) seems to be irrelevant to the total Fe(III) content of clay (Kaufhold et al., 2017). Theoretical calculations have shown that the reduction of Fe(III) mainly occurs in the octahedral sheets (Geatches *et al.*, 2012; Alexandrov *et al.*, 2013). However, tetrahedral Fe(III) was preferentially reduced during NAu-2 reduction by *Shewanella putrefaciens* CN32 with the addition of electron shuttle (Jaisi *et al.*, 2005).The typical bond lengths of Fe(III)-O in the octahedral and tetrahedral sheets of clay are ~2.01 (Soltermann *et al.*, 2014b) and 1.8 Å (Soltermann et al., 2013), respectively. The radius of structural Fe(II) is larger than that of structural Fe(III) (Meunier, 2005). Consequently, tetrahedra have to distort more than the octahedrons to accommodate the larger Fe(II) atoms produced during Fe(III) reduction. For example, near complete reduction of nontronite NAu-1 [containing only octahedral Fe(III)] and NAu-2 [~9% of total Fe(III) in tetrahedral sheets] (Figure 1.2) (Gates *et al.*, 2002; Jaisi *et al.*, 2005) increased the average Fe-O bond lengths from 2.005 to 2.073 Å (3% longer) and 2.006 to 2.100 Å (5% longer), respectively (Gorski et al., 2013). Based on these results, if we assume that 10% of total Fe is located in NAu-2 tetrahedra, ~5% of Fe-O bond extension implies that Fe(II)-O is ~16% longer than Fe(III)-O in the tetrahedral sheets. If tetrahedral Fe fraction is lower, the alteration of Fe-O bond length in tetrahedral sheets should be even greater. Besides, the redox changes in octahedral sheets also influence the tetrahedral structure (Fialips *et al.*, 2002).

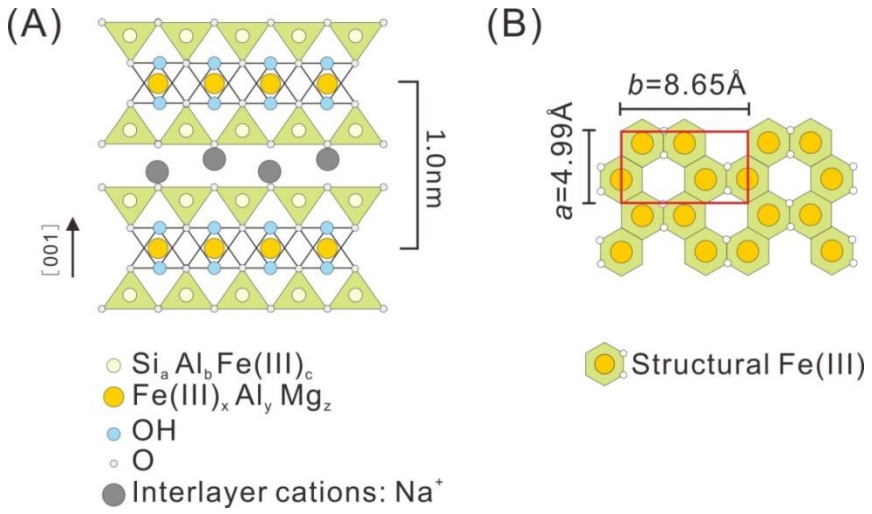

Figure 1.2. A) Side and B) top (tetrahedral sheets were omitted) views of dehydrated nontronite NAu-1 and NAu-2 structure. Subscript letters in legends of panel A indicate the stoichiometry of tetrahedral (a, b, c) and octahedral (x, y, z) cations within a unit cell. For NAu-1, a = 7.00, b = 1.00, c = 0, x = 3.38, y = 0.58, z = 0.05; for NAu-2, a = 7.57, b = 0.01, c = 0.42, x = 3.32, y = 0.52, z = 0.07 (Keeling *et al.*, 2000; Gates *et al.*, 2002). The red square in panel B indicates one unit cell in the octahedral sheets.

1.3.3.2 Secondary mineral precipitation

Microbial Fe reduction may lead to the dissolution of Fe, Si, and Al, which may precipitate as vivianite, silica, feldspar, and illite under anoxic conditions (Dong *et al.*, 2003; Zhang *et al.*, 2007; Liu *et al.*, 2015). Particularly, the transformation of smectite to illite (smectite-illitization or S-I) has been used as an indicator for hydrocarbon ripening during sediment diagenesis, as these two processes take place under similar conditions (Pevear, 1999). During diagenetic processes (high temperature and high pressure) S-I takes place after several months (Bruce, 1984; Freed and Peacor, 1989; Pevear, 1999; Brown *et al.*, 2001). Whereas, Kim *et al.* (2004) showed that S-I occurred within 14 days at room temperature and atmospheric pressure upon inoculation with a DIR bacterium (*Shewanella oneidensis* strain MR-1). S-I may cause irreversible mineralogical changes to clay, such as the increase of cation exchange capacity, layer collapse, and the fixation of Al and K (Koo *et al.*, 2014). These irreversible alterations may decrease the expandability and bioavailability of clay (Stucki, 2011; Zhao *et al.*, 2015).

Microbial Fe oxidation also contributes to secondary mineral formation. For example, the oxidation of reduced NAu-2 by an Fe-oxidizing bacteria (*Pseudogulbenkiania* sp. strain 2002) produced vivianite, ferrihydrite, and magnetite (Zhao *et al.*, 2013). The transformation of smectite to kaolinite is observed when smectite was mixed with Al-rich solution under high-temperature (150°C) condition (Ryan and Huertas, 2013). Biogenic kaolinite was observed during the microbial oxidation of an illite under room temperature, which involves both mechanisms of solid-state transformation (structural alteration in solid state) and dissolution-re-precipitation (Zhao *et al.*, 2017). During Fe redox cycling, the dissolved elements may re-precipitate at different soil horizons and form stratified mineral deposits (Altheide *et al.*, 2010; Huang *et al.*, 2018).

1.3.3.3 Surface reactions with Fe(II)

Reductively dissolved Fe(II) from clays may form inner- and outer- sphere complexes on different clay surfaces (Soltermann *et al.*, 2013). Iron(II) adsorption on the edge surface is most favorable at ferrinol FeO(H) sites (Alexandrov and Rosso, 2013). For example, Gorski and Scherer (2010) and Gorski *et al.* (2012) showed that Fe(II) adsorption to the edge of a montmorillonite (an end member in smectite group) is stabilized as Fe(III), which turns back to Fe(II) upon desorption. In contrast, Fe(II) adsorption to basal planes may reduce octahedrally coordinated structural Fe(III) and precipitate as Fe (oxyhydr)oxides, such as ferrihydrite, green-rust, and layered double hydroxides (Zhu and Elzinga, 2014; Starcher *et al.*, 2016; Jones *et al.*, 2017; Latta *et al.*, 2017). Iron(II) adsorption to nontronite surface forms Fe(III) precipitation, including ferrihydrite, lepidocrocite, and magnetite (Tsarev *et al.*, 2016).

1.3.4 Importance of clay redox cycling for soil nutrient and contaminant mobility

Iron redox cycling in clays may influence the immobilization and transportation of soil organic matter, nutrients, and contaminants. Clay serves as a shelter for organic matter during microbial interactions (Zeng *et al.*, 2016; Playter *et al.*, 2017). Soil nutrient dynamics and fertility can be directly impacted by clay redox cycling whereby important cations such as K^+ and NH_4^+ may be trapped within the interlayer space of clays during microbial Fe(III) reduction and released during clay re-oxidization (Dong, 2012). Moreover, microbially produced Fe(II) in clays is reactive towards various organic contaminants, such as p,p'-DDT, chlorinated aliphatics, nitroaromatic compounds and polychlorinated compounds, thereby representing a route for bioremediation (Dong *et al.*, 2009; Dong, 2012; Pentrakova *et al.*, 2013). The siloxane (≡Si-O-Si≡) basal plane surface can also adsorb aromatic hydrocarbons (Jaynes and Boyd, 1991). However, adsorption on siloxane inhibits the

degradation of nitroaromatic compounds, as outer-sphere Fe(II) is not reactive towards nitroaromatic compounds (Hofstetter *et al.*, 2003). Furthermore, inorganic contaminants such as chromium(VI) can be reduced and immobilized by structural Fe(II) (Bishop *et al.*, 2014; Joe-Wong *et al.*, 2017; Liu *et al.*, 2018) whereby the product, Cr(III), is not re-oxidized or remobilized when clay is exposed to O_2 (Markelova *et al.*, 2017). Similarly, the aluminol site (octahedral Al on clay edge) of kaolinite and ferrinol site of montmorillonite are favorable for uranium sorption and immobilization (Catalano and Brown, 2005; Bachmaf and Merkel, 2011). In addition, clays and other hydrous phyllosilicates in soil are capable of retaining radionuclides (Anastácio *et al.*, 2008; Bishop *et al.*, 2011; Wampler *et al.*, 2012).

1.4 Research questions and methodologies

1.4.1 Reactivity/bioavailability of clay

The Fe-rich smectite (e.g. nontronite) is more reducible than the non-expandable illite (Bishop *et al.*, 2011; Zhang *et al.*, 2012), however, the extent and rate of microbial reduction varies across experimental conditions. The maximum extents of microbial nontronite reduction only reach ~40% even when exogenous electron shuttles are added (Jaisi *et al.*, 2005; Bishop *et al.*, 2011; Zhang *et al.*, 2013a; Koo *et al.*, 2014). Moreover, bacteria can only reduce one- to a few- layer(s) of Fe atoms on the edge sites of clay (Ribeiro *et al.*, 2009; Stucki, 2011). Thus, the reactivity or bioavailability of clay is determined by the fraction of redox-active Fe on the edge. However, Jaisi *et al.* (2005) suggested that tetrahedral Fe(III) is more reducible than most octahedral Fe(III). Therefore, one of the main objectives of this thesis is to elucidate the bioavailability of Fe(III) on the edge sites and in tetrahedral sheets.

Purified nontronite NAu-1 (contains only octahedral Fe) and NAu-2 (contains octahedral and tetrahedral Fe) were subjected to a series of experiments (microbial reduction, chemical reduction, and mixing experiments). Our hypotheses were based on the experiment results including Fe concentrations and Fe isotope compositions of different phases, the dissolution of structural cations (Si, Al, Fe, Mg), and mineralogical changes. The bioavailability of NAu-1 and NAu-2 during a single microbial reduction is well reflected by the Fe isotope fractionation between different Fe phases. We hypothesize that a finite bioavailable Fe pool is in each clay mineral.

1.4.2 Reversibility of clay during Fe redox cycling

Clay minerals are expected to be renewable Fe sources for microorganisms (Ernstsen *et al.*, 1998). Variations in clay reactivity during redox cycling have been frequently studied. For example, Zhao *et al.* (2015) found that the clay structure and the fraction of reactive Fe were largely reversible during redox cycling when mediated by bacteria. The long-term incubation of NAu-1 with *S. oneidensis* MR-1 led to a permanent reduction of structural Fe(III) which was not able to be re-oxidized by pure O_2 within 24 h (Koo *et al.*, 2014). Similarly, the redox cycling of SWa-1 (a ferruginous smectite) resulted in some structural changes and increasing fraction of residual Fe(II) after re-oxidization (Stucki, 2011). On the basis of understanding that a finite bioavailable Fe pool is in each clay (research question in 1.4.1), further questions of this thesis are: 1) How does the fraction of bioavailable Fe change within and across redox cycles? and 2) What is the underlying mechanism(s) responsible?

To address the aforementioned questions, three consecutive redox cycles of NAu-1 inoculated with *S. oneidensis* were carried out while ensuring that each reducing cycle was conducted under the same conditions as the experiment in 1.4.1. The Fe(II) concentrations and the isotope compositions of different phases, the dissolution of structural cation, and the variation of particle/crystal size of clay were monitored along each redox cycle. Solid phases before and after redox cycles were carefully characterized to study the impact of secondary precipitation on the reversibility of clay.

1.4.3 Redox induced Fe isotope fractionation in clays

Most Fe(III) atoms in smectite are located in the octahedral sheets (Gates *et al.*, 2002; Baron *et al.*, 2017). The octahedral Fe(III) exposed on edge sites of nontronite coordinates similarly to that of hematite, which is capable of undergoing ETAE with aqueous and adsorbed Fe(II). Consequently, the Fe(III) atoms on edge sites of nontronite may also be exchangeable with the hydroxyl group bound Fe(II). The octahedral Fe(III) atoms are covered by tetrahedral silica sheets which are perpendicular to the [001] axis. Therefore, the atom exchange through the basal plane surface is considered difficult. The layered structure exposes less reactive Fe(III) on the surface of clay than that of Fe (oxyhydr)oxides. However, the presence of tetrahedral Fe(III), such as in NAu-2, may enhance the reactivity of clay, as tetrahedral Fe(III) is potentially exchangeable with aqueous Fe(II). The microbial reduction of clay involves the reduction of structural Fe(III) and the dissolution of Fe(II). The dissolved Fe(II) in turn will interact with the structural Fe(III) exposed on the edge and/or basal

plane surface. Iron isotope fractionations between different Fe pools in all experiments were tracked to elucidate the mechanism(s) of ETAE during Fe reduction and oxidation.

1.5 Structure of thesis

Chapters 2-4 are three research papers, aiming to answer the research questions and achieve the research goals as outlined in section 1.4. Chapter 2 has been published in *Environmental Science & Technology* and was named "The First Runner-Up of ES&T's Best Papers of 2016" (Shi *et al.*, 2016). Chapter 2 reported a model of ETAE during clay reduction and provides the mechanism for why Fe isotope fractionation decreased with increasing reduction extent. Chapter 3 further investigated the renewability of Fe(III) in NAu-1 during successive redox cycles and presents the hypothesis that decreasing Fe(III) bioavailability in NAu-1 is due to the preferential reductive dissolution of small clay particles. Lastly, in Chapter 4, the potential for ETAE through the basal plane surface was proposed while also highlighting the importance of tetrahedral Fe(III) in NAu-2 for enhanced microbial Fe redox cycling.

Chapter 2

Iron isotope fractionations reveal a finite bioavailable Fe pool for structural Fe(III) reduction in nontronite NAu-1

2.1 Summary

We report on stable Fe isotope fractionation during microbial and chemical reduction of structural Fe(III) in nontronite NAu-1. $^{56}Fe/^{54}Fe$ fractionation factors between aqueous Fe(II) and structural Fe(III) ranged from −1.2 to +0.8‰. Microbial (*Shewanella oneidensis* and *Geobacter sulfurreducens*) and chemical (dithionite) reduction experiments revealed a two-stage process. Stage 1 was characterized by rapid reduction of a finite Fe(III) pool along the edges of the clay particles, accompanied by a limited release to solution of Fe(II), which partially adsorbed onto basal planes. Stable Fe isotope compositions revealed that electron transfer and atom exchange (ETAE) occurred between edge-bound Fe(II) and octahedral (structural) Fe(III) within the clay lattice, as well as between aqueous Fe(II) and structural Fe(III) via a transient sorbed phase. The isotopic fractionation factors decreased with increasing extent of reduction as a result of the depletion of the finite bioavailable Fe(III) pool. During stage 2, microbial reduction was inhibited while chemical reduction continued. However, further ETAE between aqueous Fe(II) and structural Fe(III) was not observed. Our results imply that the pool of bioavailable Fe(III) is restricted to structural Fe sites located near the edges of the clay particles. Blockage of ETAE distinguishes Fe(III) reduction of layered clay minerals from that of Fe oxyhydroxides, where accumulation of structural Fe(II) is much more limited.

2.2 Introduction

Transformations of clay minerals in near-surface environments influence soil fertility, contaminant mobility, and hydrocarbon maturation (Hofstetter *et al.*, 2006; Stucki, 2006; Dong, 2012; Peretyazhko *et al.*, 2012; Wu *et al.*, 2012b). Iron (Fe) is ubiquitous in clay minerals (Jaisi *et al.*, 2005; Stucki, 2006). The oxidation state of structural Fe greatly influences the physical and chemical properties of clay minerals, including specific surface area, cation exchange capacity, structure and stability, as well as hydration and swelling (Stucki and Tessier, 1991; Stucki *et al.*, 2002; Stucki, 2006; Stucki, 2011). These processes in turn determine the fate of contaminants such as metal cations (Abollino *et al.*, 2003), radionuclides and analogs (Catalano and Brown, 2005; Wampler *et al.*, 2012),

and organic contaminants (Haderlein *et al.*, 1996). Structural Fe(III) in clay minerals also represents a potentially renewable source of terminal electron acceptor for dissimilatory Fe(III)-reducing bacteria in soils and sediments, as Fe(III) in clay minerals is not subjected to reductive dissolution to the same extent as in Fe(III) oxyhydroxides (Kostka *et al.*, 1999a; Kostka *et al.*, 1999b; Dong *et al.*, 2003).

Although the importance of clay transformation by microbes has been recognized over the last two decades, the electron transfer and atom exchange pathways during reduction of structural Fe(III) in clays remain unclear (Stucki *et al.*, 2002; Dong *et al.*, 2009). Microbial reduction of Fe(III) in clays has been proposed to start from the edges and progress through the octahedral sheet as a moving front (Ribeiro *et al.*, 2009), in contrast to a pseudorandom chemical reduction starting from the basal plane surfaces (Komadel *et al.*, 2006). Two mechanisms for microbial reduction of Fe(III) in clays have further been suggested: solid-state and dissolution−precipitation, where the former refers to reduction within the clay structure without significant release of Fe(II) to the aqueous phase (Lee *et al.*, 2006; Kashefi *et al.*, 2008), and the latter to dissolution of the clay structure and precipitation of secondary minerals (Kostka *et al.*, 1999a; Dong *et al.*, 2003; Kim *et al.*, 2004). Operation of either mechanism may depend on the clay mineral, growth medium composition, and the density and type of microorganisms (Dong *et al.*, 2009).

Stable Fe isotopes are a powerful tracer of biogeochemical processes involving redox transformations of Fe minerals (Johnson *et al.*, 2008b). Iron isotope compositions in natural environments span a range of up to 6‰ in δ^{56}Fe values (defined as the $^{56}Fe/^{54}Fe$ ratio of a sample relative to a reference material, such as igneous rocks) (Hofmann *et al.*, 2009; Nishizawa *et al.*, 2010), with the largest variations observed in Precambrian marine sedimentary rocks (Johnson *et al.*, 2008b; McCoy *et al.*, 2017). Both biological and abiological processes can fractionate Fe isotopes, with the largest fractionations associated with redox changes (Crosby *et al.*, 2005; Wu *et al.*, 2012a). Coupled electron and atom exchange has been shown to be the mechanism responsible for Fe isotope fractionation during microbial Fe(III) oxide reduction (Crosby *et al.*, 2007; Wu *et al.*, 2009), as well as during abiological interaction between aqueous Fe(II) and Fe(III) oxides (Beard *et al.*, 2010; Wu *et al.*, 2011). Here, we use Fe isotope fractionations as a tracer to investigate atom exchange and changes in bonding that are produced by both microbial and chemical reduction of Fe-rich smectite NAu-1. A similar approach has proven valuable in understanding electron transfer and atom exchange (ETAE) pathways during reduction of structural Fe(III) in oxides/hydroxides. Notwithstanding extensive research on microbial and chemical reduction of structural Fe(III) in clay

minerals (Dong *et al.*, 2003; Kim *et al.*, 2004), no information currently exists on the partitioning of Fe isotopes during reduction of structural Fe(III) in clays. This study aims to provide new insights into ETAE pathways during reduction of structural Fe in clay minerals.

2.3 Materials and methods

2.3.1 Clay mineral preparation

Nontronite NAu-1 [$(Ca, Na, K)_{1.05}[Si_{6.98}Al_{1.02}][Al_{0.29}Fe_{3.68}Mg_{0.04}]O_{20}(OH)_4$] was obtained from the Clay Minerals Society (Keeling *et al.*, 2000) and further treated by a size-fractionation (<0.5 µm), Na^+-homoionization and purification process (Jackson, 1956; Neumann *et al.*, 2013). The purified nontronite was freeze-dried, pulverized and then sieved (100 mesh/150 µm). X-ray diffraction (XRD) and scanning electron microscopy (SEM) coupled to energy dispersive spectroscopy (EDS) analysis showed no evidence for the presence of impurities, such as goethite, quartz, or kaolin, in the purified NAu-1 (Figure A.1 and A.2).

2.3.2 Microbial and chemical reduction experiments

An overview of the experimental design is given in Table 1, additional details can be found in Table A.1. *Shewanella oneidensis* MR-1 (Myers and Nealson, 1988a) was grown aerobically in LB media, prior to inoculation of the clay-bearing suspensions. Cells were harvested and washed twice with sterile HEPES {2-[4-(2-hydroxyethyl)piperazin-1-yl] ethanesulfonic acid, $C_8H_{18}N_2O_4S$} buffer before adding 2×10^8 cells/mL to 120 mL of HEPES buffer (100 mM, pH 6.8) containing 5 mg/mL NAu-1 [Fe(III) electron acceptor], 40 mM Na-lactate (electron donor), 100 µM KH_2PO_4, and 5 mM $(NH_4)_2SO_4$. *Geobacter sulfurreducens* strain PCA (Caccavo *et al.*, 1994) was incubated with fumarate (electron acceptor) and acetate (carbon and energy source) prior to inoculation. Cells were harvested and washed once with sterile, anaerobic PIPES buffer before adding 5×10^8 cells/mL to 120 mL anaerobic, H_2-saturated PIPES [piperazine-N,N'-bis(2-ethanesulfonic acid), $C_8H_{18}N_2O_6S_2$] buffer (10 mM, pH 6.8) containing 5 mg/mL NAu-1. Acetate (final 20 mM) and the electron shuttle anthraquinone-2,6-disulfonate (AQDS, final 0.1 mM) were successively added to the *Geobacter* reactors 137 days and 155 days after initiating the experiments, respectively.

In order to maintain anaerobic conditions, the glass reactors were crimp sealed using gas impermeable butyl rubber stoppers, and shaken at 100 rpm. Duplicate biotic and abiotic (cell-free) control reactors were prepared. The pH values in the biotic reactors remained stable at 6.8 even after

more than 400 days of incubation. Parallel abiotic reduction reactors were prepared by adding 15 to 200 mg sodium dithionite to 10 mL 100 mM HEPES buffer (pH 6.8) with NAu-1 (5 mg/mL) to achieve an analogous or greater extent of reduction as observed in the biotic reactors. The abiotic reactors were kept at room temperature, or at 70 ℃ to achieve a higher extent of reduction (Table A.1). Limited reaction time was employed to avoid a much higher extent of reduction [i.e. 20 days for nearly 100% reduction as in a previous study (Luan *et al.*, 2014)].

Table 2.1. Experimental design

Experiments	Setup	Number of reactors	Processes	Presence of Fe(II)	Electron transfer	Atom exchange
Abiotic control	NAu-1 + medium	1	Non-reductive dissolution	No	No	Yes
Biological reduction	NAu-1 + medium + cells (*Shewanella*/ *Geobacter*)	2 duplicates	Reduction, dissolution (reductive & non-reductive)	Yes	Yes	Yes
Chemical reduction	NAu-1 + dithionite	6 individuals	Reduction, dissolution (reductive & non-reductive)	Yes	Yes	Yes
Abiotic exchange	NAu-1 + Fe(II) (4:1 molar Fe ratio)	2 duplicates	Exchange (equivalent to a fixed extent of reduction)	Yes	Yes	Yes

2.3.3 Exchange experiments of Fe(II) with NAu-1

A ^{57}Fe enriched Fe(II) stock solution ($\delta^{56/54}$Fe = −0.49‰ and $\delta^{57/56}$Fe = +104.83‰) was prepared by mixing a ^{57}Fe-enriched spike with a natural abundance Fe(II) solution at a molar ratio of ca. 1:500. Batch reactors contained 15 mL of 25 mM MES buffer adjusted to pH 6.0, 50 mM NaCl to provide a constant ionic strength, and 2 mM of ^{57}Fe-enriched aqueous Fe(II). The reaction was started by adding 30.0 mg of purified NAu-1 powder to the reactors.

2.3.4 Iron extractions and chemical analysis

At selected time points during the reduction experiments, 10 mL of the clay suspensions were collected from each reactor and centrifuged (6500 rpm, 15 min). The supernatant was filtered (0.2 μm) and acidified to isolate the operational defined aqueous fraction. The remaining solid was extracted for 4 h with 1 M $CaCl_2$ (pH 7) to remove the Fe(II) sorbed on the clay mineral basal planes (Neumann *et al.*, 2013). This extraction relies on the displacement of basal plane sorbed Fe^{2+}, including interlayer Fe^{2+}, by excess Ca^{2+} (Bergaya *et al.*, 2006). The mixture was centrifuged, filtered and acidified for preservation. Then the remaining solid was mixed with 5 mL 1 M NaH_2PO_4 (pH 5) for 18 h to isolate the Fe(II) sorbed to the clay mineral edge OH-groups (Neumann *et al.*, 2013). This extraction is based on the high affinity of Fe-OH groups for phosphate ions (Schoonheydt and Johnston, 2006). In addition to edge-bound Fe(II), this extraction may also partially recover structural Fe(II) (Skulan *et al.*, 2002). The extract was filtered and acidified. The remaining solid was mixed with 5 mL 0.5 M HCl for 24 h to extract the residual structural Fe(II) (Jaisi *et al.*, 2005). Note that 0.5 M HCl may also partially remove structural Fe(III). The mixture solution was centrifuged and filtered. For chemical reactors, the residual solid after the 0.5 M HCl extraction was further treated with 48% HF to quantify any remaining structural Fe(II) (Amonette and Templeton, 1998).

Iron(II) concentrations were determined spectrophotometrically using Ferrozine (Stookey, 1970) for the reduction experiments and 1,10-phenanthroline (Schilt, 2013) for the exchange experiments. Total Fe [Fe(tot)] was measured after addition of 10% hydroxylamine hydrochloride to reduce Fe(III). The Fe(III) concentration was then calculated as the difference of Fe(tot) and Fe(II). In the HF treatment, 1,10-phenanthroline monohydrate was used to form strong tris complexes with Fe(II) in the HF-H_2SO_4 matrix (Amonette and Templeton, 1998). Next, H_3BO_4 and Na_2-citrate were added and the absorbance was measured at 510 nm. This method has been shown to quantitatively determine Fe(II) in silicate minerals (Amonette and Templeton, 1998). Aqueous silica concentrations were analyzed using a standard colorimetric method (Clesceri, 1989).

2.3.5 Iron isotope analysis

Test solutions, used to check the accuracy of Fe isotope analyses, were prepared by adding 50 μg of HPS (high purity standard) Fe to 10 mL 100 mM HEPES buffer, 0.5 to 5 mL 1 M $CaCl_2$, 0.5 to 5 mL 1 M NaH_2PO_4, or 3 to 10 mL 2.5 to 15 mg/mL dithionite in order to identify potential Fe isotope fractionation artifacts produced during the chemical extractions or by the use of dithionite as chemical reductant. Wet chemistry was performed on the solutions to separate Fe from other cations

by passing them through an anion-exchange resin (Beard *et al.*, 2003). Iron isotope compositions of the aqueous fractions, extracts and test solutions were measured by a multicollector, inductively coupled plasma mass spectrometer (MC-ICP-MS) at University of Wisconsin, Madison, following established protocols (Beard *et al.*, 2003). All Fe isotope data were reported as δ^{56}Fe in units of per mil (‰) relative to average terrestrial igneous rocks [δ^{56}Fe = 0.00 ± 0.05‰ (Beard *et al.*, 2003)]. Stable Fe isotope fractionation between two phases A and B is defined as $\Delta^{56}Fe_{A\text{-}B} = \delta^{56}Fe_A - \delta^{56}Fe_B$, following standard practice. Measured external precision for δ^{56}Fe was ±0.05‰ (2σ, n = 37). The average δ^{56}Fe value of the test solutions was 0.50 ± 0.08‰ (2σ; n = 24), which is identical to the isotope composition measured for the pure HPS Fe solutions (δ^{56}Fe = 0.49 ± 0.06‰; 2σ; n = 27). The measured Fe isotope composition of the IRMM-014 Fe isotope standard was −0.08 ± 0.05‰ (2σ; n = 48), which lies within error of the long-term value in the UW-Madison lab of −0.09‰ relative to the average of igneous rocks.

2.4 Results

2.4.1 Microbial and chemical reduction of NAu-1

Smectite has a 2:1 layer structure in which an octahedral sheet is bound by two tetrahedral sheets through sharing the apical oxygens (Kloprogge *et al.*, 1999). Structural Fe(III) in NAu-1 [~22 wt % (Keeling *et al.*, 2000)] is located in the octahedral sheet with edge sites exposed to solution. Reduction of structural Fe(III) in the biological and chemical experiments was monitored by measuring Fe(II) in the aqueous phase and in the solutions produced by the three sequential wet-chemical extraction steps: i. 1 M $CaCl_2$, which quantitatively removes Fe(II) sorbed onto basal planes; ii. 1 M NaH_2PO_4, which releases Fe(II) bound to OH-groups at edge sites and partial structural Fe(II); and iii. 0.5 M HCl, which removes structural Fe(II) and a portion of structural Fe(III). The Fe(II) and Fe(tot) data showed that Fe released to aqueous solution and Fe in the first two extractions were entirely comprised of Fe(II), while the 0.5 M HCl extracts contained a mixture of Fe(II) and Fe(III) (Table A.2). In other words, structural Fe(III) is the only Fe(III) phase throughout our experiments. The selective release of basal plane sorbed Fe(II) and edge OH-group bound Fe(II) during the first two extractions has previously been confirmed by Mössbauer analysis of Fe(II)-reacted NAu-1 and the reference Fe-free montmorillonite SYn-1 (Neumann *et al.*, 2013). It is not possible to resolve whether edge-bound Fe(II) derives from *in situ* reduction or readsorbed Fe(II).

In the biological reduction experiments with *Shewanella* and *Geobacter*, Fe(II) concentrations increased with time (Figure 2.1, Table A.2). Edge plus structural Fe(II) accounted for the largest fraction of biogenic Fe(II) (55−71%; Table A.3, Figure A.3), structural Fe(II) in the interior of the NAu-1 accounted for 13 to 21% of total produced Fe(II), and aqueous Fe(II) accounted for 4−12% total produced Fe(II). Only 2−7% of the Fe(II) released in the experiments with *Shewanella* sorbed onto basal planes. During NAu-1 reduction by *Geobacter* in the presence of AQDS, a larger fraction (15−17%) of basal plane sorbed Fe(II) was observed. However, together aqueous and basal-sorbed Fe(II) accounted for a fairly constant fraction of the total Fe(II) produced by *Shewanella* and *Geobacter* (18 ± 2%, Table A.3, Figure A.3).

In the chemical reduction experiments (i.e., without bacteria), edge plus structural Fe(II) accounted for 54−64% of total Fe(II) (Table A.3, Figure A.3), similar to that of biological experiments. Interior structural Fe(II) accounted for 22−41% of total Fe(II) and showed an increasing trend with increasing extent of reduction. Compared to the biological reduction experiments, the larger fraction of interior structural Fe(II), for a comparable extent of reduction (Table A.3, Figure A.3), suggests that dithionite was able to reduce more of the interior pool of octahedral Fe(III), probably due to the small molecular size of dithionite [S−O and S−S bond length of 1.5 and 2.3 Å, respectively (Weinrach *et al.*, 1992)], enabling it to diffuse into the clay interior through the basal planes [hexagonal cavity 2.7 Å (Meunier, 2005)] (Figure A.4C). Aqueous Fe(II) represented 4−13% of total Fe(II), and basal-sorbed Fe(II) accounted for the smallest percentage (1−5%). Further HF treatment recovered less than 2% of total produced Fe(II), indicating that 0.5 M HCl was sufficient to recover all structural Fe(II) in our experiments.

Dissolved and sorbed silica concentrations indicated a maximum of 1.6% clay mineral dissolution (Figure A.5), which is consistent with limited reductive dissolution of Fe-containing clays (Dong *et al.*, 2009). No Fe-bearing secondary minerals were observed (by SEM) on clay surfaces in biologically or chemically reduced NAu-1 after more than 400 days incubation (Figure A.6, see Appendix A for a detailed discussion).

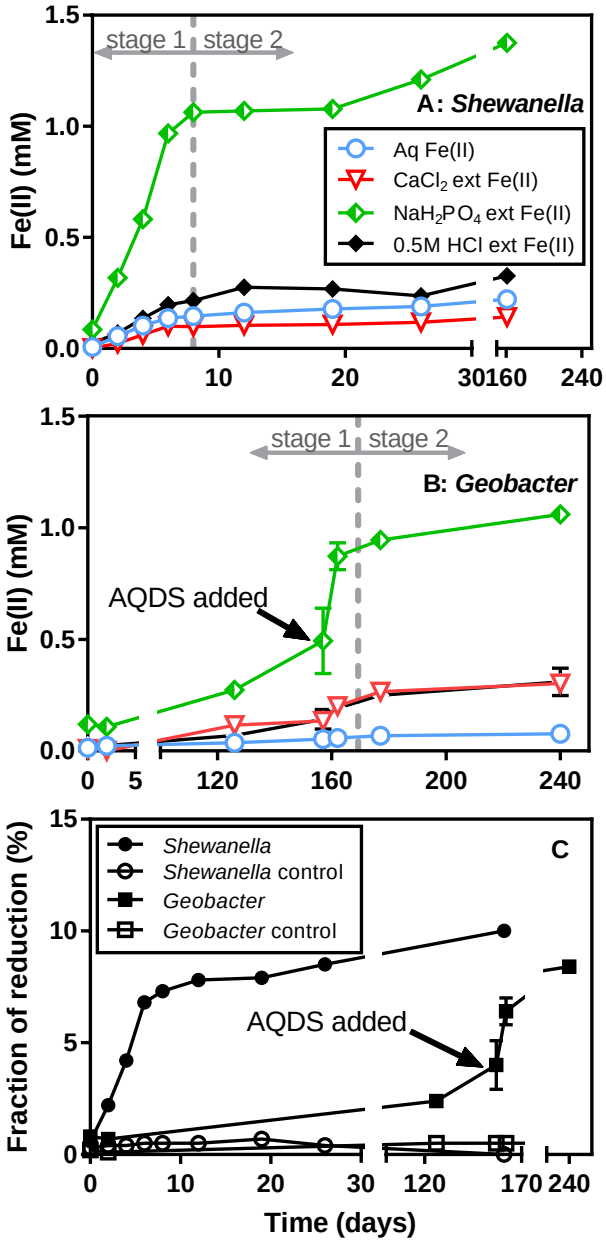

Figure 2.1. Time-dependent build-up of different Fe(II) pools during biological reduction of NAu-1 by *Shewallena* (panel A) and *Geobacter* (panel B). The pools include dissolved Fe(II), 1 M $CaCl_2$ extractable Fe(II) (basal planes), 1 M NaH_2PO_4 extractable Fe(II) (edge plus structural sites), and 0.5 M HCl extractable Fe(II) (interior sites). The electron shuttle AQDS was added after 155 days to the *Geobacter* reactors to facilitate reduction. The vertical gray

lines indicate the transition from stage 1 to stage 2. The fraction of reduction was calculated as the total Fe(II) relative to the initial total Fe of NAu-1 (panel C). Error bars indicate one standard deviation from duplicate reactors. No reduction was observed in controls where no cells were present.

2.4.2 Changes in Fe isotope composition during microbial and chemical reduction

Significant changes in the Fe isotope compositions of the various Fe(II) and Fe(III) pools occurred during biological and chemical reduction (Figure 2, Table A.4), with marked deviations from the starting bulk NAu-1 composition (δ^{56}Fe = 0.59‰). The δ^{56}Fe values for octahedral Fe(III) extracted by 0.5 M HCl were calculated by assuming that structural Fe(II) in 0.5 M HCl had the same isotope composition as the edge plus structural Fe(II) in the NaH_2PO_4 extract (see Appendix A for details of calculation and mass balance discussion).

During the initial, rapid stage of reduction, structural Fe(III) extracted by 0.5 M HCl was isotopically heavier than the starting bulk NAu-1 in all reduction experiments (stage 1, Figure 2.2), while all the δ^{56}Fe values of the different Fe(II) pools were lower than those of structural Fe(III). Basal-sorbed Fe(II) exhibited the most negative δ^{56}Fe values among all Fe(II) pools, with the lowest values observed when the extent of reduction was slightly above 2%. Edge plus structural Fe(II) generally had the heaviest Fe isotopic compositions of all the Fe(II) pools, while aqueous Fe(II) exhibited intermediate δ^{56}Fe values between those of basal and edge plus structural Fe(II). The isotopic Fe compositions of all three Fe(II) pools converged toward that of the starting bulk NAu-1 by the end of stage 1.

During the second stage of reduction, the Fe isotope composition of aqueous and basal-sorbed Fe(II) continued to become isotopically heavier, while that of edge plus structural Fe(II) decreased or remained constant (stage 2, Figure 2.2, Table A.4). The final δ^{56}Fe values of aqueous and basal-sorbed Fe(II) were close to (*Geobacter* reactors, Figure 2.2B), or even higher than (*Shewanella* and chemical reactors, Figure 2.2A and C), that of the starting bulk clay. Meanwhile, the δ^{56}Fe values of edge plus structural Fe(II) and structural Fe(III) decreased with increasing extent of reduction (Figure 2.2) until, in the chemical reduction experiments, the two eventually reached identical δ^{56}Fe values below that of the starting bulk clay (Figure 2.2C). Although three chemical reactors in stage 2 were run at elevated temperature (70 ℃) and one reactor at room temperature (Table A.1), the general trends of the Fe isotope compositions were quite similar to those observed in the microbial reduction experiments (Figure 2).

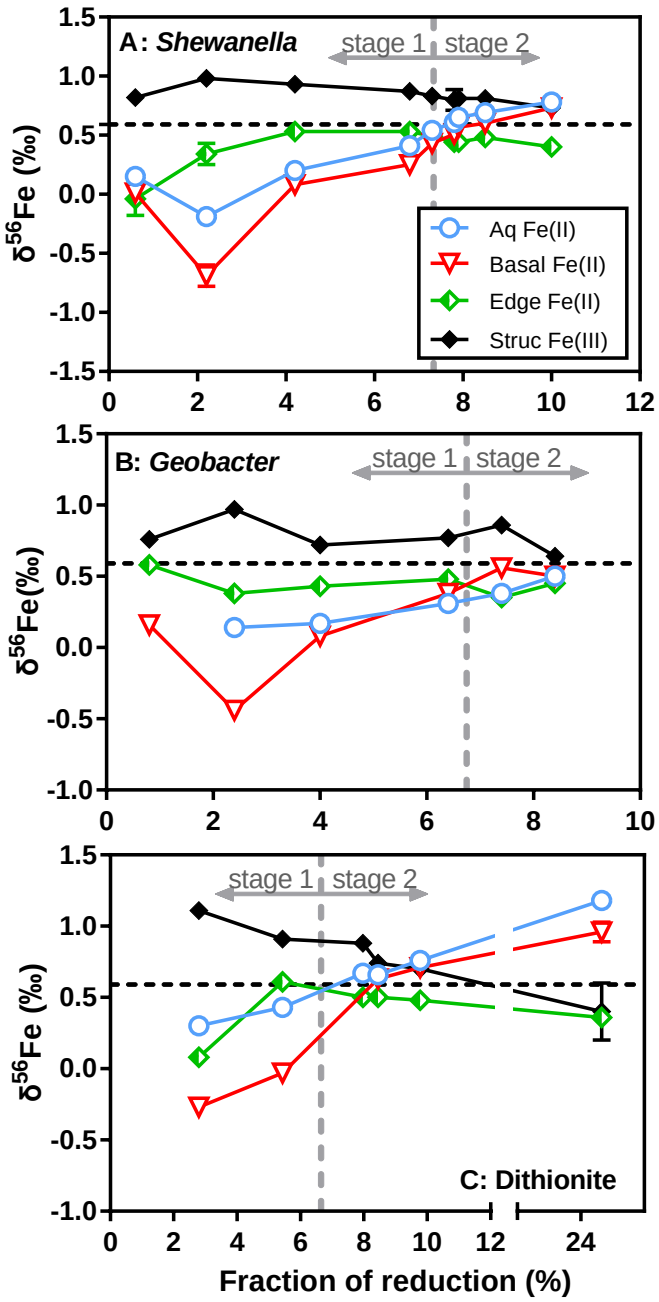

Figure 2.2. Iron isotope compositions of the different Fe(II) pools (aqueous, basal-sorbed, and edge plus structural sites) and structural Fe(III) in the 0.5 M HCl extracts (see Appendix A for calculation of the latter) during NAu-1 reduction by *Shewanella* (A), *Geobacter* (B), and dithionite (C) under pH = 6.8. Dashed horizontal lines indicate the original δ^{56}Fe value of bulk

NAu-1, representing δ^{56}Fe of the starting structural Fe(III). Note that, during stage 2, aqueous Fe(II) becomes isotopically heavier than edge plus structural Fe(II). The transition from stage 1 to stage 2 is thus characterized by systematic changes in the biological reduction kinetics (see Figure 2.1) and the Fe isotopic signatures. Error bars indicate one standard deviation based on either duplicate reactors for microbial reduction experiments or repeated analyses for chemical reduction experiments.

2.4.3 Changes in Fe isotope composition during clay–Fe(II) exchange.

In the exchange experiments, the Fe isotope compositions of the different Fe pools deviated from the δ^{56}Fe values of starting NAu-1 and aqueous Fe(II) after 30 and 57 days (Figure 2.3). Structural Fe extracted by 0.5 M HCl was isotopically heavier than the starting NAu-1. Aqueous and basal-sorbed Fe were isotopically lighter than the Fe(II) added at the start of the experiments, while NaH_2PO_4 extractable Fe was heavier. During the entire duration of the exchange experiments, pH remained stable at 6. The extent of atom exchange has been shown to be ca. 4% between aqueous Fe(II) and NAu-1 based on δ^{57}Fe values, which have been reported previously (Neumann *et al.*, 2015). The δ^{56}Fe data for the same experiments have been first reported in the current study.

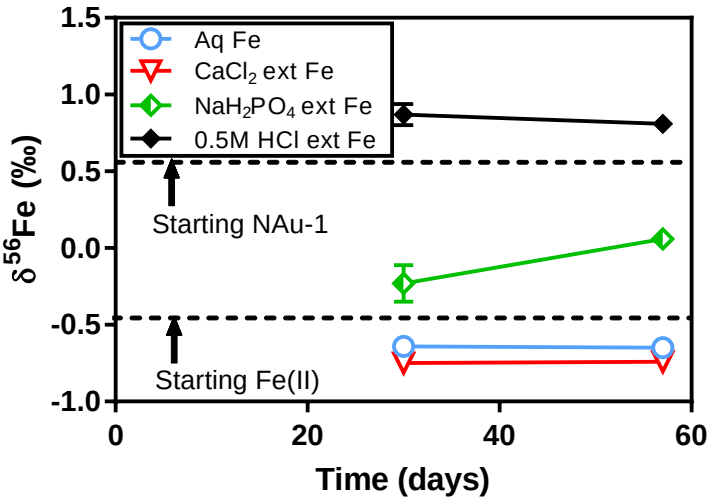

Figure 2.3. Iron isotope compositions of different Fe pools upon mixing of aqueous Fe(II) with NAu-1 (Fe molar ratio: 1:4, pH = 6.0). The black horizontal lines indicate the starting δ^{56}Fe values of bulk NAu-1 and aqueous Fe(II), respectively. Error bars indicate one standard deviation based on two duplicate reactors and are smaller than symbol size when not shown.

2.5 Discussion

2.5.1 Two-stage microbial and chemical clay reduction

We hypothesize that, in both the microbial and chemical reduction experiments, structural Fe reduction proceeds in two consecutive stages (Figure A.4A-C). During stage 1, electrons are supplied to structural Fe(III) atoms in the edge sites of NAu-1. The resulting structural Fe(II) is released from the octahedral sheet and attaches to hydroxyl groups, producing edge-bound Fe(II). A small amount of Fe(II) is released to solution, and subsequently partially adsorbs onto basal planes (Figure A.4A). Edge-bound and aqueous Fe(II) undergoes ETAE with structural Fe(III) located near to the clay particle edges. *Shewanella oneidensis*, which is able to release electron shuttling compounds (Nevin and Lovley, 2002b), reduces ~7% of total Fe(III) within 8 days (Figure 2.1C), while *G. sulfurreducens*, which does not release electron shuttling compounds and requires direct cell contact to mineral surfaces (Nevin and Lovley, 2002b), only achieves ~2% reduction after 126 days (Figure 2.1C). However, the extent of reduction by *G. sulfurreducens* increases rapidly to ~6% within 7 days after addition of AQDS as an exogenous electron shuttle.

When assessing the electron transfer pathways in our microbial reduction experiments, two models have been proposed by previous studies: a parallel-to-layer pathway initiating from the edge sites (Komadel *et al.*, 2006; Ribeiro *et al.*, 2009) vs both parallel-to-layer and perpendicular-to-layer through basal planes pathways (Bishop *et al.*, 2011). Bishop *et al.* (2011) used the correlation between the interlayer expandability and the extent of bioreduction to argue for possible perpendicular-to-layer electron transfer pathway during reduction by strain *Shewallena putrefaciens* CN32. This is inconsistent with prior Mössbauer work on bioreduced nontronite by *Shewallena oneidensis* MR-1, suggesting a parallel-to-layer pathway only (Komadel *et al.*, 2006; Ribeiro *et al.*, 2009). Both differences in bacterial strains and heterogeneity of clay particles may account for the discrepancy observed in these studies (Bishop *et al.*, 2011). It has also been shown that organic matter in the interlayer space hinders the extent and rate of bioreduction of nontronite NAu-2 by methanogens (Zhang *et al.*, 2014). However, a recent Mössbauer study of bioreduced NAu-2 reveals that perpendicular-to-layer electron transfer occurs only with the assistance of AQDS and not with *Shewanella* alone (Zhao *et al.*, 2015). Our limited extent of reduction argues for the dominance of the parallel-to-layer electron transfer pathway in the *Shewallena* experiments and the perpendicular-to-layer pathway may play a role in our *Geobacter* experiments with AQDS.

During stage 2, microbial reduction slows down significantly: the extent of reduction increases from 7% at day 8 to 10% at day 161 with *Shewanella*, and from 6% at day 162 to 8% at day 240 with *Geobacter*. Initial structural Fe(III) at edge sites (i.e., Fe(III) exposed to solution) of NAu-1 represents 2.7 to 13.6% of the total initial Fe(III) (considering particles ranging from 0.01 to 0.05 μm, see Appendix A for details of calculation). Thus, only about 10% of the Fe(III) near the clay particle edges appears to be directly accessible to the iron-reducing bacteria. This pool constitutes the finite, bioavailable Fe(III) pool (Jaisi *et al.*, 2005) (Figure A.4B). The size of this bioavailable Fe(III) pool may differ for different clay minerals considering that clay particles are heterogeneous by nature in crystallinity, particle size, surface area, and expandability (Jaisi *et al.*, 2007; Bishop *et al.*, 2011). It is worthwhile to note that the extent and rate of bioreduction is also influenced by the energetics of the system, as shown by continuing reduction after addition of fresh cells to previously ceased bioreduction experiments (Jaisi *et al.*, 2007; Jaisi *et al.*, 2009). In the chemical reduction experiments, dithionite, with its small molecular size, is able to diffuse into the interior of the clay structure along basal planes (Figure A.4C), hence explaining the higher extents of reduction of total structural Fe(III) (up to 24%, Table A.2). It is important to note that, overall, chemical reduction by dithionite proceeds markedly faster than reduction by the two iron-reducing bacteria. The same extent of reduction achieved within minutes by dithionite requires several days in the microbial reduction experiments. Reduction of structural Fe(III) in clay induces the increase in layer charge, which may be compensated through the adsorption of cation species (e.g. NH_4^+), protonation of OH groups, or dehydroxylation (Stucki, 2011).

2.5.2 Fe isotope compositions

The observed changes in Fe isotope compositions are consistent with the proposed two stage mechanism for structural Fe(III) reduction shown diagrammatically in Figure 2.4 and Figure A.4. When the extent of reduction is low (stage 1), the isotopically light aqueous Fe(II) argues for atom exchange with structural Fe(III) on the edge sites (Figure 2.4A and Figure A.4A). In the absence of atom exchange, aqueous Fe(II) would be expected to inherit the δ^{56}Fe signature of the outmost structural Fe atoms upon reductive dissolution. Partial dissolution of the starting NAu-1 shows that the outermost Fe atoms near the clay particle edges are isotopically heavy, while those located in the interior of the clay particles are isotopically light (Table A.5), which may reflect the isotope heterogeneity of the clay particles. Thus, aqueous Fe(II) would have shown a more positive δ^{56}Fe value than the bulk clay (e.g., $\delta^{56}Fe \geqslant 0.74‰$ when dissolution $\leqslant$1.5%, Table A.5), which is not the

case. The existence of atom exchange between aqueous Fe(II) and other Fe phases is consistent with a previous finding using enriched isotope tracers (Neumann *et al.*, 2015). Neumann *et al.* (2015) proposed that electron injection by sorbed Fe(II) at edge sites, followed by bulk electron conduction through the octahedral sheet, would connect oxidation of edge-bound Fe(II) with reduction of structural Fe(III) at spatially separated sites. Considering the much smaller pool of aqueous Fe(II) than edge-bound Fe(II) in our experiments, we hypothesize that ETAE between aqueous Fe(II) and structural Fe(III) occurs via a transient sorbed Fe(II) phase on edge sites, which may or may not be captured in the edge-bound Fe(II) extract.

For the same reason, edge plus structural Fe(II) would become isotopically heavy if only reduction (i.e., electron transfer) occurs without atom exchange. The observed isotopically light edge plus structural Fe(II) and isotopically heavy structural Fe(III) suggest that atom exchange is coupled with electron transfer (i.e., ETAE) during stage 1.

Basal-sorbed Fe(II) exhibits the most negative δ^{56}Fe values. We propose three hypotheses to explain the observed values: 1) kinetic adsorption of aqueous Fe(II) onto basal planes; 2) ETAE between basal-sorbed Fe(II) and structural Fe(III); and 3) partial oxidation of basal-sorbed Fe(II) due to electron transfer from sorbed Fe(II) to structural Fe(III). The first hypothesis may explain the lightest basal-sorbed Fe(II) when the extent of reduction is ca. 2% (Figure 2.2), consistent with a kinetic sorption producing isotopically heavy aqueous Fe(II) during interaction between aqueous Fe(II) and goethite (Reddy *et al.*, 2015). However, isotope data of later time points (i.e., at day 161 in *Shewanella* experiments) still showed an isotopically lighter basal-sorbed Fe(II) than that of the aqueous Fe(II) (Figure 2.2), arguing against a kinetic effect to fully explain our observed data. Electron transfer from basal-sorbed Fe(II) to sturcutral Fe(III) has been demonstrated previously (Neumann *et al.*, 2013). However, atom exchange has never been shown to occur between basal-sorbed Fe(II) and structural Fe(III), presumably due to physical blockage by a tetrahedral sheet between the two. Thus, we reject the second hypothesis. Meanwhile, if basal-sorbed Fe(II) was partially oxidized to Fe(III), then residual Fe(II) will be isotopically lighter than the original sorbed Fe(II) (Beard and Johnson, 2004; Wu *et al.*, 2013), which presumably had a similar isotope composition with the aqueous Fe(II). Due to the small quantity of this Fe(III) product, our $CaCl_2$ extraction and/or the Ferrozine method may fail to recover this Fe(III) phase. This third one remains a viable hypothesis to be tested further.

During stage 2, the progressively heavier isotopic compositions of aqueous and basal-sorbed Fe(II) (Figure 2.2) are explained by the continued reductive dissolution of the outermost pool of structural Fe(III) and the cessation of ETAE between aqueous Fe(II) and structural Fe(III). During this stage, some ETAE between edge-bound Fe(II) and adjacent structural Fe(III) is still possible, due to close site contact, but not between aqueous Fe(II) and structural Fe(III) (Figure 2.4B and Figure A.4B). In other words, the accumulation of structural Fe(II) along the edges of the clay particles causes the blocking of ETAE.

Compared to the near-edge, bioavailable Fe(III) pool, the interior Fe(III) pool is not accessible to the bacteria. The small dithionite molecules, however, are able to further reduce a significant portion of the interior Fe(III) pool (Figure 2.4C and Figure A.4C). The aqueous and basal-sorbed Fe(II) thus derives from the reductive dissolution of a relatively small portion of the outermost component of the Fe(III) pool with δ^{56}Fe values of ~1‰ (Table A.4). Structural Fe(II) and structural Fe(III) are both isotopically light (Figures 2.2C and 2.4C), reflecting the inheritance of the light δ^{56}Fe values of the bulk interior Fe(III) pool, without ETAE (see Table A.5). Alternatively, the aqueous plus basal-sorbed Fe(II) could become enriched in heavy Fe isotopes due to the precipitation of an isotopically light secondary mineral phase during stage 2. However, no secondary mineral precipitates could be detected by SEM in all the reduced samples, even at the highest extents of Fe(III) reduction (Figure A.6).

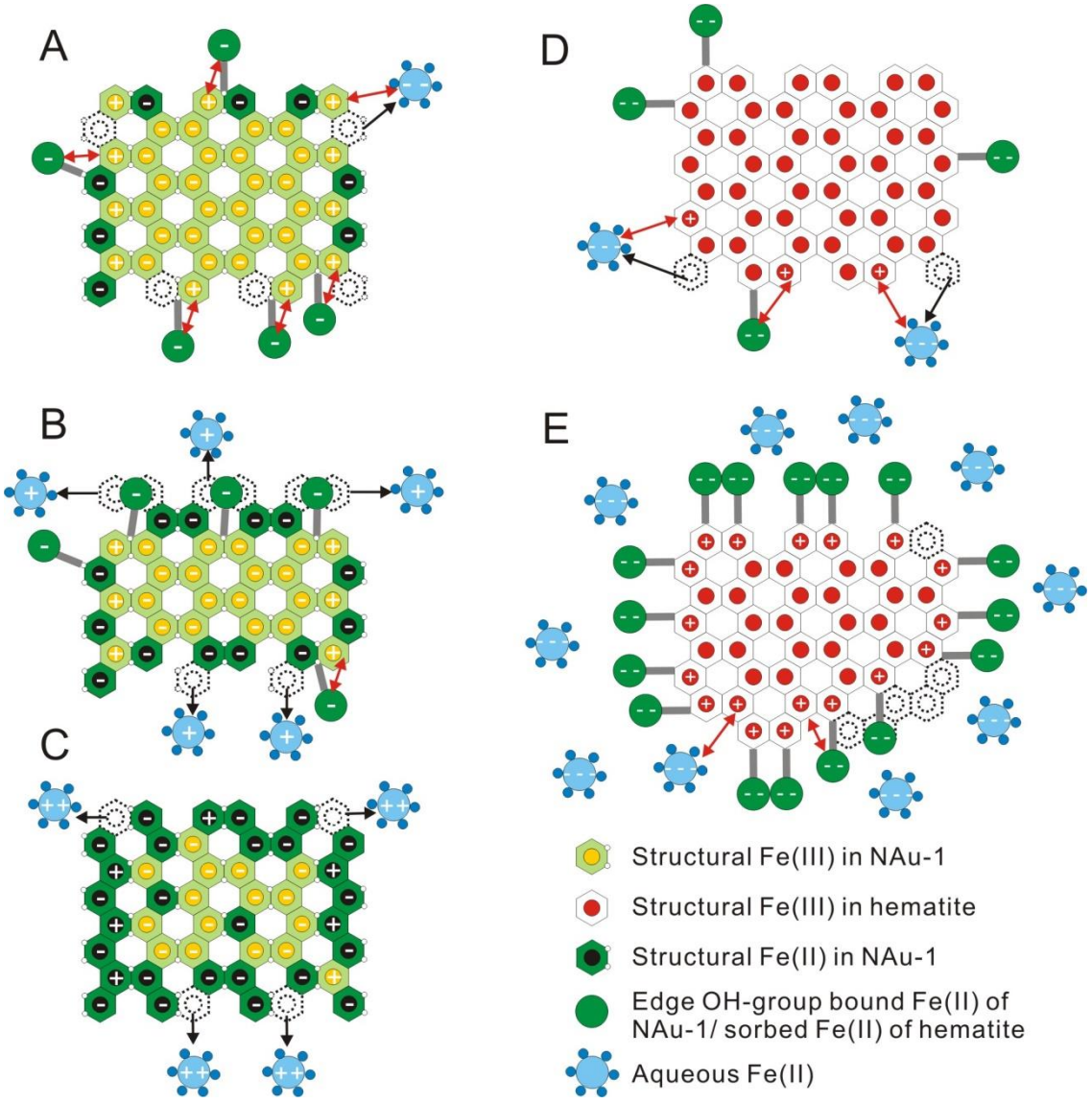

Figure 2.4. Comparison of reduction mechanisms of NAu-1 (top view) and hematite. (A) At low extent of reduction of NAu-1, the outmost structural Fe(III) is reduced by the bacteria (*Shewanella* and *Geobacter*) or dithionite to structural Fe(II). Fe(II) bound to edge hydroxyl groups and structural edge Fe(II) have the same isotope composition. The release of aqueous Fe(II) from structural Fe is indicated by the black arrow. ETAE between aqueous Fe(II) and structural Fe(III) and edge-bound Fe(II) and structural Fe(III) is shown by the red arrows. Basal-sorbed Fe(II) is not shown in the top view figures. (B) At high extent of reduction in biological experiments, residual heavy structural Fe(III) is reduced and dissolves, producing isotopically heavy aqueous phase Fe(II) (indicated by "+" and the black arrows). Edge sites are

saturated with structural and edge-bound Fe(II), inhibiting further reduction. ETAE between aqueous Fe(II) and structural Fe(III) is blocked, with minor ETAE between edge-bound Fe(II) and structural Fe(III), as indicated by the red arrow. (C) At ~ 24% reduction in chemical experiments, interior structural Fe(III) is reduced, with a small amount of the isotopically heavy outmost Fe(II) released to the aqueous phase (indicated by "++"). (D) For Fe oxyhydroxide minerals, reduction does not cause the accumulation of structural Fe(II). Both aqueous ("---" indicates lowest δ^{56}Fe) and adsorbed Fe(II) ("--" indicates lower δ^{56}Fe) undergo ETAE with structural Fe(III) on the mineral surfaces ("+" indicates high δ^{56}Fe). (E) When surface is saturated by sorbed Fe(II), no blockage of ETAE occurs due to lack of structural Fe(II), thus maintaining isotopic equilibrium.

2.5.3 Fe isotope fractionations

With the exception of the initial data points, the Fe isotope fractionation factors in the microbial and chemical reduction experiments generally decrease with increasing extent of reduction during stage 1 (Figure 2.5 and Figure A.7, Table A.4). The fractionation factors between edge plus structural Fe(II) and structural Fe(III) on the one hand (Figure 2.5A), and the combined Fe(II) pools and structural Fe(III) on the other (Figure A.7), both decrease from −1.0 to −0.3‰; their near identical trends reflect the dominant contribution of edge plus near-edge structural Fe(II) to total Fe(II). The decreasing trends are explained by the finite size of the bioavailable Fe(III) pool. At the onset of reduction, the fractionation factors are the largest due to extensive ETAE. With reduction proceeding, edge sites are progressively occupied by Fe(II), resulting in less structural Fe(III) available for ETAE, and the fractionation factors decrease. In all the reduction experiments, the maximum fractionation factors are observed for $\Delta^{56}Fe_{\text{aq Fe(II)-struc Fe(III)}}$ (−1.2 to −0.8‰) when the extent of reduction is small, ca. 2% (Figure 2.5B). These large values reflect extensive ETAE between aqueous Fe(II) and structural Fe(III) assisted by dynamic sorption/desorption via a transient sorbed Fe(II) phase (Figure 2.4A and Figure A.4A).

During stage 2, as the finite bioavailable Fe(III) pool is nearly exhausted, the reduction rates in the *Shewanella* reactors drop to very low values, while the $\Delta^{56}Fe_{\text{struc Fe(II)-struc Fe(III)}}$ values stabilize at −0.34 ± 0.02‰ (Figure 2.5A), reflecting minor ETAE between edge-bound Fe(II) and structural Fe(III) (Figure 2.4B and Figure A.4B). In the experiments with dithionite, much faster reduction ultimately results in $\Delta^{56}Fe_{\text{struc Fe(II)-struc Fe(III)}}$ values of ~0‰ (Figure 2.5A), while the extent of reduction reaches

24%. The net zero isotopic fractionation implies that 100% of the structural Fe(III) pool accessible to dithionite has been reduced at that point.

In the microbial reduction experiments, fractionation factors between aqueous Fe(II) and structural Fe(III) change from −0.3‰ to 0.1‰ during stage 2 (Figure 2.5B), which signals the progressive cessation of ETAE and the cumulative release of isotopically heavy Fe to solution (Figure 2.4B and Figure A.4B). When the two phases coincidentally attain the same isotopic composition, the bioavailable Fe(III) pool is completely consumed. At the end of the chemical reduction experiments, that is, at 24% reduction, the $\Delta^{56}Fe_{aq\ Fe(II)\text{-}struc\ Fe(III)}$ value has become positive due to the absence of atom exchange between aqueous Fe(II) and structural Fe(III) and between aqueous Fe(II) and structural Fe(II). At this stage, all the edge sites are saturated with Fe(II) and a lack of atom exchange between aqueous Fe(II) and structural Fe(II) indicates that atom exchange must be coupled with electron transfer. Facilitation of atom exchange by electron transfer has been shown previously by the higher extent of atom exchange for interactions between aqueous Fe(II) and Fe oxyhydroxides than between aqueous Fe(III) and amorphous Fe oxide (Wu *et al.*, 2012a). This in turn demonstrates that ETAE is the key mechanism for Fe isotope fractionation during the first stage of clay reduction (Figure 2.4A and Figure A.4A).

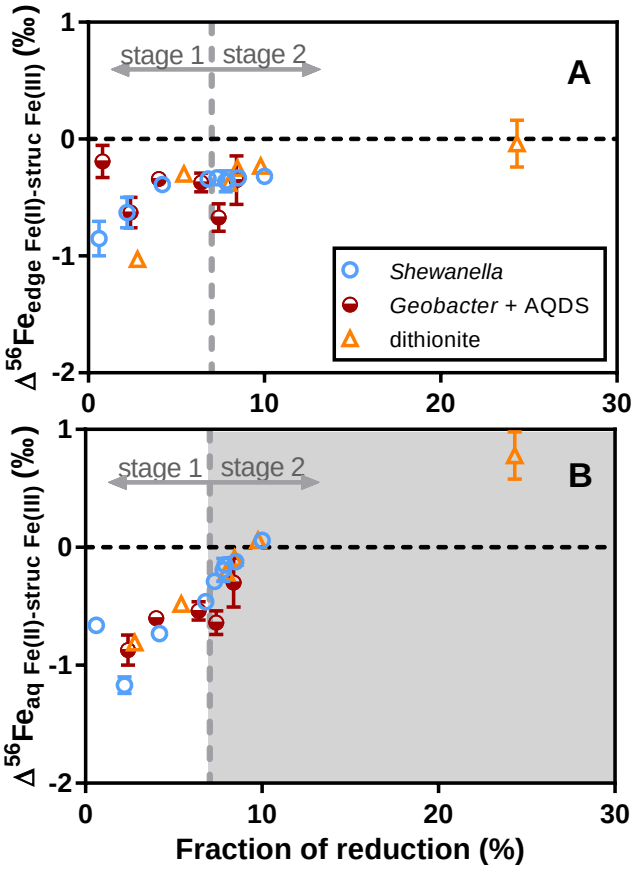

Figure 2.5. Changes in the Fe isotope fractionation factors $\Delta^{56}Fe_{\text{edge Fe(II)-struc Fe(III)}}$ (panel A) and $\Delta^{56}Fe_{\text{aq Fe(II)-struc Fe(III)}}$ (panel B) in biological and chemical reduction experiments plotted against the extent of reduction. The vertical lines indicate the transition from stage 1 to stage 2. The gray background in stage 2 of panel B shows that no ETAE occurs between aqueous Fe(II) and structural Fe(III). Error bars indicate one standard deviation of propagated errors.

2.5.4 Comparison to Fe(II)-NAu-1 exchange experiments

Similar to the stage 1 results of the microbial and chemical reduction experiments, the mixing of aqueous Fe(II) and NAu-1 produces structural Fe(III) that is isotopically heavier than the starting clay material, as well as isotopically light Fe(II) (Figure 2.3). However, the relatively constant isotopic compositions and fractionation factors during the exchange experiments contrast with the time-dependent trends seen in the reduction experiments. A previous study has shown that mixing aqueous Fe(II) and NAu-1 at pH 6 causes ~3% reduction of structural Fe(III) (Neumann *et al.*, 2013). The

isotope fractionation factors in the mixing experiments are in general comparable to those of the reduction experiments at ~3% extent of reduction (Table A.4). Due to the small extent of reduction, only limited structural Fe(II) is generated and no saturation of edge sites over time would occur in the mixing experiments. The invariant isotope fractionation factors with time imply a constant extent of ETAE throughout the mixing experiments. The small differences between the fractionation factors observed in the exchange and reduction experiments (Table A.4) could be due to differences in the amounts of Fe(II) sorbed onto basal and edge sites because of pH differences (6.0 in exchange experiments versus 6.8 in reduction experiments) (Neumann *et al.*, 2013).

2.5.5 Iron reduction in clay mineral versus Fe(III) oxyhydroxides

The *in situ* reduction of structural Fe(III) which leads to the blocking of ETAE between aqueous Fe(II) and structural Fe(III) is unique to clay minerals with layered structure, and distinct from Fe(III) oxyhydroxide mineral reduction. Before the bioavailable finite Fe(III) pool is exhausted, ETAE mainly takes place between edge-bound Fe(II) and structural Fe(III), as well as between aqueous Fe(II) and structural Fe(III) (Figure 2.4A). With the accumulation of structural Fe(II), the amount of structural Fe(III) available for ETAE with aqueous Fe(II) decreases. Ultimately, ETAE with the interior structural Fe(III) pool ceases (Figure 2.4B and Figure A.4B). Basal-sorbed Fe(II) does not undergo ETAE with structural Fe(III) due to the physical separation by the tetrahedral sheets (Figure A.4A). In contrast, Fe(II) produced during the reduction of Fe(III) oxyhydroxides mainly ends up in the aqueous and adsorbed phases (Figure 2.4D). Even when the surface of the Fe(III) oxyhydroxide mineral is saturated with adsorbed Fe(II), structural Fe(III) remains available to ETAE with aqueous and adsorbed Fe(II), due to the lack of blockage by structural Fe(II) (Figure 2.4E). Thus, aqueous Fe(II) can maintain isotopic equilibrium with solid-phase Fe(III) and remain isotopically lighter than sorbed Fe(II) (Crosby *et al.*, 2005; Wu *et al.*, 2009; Percak‐Dennett *et al.*, 2011).

2.6 Conclusions and implications

Our results imply that Fe isotope fractionations can potentially yield signatures that may allow one to distinguish reduction of structural Fe(III) in layered clay minerals by dissimilatory iron reducing bacteria from reduction of Fe(III) oxyhydroxides in reducing environments. When most bioavailable Fe(III) in clays is exhausted, microbial reduction becomes inhibited due to site saturation, and further ETAE between aqueous Fe(II) and structural Fe(III) no longer takes place. The complete conversion of bioavailable Fe(III) to Fe(II) in clay (zero fractionation between aqueous phase and structural

Fe(III) in mineral), coupled with limited reductive dissolution (~1%), indicates that Fe redox cycling mediated by microbes may be an isotopically reversible process. This conclusion is consistent with recent bulk measurements of clay redox speciation which indicate that ferruginous clay may serve as a rechargeable energy source for bacteria in soils and sediments (Zhao *et al.*, 2015). The blockage of ETAE will likely also influence the reactivity of edge plus structural Fe(II) toward nutrients and contaminants, which warrants further exploration.

The Fe isotope compositions of major Fe-bearing minerals (i.e., magnetite, siderite) in the Banded Iron Formations in the rock record have been interpreted as biosignatures of dissimilatory iron reduction (DIR) of Fe(III) oxyhydroxides either *in situ* (Johnson *et al.*, 2008a; Heimann *et al.*, 2010; Craddock and Dauphas, 2011) in the sediments or through a benthic shuttle (Severmann *et al.*, 2008; Czaja *et al.*, 2010). This interpretation is largely based on the generation of isotopically light Fe(II) by DIR of Fe(III) oxyhdroxides as demonstrated in numerous experimental studies (Crosby *et al.*, 2007; Wu *et al.*, 2009; Percak‐Dennett *et al.*, 2011). Our findings here imply that Fe bearing clay minerals may not serve as a faithful recorder of microbial activities (i.e., DIR) on ancient Earth. If bioavailable Fe was exhausted during microbial reduction, no distinctive Fe isotope signature would be detected for the end product ferrous phases when analyzing clay minerals in the rock record. On the other hand, a lack of isotope discrepancy between ferrous and ferric phases associated with clay minerals cannot be used to rule out the existence of microbial activities.

Chapter 3
Bioavailable Fe in nontronite NAu-1 decreases during consecutive Fe redox cycles

3.1 Summary

Iron-containing clay minerals can act as a renewable Fe source for microorganisms during redox cycles, as the reductive dissolution of clay is limited compared to that of Fe-(oxyhydr)oxides. Our previous study showed that the initial fraction of bioavailable Fe in unaltered NAu-1 is ~10%. However, whether the bioavailability of clay lasts after repeated redox cycles is unclear. We carried out three consecutive redox cycles of nontronite NAu-1 to investigate how and why the bioavailable Fe remaining in NAu-1 changes with repeated redox fluctuations. NAu-1 was reduced biotically by *Shewanella oneidensis* MR-1 and re-oxidized abiotically by air. The fraction of Fe(II) at the end of the 1st to 3rd reduction period (RP) decreased from 9.7 to 5.7%. This decrease is attributed to the cumulative release of Fe(II) into solution from small clay particles. We propose that following the complete consumption of bioavailable Fe in small particles, the bioavailability of large NAu-1 particles would be sustained, with 4.2% of total Fe being redox-active while remaining in the octahedral structure. This prediction was supported by the increasing crystalline domain size, preferential dissolution of Fe associated with small particles, and the decreasing Fe isotope fractionation factors [$\Delta^{56}Fe_{\text{aq Fe(II)-struc Fe(III)}}$ and $\Delta^{56}Fe_{\text{edge Fe-struc Fe(III)}}$] from RP1 to RP3. This study reports, for the first time, Fe isotope variation during the redox cycling of Fe-containing clay minerals. The results add to the knowledge on the Fe bioavailability/reversibility of clays in redox-dynamic environments.

3.2 Introduction

Clay minerals carry more than half of the total Fe in terrestrial and marine sediments, thereby playing a significant role in Fe biogeochemical cycling (Kostka *et al.*, 2002; Dong, 2012). The bioavailable pool of structural Fe in clay varies from 1 to 60% (Bishop *et al.*, 2011; Yang *et al.*, 2012; Zhao *et al.*, 2015; Zeng *et al.*, 2016; Zhao *et al.*, 2017). Several studies have shown that Fe(III) reduction from Fe(III)-containing clays (e.g., smectite) may be as favorable as that from other Fe(III)-containing minerals, in particular Fe(oxyhydr)oxides (Kostka *et al.*, 2002; Komlos *et al.*, 2007). Moreover, the large surface area and low permeability of clays render them important sorbents of nutrients, such as

potassium (K) and ammonium (NH_4) (Dong *et al.*, 2009; Dong, 2012). Structural Fe(II) in clays, converted from structural Fe(III), may enhance the reactivity of the clay by serving as a source of electrons to clay-bound, redox-sensitive components such as Tc(VII) (Jaisi *et al.*, 2009; Bishop *et al.*, 2011; Peretyazhko *et al.*, 2012; Yang *et al.*, 2012), Cr(VI) (Bishop *et al.*, 2014; Liu *et al.*, 2018), Sb(V) (Ilgen and Trainor, 2011), and nitroaromatic compounds (Haderlein *et al.*, 1996; Hofstetter *et al.*, 2006; Luan *et al.*, 2015a). The re-oxidation of structural Fe(II) in clay may cause the release of the nutrients or desorption of redox sensitive contaminants to soil and groundwater (Anastácio *et al.*, 2008; Barcellos *et al.*, 2018). Thus, the Fe redox cycling of clay deserves continued attention.

Iron redox chemistry within clays is susceptible to changing environmental redox conditions. For example, groundwater table fluctuations together with microbial activity generate a redox-dynamic environment, where Fe containing minerals such as clays undergo interconversion of Fe(III) and Fe(II) (Rezanezhad *et al.*, 2014). Upon Fe(III) reduction, the fate of the aqueous Fe(II) derived from the reductive dissolution of clay may undergo several transformations including precipitation as, among others, ferrihydrite, magnetite, and green rust (Zhao *et al.*, 2013; Latta *et al.*, 2017). Meanwhile, the remaining structural Fe(II) in clay minerals can be converted back to Fe(III) through abiotic or biotic oxidation, and be used as an electron acceptor in the next reduction phase. Thus, structural Fe in clay is potentially renewable over repeated redox cycles (Yang *et al.*, 2012; Zhao *et al.*, 2015; Zeng *et al.*, 2016). However, the fraction of structural Fe(III) that can participate in redox cycles typically decreases upon multiple successive redox cycles, especially for Fe-rich clay minerals (Ribeiro *et al.*, 2009; Stucki, 2011; Yang *et al.*, 2012; Gorski *et al.*, 2013; Zhao *et al.*, 2015; Zeng *et al.*, 2016). The decreasing reactivity of clay may be due to permanent mineralogical alterations induced by redox reactions (Kim *et al.*, 2004; Meunier, 2005; O'Reilly *et al.*, 2005; Dong *et al.*, 2009; Ribeiro *et al.*, 2009; Stucki, 2011; Dong, 2012). It has been demonstrated that microbial Fe reduction can result in smectite illitization, which is characterized by layer collapse and enrichment of Al and K (Kim *et al.*, 2004; Dong *et al.*, 2009; Koo *et al.*, 2014). Other mineralogical changes include migration of Fe atoms from *cis*- to *trans*-octahedral positions (in dioctahedral clay), dehydroxylation, change of the coordinating environment of structural cations, and precipitation of secondary minerals (Fialips *et al.*, 2002; Ribeiro *et al.*, 2009; Stucki, 2011; Gorski *et al.*, 2013; Zhao *et al.*, 2015). Even though the impact of bacteria on clay structural change has been considered to be weak and reversible (Ribeiro *et al.*, 2009; Stucki, 2011; Zhao *et al.*, 2015), the increasing crystallinity and progressive dissolution of clay particles during redox cycles implies that the residual clay is not exactly the same

as the starting material (Yang *et al.*, 2012; Zhao *et al.*, 2015; Zeng *et al.*, 2016). However, the mechanism(s) driving Fe bioavailability of clay changes across multiple redox cycles is still unclear.

Our previous study revealed that initially ~10% of structural Fe(III) in unaltered NAu-1 is accessible to microorganisms (Shi *et al.*, 2016). The goal of this study is to examine the role of multiple redox cycles on the bioavailability of Fe(III) in NAu-1 using batch experiments inoculated with the facultative anaerobe, *Shewanella oneidensis* MR-1. Specifically, we aim to: 1) quantify the changes in the fraction of bioavailable Fe(III) remaining in NAu-1 across successive redox cycles, 2) identify the number of redox cycles or time it takes to deplete bioavailable Fe(III) from NAu-1, and 3) elucidate the underlying mechanisms responsible for 1) and 2). In this study, we carried out three redox cycles of nontronite NAu-1 and systematically removed the aqueous Fe(II) at the end of each reduction period. The experiment was designed to simulate a transient water table zone where soluble Fe(II) can be leached out to the groundwater.

3.3 Materials and methods

3.3.1 Clay mineral and bacteria preparation

Raw NAu-1 [$(Ca, Na, K)_{1.05}[Si_{6.98}Al_{1.02}][Al_{0.29}Fe_{3.68}Mg_{0.04}]O_{20}(OH)_4$] (Keeling *et al.*, 2000) was purchased from the Clay Minerals Society and purified as described previously (Jackson, 1956; Neumann *et al.*, 2013; Shi *et al.*, 2016). To ensure all the impurities [e.g., Fe (oxyhydr)oxides, kaolinite, and quartz] were excluded, the purified product of NAu-1 was inspected by X-ray powder diffraction (XRD), scanning electron microscopy-energy dispersive spectroscopy (SEM-EDS), and transmission electron microscopy (TEM) (see section 3.4.3). The pure fraction (<0.5 μm) of NAu-1, hereafter referred to as unaltered NAu-1, was used as the starting material in the redox cycle experiments. The facultative anaerobe, *Shewanella oneidensis* MR-1 (Myers and Nealson, 1988b), was cultured from frozen glycerol stocks (-80 ℃) grown on Luria-Bertani (LB) agar plates, transferred to LB broth and grown aerobically to late log phase (14-18 h). Cells were washed twice using a sequence of centrifugation at 3500 rpm for 10 min (Beckman Coulter Avanti® J-E), supernatant decantation, and resuspension of the cell pellet in a minimal growth medium (MM) (VWR® vortex mixer). The MM contained 40 mM Na-lactate (sole electron donor), 10 mM ammonium chloride (NH_4Cl), 100 μM potassium dihydrogen phosphate (KH_2PO_4), 10 mM HEPES {2-[4-(2-hydroxyethyl)piperazin-1-yl]ethanesulfonic acid, $C_8H_{18}N_2O_4S$} buffer (pH 6.8) and was

filter sterilized (0.2 μm, PES). The resulting MM-cell suspension is hereafter denoted as the bacterial stock solution (BSS).

3.3.2 Redox cycle experiments

Biotic and abiotic reactors containing NAu-1 (5 mg/mL) suspensions were subjected to three consecutive redox cycles consisting of periods of reduction (RP, 20 days for the first two RPs) and oxidation (OP, 3 days for the first two OPs) conditions. The number after RP or OP denotes the round of redox cycles. For example, RP1 and OP1 indicate the first reduction and oxidation periods, respectively. The RP3 extended to 56 days, while the OP3 lasted only one day due to the low volume of material.

Four bioreactors were prepared for RP1 in an anaerobic chamber (Coy®, 98% N_2/2% H_2) by diluting the BSS into sterile 125 mL serum bottles containing 0.6 g of the unaltered NAu-1 giving a final volume of 120 mL MM and cell concentration of 2×10^8 cells (mL MM)$^{-1}$. Due to volume constraints imposed by the centrifuge configuration, bioreactors were divided into two groups that were either sampled early (B1E and B2E) or late in the experiment (B1L and B2L) (Table B.1). Reactors were sealed using butyl rubber stoppers/aluminum crimp seals, shaken at 100 rpm (VWR® 3500 standard shaker) in the dark; 8 mL slurries were sampled in the anaerobic chamber at selected time points. At the end of each RP, the residual suspensions from reactors were washed three times with 10 mM HEPES buffer using a sequence of centrifugation (6500 rpm, 30 min), decantation, and resuspension in the buffer. In the final washing step, to maintain 5 mg clay/mL, the equivalent volume of the MM removed in the first centrifugation was replaced by 10 mM HEPES buffer (pH 6.8) and vortexed. Using HEPES buffer instead of MM was to prevent bacteria growth and Fe(III) reduction during the OPs.

OPs were induced and sustained by sparging each reactor with sterile air (2.8 mL/h) using a system of two (i.e., inflow and outflow) sterile needles (22 G × 3.5'') attached to in-line gas filters (0.2 μm, nylon). During the OP, reactors were shaken at 100 rpm in the dark and 8 mL slurries were collected at 0.5 h and at the end of the OP. The remaining clay-cell suspensions were transferred to plastic centrifuge bottles, centrifuged (14,000 rpm, 1 h) and freeze-dried for use in the next RP. New sterile bioreactors were prepared at the start of all subsequent RPs and the equivalent volume of the 10 mM HEPES buffer removed in the preceding cycle was replaced by freshly inoculated MM (i.e., from a new BSS) giving the same initial cell concentration [2×10^8 cells (mL)$^{-1}$] for each RP. Likewise, the MM removed at the end of each RP was always replaced by the equivalent volume of 10 mM HEPES

buffer for use in the OP. A control serum bottle (i.e., the abiotic reactor) contained 0.5 g of NAu-1 and 100 mL of MM at the beginning of RP1. The control reactor underwent the same redox regime as the bioreactors, however, the sampling frequency was reduced in the RP. The volumes of MM and HEPES that were added to the bioreactors and control reactor throughout the experiment are listed in Table B.1.

Six mini bioreactors (10 mL serum bottles) that contained 8 mL clay-cell suspensions were prepared to provide samples for solid phase characterization. The mini bioreactors were initialized by adding the same concentrations of NAu-1 and cells to MM as in the (large) experimental reactors. When RP1 was completed, one of the mini bioreactors was sacrificed to collect the solid products, while the five others proceeded to OP1. At the end of OP1, one mini bioreactor was sacrificed and the four remaining ones proceeded into RP2, and so on. Each mini bioreactor therefore was assumed to be representative of one of the redox cycle end-points (i.e., RP1 to OP3).

3.3.3 Sampling protocol and sequential extractions

Depending on the sampling period (i.e., RP or OP), samples were either collected in the anaerobic chamber (RP) or aerobically on the bench (OP) and were transferred to 10 mL serum bottles in the anaerobic chamber. The serum bottles were crimp sealed and centrifuged (6500 rpm, 20 min). The supernatant was syringe filtered (0.2 μm, nylon) and acidified (0.5 M HCl). Briefly, solid phase sequential extractions were used to examine Fe(II) partitioning and conducted as outlined by Shi *et al.* (2016) to target: 1) basal plane sorbed Fe(II) (4 mL 1 M $CaCl_2$, pH 7, 4 h); 2) edge hydroxyl group bound Fe(II) (4 mL 1 M NaH_2PO_4, pH 5, 18 h); and 3) residual structural Fe (II) (4 mL 0.5 M HCl, 24 h) (Neumann et al., 2013). Slurries were sampled from six mini bioreactors for solid phase characterization (0.1 mL for each analysis, section 3.3.4.3), including XRD, SEM-EDS, TEM, and particle size analyses.

3.3.4 Analyses

3.3.4.1 Structural cation concentrations

Concentrations of total Fe and Fe(II) in all samples (i.e., aqueous and extracts) were determined spectrophotometrically (Thermo Scientific Spectronic 200) using the Ferrozine method (detection limit <2 μM) (Stookey, 1970; Viollier *et al.*, 2000). Concentrations of Si, Al, Fe, and Mg of selected samples were determined using inductively coupled plasma mass spectrometry (ICP-MS, Agilent

8800) and inductively coupled plasma optical emission spectrometry (ICP-OES, Thermo Scientific iCAP 6300).

3.3.4.2 Iron isotopes

Matrix-matched test solutions were prepared by adding high purity standard (HPS) Fe to acidified MM, acidified 1 M $CaCl_2$, acidified 1 M NaH_2PO_4, and 0.5 M HCl (Table B.2). These test solutions were used to evaluate the accuracy of Fe isotope analyses. The test solutions and selected experimental samples were passed through an anion-exchange resin to separate Fe from other cations (Beard *et al.*, 2003). Iron isotope compositions of test solutions and experimental samples (i.e., aqueous and extracts) were measured using multicollector inductively coupled plasma mass spectrometry (MC-ICP-MS, Nu Plasma II) at the University of Waterloo. The average Fe isotope value of the test solutions after running through columns ($\delta^{56}Fe = 0.06 \pm 0.08‰$, 1σ, n = 12) was within error of isotope composition measured for HPS before column ($\delta^{56}Fe = 0.05 \pm 0.1‰$, 1σ, n = 174), indicating negligible artificial affect was induced by the column chemistry. Iron isotope values were reported as $\delta^{56}Fe$ (‰) relative to a standard IRMM-634 ($\delta^{56}Fe = -0.04 \pm 0.06‰$; 2σ, n = 7). The Fe isotope fractionation between phases X and Y was calculated as $\Delta^{56}Fe_{X-Y} = \delta^{56}Fe_X - \delta^{56}Fe_Y$.

3.3.4.3 Solid characterization

Powder X-ray powder diffraction (XRD, Rigaku Rapid II) with Mo-Kα radiation at the University of Wisconsin-Madison was used to analyze the unaltered NAu-1 and NAu-1 OP1 and OP2. Slurries (0.1 mL) from mini bioreactors were centrifuged (14,000 rpm, 5 min). The sediments were separated from the supernatants and freeze-dried. Data were collected on a 2-D image-plate detector. Two-dimensional images were converted to produce conventional 2θ vs. intensity patterns using Rigaku's 2DP software. Crystalline domain size (targeting particles <100 nm) analysis was performed using the JADE® 9.0 software package. A pseudo-Voigt method was used for fitting the peak positions and peak widths at half-height.

Scanning electron microscopy (SEM, Quanta FEG 250) coupled with energy dispersive spectroscopy (EDS, Oxford X-act) (SEM-EDS) was used to analyze the unaltered NAu-1 and NAu-1 from RPs and OPs. Slurries (0.1 mL) were centrifuged (14,000 rpm, 5 min) and re-suspended in 1 mL ultra-pure water (18.2 MΩ cm^{-1}, Millipore). An aliquot of the slurry (~30 µL) was transferred to carbon tape covered aluminum stubs and dried overnight in the anaerobic chamber. SEM samples were transported anaerobically (BBL GasPak™ Systems) to the SEM facility and quickly (<30 s)

introduced into the sample chamber to prevent oxidation. Secondary electron (SE) images and EDS spectra were collected under high vacuum using accelerating voltages of 10 and 20 kV, respectively.

Unaltered NAu-1 and NAu-1 from OP1 and OP2 - were prepared for TEM analysis by coating distilled water suspensions of crushed solid phase of clay onto carbon-coated 200-mesh Cu grids. TEM images and selected-area electron diffraction (SAED) analyses were carried out using a Philips CM200-UT microscope operated at 200 kV at the University of Wisconsin-Madison. Chemical compositions were analyzed by TEM-EDS spectra using a Si:Li detector (Oxford instruments Link ISIS) with a beam diameter of ~50 nm (spot size 5).

Particle/aggregate size of the unaltered NAu-1 and NAu-1 from RPs and OPs were measured using a VASCO nanoparticle size analyzer (dynamic light scattering) and a FlowCam® VS series (dynamic imaging) operated in the ranges 0.5 nm - 5 μm and 5-100 μm, respectively. Slurries (0.1 mL slurry) from RPs and OPs were diluted with 5 mL of MM and 5 mL of HEPES buffer, respectively. Unaltered NAu-1 was also suspended in 10 mM HEPES buffer at the same clay concentration as experimental samples. Samples collected from RPs were diluted using serum bottles in the anaerobic chamber, crimp sealed and transported to the measurement facilities to minimize sample oxidation.

3.4 Results

3.4.1 Fe redox speciation and solid phase partitioning

The fraction of total Fe(II) [$F_{Fe(II)}$], which was equivalent to the extent of microbial Fe(III) reduction during RPs, was determined from the sum of all measured Fe(II) pools and the total Fe concentration in NAu-1 using:

$$F_{Fe(II)} = \frac{Fe(II)_{aq} + Fe(II)_{basal} + Fe(II)_{edge} + Fe(II)_{struc}}{\text{Total Fe in NAu}-1} \times 100\% \quad (3.1)$$

where $Fe(II)_{aq}$, $Fe(II)_{basal}$, $Fe(II)_{edge}$ and $Fe(II)_{struc}$ are the molar concentrations of Fe(II) in the aqueous phase, $CaCl_2$ extract, NaH_2PO_4 extract, and HCl extract, respectively. Moreover, the proportion of Fe(II) [$P_{Fe(II)_i}$] in the aqueous phase and the three extracts were compared to the total Fe(II) pool using:

$$P_{Fe(II)_i} = \frac{Fe(II)_i}{Fe(II)_{aq} + Fe(II)_{basal} + Fe(II)_{edge} + Fe(II)_{struc}} \times 100\% \quad (3.2)$$

where $Fe(II)_i$ is the Fe(II) concentration in phase i (i.e., aqueous or extracts). Lastly, the relative proportions of Fe(II) and Fe(III) in the NaH_2PO_4 or HCl extract were determined via:

$$P_{Fe(II)\text{ in }NaH_2PO_4\text{ or HCl}} = \frac{Fe(II)_{\text{edge or struc}}}{Fe(tot)_{\text{edge or struc}}} \times 100\% \quad (3.3)$$

and

$$P_{Fe(III)\text{ in }NaH_2PO_4\text{ or HCl}} = \frac{Fe(tot)_{\text{edge or struc}} - Fe(II)_{\text{edge or struc}}}{Fe(tot)_{\text{edge or struc}}} \times 100\% \quad (3.4)$$

where $Fe(II)_{\text{edge or struc}}$ and $Fe(tot)_{\text{edge or struc}}$ are the total Fe(II) and total Fe concentrations in the NaH_2PO_4 or HCl extract.

Temporal Fe(II) concentrations of all measured iron pools increased over the course of each RP, while Fe(II) concentration maxima decreased with each successive cycle (Figure 3.1A, Table B.3). Consequently, $F_{Fe(II)}$ was highest (9.7%) at the end of RP1, and within error of the maximum value (~10%) reported for the NAu-1 reduction by *S. oneidensis* after 161 days, thereby indicating all bioavailable Fe(III) had been reduced (Shi *et al.*, 2016). Accordingly, $F_{Fe(II)}$ decreased with each successive RP giving values of 7.4 and 5.7% at the ends of RP2 and RP3, respectively. Initial % Fe(III) reduction rates (i.e., within 24 h) were 1.1, 1.0 and 0.5% day^{-1} for RP1, RP2 and RP3, respectively.

More specifically, Fe(II) was the sole Fe redox species found in the aqueous phase [i.e., $Fe(II)_{aq}$] and sorbed to the basal plane [$Fe(II)_{basal}$] in each RP (Figure 3.1B, Table B.3). By contrast, iron bound to the edge hydroxyl groups [i.e., Fe_{edge}] and the residual solid contained both ferrous and ferric iron [i.e., $Fe(II)_{struc}$ and $Fe(III)_{struc}$] (Figure 3.1B&C, Table B.3). While concentrations of aqueous and basal plane sorbed Fe(II) within each RP increased over time, intra-period proportions of the same Fe(II) pools varied little. However, the proportions of each pool [i.e., $P_{Fe(II)_{aq}}$ and $P_{Fe(II)_{basal}}$] decreased between RP1 to RP3 from 18.4 to 9.9% and 9.4 to 3.0%, respectively (Figure 3.2A, Table B.4). Decreases in the proportions of the aforementioned Fe(II) pools coincided with increases in the proportions of edge hydroxyl group bound Fe(II) [i.e., $P_{Fe(II)_{edge}}$] and structural Fe(II) [$P_{Fe(II)_{struc}}$] from 55.5 to 63.5% and 16.6 to 23.5%, respectively. The relative proportions of Fe(II) in NaH_2PO_4 extract [i.e., $P_{Fe(II)\text{ in }NaH_2PO_4}$] and in HCl extract [$P_{Fe(II)\text{ in HCl}}$] both increased within each RP. Ferrous iron became dominant in the NaH_2PO_4 extract [$P_{Fe(II)\text{ in }NaH_2PO_4} > 90\%$] upon $F_{Fe(II)} > 2\%$ during RP1 and RP3 or >4% during RP2, while $P_{Fe(II)\text{ in HCl}}$ was always <30% (Figure 3.2B&C). As expected, Fe(III) reduction was not observed in the control reactor during RP1; however, the reactor

became contaminated with cells after RP1 (Table B.3) and was omitted from the rest of the experiment.

Within 30 minutes of the onset of each OP, $F_{Fe(II)}$ reached similarly low values (1.2-1.3%) and fell to less than 0.4% after 3-day oxidation in OP1 and OP2 (Figure 3.1A, Table B.3). Moreover, basal-sorbed and edge-bound Fe(II) were completely oxidized during OPs (Figure 3.1B), while incomplete structural Fe(II) oxidation was observed at the end of the OPs, with remaining Fe(II) concentrations in the range 30-70 μM (Figure 3.1C, Table B.3).

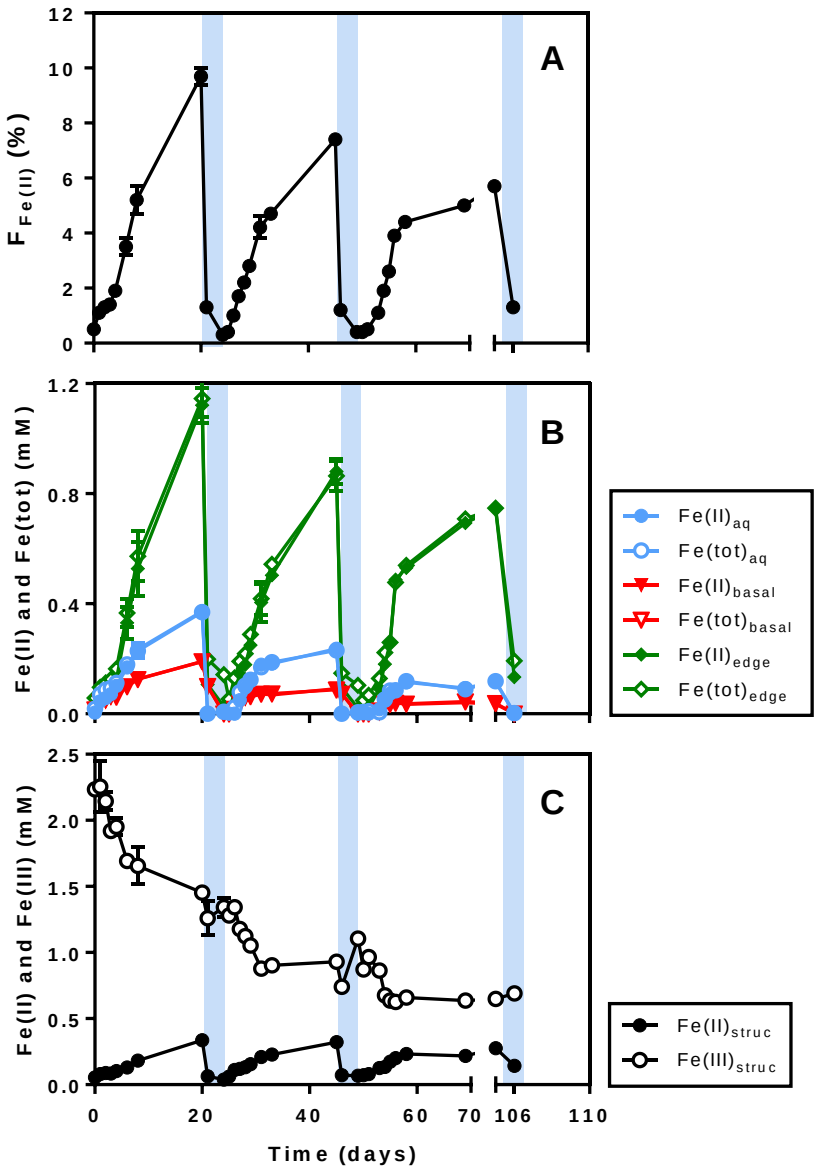

Figure 3.1. Temporal changes of A) fraction of total Fe(II) [$F_{Fe(II)}$], B) Fe(II) and Fe(tot) concentrations in aqueous phase, $CaCl_2$ extraction, and NaH_2PO_4 extraction, and C) Fe(II) and Fe(III) concentrations in HCl extraction from bioreactors during three redox cycles. Error bars indicate ranges observed in duplicate bioreactors. The white and blue backgrounds indicate RPs and OPs, respectively.

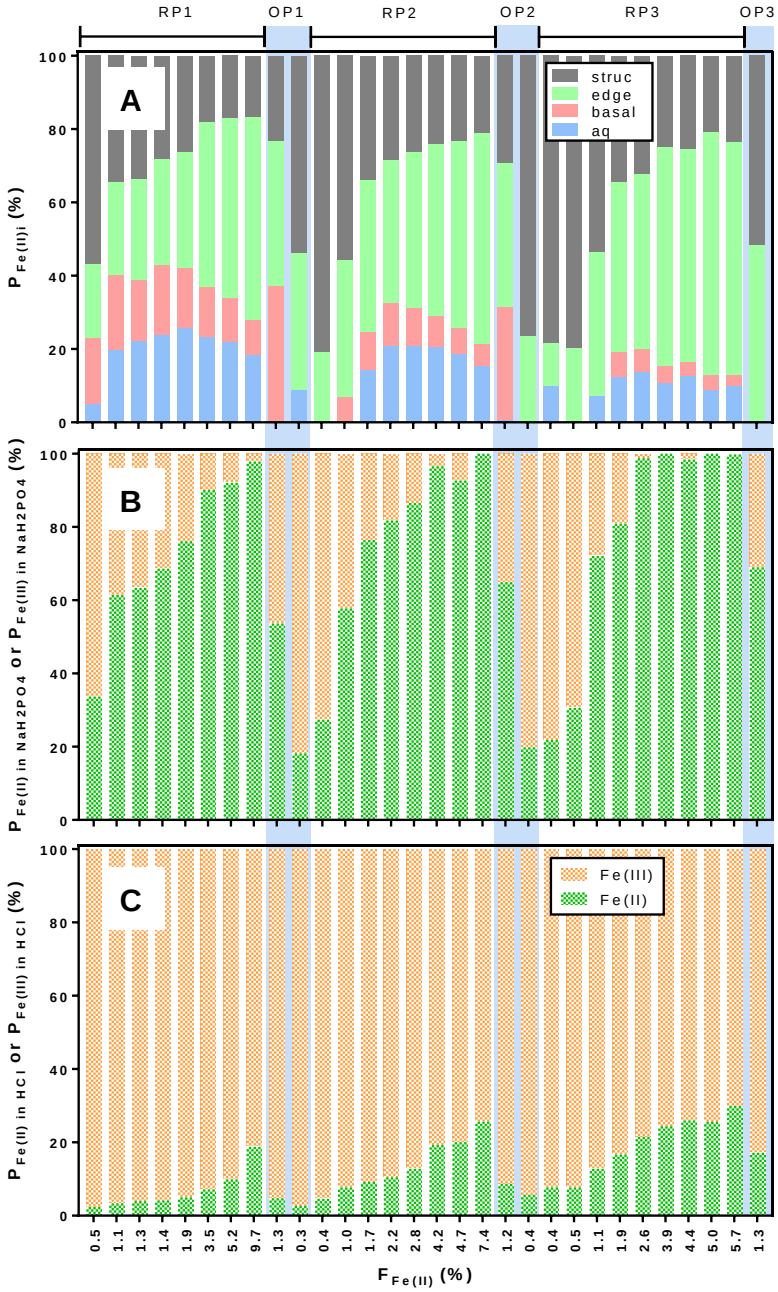

Figure 3.2. A) Proportions of Fe(II) in the aqueous phase and the three extractions relative to total Fe(II). Relative proportions of Fe(II) and Fe(III) in B) NaH_2PO_4 extractions and C) HCl extractions vs. fraction of total Fe(II) [$F_{Fe(II)}$]. RP and OP periods are indicated at the top of panel A.

3.4.2 Reductive NAu-1 dissolution

Reductive Fe dissolution is commonly observed from smectite (Dong *et al.*, 2003). Iron(III) reduction at the edge sites of NAu-1 produces a portion of dissolved Fe(II) which would partially adsorb onto the basal planes and interlayer spaces (Shi *et al.*, 2016). Therefore, the proportion of dissolved Fe [$D_{Fe(II)}$] is the sum of aqueous and basal-sorbed Fe(II) over the total Fe in NAu-1 and determined via:

$$D_{Fe(II)} = \frac{Fe(II)_{aq} + Fe(II)_{basal}}{\text{Total Fe in NAu}-1} \times 100\% \quad (3.5)$$

where $Fe(II)_{aq}$ and $Fe(II)_{basal}$ are the molar concentrations of aqueous Fe(II) and $CaCl_2$ extractable Fe(II). Each successive redox cycle resulted in decreases in the final $D_{Fe(II)}$ values: 2.7, 1.5 and 0.7% for RP1, RP2, and RP3, respectively (Figure 3.3A). During RP1, $D_{Fe(II)}$ was linearly correlated with the fraction of total Fe(II) [i.e., $F_{Fe(II)}$] ($R^2 = 0.976$, $P < 0.0001$, Figure 3.3A), thereby confirming that Fe(II) dissolution from NAu-1 was due to structural Fe(III) reduction. Moreover, the linear relationship between $D_{Fe(II)}$ and $F_{Fe(II)}$ was significantly weakened during RP2 and RP3. This was particularly evident by RP3 whereby Fe dissolution ceased [i.e., $D_{Fe(II)}$ plateaued] while Fe reduction continued [i.e., increasing $F_{Fe(II)}$].

To study the impact of redox changes on bulk NAu-1 dissolution, the major NAu-1 structural elements (i.e., Si, Al, Mg) in the aqueous phase and the three extractions were also monitored during the redox cycles (Table B.5). Even though Na^+ quantitatively occupied interlayer space during the purification of clay, Na^+ was not included as an indicator of NAu-1 dissolution because the addition of Na-lactate interfered with the detection of interlayer Na^+. Within the structure of NAu-1, >87% of the tetrahedral cations are Si atoms, which occur only in the tetrahedral sheets (Keeling *et al.*, 2000; Gates *et al.*, 2002). Meanwhile, Fe accounts for >91% of the octahedral cations and exclusively occupies the octahedral sheets (Keeling *et al.*, 2000; Gates *et al.*, 2002). Thus, the proportions of dissolved Si and dissolved Fe approximate the extent of the dissolution of tetrahedral and octahedral sheets of NAu-1, respectively. The proportion of dissolved Si is calculated according to:

$$D_{Si} = \frac{Si_{aq} + Si_{basal}}{\text{Total Si in NAu}-1} \times 100\% \quad (3.6)$$

where Si_{aq} and Si_{basal} are the molar concentrations of aqueous and $CaCl_2$ extractable Si.

In the aqueous phase and $CaCl_2$ extraction, the concentration of Si increased with the fraction of Fe(II) during each RP. During the RP1, the ratios of dissolved Fe to Si [$D_{Fe(II)}$: D_{Si}] over time were ~

1:1 (dashed line in Figure 3.3B), which was evidence of bulk NAu-1 dissolution. In other words, one Fe-containing octahedron and its corresponding two Si-containing tetrahedra (one above and the other below the octahedron) broke off simultaneously (Shi *et al.*, 2016). However, RP2 and RP3 produced higher ratios of dissolved Fe to Si (Figure 3.3B) and may reflect a higher extent of dissolution of the octahedral sheets over the tetrahedral sheets, or more Si precipitation in the RP2 and RP3. The dissolution of Fe and Si during the OPs (≤0.5%) was more limited than that during RPs due to the lack of structural Fe(III) reduction whereby $D_{Fe(II)}$: D_{Si} deviated from 1:1. Lastly, concentrations of aqueous and $CaCl_2$ extractable Al and Mg from bioreactors varied insignificantly within and across redox cycles (Table B.5), which may be due to nonstoichiometric dissolution of NAu-1 during redox cycles.

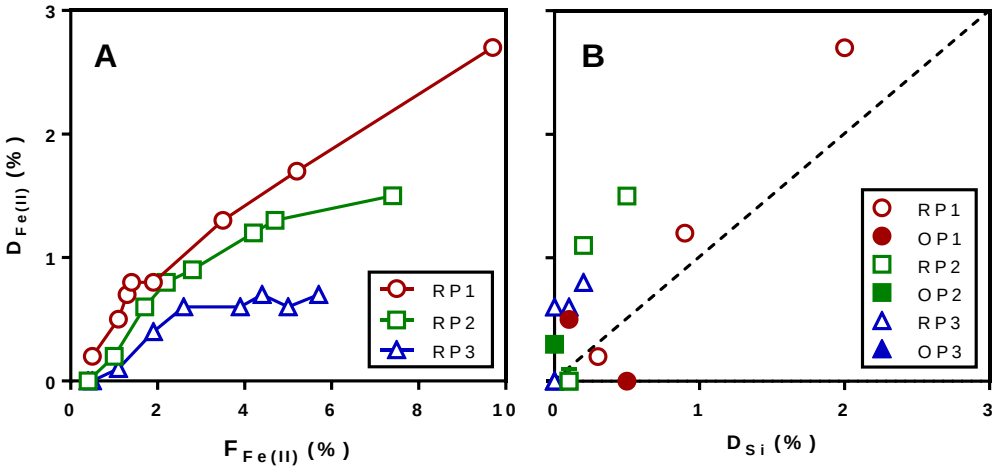

Figure 3.3. Relationships between the proportion of dissolved Fe and A) the extent of microbial Fe(III) [$F_{Fe(II)}$] during the three RPs, and B) the proportion of dissolved Si of three redox cycles. The dashed line in B) is the 1:1 line of the proportion of dissolved Fe to the proportion of dissolved Si. Error bars indicate standard deviations of triple measurements.

3.4.3 Mineralogical transformation and particle size alteration

The purity of the unaltered NAu-1 was verified by XRD, SEM, and TEM (Figures B.1A-C and B.2A). The mineral compositions of unaltered, 1st oxidized, and 2nd oxidized NAu-1 were the same as shown in the XRD patterns (Figure B.1A). The intensity of XRD patterns of re-oxidized NAu-1 is lower than that of unaltered NAu-1, may be due to the release of Fe from NAu-1 during RPs. We also could

not exclude the possibility from the changes in layer charge which induce the increase in water layers between interlayer spaces. TEM images and corresponding SAED patterns of 1st and 2nd oxidized NAu-1 show no evidence for secondary mineral formation (Figure B.1D&E).

The unaltered NAu-1 comprised two types of particles/aggregates, as shown in the SEM image (Figure B.2A). One type was large and wavy, as indicated by "L" in Figure B.2A. The large particles overlap with each other and show poorly defined edges in the SEM images. The other type was relatively small (<5 μm), as indicated by "S" in the insert of Figure B.2A. The elemental compositions of these two types of particles were both close to the NAu-1 formula (Table B.6). After six days of RP1, the chemical composition of the small particles ("S" in Figure B.2B) remained the same as that of the large particles ("L" in Figure B.2B, Table B.6). To study the mineralogical changes of NAu-1 induced by long-term reduction, the solid from the mini bioreactor that simulated RP1 was analyzed after 59-day incubation. The atomic ratio of Fe:Si of the small particle dropped slightly, below that of the surrounding large particle (Figure B.2C, Table B.6). The SEM image of the 1st oxidized NAu-1 exhibits no significant change in Fe:Si for some small particles ("S1" in Figure B.2D), while other small particles contain only Si ("S2" in Figure B.2D).

Samples of NAu-1 collected during RP2 and OP2 also contained large and small particles (Figure B.2E&F). The chemical composition of the large particles was similar to unaltered NAu-1, while the small particles were significantly depleted in Fe (Table B.6). It seemed that the dissolution of Fe from the small particles exceeded those of Si and Al, that is, Si and Al were left behind in the small particles upon reductive dissolution of Fe. This observation was consistent with the results showing that nonstoichiometric dissolution took place during RP2 (section 3.4.2).

After randomly selecting 5-10 locations on the SEM images of the 3rd reduced NAu-1, small particles were rarely seen (Figure B.2G). This may be due to the (near-)complete dissolution of the small particles after the three consecutive redox cycles. Nonstoichiometric dissolution of large particles was not observed during three redox cycles (Table B.6).

During redox cycles, the XRD patterns show the increase in the average crystal doman size along *a*- and *b*-direction (i.e. more platy shape) based on the full width at half maximum (FWHM) of (hk0) XRD peaks (Figure B.1A). The outcomes from the VASCO nanoparticle size analyzer and FlowCam® VS series may reflect the sizes of aggregates rather than sizes of single crystals. The particle size of unaltered NAu-1 varied between 112.8-595.8 nm (10-90 percentiles) and 5-23.4 μm (min-max) as measured by VASCO nanoparticle size analyzer and FlowCam® VS series, respectively

(Figure B.3, Table B.7). With redox cycles, no obvious trend was found for particle with sizes between 5-100 μm, while particles <0.6 μm were absent from the 0.5 nm – 5 μm particle size range since RP1.

3.4.4 Changes in Fe isotope composition within and across redox cycles

Significant temporal changes in the Fe isotope compositions of all Fe pools were observed within each redox cycle and were markedly different from the initial Fe isotope composition of bulk NAu-1 ($\delta^{56}Fe_{bulk\ NAu\text{-}1}$ = 0.59‰) (Shi *et al.*, 2016) (Figure 3.4, Table B.8). Measured $\delta^{56}Fe$ values for Fe in the aqueous phase and sorbed to the basal planes were assumed to reflect isotope compositions of pure Fe(II) phases [i.e., $\delta^{56}Fe_{aq\ Fe(II)}$ and $\delta^{56}Fe_{basal\ Fe(II)}$], as Fe(II) was the sole Fe redox state detected. Measured isotope values of Fe bound to the edge hydroxyl group [i.e., $\delta^{56}Fe_{edge\ Fe}$] exhibited the mixed isotope compositions of edge-bound Fe(II) and Fe(III) [or structural Fe(III)] for low reduction extents [$F_{Fe(II)}$ < 2% during RP1 and RP3, and < 4% during RP2], and represented the isotope compositions of approximately pure Fe(II) phase when reduction extents were high [$F_{Fe(II)}$ > 2% during RP1 and RP3, and > 4% during RP2]. However, $\delta^{56}Fe$ values for the 0.5 M HCl extract [i.e., $\delta^{56}Fe_{struc\ Fe}$] were a reflection of both structural Fe(II) [i.e., $\delta^{56}Fe_{struc\ Fe(II)}$] and Fe(III) [i.e., $\delta^{56}Fe_{struc\ Fe(III)}$] and described using:

$$\delta^{56}Fe_{struc\ Fe} \times Fe(tot)_{struc} = \delta^{56}Fe_{struc\ Fe(II)} \times Fe(II)_{struc} + \delta^{56}Fe_{struc\ Fe(III)} \times Fe(III)_{struc} \quad (3.7)$$

Consequently, $\delta^{56}Fe_{struc\ Fe(II)}$ and $\delta^{56}Fe_{struc\ Fe(III)}$ values need to be partitioned further in order to distinguish between the two oxidation states. The edge-bound Fe(II) neighbors the structural Fe(II), and their coordination environments are similar (Soltermann *et al.*, 2014b). The isotope composition of structural Fe(II) was therefore hypothetically assumed to be the same as that of the edge-bound Fe(II), i.e. $\delta^{56}Fe_{struc\ Fe(II)} = \delta^{56}Fe_{edge\ Fe(II)}$. When substituted into Eq. (3.7) this gives:

$$\delta^{56}Fe_{struc\ Fe(III)} = \frac{\delta^{56}Fe_{struc} \times Fe(tot)_{struc} - \delta^{56}Fe_{edge\ Fe} \times Fe(II)_{struc}}{Fe(III)_{struc}} \quad (3.8)$$

Note that we used $\delta^{56}Fe_{edge\ Fe}$ as an approximation of $\delta^{56}Fe_{edge\ Fe(II)}$ in Eq. (3.8) based on two reasons: 1) $Fe(II)_{struc} << Fe(III)_{struc}$ when reduction extents were low [$F_{Fe(II)}$ < 2%], thus the difference between $\delta^{56}Fe_{edge\ Fe}$ and $\delta^{56}Fe_{edge\ Fe(II)}$ has little effect on $\delta^{56}Fe_{struc\ Fe(III)}$, and 2) when the reduction extents were higher [$F_{Fe(II)}$ > 2%], $\delta^{56}Fe_{edge\ Fe} \approx \delta^{56}Fe_{edge\ Fe(II)}$ as illustrated above.

During the initial 3-4 days of all RPs (Figure 3.4), measured δ^{56}Fe values of the Fe(II) phases (aqueous, basal-sorbed) and the edge-bound Fe were below that of the starting bulk NAu-1, while structural Fe(III) values were isotopically heavier than the starting bulk NAu-1. Specifically, for the three isotopically light Fe pools, during the initial reduction phase of RP1 and RP2, the basal-sorbed Fe(II), edge-bound Fe, and aqueous Fe(II) exhibited the lightest, intermediate, and heaviest isotopic compositions, respectively. While, during the same time phase in RP3, the aqueous Fe(II), basal-sorbed Fe(II), and edge-bound Fe exhibited lightest, intermediate, and heaviest isotopic compositions. As $F_{Fe(II)}$ increased within RP1 and RP2, the Fe(II) pools and edge-bound Fe became isotopically heavier, while structural Fe(III) became isotopically lighter (Figures 3.4). With increasing $F_{Fe(II)}$ in RP3, the isotope values of basal-sorbed Fe(II) and edge-bound Fe decreased, while that of aqueous Fe(II) increased and finally exceeded the isotope value of structural Fe(III). At the same $F_{Fe(II)}$, δ^{56}Fe values of the Fe(II) phases (aqueous, basal-sorbed) and the edge-bound Fe became less negative with successive RPs (Figure B.4A-C), while that of structural Fe(III) became more negative in the later RPs (Figure B.4D).

Given that the aqueous Fe(II) phase was removed prior to each OP, only the basal-sorbed, edge-bound and structural Fe(II) phases were subjected to oxidation. Isotope values of basal-sorbed Fe(II) decreased significantly at the beginning of OP1 and OP2, while that of edge-bound Fe increased slightly and that of structural Fe(III) changed very little (Figure 3.4). With complete oxidation or desorption of the basal-sorbed Fe(II) at the ends of OP1 and OP2, isotope analysis was not possible. At the end of OP1, the δ^{56}Fe values of edge-bound Fe and structural Fe(III) became close to that of the bulk NAu-1. In contrast to OP1 and OP2, the Fe isotopic composition measured at 0.5 h in OP3 for edge-bound Fe and structural Fe(III) became lighter and heavier, respectively.

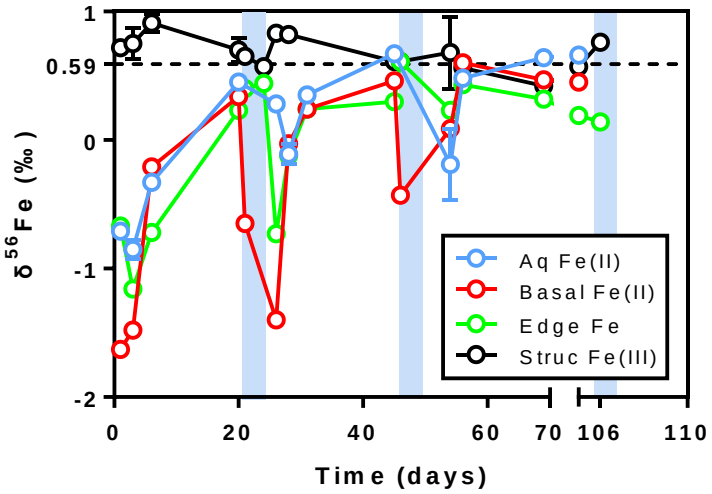

Figure 3.4. Temporal changes of Fe isotope compositions of aqueous Fe(II), basal-sorbed Fe(II), edge-bound Fe and structural Fe(III) from bioreactors. The isotope values of structural Fe(III) were calculated according to Eq. (3.8). The dashed line indicates the Fe isotope composition of the bulk NAu-1: $\delta^{56}Fe_{bulk\ NAu\text{-}1}$ = 0.59‰ (Shi *et al.*, 2016). Error bars represent ranges of duplicate measurement or observed in duplicate bioreactors. White and blue backgrounds indicate RPs and OPs, respectively.

3.5 Discussion

3.5.1 Decrease of Fe bioavailability in NAu-1

Based on our previous study (Shi *et al.*, 2016), we propose that the quantity of initial bioavailable Fe in NAu-1 is ~10%. During each RP, microbial Fe(III) reduction was accompanied with dissolution of Fe(II) and its removal from the system, while the remaining Fe(II) remained associated with the solid (Figure 3.5A). Successive Fe redox cycles decreased the remaining bioavailable Fe pool in NAu-1 [Fe_{RemBio} = final $F_{Fe(II)}$ of each RP] from 10 to 5.7% by the end of RP3. Therefore, Fe bioavailability in NAu-1 decreased due to continuous removal of dissolved Fe(II) during RPs:

$$Fe_{RemBio} = 10\% - \sum_{i=n} D^{i}_{Fe(II)} \quad (3.9)$$

where $D^{i}_{Fe(II)}$ is the final $D_{Fe(II)}$ of RPi as calculated according to Eq. (3.5), and i = 1,2 and 3.

A strong linear relationship between Fe_{RemBio} and $D^{i}_{Fe(II)}$ illustrates that the drop in remaining bioavailable Fe in NAu-1 was accompanied with inhibition of reductive Fe dissolution during latter RPs (Figure 3.5B):

$$Fe_{RemBio} = 2.06 \times D^{i}_{Fe(II)} + 4.17 \quad (3.10)$$

A simple calculation based on Eq. (3.9) and (3.10), predicts that by RP10, $D^{10}_{Fe(II)}$ is <0.01%. The y-intercept [$F_{Fe(II)}$ = 4.17 ± 0.07%, $D_{Fe(II)}$ = 0%] further predicts that ~4.2% of total Fe in NAu-1 continues to be redox-reversible upon continued redox cycling, with ultimately no more Fe dissolution occurring. In other words, ~42% of the initial bioavailable Fe in NAu-1 is insoluble, whereas the remaining ~58% is soluble during repeated redox cycles.

Our results are consistent with previous studies that showed a decreasing extent of NAu-2 reduction over three consecutive redox cycles (Yang *et al.*, 2012; Zhao *et al.*, 2015). The latter authors proposed that permanent mineralogical changes are responsible for the decreased Fe redox-activity of clay after multiple redox cycles (Kim *et al.*, 2004; Meunier, 2005; O'Reilly *et al.*, 2005; Dong *et al.*, 2009; Ribeiro *et al.*, 2009; Stucki, 2011; Dong, 2012). However, compared to the cumulative Fe dissolution, structural changes should be a minor contributor to the decrease in the remaining bioavailable Fe in NAu-1. Previous studies showed that clay structural changes during microbial Fe(III) reduction are largely reversible (Ribeiro *et al.*, 2009; Stucki, 2011; Zhao *et al.*, 2015).

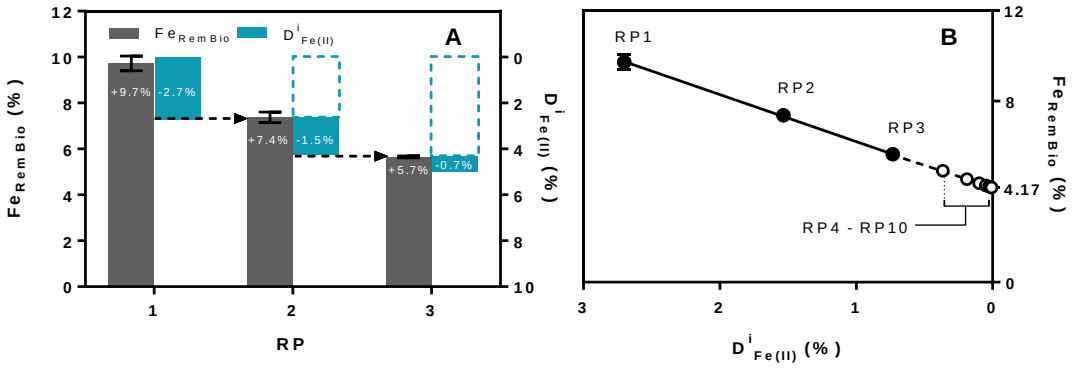

Figure 3.5. A) Remaining bioavailable Fe pool in NAu-1 decreases with cumulative dissolution of Fe(II) during RPs. Squares with blue dashed border indicate the sum of the dissolved Fe of previous RP(s). B) Linear relationship ($P \leq 0.01$, $R^2 = 0.9997$) between the remaining

bioavailable Fe pool in NAu-1 and the final proportion of dissolved Fe of each RP. Solid circles are the actual results from redox cycle experiments, empty circles are predictions for RP4 to RP10 based on the iteration calculation. Error bars indicate ranges observed in duplicate bioreactors.

3.5.2 Two bioavailable Fe pools of NAu-1

Under our experimental conditions, *S. oneidensis* seems to target the same Fe pool instead of exploring new Fe atoms. Indeed, Zhao *et al.* (2015) showed that without the aid of extra electron shuttles (e.g. AQDS), *Shewanella putrefaciens* CN32 could only reduce Fe(III) on the edge sites of clay minerals instead of reducing the interior Fe(III). Consequently, the decrease in Fe bioavailability may be attributed to the fact that less edge surface was reducible by bacteria during the latter RPs. In this case, three scenarios might have taken place during the RPs: (*i*) the reductive dissolution stripped away the edge surface thereby resulting in clay particles that exposed less edge surface to bacteria (Figure 3.6A); (*ii*) clay particles aggregated to render some edge surface inaccessible to bacteria (Figure 3.6B); or (*iii*) reductive Fe dissolution exclusively impacted the smallest particles, while the edge surface of large particles remained undissolved (Figure 3.6C).

The first scenario (Figure 3.6A) is unlikely as it is contradictory to the enlarged NAu-1 particles observed upon repeated redox cycles (section 3.4.3). Both scenarios (*ii*) and (*iii*) could explain the observations. Iron reduction increases the layer charge of clay particles, thereby promoting clay aggregation or flocculation (Kim *et al.*, 2005). Some edge sites could be occluded inside the aggregates and physically isolated from bacteria (Figure 3.6B). If scenario (*ii*) is true, the degree of aggregation may affect the quantity of insoluble bioavailable Fe(III) in two opposite ways: 1) if aggregation prevents Fe reduction on occluded edge sites, then the higher the aggregation, the less the insoluble bioavailable Fe(III) in NAu-1; 2) alternatively, if aggregation inhibits only Fe dissolution but has little impact on Fe reduction, then the insoluble bioavailable Fe would increase with more edge sequestration. The degree of aggregation did not exhibit an obvious trend across RPs except that aggregates <0.6 μm were absent in the samples after redox changes (Figure B.3, Table B.7). The absence of an obvious trend in aggregation seems in contradiction with the strong linear relationship between $F_{Fe(II)}$ and $D_{Fe(II)}$ (Figure 3.5B). Therefore, clay aggregation is unlikely responsible for the decrease in bioavailable edge surface of NAu-1.

We therefore propose that small clay particles are preferentially reduced and dissolved compared to larger ones (Yang *et al.*, 2012; Zhao *et al.*, 2015; Zeng *et al.*, 2016). SEM/EDS results of NAu-1 small particles show that the ratio of particle Fe:Si decreases with successive redox cycles (Figures B.2, Table B.6). The appearance of small particles depleted in Fe in OP1 and later redox cycles might be due to the re-precipitation of dissolved Si and Al (Dong *et al.*, 2003; Zhang *et al.*, 2007; Liu *et al.*, 2016). Alternatively, Fe(II) may have been preferentially dissolved from the small particles, leaving the other structural cations in the solid state. We prefer the latter hypothesis due to two reasons: 1) the small particles were observed in the unaltered NAu-1 before reductive dissolution occurred, indicating they were not produced through a dissolution-reprecipitation process, and 2) the formation of secondary minerals was not supported by our results (Figure B.1A&D&E).

In contrast, the large particles exhibited insignificant change in the Fe:Si ratios (Table B.6), implying stoichiometric or negligible dissolution of the large particles. Additionally, the interior structural Fe(III) in large particles did not participate in the redox reactions, only the Fe(III) atoms on the edge sites of clay particles were reduced during RPs (Ribeiro *et al.*, 2009; Stucki, 2011; Zhao *et al.*, 2015). Because the ratio of edge-site Fe(III) to interior Fe(III) decreases with the increasing particle size, the extent of Fe(III) reduction in the large particles was lower than that in the small particles. Correspondingly, the degree of Fe(II) dissolution from the large particles should also be lower than from the small particles. Limited Fe(II) dissolution would have had minor impact on the elemental composition of the large particles.

Yang *et al.* (2012) assumed that a fraction of "reactive Fe(II)", which adsorbed on the surface of clay, participated in the redox cycling of NAu-2. They attributed the enhanced rate of NAu-2 reduction during the early few hours to the increasing concentration of the "reactive Fe(II)" with consecutive redox cycles. In contrast, our results show decreasing NAu-1 reduction rates within the initial 24 h from RP1 to RP3. (Table B.3). Moreover, $Fe(II)_{basal}$ and $Fe(II)_{edge}$ – the adsorbed phases in our experiments – both decreased from RP1 to RP3 (Figure 3.1B, Table B.3). Adsorbed reactive Fe(II), if it existed at all in our experiments, would have turned into Fe (oxyhydr)oxides during OPs. However, the formation of Fe (oxyhydr)oxides during OP1 and OP2 was not detected in neither the XRD nor the TEM analyses (Figure B.1A&D&E).

Consequently, we hypothesize that the bioavailable Fe in NAu-1 is located along the edges of the large and small particles. The y-intercept (4.2 %) in Figure 3.5B may provide a minimum for the extent to which bioavailable Fe(III) may be reduced without Fe(II) being released into solution. The

gradual consumption of the bioavailable Fe in the small particles then explains the decrease of Fe reduction and dissolution (Figures 3.5B and 3.6C). Based on our results, scenario (*iii*) is at least a valid hypothesis. However, it may be difficult to define a clear boundary separating "large" from "small" particles, as this critical size varies when the number of reducible Fe(III) layers differs. Also, in most natural settings a large (but not necessarily well-known) size distribution of Fe containing clay mineral particles can be expected.

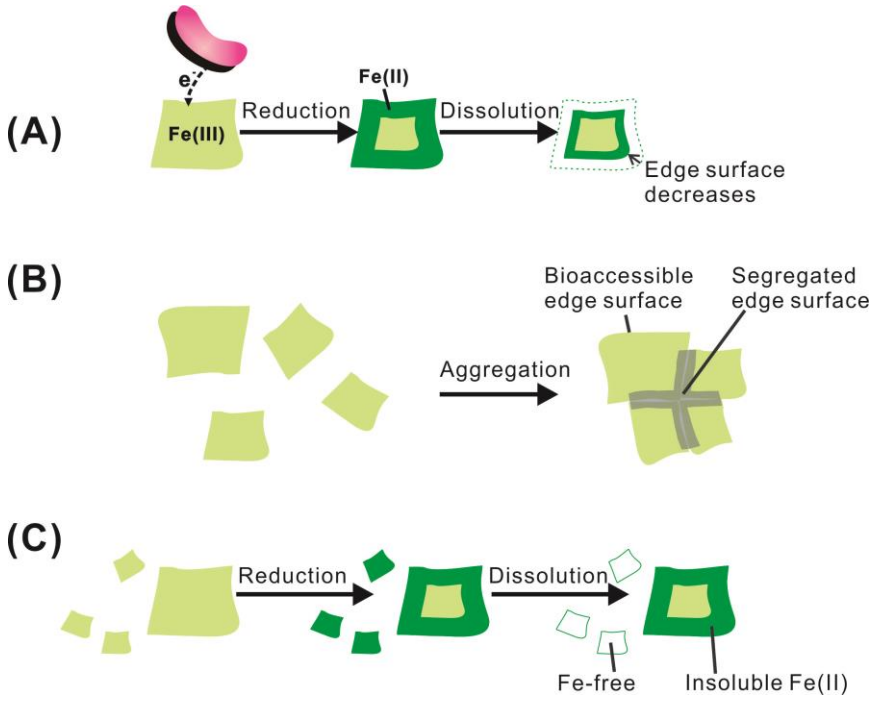

Figure 3.6. Three hypothetical scenarios that produce smaller edge surfaces of NAu-1 particles during RPs. A) In scenario (*i*) the reductive dissolution strips edge surface off and results in smaller clay particles, exposing less edge surface to bacteria. B) In scenario (*ii*) clay particles aggregate to occlude edge surfaces from bacteria. C) In scenario (*iii*) edge surface dissolution results in the complete dissolution of the small particles, while the large particles remain undissolved.

3.5.3 Minimization of exchangeable edge surface: implication from Fe isotopes

Using Fe isotopes we previously revealed that the reduction of clay produces structural Fe(II), in contrast to the reduction of Fe-(oxyhydr)oxides where reduction produces only soluble/adsorbed Fe(II) (Shi *et al.*, 2016). In this study, we used Fe isotopes to trace the redox cycles of NAu-1,

examine the validity of scenario (*iii*) proposed above, and further elucidate the mechanism(s) responsible for the decreasing Fe bioavailability of NAu-1.

Iron isotope fractionation between microbially produced Fe(II) and Fe(III) minerals is maintained by electron transfer coupled with atom exchange (ETAE) (Crosby *et al.*, 2005; Crosby *et al.*, 2007). The *in-situ* reduction of structural Fe(III) to structural Fe(II) forms a barrier that hinders the electron transfer between aqueous/edge-bound Fe(II) and the interior structural Fe(III) (Shi *et al.*, 2016). The higher the proportion of Fe(II) located within the structure, the less structural Fe(III) on the edge surface is available for the atom exchange. Large Fe isotope fractionation factors therefore correspond to a relative high abundance of exchangeable edge surface Fe.

According to the earliest samples we measured in RP1 [$F_{Fe(II)}$ = 1.1%], isotope fractionation between aqueous Fe(II) and edge-bound Fe was minimal [$\Delta^{56}Fe_{aq\ Fe(II)\text{-}edge\ Fe}$ = -0.04‰] (Table B.8), indicating that the aqueous Fe(II) likely derived from the Fe(II) bound to the edge sites.

During RP2, $\Delta^{56}Fe_{aq\ Fe(II)\text{-}struc\ Fe(III)}$ and $\Delta^{56}Fe_{edge\ Fe\text{-}struc\ Fe(III)}$ were smaller than those during RP1 at the same $F_{Fe(II)}$ (Figure 3.7, Table B.8), indicating that less extensive ETAE occurred during RP2 than during RP1 (Figure 3.8). In other words, less structural Fe(III) was exchangeable for Fe(II) phases in RP2 than in RP1. The loss of exchangeable edge surface might be induced by the consumption (through reductive dissolution) of structural Fe(III) on the edge sites during RP1 (Figure 3.8A). This direct deprivation of structural Fe(III) on the edge sites was supported by the preferential dissolution of Fe over Si and Al in the small particles (Figure B.2, Table B.6). The small particles became "Fe-free" (Figure 3.6C) and thereby lost the ability to exchange with edge-bound Fe(II) or aqueous Fe(II) during RP2. In turn, more insoluble bioavailable Fe(III) in the large particles had to be reduced during RP2 to reach the same $F_{Fe(II)}$ as that during RP1 (Figure 3.8). Consequently, higher $P_{Fe(II)_{struc}}$ was observed during RP2 than during RP1 at the same $F_{Fe(II)}$ (Figure 3.2A, Table B.4). The enhanced $P_{Fe(II)_{struc}}$ further decreased the exchangeable edge surface of NAu-1.

As expected, $\Delta^{56}Fe_{aq\ Fe(II)\text{-}struc\ Fe(III)}$ and $\Delta^{56}Fe_{edge\ Fe\text{-}struc\ Fe(III)}$ were smaller during RP3 than during RP2 at the same $F_{Fe(II)}$ (Figure 3.7, Table B.8), indicating less ETAE linked with a further decrease in the exchangeable edge surface. At the end of RP3, $\Delta^{56}Fe_{aq\ Fe(II)\text{-}struc\ Fe(III)}$ became positive (Figure 3.7A, Table B.8), indicating the complete blockage of ETAE between aqueous Fe(II) and structural Fe(III). The Fe isotope fractionation factor $\Delta^{56}Fe_{edge\ Fe\text{-}struc\ Fe(III)}$ decreased from -0.45 to -0.10‰ over 19 days [$F_{Fe(II)}$ = 1.9-5.0%] and returned to -0.38‰ after 55 days [$F_{Fe(II)}$ = 5.7%] of the prolonged RP3

(Figure 3.7B, Table B.8), implying that complete exchange between edge-bound Fe(II) and structural Fe(III) was not achieved within 19 days of RP3. From day 19 to day 55 of RP3, the low reduction rate allowed the (near-) complete atom exchange between edge-bound Fe(II) and structural Fe(III).

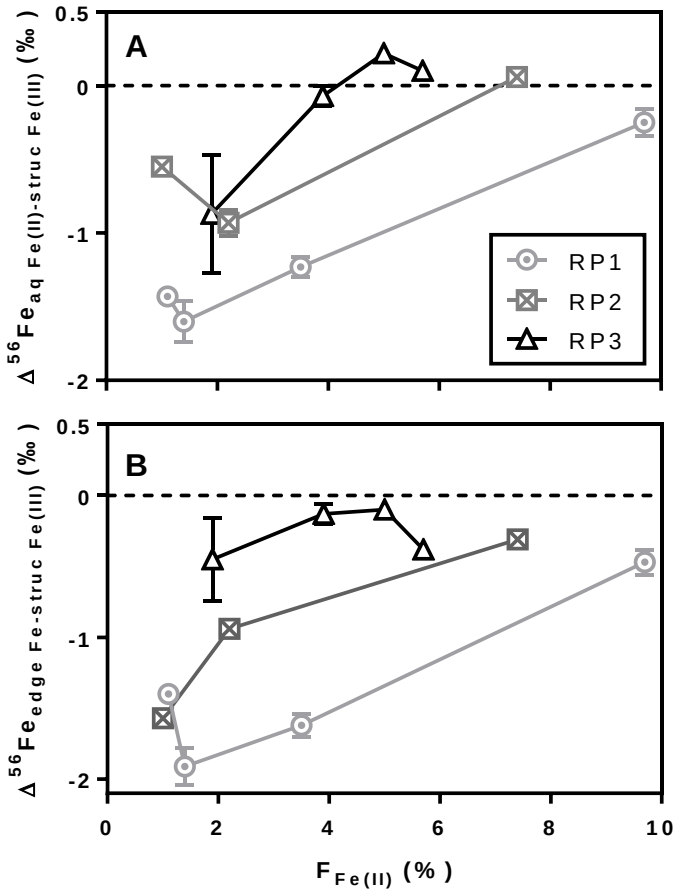

Figure 3.7. Iron isotope fractionations between A) aqueous Fe(II) and structural Fe(III) and B) edge-bound Fe and structural Fe(III) vs. fraction of total Fe(II) [$F_{Fe(II)}$] during three RPs. The isotope value of structural Fe(III) is calculated according to Eq (3.8). Error bars indicate one standard deviation of propagated errors.

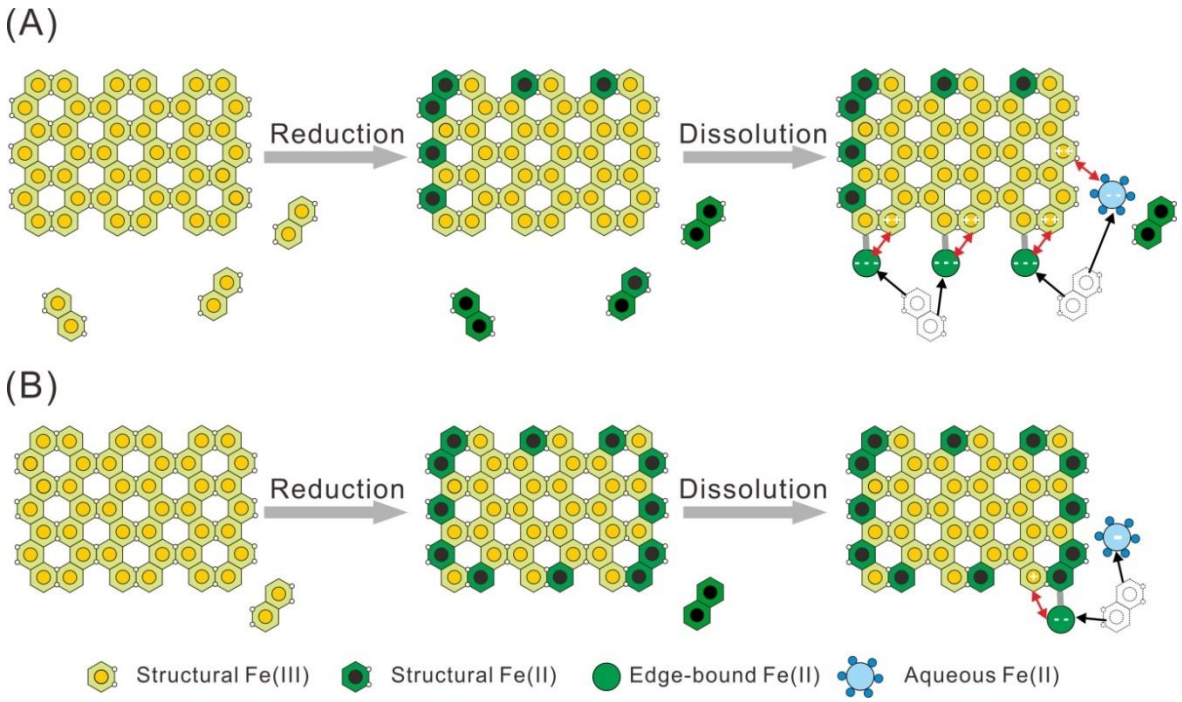

Figure 3.8. Hypothetical model of microbial Fe(III) reduction and ETAE for NAu-1 during RPs. A) The bioavailable Fe(III) is located on the edge sites of large and small particles of the unaltered NAu-1. If we assume ~50% of the initial bioavailable Fe(III) is reduced during RP1, Fe(II) in small particles is dissolved (black arrows), while Fe(II) in large particles remains undissolved. ETAE (red arrows) between aqueous/edge-bound Fe(II) and structural Fe(III) produces isotopically light aqueous and edge-bound Fe(II) (as indicated by "--" and "---", respectively) and isotopically heavy structural Fe(III) (as indicated by "++"). B) Based on the premise that a fraction of bioavailable Fe is released from the small particles and removed during the former RP(s), the remaining bioavailable Fe in the NAu-1 particles decreases correspondingly during the latter RPs. Dissolution of Fe(II) (black arrows) decreases as fewer small particles remain. At the same $F_{Fe(II)}$ as in RP1 [~50% of initial bioavailable Fe(III) reduction], the proportion of structural Fe(II) increases and the exchangeable edge surface decreases in RP2 and RP3. ETAE is less extensive between aqueous/edge-bound Fe(II) (as indicated by "-" and "--", respectively) and structural Fe(III) (as indicated by "+") during the latter RPs than the former ones. The Fe isotope fractionation between the same Fe(II)-Fe(III) pairs decreases with consecutive redox cycles, at the same $F_{Fe(II)}$ (Figure 3.7).

3.6 Conclusions and environmental implications

Two bioavailable Fe(III) pools were found to explain the results of the three redox cycles experiment with NAu-1: 1) microbially reducible and soluble Fe in small particles, and 2) microbially reducible but insoluble Fe in large particles. Repeated redox cycles gradually depleted the Fe in the small particles, thereby decreasing the remaining bioavailable Fe in NAu-1. Approximately 4.2% of total Fe was predicted to be renewable for microorganisms. We report for the first time that Fe isotope fractionation between aqueous Fe(II)/edge-bound Fe and structural Fe(III) decreases during repeated redox cycles, because of the progressive loss of exchangeable edge surface.

Our study mimics some of the effects of redox fluctuations in the vadose zone, where dissolved Fe(II) from clay reduction is leached to the groundwater, before it can be oxidized. Clearly given different starting clay materials, the fraction of the renewable Fe would vary. For example, if we assume clay *A* contains only soluble bioavailable Fe, then the reductive dissolution would eventually eliminate all bioavailable Fe after a certain number of redox cycles. At the other extreme, if clay *B* contains only insoluble bioavailable Fe, then *B* could be completely reversible irrespective of the number of redox cycles. Like many clay minerals, NAu-1 contains both soluble and insoluble bioavailable Fe thereby highlighting the importance of quantifying the degree to which the Fe is renewable. The presence of soluble and insoluble bioavailable Fe pools in clay may influence the fate of nutrients and contaminants that are attached to the clay surface or intercalated between interlayer space. For example, Zeng *et al.* (2016) showed that the reversibility/solubility of Fe(III) in clay particles has direct implications on the mobility of certain organic compounds. Compared to clay minerals, Fe (oxyhydr)oxides are not a truly renewable Fe source as they dissolve upon reduction, thereby releasing the adsorbed contaminants. Further research on the role of redox fluctuations on clay-bound Fe will be needed to verify the preliminary, hypothetical model of clay Fe reactivity presented in this study.

Chapter 4
Importance of tetrahedral Fe during microbial reduction of nontronite NAu-2

4.1 Summary

Iron-containing clay minerals play a significant role in Fe redox cycling in the environment. However, the role of tetrahedral Fe during structural Fe(III) reduction remains uncertain. To probe this role, NAu-2 was subjected to a series of experiments, including microbial reduction by *Shewanella oneindensis* MR-1, chemical reduction by sodium dithionite, and a mixing experiment with dissolved Fe(II). Microbial reduction of NAu-2 was divided into three stages on the basis of the observed Fe isotope fractionations: 1) stage 1 exhibited low to medium reduction extent (0-12.7%), with increasing isotope fractionation between aqueous Fe(II)/edge-bound Fe and structural Fe as a result of extensive electron transfer and atom exchange (ETAE) through the edge surface; 2) during stage 2, medium to high reduction extent (12.7-19.5%) was accompanied by a decrease in the isotope fractionation between edge-bound Fe and structural Fe and an increase in the isotope fractionations between aqueous Fe(II)/basal-sorbed Fe(II) and structural Fe, indicating that ETAE took place through the basal plane surface; 3) the reduction extent reached its maximum (19.5-22%) during stage 3, as the isotope fractionations between aqueous Fe(II)/basal-sorbed Fe(II) and structural Fe decreased, indicating that ETAE through the basal plane was inhibited. The bioreducible structural Fe(III) in NAu-2 (~22%) was approximately double that in NAu-1 (~10%). However, the reductive dissolution of NAu-2 was lower than that of NAu-1 at the same extent of reduction, leading us to attribute the more extensive reduction observed in NAu-2 to structural Fe(III) reduction in the solid state. The latter was likely associated with tetrahedral Fe(III), via the transfer of electrons from basal-sorbed Fe(II) produced during stage 2. Our study shows that the tetrahedral Fe(III)-containing clay minerals may be more redox-reactive than those with only octahedral Fe(III). The basal planes with their adjacent tetrahedral Fe(III) provide exchange surfaces, in addition to the clay edge surfaces, capable of interacting with aqueous Fe(II). It is particularly important to recognize the reactivity of the basal plane surfaces under acidic condition, as redox-active cation [e.g., Cr(VI), Tc(VII)] adsorption mainly takes place on these basal planes at low pH where they can react with reduced tetrahedral Fe.

4.2 Introduction

Clay minerals are of great significance for Fe redox cycling in surface environments as clays carry more than half of the total Fe in the soils and sediments (Kostka *et al.*, 2002; Dong, 2012). Structural ferric iron in clay is susceptible to microbial reduction by a wide range of bacteria without the aid of external electron shuttles (Jaisi *et al.*, 2005; Bishop *et al.*, 2011; Zhang *et al.*, 2012; Zhang *et al.*, 2013a; Zhao *et al.*, 2015). Moreover, clays are important in soil remediation, as the bioreduced Fe in clay minerals renders it reactive towards redox-active toxic metals (Yang *et al.*, 2012; Bishop *et al.*, 2014) and organic compounds (Fialips *et al.*, 2010; Luan *et al.*, 2015a; Luan *et al.*, 2015b).

Various studies have shown that microbial Fe reduction (Ribeiro *et al.*, 2009; Zhao *et al.*, 2015), Fe atom exchange (Neumann *et al.*, 2015; Shi *et al.*, 2016), and surface complexation (Catalano and Brown, 2005; Bachmaf and Merkel, 2011; Soltermann *et al.*, 2014a) occur at the edge surfaces of clay. However, a recent study proposed that Cr(VI) was possibly reduced by electrons originating from structural Fe(II) and penetrating through the basal planes (Joe-Wong *et al.*, 2017). Basal-sorbed Fe(II) can also reduce structural Fe(III) by passing electrons perpendicular to the clay layers (Neumann *et al.*, 2013; Latta *et al.*, 2017). The proportion of atom exchange may be enhanced between dissolved Fe(II) and clays which have tetrahedral Fe(III) in addition to octahedral Fe(III) (Neumann *et al.*, 2015). While not found extensively in the environment, NAu-2 serves as a model clay, containing tetrahedral Fe(III) (Gates *et al.*, 2002), that can be used to elucidate bioavailability of clay minerals, mineralogical changes after redox changes, and contaminant-clay interactions (Jaisi *et al.*, 2005; Yang *et al.*, 2012; Zhao *et al.*, 2015; Zeng *et al.*, 2016). However, the relative contributions of tetrahedral and octahedral Fe to abiotic and biotic redox cycling in NAu-2 is not well constrained.

The presence of tetrahedral Fe(III) may change clay reactivity in three ways: 1) promoting the bioavailability of clay by serving as a source of additional electron acceptor during microbial reduction (Jaisi *et al.*, 2005); 2) reacting with basal-sorbed species (e.g. Fe^{2+}); and 3) providing alternative electron pathways by acting as electron bridge between different octahedral Fe(III) atoms or between basal-sorbed Fe(II) and octahedral Fe(III). Our previous study showed that ~10% of the total Fe(III) in nontronite NAu-1 is bioreducible (Shi *et al.*, 2016). With a similar total Fe content, ~9% of the total Fe(III) in nontronite NAu-2 is located in the tetrahedral sheets (Gates *et al.*, 2002). Therefore, the reactivity of the NAu-2 basal plane surface is potentially as important as the edge surface, especially under acidic conditions – as reducible heavy metals adsorb onto basal planes at low pH values (Abollino *et al.*, 2003).

In this study, we carried out two batches of microbial reduction experiments to elucidate the impact of tetrahedral Fe on: 1) the bioavailability of NAu-2, and 2) the partitioning of Fe isotopes during the microbial reduction of NAu-2. To further study the influence of different reduction pathways on Fe isotope fractionation, chemical reduction of NAu-2 was performed as a basis for comparison with the biotic experiments. We also carried out mixing experiments using NAu-2 (Fe-rich nontronite) and SYn-1 (Fe-free montmorillonite) to independently assess the role of Fe(II) adsorption without the interference from reduction.

4.3 Materials and methods

4.3.1 Clay mineral preparation

Nontronite NAu-2 [$Na_{0.72}(Si_{7.55}Al_{0.16}Fe_{0.29})(Al_{0.34}Fe_{3.54}Mg_{0.05})O_{20}(OH)_4$] (Gates *et al.*, 2002) and Fe-free montmorillonite SYn-1 [$Na_{0.024}(Al_{4.44}Mg_{0.04}Fe_{tr})(Si_{6.5}Al_{1.5})O_{20}(OH)_4$] (Mermut and Cano, 2001; Neumann *et al.*, 2013) were purchased from the Clay Minerals Society. The raw materials were purified as described in our previous study to obtain the pure clay fraction (<0.5 μm) (Jackson, 1956; Neumann *et al.*, 2013; Shi *et al.*, 2016), which was verified by X-ray diffraction (XRD) (Figure C.1A), transmission electron microscopy (TEM) (Figure C.1B&C), and scanning electron microscopy (SEM) coupled to energy dispersive spectroscopy (EDS) (Figure C.4A&D) (See Section 4.3.3.4). The purified NAu-2 is denoted as "unaltered NAu-2", which was the starting material for the reduction, mixing and partial dissolution experiments.

4.3.2 Experiments

4.3.2.1 Microbial reduction

Two batches of microbial reduction experiments were conducted to study the variation in isotope fractionation during the long-term (100 days for batch I) and short-term (21 days for batch II) incubation of clay with bacteria. The minimal growth medium (MM) for the reduction experiments contained 10 mM HEPES {2-[4-(2-hydroxyethyl)piperazin-1-yl]ethanesulfonic acid, $C_8H_{18}N_2O_4S$} buffer (pH 6.8), Na-lactate (40 mM, sole electron donor), 100 μM KH_2PO_4, and 5 mM $(NH_4)_2SO_4$ (batch I) or 10 mM NH_4Cl (batch II). The model Fe reducing bacteria *Shewanella oneidensis* MR-1 (Myers and Nealson, 1988b) was cultured in LB medium to late-log phase (~16 h) and cells were centrifuged (3500 rpm, 10 min), then washed three times with MM. Cells were inoculated into 120 mL (batch I) or 150 mL (batch II) of MM in serum bottles containing 5 mg/mL NAu-2 [~22.7 mM

Fe(III)], giving a final cell concentration of 2×10^8 cells/mL. Duplicate serum bottles for both batch experiments were sealed with thick butyl rubber stoppers and aluminum crimp seals. One control group was prepared in parallel with batch I and contained no cells. Bioreactors and controls were incubated at ~20 ℃ in the dark and shaken at 100 rpm (VWR® 3500 standard shaker). At selected sampling points, 8 or 10 mL slurries were sampled anaerobically from the bioreactors and control reactor in an anaerobic chamber (2% H_2, 98% N_2, Coy®).

4.3.2.2 Chemical reduction

Chemical reduction experiments were performed to achieve analogous or greater extents of reduction as observed in the biotic reactors (Table C.1). Samples were prepared inside an anaerobic chamber by adding sodium dithionite ($Na_2S_2O_4$, 20-150 mg) to 10 mL HEPES buffer (10 mM, pH 6.8) containing NAu-2 (5 mg/mL). Different reduction extents were achieved by sacrificially sampling each bioreactor at selected time points which was followed by centrifugation (6500 rpm, 20 min).

4.3.2.3 Mixing experiments

To check the adsorption effect on Fe isotope fractionation, 50 mL Fe(II) solution (2.0 mM), which was prepared by adding $FeCl_2 \cdot 4H_2O$ to 10 mM HEPES buffer (pH 6.8) in the anaerobic chamber, was mixed with either 0.1 g NAu-2 or SYn-1 in duplicate serum bottles. An additional control reactor was prepared containing only NAu-2 and HEPES buffer [i.e., no Fe(II) addition]. All reactors were sealed with thick butyl rubber stoppers and aluminum crimps and shaken continuously at 100 rpm in the dark. At selected time points, 8 or 16 mL slurries were sampled anaerobically from the experimental and control reactors.

4.3.2.4 Partial dissolution

NAu-2 was partially dissolved to investigate the Fe isotope distribution in the clay particles (Table C.2). NAu-2 (50 mg) was mixed with 5 mL HCl (0.5 M) for selected time points, centrifuged (6500 rpm, 20 min), and the supernatant was filtered (0.2 μm, nylon) before isotope wet chemistry. Following the same procedure, fresh HCl was added to the residual solid to dissolve more Fe, followed by centrifugation and filtration which were repeated until ~22% of the total Fe in NAu-2 was removed (Figure C.3A).

4.3.3 Iron phase separation and sample analyses

4.3.3.1 Iron phase separation

Samples collected from reduction and mixing experiments were centrifuged (6500 rpm, 20 min). The supernatants were filtered (0.2 μm, nylon) and acidified (0.5 M HCl). Each residual solid was subjected to sequential extractions as previously described: basal-sorbed Fe, edge-bound Fe, and structural Fe were extracted by 1 M $CaCl_2$ (pH 7), 1 M NaH_2PO_4 (pH 5), and 0.5 M HCl, respectively (Shi *et al.*, 2016). All of the extracts were filtered (0.2 μm, nylon) and acidified (0.5 M HCl, except for the 0.5 M HCl extracts).

4.3.3.2 Structural cation concentrations

Total Fe and Fe(II) concentrations were measured using the Ferrozine method [detection limit (DL) <2 μM] (Stookey, 1970; Viollier *et al.*, 2000). Si concentrations of batch I were analyzed using a standard colorimetric method (DL = 0.83 μM) (Clesceri, 1989). While, inductively coupled plasma optical emission spectrometry (ICP-OES) was used to measure Si (DL = 0.33 μM) and Al (DL = 0.02 μM) concentrations of batch II.

4.3.3.3 Iron isotope analysis

Iron in the following samples was separated from other cations using an anion-exchange resin (Beard *et al.*, 2003): 1) aqueous phase samples and the three extracts from the reduction and mixing experiments, 2) solutions collected from the partial dissolution experiment, and 3) test solutions, which were used to examine the artifacts or matrix effects of the wet chemistry which contained known concentrations of high-purity Fe standard (HPS) and one of the matrices (i.e. MM, 10 mM HEPES buffer, 1 M $CaCl_2$, 1 M NaH_2PO_4, 0.5 M HCl, dithionite solution). Solutions after wet chemistry were analyzed by a multi-collector inductively coupled plasma mass spectrometer (MC-ICP-MS) at University of Wisconsin-Madison. Prior to the wet chemistry, the Fe isotope compositions of HPS for batch II and all other experiments were 0.21 ± 0.02‰ (2σ, n = 3) and 0.49 ± 0.06‰ (2σ, n = 27), respectively. After the wet chemistry, the average $\delta^{56}Fe$ values of test solutions for batch II and all other experiments were 0.20 ± 0.1‰ (2σ, n = 12) and 0.50 ± 0.08‰ (2σ, n = 24), respectively. Iron isotope values were reported relative to the average of igneous rocks. The Fe isotope fractionation between phases X and Y was calculated as $\Delta^{56}Fe_{X-Y} = \delta^{56}Fe_X - \delta^{56}Fe_Y$.

4.3.3.4 Solid characterization

The purity of unaltered NAu-2 was verified by XRD and TEM at the University of Wisconsin-Madison. Powder XRD data of unaltered NAu-2 were collected on a 2-D image-plate detector using a Rigaku Rapid II instrument (Mo-Kα radiation). Two-dimensional images were converted to produce conventional 2θ vs. intensity patterns using Rigaku's 2DP software. Crystalline domain size analysis was performed using the JADE® 9.0 software package. A pseudo-Voigt method was used for fitting the peak positions and peak widths at half-height. TEM sample was prepared by coating crushed unaltered NAu-2 suspended in distilled water onto carbon-coated 200-mesh Cu grids. TEM images and selected-area electron diffraction (SAED) analyses were carried out using a Philips CM200-UT microscope operated at 200 kV. The chemical composition was analyzed by TEM-EDS spectra using a Si:Li detector (Oxford instruments Link ISIS) with a beam diameter of ~50 nm (spot size 5).

The unaltered, microbially reduced and chemically reduced NAu-2 were analyzed by scanning electron microscopy (SEM, Quanta FEG 250) coupled with energy dispersive spectroscopy (EDS, Oxford X-act) to observe any morphological differences in NAu-2 undergoing microbial or chemical reduction. A small amount (~15 μg) of unaltered NAu-2 was suspended in ultra-pure water (18.2 MΩ cm^{-1} water, Millipore) was loaded onto aluminum SEM stubs covered with carbon tape. The microbially and chemically reduced NAu-2 was centrifuged inside of the anaerobic chamber. The supernatants were discarded, while the solids were washed with ultra-pure water before loading onto SEM stubs. The unaltered NAu-2 and the reduced NAu-2 were dried overnight outside and inside the anaerobic chamber, respectively. The samples were brought to the SEM in an impermeable container (BBL GasPak™ Systems) filled with anaerobic gas. Under high vacuum mode, the secondary electron (SE) images were taken under accelerating voltages of 10 or 15 kV, and the EDS spectra under accelerating voltages of 20 kV.

4.4 Results

4.4.1 Microbial reduction of NAu-2

4.4.1.1 Concentrations of Fe

The reduction extent was calculated according to:

$$F_{Fe(II)} = \frac{Fe(II)_{aq}+Fe(II)_{basal}+Fe(II)_{edge}+Fe(II)_{struc}}{\text{Total Fe in NAu}-2} \times 100\% \quad (4.1)$$

where $Fe(II)_{aq}$, $Fe(II)_{basal}$, $Fe(II)_{edge}$ and $Fe(II)_{struc}$ are the molar concentrations of Fe(II) in the aqueous phase, $CaCl_2$ extract, NaH_2PO_4 extract, and HCl extract, respectively. Authigenic Fe(II) in NAu-2 was negligible, as confirmed by the control group (Figure 4.1, Table C.3). In the biotic batch I and II experiments, $F_{Fe(II)}$ reached 19.4 and 13.9% after 22 and 21 days, respectively. The longer incubation time of batch I (100 days) gave a slightly higher $F_{Fe(II)}$ of 21.9%. The initial rate of reduction (i.e., over 24 h) for batch I (1.9%·day^{-1}) was nearly two times higher than that of batch II (1.0%·day^{-1}). Moreover, Fe(II) concentrations of all phases increased with time in both batch I and II (Table C.3).

The proportion of Fe(II) in the aqueous phase or any of the three extracts was calculated according to:

$$P_{Fe(II)_i} = \frac{Fe(II)_i}{Fe(II)_{aq}+Fe(II)_{basal}+Fe(II)_{edge}+Fe(II)_{struc}} \times 100\% \quad (4.2)$$

where $Fe(II)_i$ is the molar concentration of Fe(II) in phase i (i.e. aqueous or extract). When the reduction extent was low [$F_{Fe(II)}$ <7%], structural Fe(II) [i.e., 0.5 M HCl extractable Fe(II), $P_{Fe(II)_{struc}}$] accounted for >90% of the total Fe(II) for both batch I and batch II (Figure 4.2A&B). As reduction proceeded, the proportions of aqueous Fe(II) [$P_{Fe(II)_{aq}}$], basal-sorbed Fe(II) [1 M $CaCl_2$ extractable Fe(II), $P_{Fe(II)_{basal}}$], and edge-bound Fe(II) [1 M NaH_2PO_4 extractable Fe(II), $P_{Fe(II)_{edge}}$] increased. When microbial reduction ceased, $P_{Fe(II)_{struc}}$ of batch I and II decreased to ~40 and ~60%, respectively. At a comparable reduction stage, e.g. $F_{Fe(II)}$ = 15.9 and 13.9% for batch I and II, the proportions of Fe(II) in the same phase were nearly identical thereby allowing us to compare batch I and II as a function of the reduction extent.

The aqueous phase and $CaCl_2$ extracts contained only Fe(II), whereas the NaH_2PO_4 and HCl extracts were both comprised of Fe(II) and Fe(III) (Figure 4.2D&E&G&H, Table C.3). The relative proportions of Fe(II) and Fe(III) in the NaH_2PO_4 or HCl extracts were calculated according to:

$$P_{Fe(II)\text{in } NaH_2PO_4 \text{ or HCl}} = \frac{Fe(II)_{edge \text{ or } struc}}{Fe(tot)_{edge \text{ or } struc}} \times 100\% \quad (4.3) \quad \text{and}$$

$$P_{Fe(III) \text{ in } NaH_2PO_4 \text{ or HCl}} = \frac{Fe(tot)_{edge \text{ or } struc} - Fe(II)_{edge \text{ or } struc}}{Fe(tot)_{edge \text{ or } struc}} \times 100\% \quad (4.4)$$

where $Fe(II)_{edge \text{ or } struc}$ and $Fe(tot)_{edge \text{ or } struc}$ are the total Fe(II) and total Fe concentrations in NaH_2PO_4 or HCl extracts. The relative proportions of Fe(III) in NaH_2PO_4 (Figure 4.2D&E) and HCl

(Figure 4.2G&H) extracts decreased with the increasing extent of reduction. The relative proportion of Fe(III) in NaH_2PO_4 extracts was lower than that in HCl extracts at the same reduction extent.

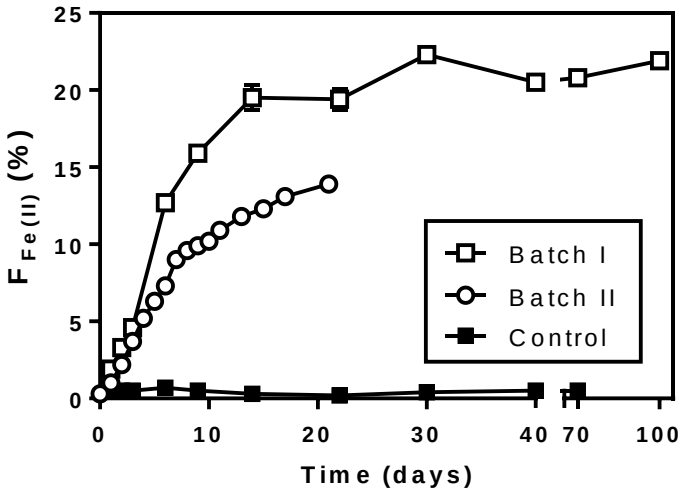

Figure 4.1. Temporal variation of reduction extent during the microbial reduction of NAu-2.

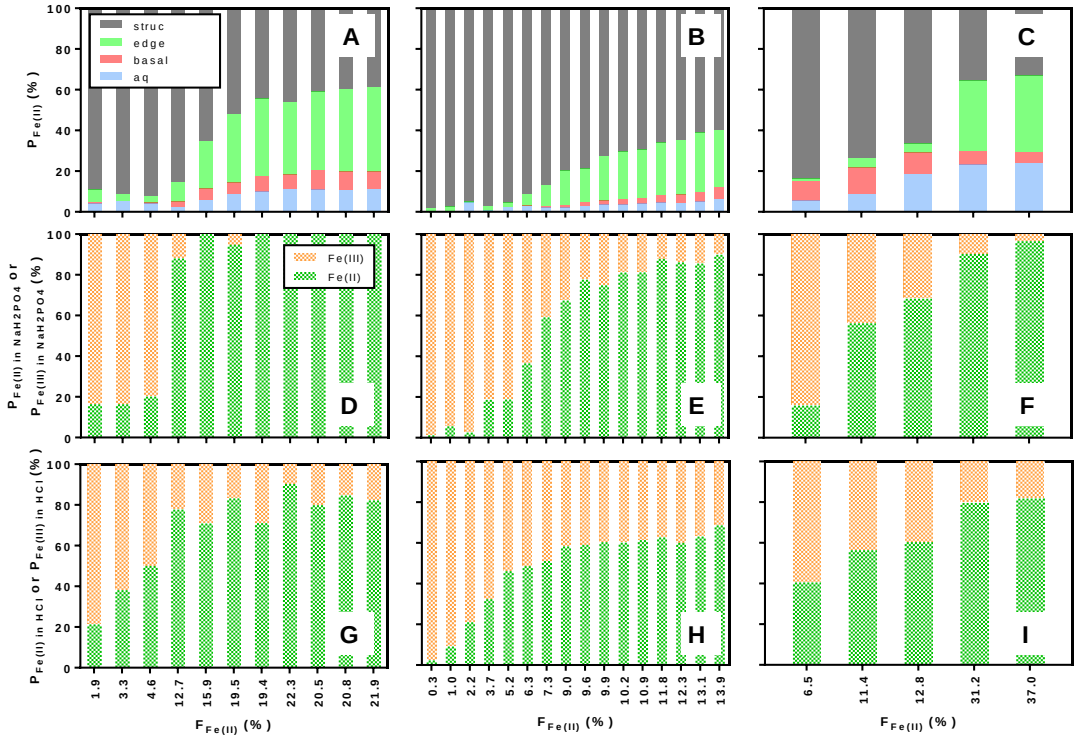

Figure 4.2. Proportions of Fe(II) in aqueous phase and three extracts vs. the reduction extent: A) batch I, B) batch II, and C) chemical reduction. Relative proportions of Fe(II) and Fe(III) in NaH_2PO_4 extracts vs. reduction extent: D) batch I, E) batch II, and F) chemical reduction. Relative proportions of Fe(II) and Fe(III) in HCl extracts vs. reduction extent: G) batch I, H) batch II, and I) chemical reduction.

4.4.1.2 NAu-2 dissolution during microbial reduction

Our previous study (Shi *et al.*, 2016) showed that the dissolved structural Fe and Si from clay either stayed in the aqueous phase or sorbed onto the basal planes. We calculated the proportions of dissolved Fe, Si and Al during microbial reduction at selected time points according to:

$$D_{Fe(II)} = \frac{Fe(II)_{aq} + Fe(II)_{basal}}{\text{Total Fe in NAu}-2} \times 100\% \quad (4.5)$$

$$D_{Si} = \frac{Si_{aq} + Si_{basal}}{\text{Total Si in NAu}-2} \times 100\% \quad (4.6)$$

$$D_{Al} = \frac{Al_{aq} + Al_{basal}}{\text{Total Al in NAu}-2} \times 100\% \quad (4.7)$$

where $Fe(II)_{aq}$, Si_{aq} and Al_{aq} are the molar concentrations of aqueous Fe(II), Si, and Al; $Fe(II)_{basal}$, Si_{basal} and Al_{basal} are the molar concentrations of $CaCl_2$ extractable Fe(II), Si, and Al. The reductive dissolution of Fe(II) and Si increased with the microbial reduction extent (Table C.4). $D_{Fe(II)}$ and D_{Si} were nearly identical at the same reduction extent of batch I and II. Overall, a stoichiometric dissolution between Si and Fe was observed for batch I and II [D_{Si}: $D_{Fe(II)}$ = 1:1] (Figure 4.3). While D_{Al} poorly correlated with the reduction extent and was lower than $D_{Fe(II)}$ and D_{Si} (Figure 4.3, Table C.4).

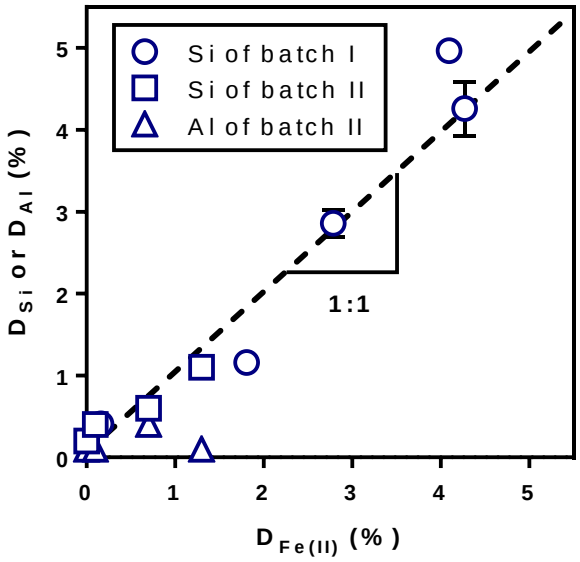

Figure 4.3. The proportion of dissolved Si or Al vs. the proportion of dissolved Fe from batch I and II (See equations 4.5-4.7 for calculation). The dashed line indicates the 1:1 ratio of D_{Si}:$D_{Fe(II)}$ or D_{Al}:$D_{Fe(II)}$. Error bars indicate one standard deviation of propagated errors.

4.4.1.3 Variation of Fe isotope compositions

Iron isotope compositions of the aqueous Fe(II) and three extracts from batch I changed with the reduction extent relative to that of the bulk NAu-2 ($\delta^{56}Fe_{bulk\ NAu\text{-}2}$ = 1.31‰) (Figure 4.4A). The reduction of batch I can be divided into three stages according to the Fe isotopic changes of different Fe pools. Early in stage 1 [$F_{Fe(II)}$ = 4.6%], similar Fe isotope compositions of aqueous Fe(II) [$\delta^{56}Fe_{aq\ Fe(II)}$ = 1.02‰], edge-bound Fe ($\delta^{56}Fe_{edge\ Fe}$ = 1.12‰) and structural Fe ($\delta^{56}Fe_{struc\ Fe}$ = 1.13‰) were observed. At the end of stage 1 [$F_{Fe(II)}$ = 12.7%], the Fe isotope compositions of the aqueous Fe(II) and edge-bound Fe became isotopically negative to -0.65 and -0.89‰, respectively; while that of structural Fe increased to 1.39‰. During stage 2 [$F_{Fe(II)}$ = 12.7-19.5%], the isotope composition of edge-bound Fe returned to positive and approached that of structural Fe; in contrast, the Fe isotope values of aqueous Fe(II) and basal-sorbed Fe(II) became further negative. Stage 3 [$F_{Fe(II)}$ > 19.5%] was characterized by increasing Fe isotope values of aqueous Fe(II) and basal-sorbed Fe(II); meanwhile the Fe isotope value of structural Fe decreased slightly.

In contrast to the large variations in the isotope compositions observed in the different Fe pools in batch I, batch II showed minor changes in Fe isotope compositions (Figure 4.4B). Throughout the experiment, the Fe isotope values of the different Fe phases partitioned well and were overall isotopically lighter according to the sequence: $\delta^{56}Fe_{struc\ Fe} > \delta^{56}Fe_{edge\ Fe} > \delta^{56}Fe_{aq\ Fe(II)} > \delta^{56}Fe_{basal\ Fe(II)}$. However, with increasing $F_{Fe(II)}$, the aqueous Fe(II) and basal-sorbed Fe(II) became isotopically lighter while the structural Fe became isotopically heavier.

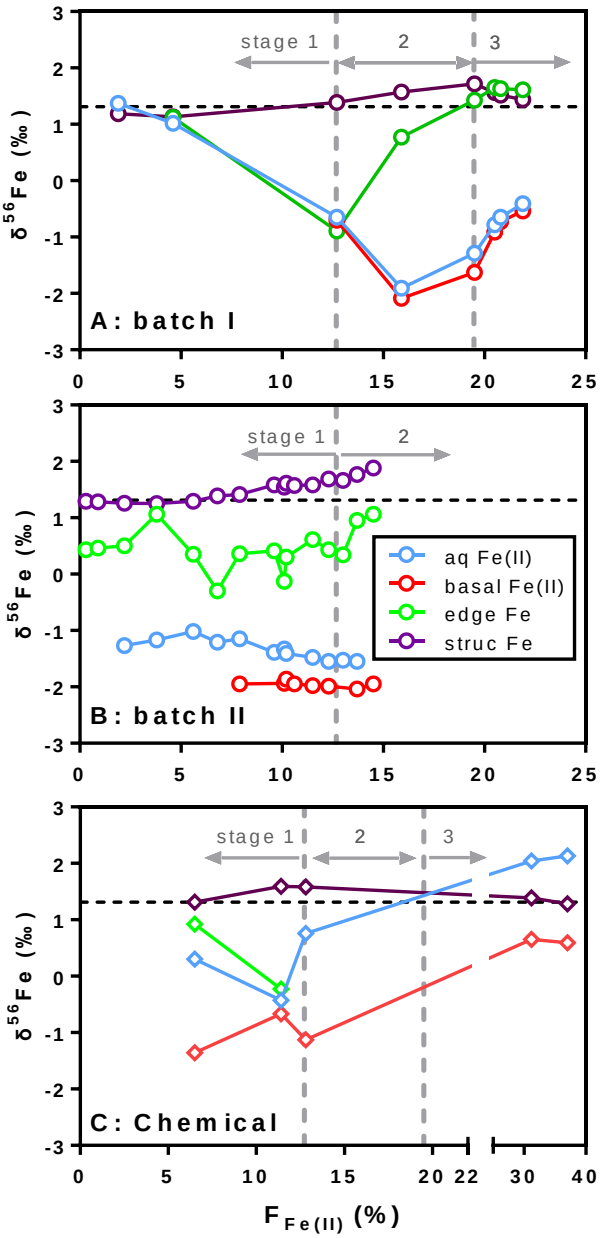

Figure 4.4. Iron isotope compositions of aqueous Fe(II), basal-sorbed Fe(II) ($CaCl_2$ extractable Fe), edge-bound Fe (NaH_2PO_4 extractable Fe), and structural Fe (HCl extractable Fe) vs. the reduction extent during A) batch I, B) batch II, and C) chemical reduction of NAu-2. The horizontal black dashed line indicates the Fe isotope composition of the bulk NAu-2: $\delta^{56}Fe_{bulk}$

$_{NAu\text{-}2}$ = 1.31‰. The vertical grey dashed lines divide the reduction processes into three stages at $F_{Fe(II)}$ = 12.7 and 19.5%. Error bars indicate ranges of repeated analyses.

4.4.2 Chemical reduction of NAu-2

4.4.2.1 Concentrations of Fe

The chemical reduction extent of NAu-2 varied from 6.5 to 37.0% (Table C.3). At a low reduction extent [$F_{Fe(II)}$ = 6.5%], Fe(II) was predominantly located in the NAu-2 structure (Figure 4.2C). As $F_{Fe(II)}$ increased over time, $P_{Fe(II)_{struc}}$ decreased while $P_{Fe(II)_{edge}}$ and $P_{Fe(II)_{aq}}$ increased. The basal-sorbed Fe(II) was the second largest Fe(II) pool at $F_{Fe(II)}$ = 6.5-11.4%, but $P_{Fe(II)_{basal}}$ decreased when $F_{Fe(II)}$ further increased.

4.4.2.2 Variation of Fe isotope compositions

When the reduction extent was low [$F_{Fe(II)} \leq 11.4\%$], the Fe isotope values decreased in the following order: $\delta^{56}Fe_{struc\ Fe} > \delta^{56}Fe_{edge\ Fe} > \delta^{56}Fe_{aq\ Fe(II)} > \delta^{56}Fe_{basal\ Fe(II)}$ (Figure 4.4C, Table C.5). However, when the reduction extent increased to $F_{Fe(II)} \geq 31.2\%$, the Fe isotope values of the aqueous Fe(II) exceeded those of the structural Fe, while the basal-sorbed Fe(II) remained isotopically lighter than structural Fe. Unfortunately, the Fe isotope measurements on the edge-bound Fe extracts was not completed due to technical difficulties.

4.4.3 Mixing Fe(II) with NAu-2 and SYn-1

4.4.3.1 Concentrations of Fe

Upon mixing Fe(II) solution with NAu-2 for 0.7 h, 44% of the Fe(II) remained in the aqueous phase while 38 and 17% was partitioned to the basal-sorbed phase and structural NAu-2, respectively (Figure 4.5A, Table C.3). Within three days, aqueous Fe(II) and basal-sorbed Fe(II) decreased with a concomitant increase in structural Fe(II). The Fe(II) concentrations of these three phases changed very little between days 3 and 23. Note that the final concentration of structural Fe(II) was equivalent to 35% of the total Fe(II) and 7% of total structural Fe in NAu-2. The edge-bound Fe(II) represented less than 1% of the total Fe(II) through the entire duration of the mixing experiment.

When the dissolved Fe(II) was mixed with SYn-1 (i.e., an Fe-free montmorillonite), the majority (~94%) of Fe(II) remained in the aqueous phase after 17 days with minor Fe(II) adsorption onto the

basal planes (~5%) (Figure 4.5B, Table C.3). Iron(II) adsorption on the edge surface was minimal under the experimental pH 6.8. As expected, the concentration of structural Fe(II) was negligible as SYn-1 is free of structural Fe.

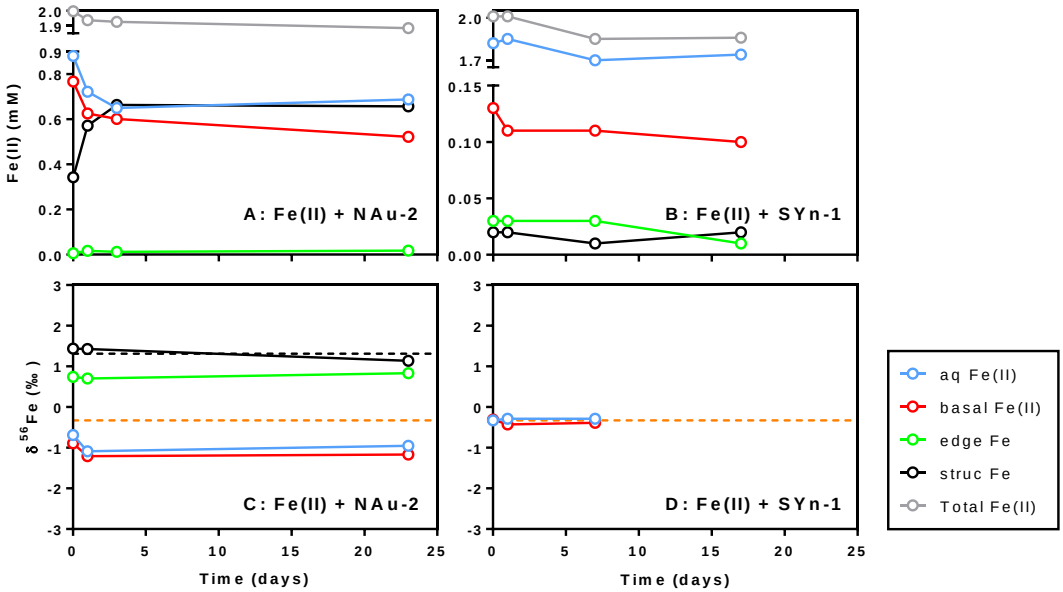

Figure 4.5. Temporal changes of Fe(II) concentrations of the aqueous phase and three extracts during the mixing experiments with A) NAu-2 and B) SYn-1, respectively. Note the breaks in different Y axes of panels A and B. Iron isotope compositions of aqueous Fe(II), basal-sorbed Fe(II), edge-bound Fe, and structural Fe during the mixing experiments with C) NAu-2 and D) SYn-1, respectively. Dashed lines in black and orange indicate the Fe isotope compositions of bulk NAu-2 ($\delta^{56}Fe_{bulk\ NAu\text{-}2}$ = 1.31‰) and starting Fe(II) solution [$\delta^{56}Fe_{starting\ Fe(II)}$ = -0.33‰], respectively. Error bars (smaller than data points) indicate ranges observed in duplicate reactors or repeated analyses.

4.4.3.2 Variation of Fe isotope compositions

During the NAu-2 mixing experiment, isotope compositions of the aqueous Fe(II) and the basal-sorbed Fe(II) became isotopically lighter than the starting Fe(II) within 0.7 h with values plateauing within 24 h (Figure 4.5C, Table C.5). At day 23, aqueous Fe(II) and basal-sorbed Fe(II) were 0.62 and 0.84‰ lighter than the starting Fe(II) solution [$\delta^{56}Fe_{starting\ Fe(II)}$ = -0.33‰], respectively. Following 23 days of mixing, the isotope composition of the structural Fe changed from slightly heavier to

slightly lighter than that of the bulk NAu-2 ($\delta^{56}Fe_{bulk\ NAu\text{-}2}$ = 1.31‰). The isotope composition of edge-bound Fe was between those of the added Fe(II) solution and bulk NAu-2.

After Fe(II) was added to SYn-1 for 7 days, the isotope compositions of aqueous Fe(II) and basal-sorbed Fe(II) were equivalent to Fe isotope signature of the added Fe(II) solution (Figure 4.5D, Table C.5). The Fe isotope values of edge-bound Fe and structural Fe were not reported due to their low concentrations.

4.4.4 Partial dissolution of NAu-2

Upon mixing with 0.5 M HCl for 1 h, 5.8% of the Fe from NAu-2 was rapidly dissolved (Figure C.2A) and the rate of dissolution decreased after 10.7% of the structural Fe was dissolved. Overall, 22% of the structural Fe in NAu-2 was dissolved after 30 days (Table C.2).

The Fe isotope values of partially dissolved NAu-2 varied (Figure C.2B, Table C.2). The sample (aliquot 1 in Table C.2) collected during the early dissolution of structural Fe (i.e., 7.5 % dissolution) were isotopically lighter ($\delta^{56}Fe_{aliquote\ 1}$ = 1.10‰) than the bulk NAu-2 ($\delta^{56}Fe_{bulk\ NAu\text{-}2}$ = 1.31‰). The isotope composition of the closest inner Fe (aliquot 2 in Table C.2) was 1.41‰. With further dissolution, the Fe atoms became isotopically lighter when they are located deeper in the structure of NAu-2.

4.5 Discussion

4.5.1 Microbial Fe reduction in NAu-2

4.5.1.1 Higher Fe(III) reduction extent in NAu-2 than NAu-1

Long-term incubations (100 days) of *S. oneidensis* MR-1 with NAu-2 (batch I) resulted in a 21.9% reduction of structural Fe(III) (Figure 4.1, Table C.3). This is consistent with previous studies that showed extents of up to 14-27% for Fe(III) reduction in NAu-2 by bacteria in the absence of external electron shuttles (Jaisi *et al.*, 2005; Bishop *et al.*, 2011; Zhang *et al.*, 2012; Zhang *et al.*, 2013a; Zhao *et al.*, 2015). In spite of similar total structural Fe(III) contents in NAu-1 and NAu-2, the maximum reduction extent of NAu-2 was ~12% higher than that of NAu-1 under the same experimental conditions (Shi *et al.*, 2016).

The stoichiometric dissolution of Si and Fe from NAu-2 (Figure 4.3, Table C.4) showed no preferential dissolution of octahedral or tetrahedral cations, indicating that the mineralogy of NAu-2

remained unchanged during microbial reduction. Moreover, no evidence for secondary precipitation was found using SEM-EDS (Figure C.3B&E), consistent with our previous findings that microbial reduction of NAu-1 produced undetectable secondary mineral precipitates (Shi *et al.*, 2016). Structural Fe(III) in NAu-2 was primarily reduced in the solid state, whereby ~80 % of the total Fe(II) was found within the NAu-2 structure when the reduction extent reached ~10% (days 6 and 10 for batch I and II, respectively) (Figure 4.2A&B). Nevertheless, structural Fe(II) represented only ~30% of the total Fe(II) found at the same reduction extent during the microbial reduction of Fe(III) from NAu-1 (Shi *et al.*, 2016). Actually, Fe(II) dissolution [aqueous Fe(II) + basal-sorbed Fe(II)] from NAu-2 was much lower than that from NAu-1 at the same reduction extent (Shi *et al.*, 2016). These results illustrate that NAu-2 is less soluble than NAu-1 during microbial Fe(III) reduction, even though NAu-2 has a larger surface area (Jaisi *et al.*, 2007) that may correspond to a higher fraction of soluble edge sites.

4.5.1.2 Impact by crystal size and layer charge

Microbial reduction of nontronite is proposed to reduce Fe(III) atoms on the octahedral edge sites (Komadel *et al.*, 2006; Ribeiro *et al.*, 2009; Stucki, 2011). Based on this assumption, smaller crystals with larger specific edge surface area may provide a higher fraction of reducible Fe(III). As measured by XRD, the crystalline domain sizes of the unaltered NAu-2 and NAu-1 are 50 ± 2 and 61 ± 3 Å, respectively. Based on these values, Fe(III) atoms on the edge of NAu-2 may only represent up to 15% more than that of NAu-1. Consequently, it is not expected that crystal size alone is responsible for the high reduction extent of NAu-2.

In both NAu-2 and NAu-1, ~90% of octahedral cations are Fe(III) (Gates *et al.*, 2002). The octahedral charge of NAu-2 (0.05-0.27 esu/unit cell) is higher than that of NAu-1 (0.03-0.04 esu/unit cell) (Gates *et al.*, 2002; Bailey *et al.*, 2015). The octahedral Fe(III) in NAu-2 should be less reducible than that in NAu-1, leading to lower reduction extent of NAu-2 than that of NAu-1. With a lower tetrahedral charge of NAu-2 (0.45 esu/unit cell) as compared to that of NAu-1 (1.02 esu/unit cell) (Bailey *et al.*, 2015), electrons may enter NAu-2's tetrahedral sheets more easily. In addition, with Fe(III) reduction proceeding, the octahedral charge increases due to the electron addition to the octahedral layers. Theoretically, when octahedral Fe(II) reaches ≥11% of the total structural Fe, the octahedral charge should exceed the tetrahedral charge. At this point, tetrahedral Fe(III) within NAu-2 might become reducible.

4.5.1.3 Additional electron pathways

Besides intra-layer electron hopping within octahedral sheets, additional electron pathways in NAu-2 may be involved in *in situ* structural Fe(III) reduction. Jaisi *et al.* (2005) observed that tetrahedrally and *trans*-octahedrally occupying Fe(III) became undetectable with Mössbauer spectroscopy after NAu-2 was reduced by *Shewanella putrefaciens* CN32 with AQDS as the electron shuttle, and suggested that tetrahedral Fe(III) [~9% of total structural Fe (Gates *et al.*, 2002)] was more reducible than *cis*-octahedral Fe(III). However, a similar experiment by Luan *et al.* (2015b) in the absence of AQDS showed that most tetrahedral NAu-2 Fe(III) remained unreduced even though the reduction extent reached 34.5%. It seems that tetrahedral Fe(III) is not preferentially reduced over octahedral Fe(III) without the aid of external electron shuttles, which facilitate electron penetration through basal planes to reduce the interior structural Fe (Zhao *et al.*, 2015).

Alexandrov *et al.* (2013) suggested that tetrahedral Fe(III) might be reducible by the aqueous Fe(II) and the resulting tetrahedral Fe(II) tends to remain in the structure of clay without passing electrons to the octahedral Fe(III), because the electron transfer from tetrahedral Fe(II) to octahedral Fe(III) is energetically unfavorable according to first-principles calculations. During our mixing experiment with NAu-2, ~7% of the structural Fe(III) was reduced by the basal-sorbed Fe(II), whereas only 3% of structural Fe(III) in NAu-1 was reduced by the electrons passing through basal planes under similar experimental conditions (Neumann *et al.*, 2013). The extra 4% reduction in NAu-2 may be attributed to the reduction of tetrahedral Fe(III) by basal-sorbed Fe(II).

4.5.2 Three stages of microbial Fe reduction of NAu-2

4.5.2.1 Stage 1: Fe atom exchange through edge surface

Despite a considerable extent of Fe reduction [$F_{Fe(II)}$ = 4.6%] during stage 1 (batch I), close to zero isotope fractionation between edge-bound Fe and structural Fe was produced (Figure 4.6A, Table C.5). At this point, the isotope fractionation between aqueous Fe(II) and edge Fe was also negligible. These results demonstrate that neither the reducing process nor the dissolving process induced isotope fractionation. There was minimal (≤0.6%) adsorption of Fe(II) on the basal planes (Figure 4.2A, Table C.3).

After $F_{Fe(II)}$ reached 12.7%, the fractionation factor $\Delta^{56}Fe_{\text{edge Fe-struc Fe}}$ increased to -2.28‰ due to the persistent atom exchange between edge-bound Fe(II) and structural Fe(III) (Figures 4.6A and 4.7A, Table C.5). The fractionation factor between aqueous Fe(II) and edge-bound Fe was slightly

positive, implying that the atom exchange between edge-bound Fe(II) and structural Fe(III) at that time point was more extensive than that between aqueous Fe(II) and structural Fe(III) (Shi *et al.*, 2016). The concentration of basal-sorbed Fe(II) increased and accounted for 2.9% of the total Fe(II) (Figure 4.2A). The adsorption of aqueous Fe(II) onto the basal planes of NAu-2 induced little isotope fractionation ($\Delta^{56}Fe_{\text{basal Fe(II)-aq Fe(II)}}$ = -0.05‰). When Fe(II) solution was mixed with SYn-1 (Fe-free), the fractionation factor $\Delta^{56}Fe_{\text{basal Fe(II)-aq Fe(II)}}$ ranged from 0.02 to -0.14 ‰ during seven days (Figure C.4B, Table C.5). These two experiments showed that the kinetic sorption effect on isotope fractionation was minimal.

4.5.2.2 Stage 2: Fe atom exchange through basal planes

During stage 2 [$F_{Fe(II)}$ = 12.7-19.5%] of batch I, $\Delta^{56}Fe_{\text{edge Fe-struc Fe}}$ decreased from -2.28 to -0.29‰ (Figures 4.6A and 4.7B, Table C.5). The concentration of structural Fe(II) during stage 2 was over two times higher than that during the stage 1 (Table C.3). With higher $F_{Fe(II)}$, structural Fe(II) shielded the edge surface and segregated edge-bound Fe(II) from structural Fe(III). The atom exchange between edge-bound Fe(II) and structural Fe(III) became highly inhibited. However, $\Delta^{56}Fe_{\text{aq Fe(II)-struc Fe}}$ and $\Delta^{56}Fe_{\text{basal Fe(II)-struc Fe}}$ continued to increase to -3.01 and -3.35‰, respectively (Figures 4.6A and 4.7B, Table C.5). The increasing fractionation factor between aqueous Fe(II) and structural Fe cannot be explained by atom exchange through the edge surface, as the structural Fe(III) was physically isolated from the external aqueous Fe(II).

When mixing Fe(II) solution with SYn-1, the Fe isotope compositions of the aqueous Fe(II) and basal-sorbed Fe(II) remained consistent with that of the starting Fe(II) (Figure 4.5D). However, mixing Fe(II) solution with NAu-2 resulted in both aqueous Fe(II) and basal-sorbed Fe(II) becoming isotopically lighter than the starting Fe(II) (Figure 4.5C), maybe owing to the partial oxidation of basal-sorbed Fe(II) by structural Fe(III) (Bullen *et al.*, 2001; Johnson *et al.*, 2008b). Latta *et al.* (2017) showed that direct electron transfer from basal-sorbed Fe(II) reduced octahedral Fe(III) in SWy-2 (a montmorillonite with low Fe content) via electron transfer perpendicular to the clay layers. Reduction of structural Fe(III) was coupled with partial oxidation of the basal-sorbed Fe(II), which may lead to the formation of Fe (oxyhydr)oxides (e.g. ferrihydrite, green rust) on the basal planes (Latta *et al.*, 2017). With <1% of the total Fe(II) attached to the NAu-2 edge surface (Table C.3), the atom exchange only between edge-bound Fe(II) and structural Fe(III) would be too infrequent to influence the isotopic changes of aqueous Fe(II) and basal-sorbed Fe(II).

In contrast to the decreasing concentration of the basal-sorbed Fe(II) and equilibrium fractionation during the mixing experiment with NAu-2 (Figures 4.5A and C.4A, Table C.5), microbial reduction coupled increasing concentrations of basal-sorbed Fe(II) with enhanced isotope fractionation during stage 2 (Figures 4.6A and 4.7B, Table C.5). Partial oxidation of the basal-sorbed Fe(II) is not able to explain the increasing $\Delta^{56}Fe_{\text{basal Fe(II)-struc Fe}}$ as partial oxidation should produce an opposite trend (Bullen *et al.*, 2001; Johnson *et al.*, 2008b). In addition, during the microbial reduction experiment, electrons were continuously delivered to the surface of clay and the newly formed Fe(III) phase (if any) was likely to quickly turn back to Fe(II). Secondary Fe-containing precipitates were not found using SEM-EDS (Figure C.3B&E).

Neumann *et al.* (2013) mixed pure ^{56}Fe(II) with NAu-1 at acidic pH [resulting in little edge-bound Fe(II)] and produced ^{57}Fe(II) that coordinated similarly to the basal-sorbed Fe(II), implying that basal-sorbed ^{56}Fe(II) may be able to exchange with structural ^{57}Fe(III). The extent of atom exchange between aqueous Fe(II) and clay was significantly increased with the involvement of tetrahedral Fe(III) in the system (Neumann *et al.*, 2015). Therefore, we propose that the increasing $\Delta^{56}Fe_{\text{basal Fe(II)-struc Fe}}$ during stage 2 was induced by not only the electron transfer from basal-sorbed Fe(II) to structural Fe(III) but also the atom exchange between these two Fe pools. Tetrahedral Fe(III) was possibly involved in the process of electron transfer and atom exchange (ETAE), as basal-sorbed Fe(II) is physically closer to tetrahedral Fe(III) than to octahedral Fe(III). The basal-sorbed Fe(II) during stage 2 replaced the role of the edge-bound Fe(II) during stage 1, which was the driving force of isotopic change of aqueous Fe(II).

4.5.2.3 Stage 3: closed ETAE

During stage 3 [$F_{Fe(II)} > 19.5\%$] of microbial NAu-2 reduction, the isotope fractionation factors between aqueous Fe(II)/basal-sorbed Fe(II) and structural Fe decreased from about -3 to about -2‰ (Figures 4.6A and 4.7C, Table C.5), indicating that ETAE between basal-sorbed Fe(II) and structural Fe(III) became more limited. The adsorption of Fe(II) onto the basal planes could promptly reduce structural Fe(III) in NAu-2 as shown in the mixing experiment (Figure 4.5A, Table C.3). If basal-sorbed Fe(II) reduced octahedral Fe(III) with the aid of tetrahedral Fe(III) that remained unreduced, ETAE would continue between basal-sorbed Fe(II) and tetrahedral Fe(III). If tetrahedral Fe(III) was reduced, no atom exchange would occur between basal-sorbed Fe(II) and tetrahedral Fe(II) due to a lack of electron transfer. In conclusion, basal-sorbed Fe(II) completely reduced tetrahedral Fe(III) at the end of stage 3 when ETAE was inhibited through the basal plane surface.

The outermost structural Fe(III) became isotopically heavier than the bulk NAu-2 due to the ETAE during stage 1 and 2 (Figure 4.4A, Table C.5). During stage 3, this heavy structural Fe(III) was reduced and dissolved to make the aqueous Fe(II) and basal-sorbed Fe(II) isotopically heavier than they were in stage 2 (Figure 4.4A, Table C.5). The isotope fractionation between edge-bound Fe and structural Fe was close to zero (Figure 4.6A, Table C.5), indicating the complete conversion of the bioavailable Fe(III) on the edge sites to Fe(II).

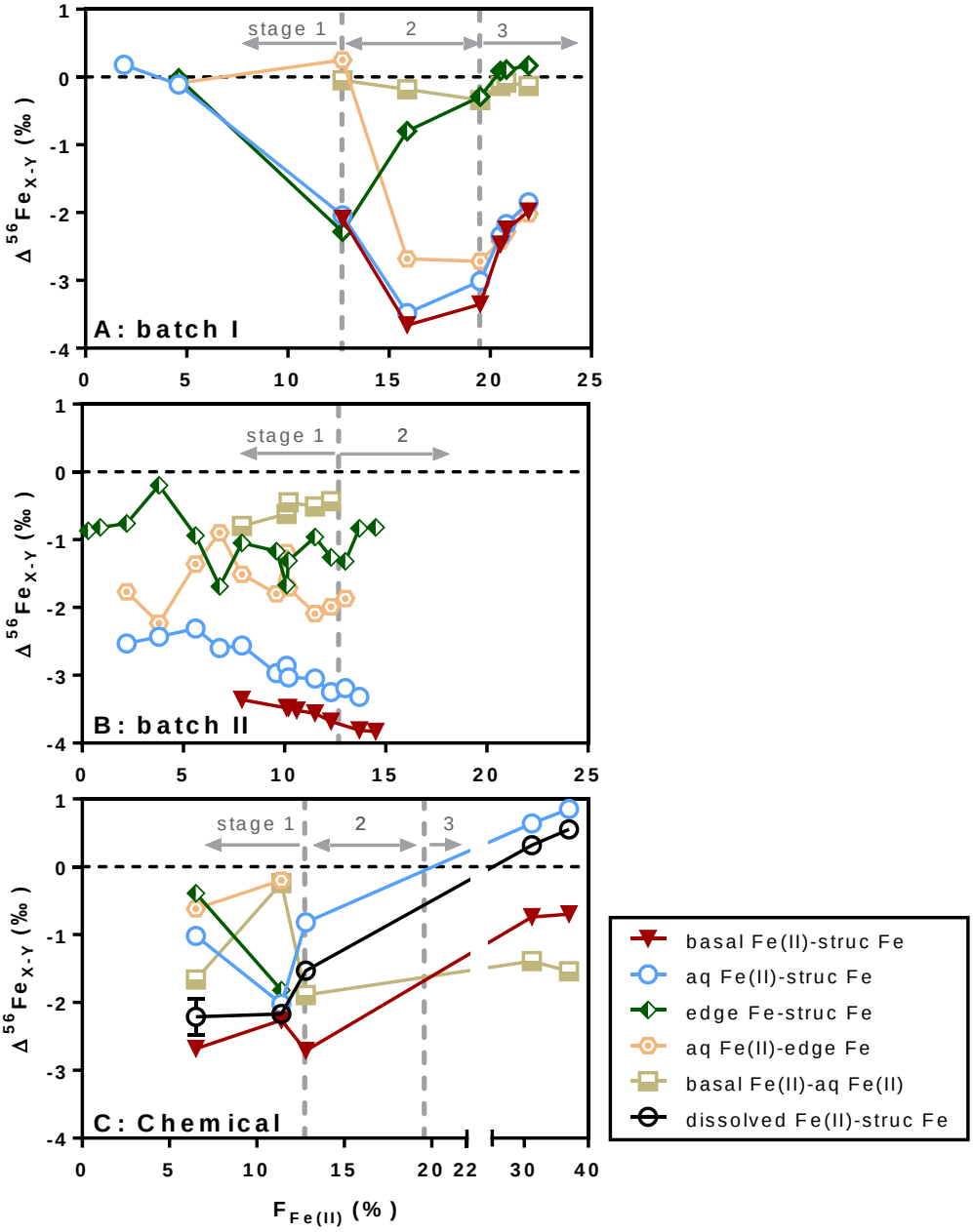

Figure 4.6. Iron isotope fractionation factors between Fe phase X and Y vs. reduction extent of A) batch I, B) batch II, and C) chemical reduction of NAu-2. See legend for the assignment of X and Y to aqueous Fe(II), basal-sorbed Fe(II), edge-bound Fe, structural Fe, and dissolved Fe(II) [calculated according to Eq. (4.8)]. The horizontal black dashed line indicates zero Fe isotope

fractionation. The vertical grey dashed lines at reduction extent of 12.7 and 19.5% divide the reaction into three stages. Error bars indicate one standard deviation of propagated errors.

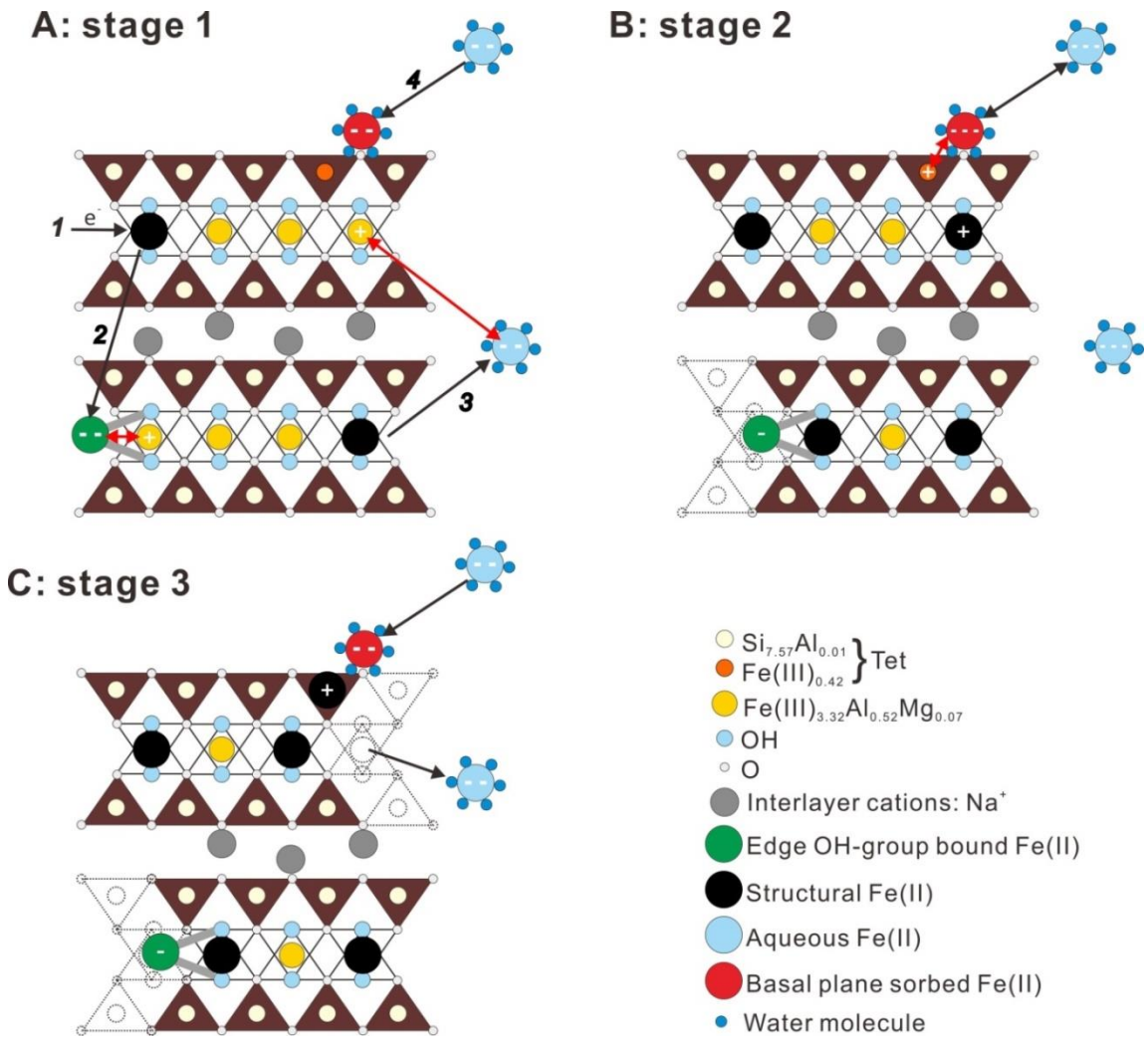

Figure 4.7. Hypothetical model of ETAE during microbial Fe(III) reduction in NAu-2. A) Microbial reduction of NAu-2 turns structural Fe(III) on the edge sites to structural Fe(II) (step 1), which is partially released to form the edge-bound Fe(II) (step 2) and aqueous Fe(II) (step 3). The aqueous Fe(II) adsorbs onto basal planes, identified as basal-sorbed Fe(II) (step 4). With reduction extent increasing to 12.7% during stage 1, extensive ETAE occurs between aqueous Fe(II)/edge-bound Fe(II) (negative δ^{56}Fe indicated by "- -") and structural Fe(III) (positive δ^{56}Fe indicated by "+"), inducing enhanced Fe isotope fractionation. B) Edge sites of NAu-2 are fully covered by structural Fe(II), which prevents ETAE between edge-bound Fe(II) (less negative δ^{56}Fe indicated by "-") and structural Fe(III). Meanwhile, ETAE takes place

between basal-sorbed Fe(II) (most negative δ^{56}Fe indicated by "- - -") and structural (tetrahedral) Fe(III) (positive δ^{56}Fe indicated by "+"), resulting in further expanded isotope fractionation between aqueous Fe(II) (most negative δ^{56}Fe indicated by "- - -") and structural Fe(III). C) Basal-sorbed Fe(II) reduces tetrahedral Fe(III) to structural Fe(II), which inhibits further ETAE between basal-sorbed Fe(II) (negative δ^{56}Fe indicated by "- -") and structural Fe(III).

4.5.3 Comparison of batch I and II

Early in the batch II experiments, the isotope fractionation factors between aqueous Fe(II)/basal-sorbed Fe(II) and structural Fe increased with increasing reduction extent (Figure 4.6B). This general trend was consistent with stages 1 of batch I. Nevertheless, the magnitude of the fractionation factors of batch II was significantly larger than those of batch I at the same reduction extent during stage 1 (Figure 4.6A&B, Table C.5). The starting experimental conditions were nearly identical for batch I and II. As discussed above, the reductive dissolution of structural Fe(III) does not induce isotope fractionation. The fractionation factors revealed the balance between the reduction dynamics and the extent of ETAE. The rapid reduction exceeded the rate of ETAE during the stage 1 of batch I, which exhibited kinetic Fe isotope fractionation. In contrast to batch I, the low reduction rate of batch II allowed for near-complete ETAE and close to equilibrium isotope fractionation between aqueous Fe(II) and structural Fe(III).

At the end of batch II (equivalent to the stage 2 of batch I), $\Delta^{56}Fe_{\text{aq Fe(II)-struc Fe}}$, $\Delta^{56}Fe_{\text{basal Fe(II)-struc Fe}}$, and $\Delta^{56}Fe_{\text{edge Fe-struc Fe}}$ were nearly the same as those of batch I at the comparable reduction extent (Figure 4.6A&B, Table C.5). This similarity implied that reduction and ETAE were balanced at these time points for both batches I and II. During microbial reduction of NAu-2, the maximum fractionation factors between aqueous Fe(II) and structural Fe were double those during NAu-1 microbial reduction, highlighting the importance of the exchangeable basal plane surface of NAu-2.

4.5.4 Comparison of microbial and chemical reduction

Dithionite reduces clay minerals by passing electrons perpendicular to the clay layers (Ribeiro *et al.*, 2009; Stucki, 2011). Our chemical reduction results seem to imply that tetrahedral Fe(III) was substantially reduced and dissolved with Fe(II) then preferentially adsorbing onto basal planes, because $P_{Fe(II)_{aq}}$ and especially $P_{Fe(II)_{basal}}$ were much higher during chemical reduction than during microbial reduction at the same reduction extent (Figure 4.2A-C). The increasing $F_{Fe(II)}$ of chemical

NAu-2 reduction led to a decrease in $P_{Fe(II)_{struc}}$ and an increase in the sum of $P_{Fe(II)_{aq}}$ plus $P_{Fe(II)_{basal}}$ (Figure 4.2C). The results of this study are in contrast with our previous research on the chemical reduction of NAu-1, which produced a larger $P_{Fe(II)_{struc}}$ and smaller $P_{Fe(II)_{aq}}$ and $P_{Fe(II)_{basal}}$ with increasing $F_{Fe(II)}$ (Shi *et al.*, 2016), as NAu-1 contains little tetrahedral Fe. Tetrahedral Fe(III) is likely more susceptible to chemical reduction than octahedral Fe(III) (Russell *et al.*, 1979). Moreover, the reduction of octahedral Fe(III) distorts the tetrahedral structure significantly (Fialips *et al.*, 2002). Therefore, chemical reduction may release the tetrahedral Fe(II) and produce defects in tetrahedral sheets, exposing underlying octahedral Fe(III) thereby enhancing the reducibility and solubility of NAu-2.

During the chemical reduction experiments, the isotope compositions of aqueous Fe(II) and basal-sorbed Fe(II) were distinct from each other, however their trends were generally the same. To compare the results of chemical reduction experiments with those of other experiments, we calculated the overall isotope composition of dissolved Fe(II) as:

$$\delta^{56}Fe_{\text{dissolved Fe(II)}} = \frac{\delta^{56}Fe_{\text{aq Fe(II)}} \times Fe(II)_{aq} + \delta^{56}Fe_{\text{basal Fe(II)}} \times Fe(II)_{basal}}{Fe(II)_{aq} + Fe(II)_{basal}} \quad (4.8)$$

The isotope fractionation between the dissolved Fe(II) and structural Fe decreased with increasing $F_{Fe(II)}$ (Figure 4.6C). The increasing $F_{Fe(II)}$ decreased the exchangeable basal plane and edge surface, resulting in less ETAE and thereby smaller isotope fractionation. Comparing the chemical reduction and mixing experiment at a similar reduction extent (e.g., $F_{Fe(II)}$ = 6.5 and 7.0%, respectively), shows that the isotope fractionation factors between dissolved Fe(II) and structural Fe were -2.21 and -2.19‰. As discussed above, it is possible that the isotope fractionation during the mixing experiment with NAu-2 was induced by partial oxidation of basal-sorbed Fe(II). However, the isotope fractionation for the chemical reduction is unlikely related to Fe (oxyhydr)oxides, which are not expected to form in the presence of excess dithionite. Thus, the isotope fractionation between dissolved Fe(II) and structural Fe should be due to ETAE between basal-sorbed Fe(II) and structural Fe(III) in both chemical reduction and mixing experiments. At this point, the fractionation between edge-bound Fe and structural Fe were -0.39 and -0.32‰, indicating less importance of the edge surface in influencing the isotopic change of the dissolved Fe.

At the highest extent of chemical reduction [$F_{Fe(II)}$ = 37%], structural Fe dissolution [$D_{Fe(II)}$] reached over 10%. The dissolved Fe(II) formed an Fe-rich shell on the clay surface by either re-

precipitation and/or adsorption as shown by the SEM-EDS analysis (Figure C.3C&F). This shell may hinder ETAE between aqueous Fe(II) and structural Fe(III) on either the edge or basal surface. The isotope composition of aqueous Fe(II) exceeded that of the bulk NAu-2 maybe due to kinetic reductive dissolution (Figure 4.4C). We could not exclude the possibility of the formation of Fe sulfide, as the decomposition of dithionite in aqueous solution may produce H_2S (Wayman and Lem, 1970). The precipitation of FeS_x may result in ^{56}Fe enriched aqueous Fe(II) (Guilbaud *et al.*, 2011). This may explain that $\delta^{56}Fe_{aq\ Fe(II)}$ is less negative than $\delta^{56}Fe_{basal\ Fe(II)}$ by up to 1.9‰ in chemical reduction, while the isotope fractionation between these two Fe(II) pools are <0.8‰ in microbial reduction and mixing experiments (Table C.5). Overall, the chemical reduction experiment confirmed that NAu-2 is distinct from NAu-1 owing to the presence of tetrahedral Fe(III), which turns basal planes of clay minerals into reactive/exchangeable surfaces during redox reactions.

4.6 Conclusions and environmental implications

Our study shows that the Fe bioavailability of NAu-2 is approximately two times higher than that of NAu-1, whereas the dissolution of Fe from NAu-2 is lower than that of NAu-1. Therefore, NAu-2 may represent a better source of (redox) renewable Fe for microorganisms. During stage 2 of microbial NAu-2 reduction, isotope fractionation factors between aqueous Fe(II) and structural Fe reached their maximum, and they were double those during microbial reduction of NAu-1, indicating that the basal plane surfaces offer ETAE-active surfaces, in addition to the edge surfaces. The reactivity of basal planes is linked to the presence of tetrahedral Fe in NAu-2.

Traditionally, the reactivity of tetrahedral Fe has been ignored due to its low contents in clay minerals. However, a high proportion (~90%) of the interior octahedral Fe(III) remains unreactive during interactions with iron reducing microorganisms (Shi *et al.*, 2016). Given that about 9% of total Fe(III) is present in the tetrahedral sheets, the reactivity of NAu-2 basal plane surfaces appears comparable with that of the edge surfaces. It is particularly important to recognize the reactivity of the basal plane surface under acidic conditions (e.g., in acid mine drainage), because at low pH various cation species predominantly adsorb onto basal planes of clay minerals instead of the edge sites. The tetrahedral Fe may potentially react with these basal-sorbed cations species [e.g., Cr(VI), Tc(VII)], thus contributing to soil remediation. Our study shows that the reactivity of NAu-2 basal planes likely derives from the tetrahedral Fe(III). Further investigations are needed to confirm the participation of tetrahedral Fe(III) during clay-microbe interaction.

Chapter 5
Conclusions

5.1 Summary

Iron redox cycling is ubiquitous in the shallow subsurface because of the large spatial and temporal gradients in redox conditions that characterize these environments. Microbial activity is closely involved in natural Fe redox cycling. Iron-containing clay minerals have been recognized as a potential renewable Fe source for subsurface microorganisms. Clay minerals are also effective in sequestering contaminants and acting as a reservoir of essential soil nutrients due to their large reactive surface areas. Therefore, the Fe redox cycling of clays in soils and sediments is critical for the immobilization/mobilization of contaminants and nutrients. The redox reactivity of clay minerals derives from the content and location of Fe in the mineral structure. This study focused on the nature and fate of the reactive Fe pool in two Fe-rich clay minerals (NAu-1 and NAu-2) in the presence of Fe-reducing bacteria. The NAu-1 and NAu-2 samples were purified and checked by XRD, SEM, and TEM prior to all the experiments. Iron isotopes were employed to track the Fe redox cycling process of NAu-1 and NAu-2.

5.1.1 Reactivity and bioavailability of clay

5.1.1.1 Reactivity and bioavailability of NAu-1

Purified nontronite NAu-1 was reduced by *Shewanella oneidensis* MR-1 and *Geobacter sulfurreducens* PCA with Na-lactate as the electron donor at pH 6.8 under anaerobic conditions. During the long-term incubation of NAu-1 with bacteria, no secondary precipitate formation was observed. Despite different rates of reduction, the final extents of reduction were similar with both bacterial species. Approximately 10% of the structural Fe in NAu-1 was found to be reducible. About 18% of the total reduced Fe(II) was released to solution. The reduction process was accompanied by changes in Fe isotope fractionation. Microbial reduction started from the clay edges. Most of the resulting Fe(II) partially dissociated from the octahedral sheet and became edge-bound Fe(II), while a small fraction of Fe(II) dissolved and re-adsorbed onto the basal planes. The unreduced structural Fe(III) along the edges exchanged with the edge-bound Fe(II) and aqueous Fe(II). The electron transfer coupled atom exchange (ETAE) produced isotope fractionation between edge-bound/aqueous Fe(II) and structural Fe(III). With the gradual transformation of the structural Fe(III)

to Fe(II) on the edge surface, the exchangeable edge surface sites were completely exhausted. At the same time, the isotope fractionation between aqueous Fe(II) and structural Fe(III) gradually decreased to zero. Upon NAu-1 reaction with dithionite, the maximum fraction of Fe(II) reached 24% of the total amount of structural Fe. Meanwhile, the isotope fractionation between aqueous Fe(II) and structural Fe(III) was positive. This fact confirms that, in the absence of ETAE, the dissolved Fe(II) simply inherits the isotope composition of the outmost Fe atoms on the clay edge sites.

Dissimilatory Fe reduction (DIR) of Fe(III)-containing minerals has been proposed to be the predominant reason for the large Fe isotope fractionations measured in banded iron formations (BIFs) deposited between 3.1 and 2.4 Ga. The underlying reason is that ETAE closely maintains isotope fractionation during the microbial reduction of Fe(III) (oxyhydr)oxides. In contrast, this study showed that the Fe isotope fractionation between aqueous Fe(II) and structural Fe(III) decreases from negative values to zero during the microbial reduction of NAu-1. It is therefore unlikely that DIR of Fe-containing clay minerals supplied the raw material for BIFs. This is the first time that Fe isotope signatures are applied to track the bio-reduction of clay minerals. In particular, we show that the fraction of bioavailable Fe in the clay samples is fixed. The Fe redox reactivity of NAu-1 is coupled to the bioavailable Fe(III) exposed along the clay edges, as NAu-1 only contains octahedral Fe(III).

5.1.1.2 Reactivity and bioavailability of NAu-2

Purified NAu-2 was reduced under the same conditions as the microbial reduction of NAu-1. The maximum extent of NAu-2 reduction reached 22% of the total Fe. The reduction process occurred in three stages according to the changes in isotope fractionation. During Stage 1, the Fe isotope fractionation between aqueous Fe(II) and structural Fe increased with the extent of reduction. This is explained by ETAE between edge-bound Fe and octahedral Fe. During Stage 2, bioavailable Fe(III) on the edge sites was fully converted to structural Fe(II) and, consequently, ETAE along the edge surface stopped. The basal-sorbed Fe(II) exchanged with tetrahedral Fe(III) and resulted in increasing isotope fractionation. Meanwhile, tetrahedral Fe(III) was reduced by basal-sorbed Fe(II), which transferred electrons across the basal planes. As the exchangeable tetrahedral Fe(III) was completely reduced during Stage 3, the fractionation factor between basal-sorbed Fe(II) and structural Fe decreased.

The mixing experiment with SYn-1 demonstrated that the kinetic effect of adsorption was negligible. By mixing Fe(II) anaerobically with NAu-2, 7% of the total structural Fe(III) was reduced by the basal-sorbed Fe(II). Chemical reduction of NAu-2 also involved electron transfer across basal

planes. Both of the mixing and chemical reduction experiments produced the same isotope fractionation factors at similar extents of reduction. These results support the occurrence of ETAE between basal-sorbed Fe(II) and tetrahedral Fe(III).

Our results emphasize the importance of tetrahedral Fe(III) in reacting with species that adsorb onto the basal planes. The redox reactivity of tetrahedral Fe(III) may be as strong as that of octahedral Fe(III), with ~90% of the latter remaining unreactive. Environmental cations predominantly adsorb onto the basal planes of clay minerals under low pH conditions. The ability of reduced Fe-containing clay minerals to reduce the oxidized forms of adsorbed elements may therefore be coupled to the presence of tetrahedral Fe(II).

5.1.2 Reversibility of clay during Fe redox cycling

Three consecutive redox cycles were imposed to NAu-1 to investigate the Fe redox reversibility of the clay mineral. The 1st reducing period (RP1) started with reducing purified NAu-1 by *Shewanella oneidensis* MR-1, with Na-lactate as the electron donor. After the microbial reduction was completed after 20 days, the aqueous phase was removed. The residual solid was near-entirely re-oxidized abiotically by air for three days during the 1st and 2nd oxidation periods (OP1 and OP2). The total extent of reduction decreased from 9.7 to 5.7% from RP1 to RP3, while the dissolution of Fe(II) decreased from 2.7 to 0.7%. A linear relation between the extent of reduction and the dissolved Fe(II) was observed. Thus, the decreasing fraction of bioavailable Fe was due to the cumulative dissolution during the three RPs. Extrapolation of the linear trend predicts that approximately 42% of the initial bioavailable Fe (10% of the total structural Fe) would remain in the clay structure upon continued redox cycling. This fraction of bioavailable Fe, which is located on the edge sites of the larger clay particles, is entirely redox reversible during redox cycles. The increasing crystal size of NAu-1 with successive redox cycles confirmed that the dissolution of bioavailable Fe was predominantly from the smallest clay particles.

As a result of the progressive removal of the small particles, the amount of the exchangeable edge surface decreased with the successive redox cycles. Correspondingly, the maximum isotope fractionation between aqueous Fe(II) and structural Fe(III) decreased from -1.60 to -0.87‰, while that between edge-bound Fe(II) and structural Fe(III) decreased from -1.91 to -0.45‰. The trends of Fe isotope fractionation therefore tracked the decrease in the bioavailability/reactivity of clay during the redox cycles.

5.2 Perspective

5.2.1 Future research

The primary goal for this thesis was to delineate the bioavailability and reversibility of Fe(III) in clay minerals using Fe isotopes. Although we developed a hypothetical model explaining the fraction of reversible Fe(III) in NAu-1 based on the results of the three redox cycles of NAu-1, this theoretical model needs to be verified by further experiments that would involve many more redox cycles. It would further be very worthwhile to conduct experiments in which the duration of the redox cycles would be varied, because this is likely to also impact the reduction rate of clay (Barcellos *et al.*, 2018).

Compared to NAu-1, the reduction of NAu-2 produced less Fe dissolution and larger Fe isotope fractionations between aqueous Fe(II) and Fe(III) in the clay, indicating that NAu-2 potentially possesses more bioavailable Fe(III). In other words, the reversibility of Fe(III) in NAu-2 might be higher than that in NAu-1. Additional redox cycling experiments with NAu-2 will be needed to better understand the importance of tetrahedral Fe(III) and its role in controlling redox reactivity of clay minerals.

5.2.2 Environmental implications

Compared to the controlled experimental conditions in our study, clays in real-world environments encounter doubtless more complicated situations. Some studies have shown that clays may be even more reactive than ferric iron (oxyhydr)oxides (Kostka *et al.*, 2002; Komlos *et al.*, 2007). However, in an earlier experimental study, Wu *et al.* (2017) suggested that while 70-100% of Fe(III) in Fe(III) (oxyhydr)oxides was reduced, the phyllosilicate-associated Fe(III) remained unreduced in the presence of *G. sulfurreducens*. In a similar vein, our work implies that *G. sulfurreducens* reduces little Fe(III) in NAu-1 in the absence of AQDS (Chapter 2). However, natural bacterial consortia inhabiting the natural soil environment are likely more effective at reducing Fe(III) in clay minerals than single culture species (Gates and Wilkinson, 1993; Pentrakova *et al.*, 2013).

The Fe isotopic signatures measured in our study indicate that dissimilatory iron reduction (DIR) of clay minerals is distinct from that of Fe (oxyhydr)oxides. Specifically, a fraction of bioavailable Fe(III) remains in the structure of clay. This part of the bioavailable Fe is potentially recycled during alternating redox conditions. This recycling explains the unique isotope signatures produced during DIR of clay. Our results therefore show that clay minerals may be a more permanent Fe reservoir in

soils than Fe oxides, because of the redox reversibility of structural Fe. Overall, our work contributes to a better understanding of the geomicrobial role of iron-containing clay minerals and the potential use of iron isotopes in geo-environmental studies.

Bibliography

Abollino O., Aceto M., Malandrino M., Sarzanini C. and Mentasti E. Adsorption of heavy metals on Na-montmorillonite. Effect of pH and organic substances. Water research. 2003. 37(7): 1619-1627.

Alexandrov V., Neumann A., Scherer M. M. and Rosso K. M. Electron exchange and conduction in nontronite from first-principles. The Journal of Physical Chemistry C. 2013. 117(5): 2032-2040.

Alexandrov V. and Rosso K. M. Insights into the mechanism of Fe(II) adsorption and oxidation at Fe–Clay mineral surfaces from first-principles calculations. The Journal of Physical Chemistry C. 2013. 117(44): 22880-22886.

Altheide T. S., Chevrier V. F. and Dobrea E. N. Mineralogical characterization of acid weathered phyllosilicates with implications for secondary Martian deposits. Geochimica et Cosmochimica Acta. 2010. 74(21): 6232-6248.

Amonette J. E. and Templeton J. C. Improvements to the quantitative assay of nonrefractory minerals for Fe(II) and total Fe using 1, 10-phenanthroline. Clays and Clay Minerals. 1998. 46(1): 51-62.

Anastácio A. S., Aouad A., Sellin P., Fabris J. D., Bergaya F. and Stucki J. W. Characterization of a redox-modified clay mineral with respect to its suitability as a barrier in radioactive waste confinement. Applied Clay Science. 2008. 39(3-4): 172-179.

Anbar A., Jarzecki A. and Spiro T. Theoretical investigation of iron isotope fractionation between $Fe(H_2O)_6^{3+}$ and $Fe(H_2O)_6^{2+}$: implications for iron stable isotope geochemistry. Geochimica et Cosmochimica Acta. 2005. 69(4): 825-837.

Anbar A. D. and Rouxel O. Metal stable isotopes in paleoceanography. Annual Review of Earth and Planetary Sciences. 2007. 35: 717-746.

Bachmaf S. and Merkel B. J. Sorption of uranium(VI) at the clay mineral–water interface. Environmental Earth Sciences. 2011. 63(5): 925-934.

Bailey L., Lekkerkerker H. N. and Maitland G. C. Smectite clay–inorganic nanoparticle mixed suspensions: phase behaviour and rheology. Soft Matter. 2015. 11(2): 222-236.

Balashova V. and Zavarzin G. Anaerobic reduction of ferric iron by hydrogen bacteria. Mikrobiologiia. 1979. 48(5): 773-778.

Baldermann A., Warr L. N., Letofsky-Papst I. and Mavromatis V. Substantial iron sequestration during green-clay authigenesis in modern deep-sea sediments. Nature Geoscience. 2015. 8: 885-889.

Barbeau K., Rue E., Bruland K. W. and Butler A. Photochemical cycling of iron in the surface ocean mediated by microbial iron(III)-binding ligands. Nature. 2001. 413(6854): 409.

Barcellos D., Cyle K. T. and Thompson A. Faster redox fluctuations can lead to higher iron reduction rates in humid forest soils. Biogeochemistry. 2018. 137(3): 367-378.

Baron F., Petit S., Pentrák M., Decarreau A. and Stucki J. W. Revisiting the nontronite Mössbauer spectra. American Mineralogist: Journal of Earth and Planetary Materials. 2017. 102(7): 1501-1515.

Beard B., Johnson C. and Nealson K. (1998). Precise iron isotopic measurements reveals naturally occurring, mass-dependent iron isotope fractionations. Abstracts with programs - Geological Society of America

Beard B. L., Handler R. M., Scherer M. M., Wu L., Czaja A. D., Heimann A. and Johnson C. M. Iron isotope fractionation between aqueous ferrous iron and goethite. Earth and Planetary Science Letters. 2010. 295(1): 241-250.

Beard B. L. and Johnson C. M. High precision iron isotope measurements of terrestrial and lunar materials. Geochimica et Cosmochimica Acta. 1999. 63(11-12): 1653-1660.

Beard B. L. and Johnson C. M. Fe isotope variations in the modern and ancient earth and other planetary bodies. Reviews in Mineralogy and Geochemistry. 2004. 55(1): 319-357.

Beard B. L., Johnson C. M., Cox L., Sun H., Nealson K. H. and Aguilar C. Iron isotope biosignatures. Science. 1999. 285(5435): 1889-1892.

Beard B. L., Johnson C. M., Skulan J. L., Nealson K. H., Cox L. and Sun H. Application of Fe isotopes to tracing the geochemical and biological cycling of Fe. Chemical Geology. 2003. 195(1): 87-117.
Bergaya F., Lagaly G. and Vayer M. Chapter 12.10 Cation and anion exchange. Developments in Clay Science. 2006. 1: 979-1001.
Bishop M. E., Dong H., Kukkadapu R. K., Liu C. and Edelmann R. E. Bioreduction of Fe-bearing clay minerals and their reactivity toward pertechnetate (Tc-99). Geochimica et Cosmochimica Acta. 2011. 75(18): 5229-5246.
Bishop M. E., Glasser P., Dong H., Arey B. and Kovarik L. Reduction and immobilization of hexavalent chromium by microbially reduced Fe-bearing clay minerals. Geochimica et Cosmochimica Acta. 2014. 133: 186-203.
Brock T. D. and Gustafson J. Ferric iron reduction by sulfur-and iron-oxidizing bacteria. Applied and Environmental Microbiology. 1976. 32(4): 567-571.
Brown K. M., Saffer D. M. and Bekins B. A. Smectite diagenesis, pore-water freshening, and fluid flow at the toe of the Nankai wedge. Earth and Planetary Science Letters. 2001. 194(1-2): 97-109.
Bruce C. H. Smectite dehydration--its relation to structural development and hydrocarbon accumulation in northern Gulf of Mexico basin. AAPG Bulletin. 1984. 68(6): 673-683.
Bullen T. Using stable Fe isotopes to assess microbially-mediated Fe^{3+} reduction in a jet-fuel contaminated aquifer. Mineralogical Magazine. 1998. 62: 255-256.
Bullen T. D., White A. F., Childs C. W., Vivit D. V. and Schulz M. S. Demonstration of significant abiotic iron isotope fractionation in nature. Geology. 2001. 29(8): 699-702.
Busigny V., Planavsky N. J., Jézéquel D., Crowe S., Louvat P., Moureau J., Viollier E. and Lyons T. W. Iron isotopes in an Archean ocean analogue. Geochimica et Cosmochimica Acta. 2014. 133: 443-462.
Butler A. Marine siderophores and microbial iron mobilization. Biometals. 2005. 18(4): 369-374.
Caccavo F., Lonergan D. J., Lovley D. R., Davis M., Stolz J. F. and McInerney M. J. *Geobacter sulfurreducens* sp. nov., a hydrogen-and acetate-oxidizing dissimilatory metal-reducing microorganism. Applied and Environmental Microbiology. 1994. 60(10): 3752-3759.
Carlson H. K., Clark I. C., Blazewicz S. J., Iavarone A. T. and Coates J. D. Fe(II) oxidation is an innate capability of nitrate-reducing bacteria that involves abiotic and biotic reactions. Journal of Bacteriology. 2013. 195(14): 3260-3268.
Castresana J. and Moreira D. Respiratory chains in the last common ancestor of living organisms. Journal of Molecular Evolution. 1999. 49(4): 453-460.
Catalano J. G. and Brown G. E. Uranyl adsorption onto montmorillonite: evaluation of binding sites and carbonate complexation. Geochimica et Cosmochimica Acta. 2005. 69(12): 2995-3005.
Chen C., Barcellos D., Richter D. D., Schroeder P. A. and Thompson A. Redoximorphic Bt horizons of the Calhoun CZO soils exhibit depth-dependent iron-oxide crystallinity. Journal of Soils and Sediments. 2018. 1-13.
Chen J.-B., Busigny V., Gaillardet J. m., Louvat P. and Wang Y.-N. Iron isotopes in the Seine River (France): natural versus anthropogenic sources. Geochimica et Cosmochimica Acta. 2014. 128: 128-143.
Clesceri L. S. Standard methods for the examination of water and wastewater. Washington, D.C, American Public Health Association.1989.
Craddock P. R. and Dauphas N. Iron and carbon isotope evidence for microbial iron respiration throughout the Archean. Earth and Planetary Science Letters. 2011. 303(1): 121-132.
Crosby H. A., Johnson C. M., Roden E. E. and Beard B. L. Coupled Fe(II)− Fe(III) electron and atom exchange as a mechanism for Fe isotope fractionation during dissimilatory iron oxide reduction. Environmental Science & Technology. 2005. 39(17): 6698-6704.
Crosby H. A., Roden E. E., Johnson C. M. and Beard B. L. The mechanisms of iron isotope fractionation produced during dissimilatory Fe(III) reduction by *Shewanella putrefaciens* and *Geobacter sulfurreducens*. Geobiology. 2007. 5(2): 169-189.

Czaja A. D., Johnson C. M., Beard B. L., Eigenbrode J. L., Freeman K. H. and Yamaguchi K. E. Iron and carbon isotope evidence for ecosystem and environmental diversity in the~ 2.7 to 2.5 Ga Hamersley Province, Western Australia. Earth and Planetary Science Letters. 2010. 292(1): 170-180.
Czaja A. D., Johnson C. M., Yamaguchi K. E. and Beard B. L. Comment on "Abiotic pyrite formation produces a large Fe isotope fractionation". Science. 2012. 335(6068): 538-538.
Dong H. Clay–microbe interactions and implications for environmental mitigation. Elements. 2012. 8(2): 113-118.
Dong H., Jaisi D. P., Kim J. and Zhang G. Microbe-clay mineral interactions. American Mineralogist. 2009. 94(11-12): 1505-1519.
Dong H., Kostka J. E. and Kim J. Microscopic evidence for microbial dissolution of smectite. Clays and Clay Minerals. 2003. 51(5): 502-512.
Ehlmann B. L., Mustard J. F., Murchie S. L., Bibring J.-P., Meunier A., Fraeman A. A. and Langevin Y. Subsurface water and clay mineral formation during the early history of Mars. Nature. 2011. 479(7371): 53.
Eickmann B., Hofmann A., Wille M., Bui T. H., Wing B. A. and Schoenberg R. Isotopic evidence for oxygenated Mesoarchaean shallow oceans. Nature Geoscience. 2018. 1.
Emerson D. and Moyer C. Isolation and characterization of novel iron-oxidizing bacteria that grow at circumneutral pH. Applied and Environmental Microbiology. 1997. 63(12): 4784-4792.
Ernstsen V., Gates W. P. and Stucki J. W. Microbial reduction of structural iron in clays—a renewable source of reduction capacity. Journal of Environmental Quality. 1998. 27(4): 761-766.
Fialips C.-I., Huo D., Yan L., Wu J. and Stucki J. W. Infrared study of reduced and reduced-reoxidized ferruginous smectite. Clays and Clay Minerals. 2002. 50(4): 455-469.
Fialips C. I., Cooper N. G., Jones D. M., White M. L. and Gray N. D. Reductive degradation of p, p'-DDT by Fe(II) in nontronite NAu-2. Clays and Clay Minerals. 2010. 58(6): 821-836.
Freed R. L. and Peacor D. R. Geopressured shale and sealing effect of smectite to illite transition. AAPG bulletin. 1989. 73(10): 1223-1232.
Frierdich A. J., Helgeson M., Liu C., Wang C., Rosso K. M. and Scherer M. M. Iron atom exchange between hematite and aqueous Fe(II). Environmental Science & Technology. 2015. 49(14): 8479-8486.
Géhin A., Greneche J.-M., Tournassat C., Brendle J., Rancourt D. G. and Charlet L. Reversible surface-sorption-induced electron-transfer oxidation of Fe(II) at reactive sites on a synthetic clay mineral. Geochimica et Cosmochimica Acta. 2007. 71(4): 863-876.
Gainey S. R., Hausrath E. M., Adcock C. T., Tschauner O., Hurowitz J. A., Ehlmann B. L., Xiao Y. and Bartlett C. L. Clay mineral formation under oxidized conditions and implications for paleoenvironments and organic preservation on Mars. Nature Communications. 2017. 8(1): 1230.
Gates W., Slade P., Manceau A. and Lanson B. Site occupancies by iron in nontronites. Clays and Clay Minerals. 2002. 50(2): 223-239.
Gates W. P. and Wilkinson H. T. Swelling properties of microbially reduced ferruginous smectite. Clays and Clay Miner. 1993.
Geatches D., Clark S. and Greenwell H. Iron reduction in nontronite-type clay minerals: modelling a complex system. Geochimica et Cosmochimica Acta. 2012. 81: 13-27.
Goldblatt C., Lenton T. M. and Watson A. J. Bistability of atmospheric oxygen and the Great Oxidation. Nature. 2006. 443(7112): 683.
Gorby Y. A., Yanina S., McLean J. S., Rosso K. M., Moyles D., Dohnalkova A., Beveridge T. J., Chang I. S., Kim B. H. and Kim K. S. Electrically conductive bacterial nanowires produced by *Shewanella oneidensis* strain MR-1 and other microorganisms. Proceedings of the National Academy of Sciences. 2006. 103(30): 11358-11363.

Gorski C. A., Klüpfel L. E., Voegelin A., Sander M. and Hofstetter T. B. Redox properties of structural Fe in clay minerals: 3. relationships between smectite redox and structural properties. Environmental Science & Technology. 2013. 47(23): 13477-13485.
Gray H. B. and Winkler J. R. Electron flow through proteins. Chemical Physics Letters. 2009. 483(1-3): 1-9.
Guilbaud R., Butler I. B. and Ellam R. M. Abiotic pyrite formation produces a large Fe isotope fractionation. Science. 2011. 332(6037): 1548-1551.
Guo H., Liu C., Lu H., Wanty R. B., Wang J. and Zhou Y. Pathways of coupled arsenic and iron cycling in high arsenic groundwater of the Hetao basin, Inner Mongolia, China: an iron isotope approach. Geochimica et Cosmochimica Acta. 2013. 112: 130-145.
Haderlein S. B., Weissmahr K. W. and Schwarzenbach R. P. Specific adsorption of nitroaromatic explosives and pesticides to clay minerals. Environmental Science & Technology. 1996. 30(2): 612-622.
Handler R. M., Frierdich A. J., Johnson C. M., Rosso K. M., Beard B. L., Wang C., Latta D. E., Neumann A., Pasakarnis T. and Premaratne W. Fe(II)-catalyzed recrystallization of goethite revisited. Environmental Science & Technology. 2014. 48(19): 11302-11311.
Heimann A., Johnson C. M., Beard B. L., Valley J. W., Roden E. E., Spicuzza M. J. and Beukes N. J. Fe, C, and O isotope compositions of banded iron formation carbonates demonstrate a major role for dissimilatory iron reduction in ~2.5 Ga marine environments. Earth and Planetary Science Letters. 2010. 294(1): 8-18.
Hernandez M. and Newman D. Extracellular electron transfer. Cellular and Molecular Life Sciences CMLS. 2001. 58(11): 1562-1571.
Hofmann A., Bekker A., Rouxel O., Rumble D. and Master S. Multiple sulphur and iron isotope composition of detrital pyrite in Archaean sedimentary rocks: a new tool for provenance analysis. Earth and Planetary Science Letters. 2009. 286(3): 436-445.
Hofstetter T. B., Neumann A. and Schwarzenbach R. P. Reduction of nitroaromatic compounds by Fe(II) species associated with iron-rich smectites. Environmental Science & Technology. 2006. 40(1): 235-242.
Hofstetter T. B., Schwarzenbach R. P. and Haderlein S. B. Reactivity of Fe(II) species associated with clay minerals. Environmental Science & Technology. 2003. 37(3): 519-528.
Holland H. D. The chemical evolution of the atmosphere and oceans, Princeton University Press.1984.
Homoky W., Severmann S., Mills R., Statham P. and Fones G. Pore-fluid Fe isotopes reflect the extent of benthic Fe redox recycling: evidence from continental shelf and deep-sea sediments. Geology. 2009. 37(8): 751-754.
Huang L., Jia X., Shao M. a., Chen L., Han G. and Zhang G. Phases and rates of iron and magnetism changes during paddy soil development on calcareous marine sediment and acid Quaternary red-clay. Scientific Reports. 2018. 8(1): 444.
Ilgen A. G. and Trainor T. P. Sb(III) and Sb(V) sorption onto Al-rich phases: hydrous Al oxide and the clay minerals kaolinite KGa-1b and oxidized and reduced nontronite NAu-1. Environmental Science & Technology. 2011. 46(2): 843-851.
Jackson M. L. Soil chemical analysis: advanced course. Madison, WI. 1956.
Jaisi D. P., Dong H. and Liu C. Influence of biogenic Fe(II) on the extent of microbial reduction of Fe(III) in clay minerals nontronite, illite, and chlorite. Geochimica et Cosmochimica Acta. 2007. 71(5): 1145-1158.
Jaisi D. P., Dong H., Plymale A. E., Fredrickson J. K., Zachara J. M., Heald S. and Liu C. Reduction and long-term immobilization of technetium by Fe(II) associated with clay mineral nontronite. Chemical Geology. 2009. 264(1): 127-138.
Jaisi D. P., Kukkadapu R. K., Eberl D. D. and Dong H. Control of Fe(III) site occupancy on the rate and extent of microbial reduction of Fe(III) in nontronite. Geochimica et Cosmochimica Acta. 2005. 69(23): 5429-5440.

Jaynes W. and Boyd S. Hydrophobicity of siloxane surfaces in smectites as revealed by aromatic hydrocarbon adsorption from water. Clays and Clay Minerals. 1991. 39(4): 428-436.
Joe-Wong C., Brown Jr G. E. and Maher K. Kinetics and products of chromium(VI) reduction by iron(II/III)-bearing clay minerals. Environmental Science & Technology. 2017. 51(17): 9817-9825.
Johnson C. M., Beard B. L., Klein C., Beukes N. J. and Roden E. E. Iron isotopes constrain biologic and abiologic processes in banded iron formation genesis. Geochimica et Cosmochimica Acta. 2008a. 72(1): 151-169.
Johnson C. M., Beard B. L. and Roden E. E. The iron isotope fingerprints of redox and biogeochemical cycling in modern and ancient Earth. Annual Review of Earth and Planetary Sciences. 2008b. 36: 457-493.
Johnson C. M., Skulan J. L., Beard B. L., Sun H., Nealson K. H. and Braterman P. S. Isotopic fractionation between Fe(III) and Fe(II) in aqueous solutions. Earth and Planetary Science Letters. 2002. 195(1-2): 141-153.
Jones A. M., Murphy C. A., Waite T. D. and Collins R. N. Fe(II) interactions with smectites: temporal changes in redox reactivity and the formation of green rust. Environmental Science & Technology. 2017. 51(21): 12573-12582.
Joshi P. and Gorski C. A. Anisotropic morphological changes in goethite during Fe^{2+}-catalyzed recrystallization. Environmental Science & Technology. 2016.
Kane S. R., Beller H. R., Legler T. C. and Anderson R. T. Biochemical and genetic evidence of benzylsuccinate synthase intoluene-degrading, ferric iron-reducing Geobacter metallireducens. Biodegradation. 2002. 13(2): 149-154.
Kappler A., Pasquero C., Konhauser K. O. and Newman D. K. Deposition of banded iron formations by anoxygenic phototrophic Fe(II)-oxidizing bacteria. Geology. 2005. 33(11): 865-868.
Kashefi K., Shelobolina E. S., Elliott W. C. and Lovley D. R. Growth of thermophilic and hyperthermophilic Fe(III)-reducing microorganisms on a ferruginous smectite as the sole electron acceptor. Applied and Environmental Microbiology. 2008. 74(1): 251-258.
Kaufhold S., Stucki J., Finck N., Steininger R., Zimina A., Dohrmann R., Ufer K., Pentrák M. and Pentrákov á L. Tetrahedral charge and Fe content in dioctahedral smectites. Clay Minerals. 2017. 52(1): 51-65.
Keeling J. L., Raven M. D. and Gates W. P. Geology and characterization of two hydrothermal nontronites from weathered metamorphic rocks at the Uley graphite mine, South Australia. Clays and Clay Minerals. 2000. 48(5): 537-548.
Kim J.-W., Furukawa Y., Dong H. and Newell S. W. The effect of microbial Fe(III) reduction on smectite flocculation. Clays and Clay Minerals. 2005. 53(6): 572-579.
Kim J., Dong H., Seabaugh J., Newell S. W. and Eberl D. D. Role of microbes in the smectite-to-illite reaction. Science. 2004. 303(5659): 830-832.
Kloprogge J. T., Komarneni S. and Amonette J. E. Synthesis of smectite clay minerals: a critical review. Clays and Clay Minerals. 1999. 47(5): 529-554.
Komadel P., Madejov á J. and Stucki J. W. Structural Fe(III) reduction in smectites. Applied Clay Science. 2006. 34(1): 88-94.
Komlos J., Kukkadapu R. K., Zachara J. M. and Jaffe P. R. Biostimulation of iron reduction and subsequent oxidation of sediment containing Fe-silicates and Fe-oxides: effect of redox cycling on Fe(III) bioreduction. Water Research. 2007. 41(13): 2996-3004.
Koo T., Jang Y., Kogure T., Kim J., Park B., Sunwoo D. and Kim J. Structural and chemical modification of nontronite associated with microbial Fe(III) reduction: indicators of “illitization”. Chemical Geology. 2014. 377: 87-95.
Kostka J. E., Dalton D. D., Skelton H., Dollhopf S. and Stucki J. W. Growth of iron (III)-reducing bacteria on clay minerals as the sole electron acceptor and comparison of growth yields on a variety of oxidized iron forms. Applied and Environmental Microbiology. 2002. 68(12): 6256-6262.

Kostka J. E., Haefele E., Viehweger R. and Stucki J. W. Respiration and dissolution of iron(III)-containing clay minerals by bacteria. Environmental Science & Technology. 1999a. 33(18): 3127-3133.
Kostka J. E., Wu J., Nealson K. H. and Stucki J. W. The impact of structural Fe(III) reduction by bacteria on the surface chemistry of smectite clay minerals. Geochimica et Cosmochimica Acta. 1999b. 63(22): 3705-3713.
Labatut M., Lacan F., Pradoux C., Chmeleff J., Radic A., Murray J. W., Poitrasson F., Johansen A. and Thil F. Iron sources and dissolved - particulate interactions in the seawater of the Western Equatorial Pacific, iron isotope perspectives. Global Biogeochemical Cycles. 2014. 28(10): 1044-1065.
Latta D. E., Neumann A., Premaratne W. and Scherer M. M. Fe(II)–Fe(III) electron transfer in a clay mineral with low Fe content. ACS Earth and Space Chemistry. 2017. 1(4): 197-208.
Lee K., Kostka J. E. and Stucki J. W. Comparisons of structural Fe reduction in smectites by bacteria and dithionite: an infrared spectroscopic study. Clays and Clay Minerals. 2006. 54(2): 195-208.
Li Y.-L., Vali H., Sears S. K., Yang J., Deng B. and Zhang C. L. Iron reduction and alteration of nontronite NAu-2 by a sulfate-reducing bacterium1. Geochimica et Cosmochimica Acta. 2004. 68(15): 3251-3260.
Liu D., Dong H., Agrawal A., Singh R., Zhang J. and Wang H. Inhibitory effect of clay mineral on methanogenesis by *Methanosarcina mazei* and *Methanothermobacter thermautotrophicus*. Applied Clay Science. 2016. 126: 25-32.
Liu D., Dong H., Bishop M., Zhang J., Wang H., Xie S., Wang S., Huang L. and Eberl D. Microbial reduction of structural iron in interstratified illite - smectite minerals by a sulfate - reducing bacterium. Geobiology. 2012. 10(2): 150-162.
Liu D., Dong H., Bishop M. E., Wang H., Agrawal A., Tritschler S., Eberl D. D. and Xie S. Reduction of structural Fe(III) in nontronite by methanogen *Methanosarcina barkeri*. Geochimica et Cosmochimica Acta. 2011. 75(4): 1057-1071.
Liu D., Dong H., Wang H. and Zhao L. Low-temperature feldspar and illite formation through bioreduction of Fe(III)-bearing smectite by an alkaliphilic bacterium. Chemical Geology. 2015. 406: 25-33.
Liu X., Dong H., Yang X., Kovarik L., Chen Y. and Zeng Q. Effects of citrate on hexavalent chromium reduction by structural Fe(II) in nontronite. Journal of Hazardous Materials. 2018. 343: 245-254.
Lovley D. R. Dissimilatory Fe(III) and Mn(IV) reduction. Microbiological Reviews. 1991. 55(2): 259-287.
Lovley D. R., Holmes D. E. and Nevin K. P. Dissimilatory Fe(III) and Mn(IV) reduction. 2004.
Lovley D. R. and Phillips E. J. Novel mode of microbial energy metabolism: organic carbon oxidation coupled to dissimilatory reduction of iron or manganese. Applied and Environmental Microbiology. 1988. 54(6): 1472-1480.
Lovley D. R., Ueki T., Zhang T., Malvankar N. S., Shrestha P. M., Flanagan K. A., Aklujkar M., Butler J. E., Giloteaux L. and Rotaru A.-E. *Geobacter*: the microbe electric's physiology, ecology, and practical applications. Advances in Microbial Physiology, Elsevier. 2011. 59**:** 1-100.
Luan F., Gorski C. A. and Burgos W. D. Thermodynamic controls on the microbial reduction of iron-bearing nontronite and uranium. Environmental Science & Technology. 2014. 48(5): 2750-2758.
Luan F., Gorski C. A. and Burgos W. D. Linear free energy relationships for the biotic and abiotic reduction of nitroaromatic compounds. Environmental Science & Technology. 2015a. 49(6): 3557-3565.
Luan F., Liu Y., Griffin A. M., Gorski C. A. and Burgos W. D. Iron(III)-bearing clay minerals enhance bioreduction of nitrobenzene by *Shewanella putrefaciens* CN32. Environmental Science & Technology. 2015b. 49(3): 1418-1426.
Markelova E., Couture R.-M., Parsons C. T., Markelov I., Madé B., Van Cappellen P. and Charlet L. Speciation dynamics of oxyanion contaminants (As, Sb, Cr) in argillaceous suspensions during oxic-anoxic cycles. Applied Geochemistry. 2017.

Marsili E., Baron D. B., Shikhare I. D., Coursolle D., Gralnick J. A. and Bond D. R. *Shewanella* secretes flavins that mediate extracellular electron transfer. Proceedings of the National Academy of Sciences. 2008. 105(10): 3968-3973.

Mawji E., Gledhill M., Milton J. A., Tarran G. A., Ussher S., Thompson A., Wolff G. A., Worsfold P. J. and Achterberg E. P. Hydroxamate siderophores: occurrence and importance in the Atlantic Ocean. Environmental Science & Technology. 2008. 42(23): 8675-8680.

McCoy V., Asael D. and Planavsky N. Benthic iron cycling in a high‐oxygen environment: implications for interpreting the Archean sedimentary iron isotope record. Geobiology. 2017. 15(5): 619-627.

Melton E. D., Swanner E. D., Behrens S., Schmidt C. and Kappler A. The interplay of microbially mediated and abiotic reactions in the biogeochemical Fe cycle. Nature Reviews Microbiology. 2014. 12(12): 797.

Mermut A. R. and Cano A. F. Baseline studies of the clay minerals society source clays: chemical analyses of major elements. Clays and Clay Minerals. 2001. 49(5): 381-386.

Meunier A. Clays, Springer Science & Business Media.2005.

Meunier A. and El Albani A. The glauconite–Fe‐illite–Fe‐smectite problem: a critical review. Terra Nova. 2007. 19(2): 95-104.

Michalopoulos P. and Aller R. C. Rapid clay mineral formation in Amazon delta sediments: reverse weathering and oceanic elemental cycles. Science. 1995. 270(5236): 614-617.

Myers C. R. and Nealson K. H. Bacterial manganese reduction and growth with manganese oxide as the sole electron acceptor. Science. 1988a. 240(4857): 1319.

Myers C. R. and Nealson K. H. Bacterial manganese reduction and growth with manganese oxide as the sole electron acceptor. Science. 1988b. 240: 1319-1321.

Myers C. R. and Nealson K. H. Respiration-linked proton translocation coupled to anaerobic reduction of manganese(IV) and iron(III) in *Shewanella putrefaciens* MR-1. Journal of Bacteriology. 1990. 172(11): 6232-6238.

Neumann A., Olson T. L. and Scherer M. M. Spectroscopic evidence for Fe(II)–Fe(III) electron transfer at clay mineral edge and basal sites. Environmental Science & Technology. 2013. 47(13): 6969-6977.

Neumann A., Wu L., Li W., Beard B. L., Johnson C. M., Rosso K. M., Frierdich A. J. and Scherer M. M. Atom exchange between aqueous Fe(II) and structural Fe in clay minerals. Environmental Science & Technology. 2015. 49(5): 2786-2795.

Nevin K. P. and Lovley D. R. Mechanisms for Fe (III) oxide reduction in sedimentary environments. Geomicrobiology Journal. 2002a. 19(2): 141-159.

Nevin K. P. and Lovley D. R. Mechanisms for Fe(III) oxide reduction in sedimentary environments. Geomicrobiology Journal. 2002b. 19(2): 141-159.

Nishizawa M., Yamamoto H., Ueno Y., Tsuruoka S., Shibuya T., Sawaki Y., Yamamoto S., Kon Y., Kitajima K. and Komiya T. Grain-scale iron isotopic distribution of pyrite from Precambrian shallow marine carbonate revealed by a femtosecond laser ablation multicollector ICP-MS technique: possible proxy for the redox state of ancient seawater. Geochimica et Cosmochimica Acta. 2010. 74(9): 2760-2778.

O'Reilly S. E., Watkins J. and Furukawa Y. Secondary mineral formation associated with respiration of nontronite, NAu-1 by iron reducing bacteria. Geochemical Transactions. 2005. 6(4): 1.

Olson J. M. Photosynthesis in the Archean era. Photosynthesis Research. 2006. 88(2): 109-117.

Pentrakova L., Su K., Pentrák M. and Stucki J. A review of microbial redox interactions with structural Fe in clay minerals. Clay Minerals. 2013. 48(3): 543-560.

Percak‐Dennett E., Beard B., Xu H., Konishi H., Johnson C. and Roden E. Iron isotope fractionation during microbial dissimilatory iron oxide reduction in simulated Archaean seawater. Geobiology. 2011. 9(3): 205-220.

Peretyazhko T., Zachara J. M., Kukkadapu R. K., Heald S. M., Kutnyakov I. V., Resch C. T., Arey B. W., Wang C. M., Kovarik L. and Phillips J. L. Pertechnetate (TcO_4^-) reduction by reactive ferrous iron forms in naturally anoxic, redox transition zone sediments from the Hanford Site, USA. Geochimica et Cosmochimica Acta. 2012. 92: 48-66.

Pevear D. R. Illite and hydrocarbon exploration. Proceedings of the National Academy of Sciences. 1999. 96(7): 3440-3446.

Planavsky N. J., Asael D., Hofmann A., Reinhard C. T., Lalonde S. V., Knudsen A., Wang X., Ossa F. O., Pecoits E. and Smith A. J. Evidence for oxygenic photosynthesis half a billion years before the Great Oxidation Event. Nature Geoscience. 2014. 7(4): 283.

Playter T., Konhauser K., Owttrim G., Hodgson C., Warchola T., Mloszewska A. M., Sutherland B., Bekker A., Zonneveld J.-P. and Pemberton S. G. Microbe-clay interactions as a mechanism for the preservation of organic matter and trace metal biosignatures in black shales. Chemical Geology. 2017. 459: 75-90.

Poulton S. W. and Canfield D. E. Ferruginous conditions: a dominant feature of the ocean through Earth's history. Elements. 2011. 7(2): 107-112.

Raiswell R. Iceberg-hosted nanoparticulate Fe in the Southern Ocean: mineralogy, origin, dissolution kinetics and source of bioavailable Fe. Deep Sea Research Part II: Topical Studies in Oceanography. 2011. 58(11-12): 1364-1375.

Raiswell R. and Canfield D. E. Sources of iron for pyrite formation in marine sediments. American Journal of Science. 1998. 298(3): 219-245.

Raiswell R. and Canfield D. E. The iron biogeochemical cycle past and present. Geochemical Perspectives. 2012. 1(1): 1-2.

Reddy T. R., Frierdich A. J., Beard B. L. and Johnson C. M. The effect of pH on stable iron isotope exchange and fractionation between aqueous Fe(II) and goethite. Chemical Geology. 2015. 397: 118-127.

Reguera G., McCarthy K. D., Mehta T., Nicoll J. S., Tuominen M. T. and Lovley D. R. Extracellular electron transfer via microbial nanowires. Nature. 2005. 435(7045): 1098.

Rezanezhad F., Couture R.-M., Kovac R., O'Connell D. and Van Cappellen P. Water table fluctuations and soil biogeochemistry: an experimental approach using an automated soil column system. Journal of Hydrology. 2014. 509: 245-256.

Ribeiro F. R., Fabris J. D., Kostka J. E., Komadel P. and Stucki J. W. Comparisons of structural iron reduction in smectites by bacteria and dithionite: II. a variable-temperature Mössbauer spectroscopic study of Garfield nontronite. Pure and Applied Chemistry. 2009. 81(8): 1499-1509.

Roberts J. L. Reduction of ferric hydroxide by strains of *bacillus polymyxa*. Soil Science. 1947. 63(2): 135-140.

Roden E. E. Microbial iron-redox cycling in subsurface environments, Portland Press Limited. 2012.

Rolison J. M., Stirling C. H., Middag R., Gault-Ringold M., George E. and Rijkenberg M. J. Iron isotope fractionation during pyrite formation in a sulfidic Precambrian ocean analogue. Earth and Planetary Science Letters. 2018. 488: 1-13.

Rouxel O., Sholkovitz E., Charette M. and Edwards K. J. Iron isotope fractionation in subterranean estuaries. Geochimica et Cosmochimica Acta. 2008. 72(14): 3413-3430.

Rouxel O. J., Bekker A. and Edwards K. J. Iron isotope constraints on the Archean and Paleoproterozoic ocean redox state. Science. 2005. 307(5712): 1088-1091.

Russell J., Goodman B. and Fraser A. Infrared and Mössbauer studies of reduced nontronites. Clays and Clay Minerals. 1979. 27(1): 63-71.

Ryan P. C. and Huertas F. J. Reaction pathways of clay minerals in tropical soils: Insights from kaolinite-smectite synthesis experiments. Clays and Clay Minerals. 2013. 61(4): 303-318.

Schilt A. A. Analytical applications of 1, 10-phenanthroline and related compounds: international series of monographs in analytical chemistry, Elsevier.2013.

Scholz F., Löscher C. R., Fiskal A., Sommer S., Hensen C., Lomnitz U., Wuttig K., Göttlicher J., Kossel E. and Steininger R. Nitrate-dependent iron oxidation limits iron transport in anoxic ocean regions. Earth and Planetary Science Letters. 2016. 454: 272-281.
Schoonheydt R. and Johnston C. Surface and interface chemistry of clay minerals. Developments in Clay Science. 2006. 1: 87-113.
Severmann S., Lyons T. W., Anbar A., McManus J. and Gordon G. Modern iron isotope perspective on the benthic iron shuttle and the redox evolution of ancient oceans. Geology. 2008. 36(6): 487-490.
Shelobolina E., Xu H., Konishi H., Kukkadapu R., Wu T., Blöthe M. and Roden E. Microbial lithotrophic oxidation of structural Fe(II) in biotite. Applied and Environmental Microbiology. 2012a. 78(16): 5746-5752.
Shelobolina E. S., Konishi H., Xu H., Benzine J., Xiong M. Y., Wu T., Blöthe M. and Roden E. Isolation of phyllosilicate–iron redox cycling microorganisms from an illite–smectite rich hydromorphic soil. Frontiers in Microbiology. 2012b. 3: 134.
Shelobolina E. S., VanPraagh C. G. and Lovley D. R. Use of ferric and ferrous iron containing minerals for respiration by *Desulfitobacterium frappieri*. Geomicrobiology Journal. 2003. 20(2): 143-156.
Shi B., Liu K., Wu L., Li W., Smeaton C. M., Beard B. L., Johnson C. M., Roden E. E. and Van Cappellen P. Iron isotope fractionations reveal a finite bioavailable Fe pool for structural Fe(III) reduction in nontronite. Environmental Science & Technology. 2016. 50(16): 8661-8669.
Shi L., Richardson D. J., Wang Z., Kerisit S. N., Rosso K. M., Zachara J. M. and Fredrickson J. K. The roles of outer membrane cytochromes of *Shewanella* and *Geobacter* in extracellular electron transfer. Environmental Microbiology Reports. 2009. 1(4): 220-227.
Skulan J. L., Beard B. L. and Johnson C. M. Kinetic and equilibrium Fe isotope fractionation between aqueous Fe(III) and hematite. Geochimica et Cosmochimica Acta. 2002. 66(17): 2995-3015.
Soltermann D., Baeyens B., Bradbury M. H. and Fernandes M. M. Fe(II) uptake on natural montmorillonites. II. Surface complexation modeling. Environmental Science & Technology. 2014a. 48(15): 8698-8705.
Soltermann D., Fernandes M. M., Baeyens B., Dähn R., Miehé-Brendlé J., Wehrli B. and Bradbury M. H. Fe(II) sorption on a synthetic montmorillonite. A combined macroscopic and spectroscopic study. Environmental Science & Technology. 2013. 47(13): 6978-6986.
Soltermann D., Marques Fernandes M., Baeyens B., Dähn R., Joshi P. A., Scheinost A. C. and Gorski C. A. Fe(II) uptake on natural montmorillonites. I. Macroscopic and spectroscopic characterization. Environmental Science & Technology. 2014b. 48(15): 8688-8697.
Starcher A. N., Li W., Kukkadapu R. K., Elzinga E. J. and Sparks D. L. Fe(II) sorption on pyrophyllite: effect of structural Fe(III) (impurity) in pyrophyllite on nature of layered double hydroxide (LDH) secondary mineral formation. Chemical Geology. 2016. 439: 152-160.
Stookey L. L. Ferrozine - a new spectrophotometric reagent for iron. Analytical Chemistry. 1970. 42(7): 779-781.
Straub K. L., Benz M., Schink B. and Widdel F. Anaerobic, nitrate-dependent microbial oxidation of ferrous iron. Applied and Environmental Microbiology. 1996. 62(4): 1458-1460.
Stucki J. Properties and behaviour of iron in clay minerals. Developments in Clay Science. 2006. 1: 423-475.
Stucki J. W. A review of the effects of iron redox cycles on smectite properties. Comptes Rendus Geoscience. 2011. 343(2): 199-209.
Stucki J. W. and Kostka J. E. Microbial reduction of iron in smectite. Comptes Rendus Geoscience. 2006. 338(6): 468-475.
Stucki J. W., Lee K., Zhang L. and Larson R. A. Effects of iron oxidation states on the surface and structural properties of smectites. Pure and Applied Chemistry. 2002. 74(11): 2145-2158.
Stucki J. W. and Tessier D. Effects of iron oxidation state on the texture and structural order of Na-nontronite gels. Clays and Clay Minerals. 1991. 39(2): 137-143.

Sun Z., Zhou H., Glasby G., Yang Q., Yin X., Li J. and Chen Z. Formation of Fe–Mn–Si oxide and nontronite deposits in hydrothermal fields on the Valu Fa Ridge, Lau Basin. Journal of Asian Earth Sciences. 2012. 43(1): 64-76.

Swanner E. D., Bayer T., Wu W., Hao L., Obst M., Sundman A., Byrne J. M., Michel F. M., Kleinhanns I. C. and Kappler A. Iron isotope fractionation during Fe(II) oxidation mediated by the oxygen-producing marine cyanobacterium *Synechococcus* PCC 7002. Environmental Science & Technology. 2017. 51(9): 4897-4906.

Swanner E. D., Wu W., Schoenberg R., Byrne J., Michel F. M., Pan Y. and Kappler A. Fractionation of Fe isotopes during Fe(II) oxidation by a marine photoferrotroph is controlled by the formation of organic Fe-complexes and colloidal Fe fractions. Geochimica et Cosmochimica Acta. 2015. 165: 44-61.

ThomasArrigo L. K., Mikutta C., Byrne J., Kappler A. and Kretzschmar R. Iron(II)-catalyzed iron atom exchange and mineralogical changes in iron-rich organic freshwater flocs: an iron isotope tracer study. Environmental Science & Technology. 2017. 51(12): 6897-6907.

Thompson A., Chadwick O. A., Rancourt D. G. and Chorover J. Iron-oxide crystallinity increases during soil redox oscillations. Geochimica et Cosmochimica Acta. 2006. 70(7): 1710-1727.

Tishchenko V., Meile C., Scherer M. M., Pasakarnis T. S. and Thompson A. Fe^{2+} catalyzed iron atom exchange and re-crystallization in a tropical soil. Geochimica et Cosmochimica Acta. 2015. 148: 191-202.

Tsarev S., Waite T. D. and Collins R. N. Uranium reduction by Fe(II) in the presence of montmorillonite and nontronite. Environmental Science & Technology. 2016. 50(15): 8223-8230.

Viollier E., Inglett P., Hunter K., Roychoudhury A. and Van Cappellen P. The ferrozine method revisited: Fe(II)/Fe(III) determination in natural waters. Applied Geochemistry. 2000. 15(6): 785-790.

Vorhies J. S. and Gaines R. R. Microbial dissolution of clay minerals as a source of iron and silica in marine sediments. Nature Geoscience. 2009. 2(3).

Wampler J., Krogstad E. J., Elliott W. C., Kahn B. and Kaplan D. I. Long-term selective retention of natural Cs and Rb by highly weathered coastal plain soils. Environmental Science & Technology. 2012. 46(7): 3837-3843.

Wang X., Dong H., Zeng Q., Xia Q., Zhang L. and Zhou Z. Reduced iron-containing clay minerals as antibacterial agents. Environmental Science & Technology. 2017. 51(13): 7639-7647.

Wayman M. and Lem W. Decomposition of aqueous dithionite. Part II. A reaction mechanism for the decomposition of aqueous sodium dithionite. Canadian Journal of Chemistry. 1970. 48(5): 782-787.

Weinrach J. B., Meyer D. R., Guy J. T., Michalski P. E., Carter K. L., Grubisha D. S. and Bennett D. W. A structural study of sodium dithionite and its ephemeral dihydrate: a new conformation for the dithionite ion. Journal of Chemical Crystallography. 1992. 22(3): 291-301.

Widdel F., Schnell S., Heising S., Ehrenreich A., Assmus B. and Schink B. Ferrous iron oxidation by anoxygenic phototrophic bacteria. Nature. 1993. 362(6423): 834.

Wu L., Beard B. L., Roden E. E. and Johnson C. M. Influence of pH and dissolved Si on Fe isotope fractionation during dissimilatory microbial reduction of hematite. Geochimica et Cosmochimica Acta. 2009. 73(19): 5584-5599.

Wu L., Beard B. L., Roden E. E. and Johnson C. M. Stable iron isotope fractionation between aqueous Fe(II) and hydrous ferric oxide. Environmental Science & Technology. 2011. 45(5): 1847-1852.

Wu L., Brucker R. P., Beard B. L., Roden E. E. and Johnson C. M. Iron isotope characteristics of hot springs at Chocolate Pots, Yellowstone National Park. Astrobiology. 2013. 13(11): 1091-1101.

Wu L., Percak-Dennett E. M., Beard B. L., Roden E. E. and Johnson C. M. Stable iron isotope fractionation between aqueous Fe(II) and model Archean ocean Fe–Si coprecipitates and implications for iron isotope variations in the ancient rock record. Geochimica et Cosmochimica Acta. 2012a. 84: 14-28.

Wu L. M., Zhou C. H., Keeling J., Tong D. S. and Yu W. H. Towards an understanding of the role of clay minerals in crude oil formation, migration and accumulation. Earth-Science Reviews. 2012b. 115(4): 373-386.
Wu T., Griffin A., Gorski C. A., Shelobolina E., Xu H., Kukkadapu R. K. and Roden E. E. Interactions between Fe(III)-oxides and Fe(III)-phyllosilicates during microbial reduction 2: natural subsurface sediments. Geomicrobiology Journal. 2017. 34(3): 231-241.
Yang J., Kukkadapu R. K., Dong H., Shelobolina E. S., Zhang J. and Kim J. Effects of redox cycling of iron in nontronite on reduction of technetium. Chemical Geology. 2012. 291: 206-216.
Yuan S., Liu X., Liao W., Zhang P., Wang X. and Tong M. Mechanisms of electron transfer from structrual Fe(II) in reduced nontronite to oxygen for production of hydroxyl radicals. Geochimica et Cosmochimica Acta. 2018.
Zarzycki P. and Rosso K. M. Stochastic simulation of isotopic exchange mechanisms for Fe(II)-catalyzed recrystallization of goethite. Environmental Science & Technology. 2017. 51(13): 7552-7559.
Zeng Q., Dong H., Zhao L. and Huang Q. Preservation of organic matter in nontronite against iron redox cycling. American Mineralogist. 2016. 101(1): 120-133.
Zhang G., Dong H., Kim J. and Eberl D. Microbial reduction of structural Fe^{3+} in nontronite by a thermophilic bacterium and its role in promoting the smectite to illite reaction. American Mineralogist. 2007. 92(8-9): 1411-1419.
Zhang J., Dong H., Liu D. and Agrawal A. Microbial reduction of Fe(III) in smectite minerals by thermophilic methanogen *Methanothermobacter thermautotrophicus*. Geochimica et Cosmochimica Acta. 2013a. 106: 203-215.
Zhang J., Dong H., Liu D., Fischer T. B., Wang S. and Huang L. Microbial reduction of Fe(III) in illite–smectite minerals by methanogen *Methanosarcina mazei*. Chemical Geology. 2012. 292: 35-44.
Zhang J., Dong H., Zeng Q. and Agrawal A. The role of Fe(III) bioreduction by methanogens in the preservation of organic matter in smectite. Chemical Geology. 2014. 389: 16-28.
Zhang T., Tremblay P.-L., Chaurasia A. K., Smith J. A., Bain T. S. and Lovley D. R. Anaerobic benzene oxidation via phenol in *Geobacter metallireducens*. Applied and Environmental Microbiology. 2013b. 79(24): 7800-7806.
Zhao L., Dong H., Edelmann R. E., Zeng Q. and Agrawal A. Coupling of Fe(II) oxidation in illite with nitrate reduction and its role in clay mineral transformation. Geochimica et Cosmochimica Acta. 2017. 200: 353-366.
Zhao L., Dong H., Kukkadapu R., Agrawal A., Liu D., Zhang J. and Edelmann R. E. Biological oxidation of Fe(II) in reduced nontronite coupled with nitrate reduction by *Pseudogulbenkiania* sp. Strain 2002. Geochimica et Cosmochimica Acta. 2013. 119: 231-247.
Zhao L., Dong H., Kukkadapu R. K., Zeng Q., Edelmann R. E., Pentrák M. and Agrawal A. Biological redox cycling of iron in nontronite and its potential application in nitrate removal. Environmental Science & Technology. 2015. 49(9): 5493-5501.
Zhu Y. and Elzinga E. J. Formation of layered Fe(II)-hydroxides during Fe(II) sorption onto clay and metal-oxide substrates. Environmental Science & Technology. 2014. 48(9): 4937-4945.

Appendix A

Supporting Information: Chapter 2

Iron isotope fractionations reveal a finite bioavailable Fe pool for structural Fe(III) reduction in nontronite NAu-1

A.1 Materials and Methods

A.1.1 Solid characterization

To verify the efficiency of the purification of clay mineral, unpurified and purified NAu-1 was grinded and sieved through 63 μm mesh for XRD. Powder was scanned by an EMPYREAN diffractometer with Cu–Kα radiation and a PIXcel3D fixed slit scintillation detector (40 mA, 45 kV) at the University of Waterloo. The XRD profile over a wide range of 2θ angles (10-70 °) was recorded at a scan speed of 0.026 °s under a continuous scanning mode. Data were collected and treated by Data Collector and HighScore Plus softwares produced by PANalytical B.V. Almelo, the Netherlands.

To detect secondary mineralization, microbially and chemically reduced NAu-1 was analyzed using scanning electron microscopy (SEM) and energy dispersive spectroscopy (EDS). All samples were prepared inside an anaerobic chamber (98% N_2/ 2% H_2, Coy®). Purified NAu-1 incubated with *S. oneidensis* for over 424 days and the slurry was diluted 2 times with MilliQ water. Chemically reduced solids with a high extent of reduction were mixed with a small amount of the same 10 mM HEPES buffer (pH = 6.8) used in the chemical reduction experiments. Aliquots of all suspensions were deposited onto aluminum SEM stubs covered with carbon tape. Excess moisture was wicked away using a Kimwipe©, and samples were dried overnight inside the anaerobic chamber. To minimize sample oxidation, samples were transported to the SEM facility at the University of Waterloo in an anaerobic sample container (BBL GasPak™ Systems). The samples were quickly transferred to the SEM/EDS sample chamber within 1-2

minutes of opening the container. The SEM (Quanta FEG 250) was operated under both low and high vacuum conditions using secondary electron (SE) and backscattered electron (BSE) detectors at accelerating voltages of 5, 10 and 15 kV. EDS (Oxford X-act) spectra were collected at selected locations at 15 kV under high vacuum conditions.

A.2 Supplementary Text

A.2.1 Potential formation of secondary Fe minerals in microbial and chemical reduction experiments

No Fe-bearing secondary minerals were observed (by SEM) on clay surfaces in biologically or chemically reduced NAu-1 after more than 400 days incubation (Figure A.6). Energy dispersive spectroscopy (EDS) shows relative elemental concentrations in the solid phase and the spectra will change based on the elements in the sample thereby changing the relative intensities of the peaks. In the case of the microbially reduced sample/spectra (Figure A.6D), a carbon peak is observed but not seen in the chemically reduced sample and likely reflects the lactate used in the biotic experiments which is subsequently oxidized to HCO_3^- and acetate, and potentially sorbed to the surface or alternatively reflects necromass on the mineral phase. It is possible that an Fe carbonate is precipitated, but given the large value for the atomic % C (46.6%), if a secondary Fe carbonate phase such as siderite was precipitated, a larger enrichment of Fe in the Fe:Si ratio would be expected. However, this is not observed. The Fe:Si and Al:Si ratios remain nearly identical in both the starting material, chemically reduced and microbially reduced samples (Table A.6). A small C peak in the original purified sample is likely due to the carbon tape (Figure A.6B).

Below we present an elemental mass balance calculation to illustrate the potential contribution of aqueous (from the growth medium) and structural K to illitization which is the dominant pathway for secondary mineral precipitation observed in nutrient-rich clay bioreduction studies (Kim *et al.*, 2004; O'Reilly *et al.*, 2005). We used the aqueous K available in the medium [0.1 mM, in contrast to 5.7 mM K_2HPO_4, 3.3 mM KH_2PO_4 used in previous studies (Kim *et al.*, 2004; O'Reilly *et al.*, 2005)] and the chemical formula of the glauconite (illite) end member with a corresponding Fe(II):K ratio of 0.67 (Meunier and El Albani, 2007) to predict the maximum amount of Fe as glauconite that could be

precipitated from the K in the medium, which is 0.067 mM Fe(II). This corresponds to a maximum of ~3% of the total Fe(II) produced at 10% reduction (Table A.2). In addition, Na was repeatedly used to saturate the surface sites of clay during the purification, thus there is negligible K provided from the clay structure. This analysis demonstrates that based on the observed 10% structural Fe reduction in this study, only 0.3% of the total Fe could be either precipitated or transformed to glauconite. Therefore, we conclude that the typical illitization pathway observed in many of the nutrient-rich bioreduction studies (Kim *et al.*, 2004; O'Reilly *et al.*, 2005) is not a dominant pathway in this study.

A.2.2 Calculation of isotope composition for structural Fe(III) extracted by 0.5 M HCl

Iron isotope compositions for aqueous Fe(II), basal-sorbed Fe(II) and edge plus structural Fe(II) were analyzed directed for aqueous, $CaCl_2$ extract and NaH_2PO_4 extract because all Fe in these phases were almost purely Fe(II) (Table A.2). The 0.5 M HCl extract contained both Fe(II) and Fe(III) (Table A.2). In order to tease out the isotope composition of Fe(III) in 0.5 M HCl extract, we assumed that the structural Fe(II) in 0.5 M HCl extract had the same isotope composition as edge plus structural Fe(II). This assumption is partially supported by identical isotope composition for edge sites Fe(III) and structural Fe(III) during non-reductive dissolution in abiotic control reactors (Table A.4). The isotope composition for structural Fe(III) in 0.5 M HCl extract can thus be calculated by the following mass balance equation:

$$M_{Fe(II)} \bullet \delta^{56}Fe_{struc\ Fe(II)} + M_{Fe(III)} \bullet \delta^{56}Fe_{struc\ Fe(III)} = (M_{Fe(II)} + M_{Fe(III)}) \bullet \delta^{56}Fe_{0.5M\ HCl\ ext} \qquad (A.1)$$

where $\delta^{56}Fe_{struc\ Fe(III)}$ is the isotope composition for structural Fe(III) (unknown), $\delta^{56}Fe_{0.5M\ HCl\ ext}$ is the measured isotope composition for 0.5 M HCl extract, $\delta^{56}Fe_{struc\ Fe(II)}$ is the measured isotope composition for NaH_2PO_4 extraction, and $M_{Fe(II)}$ and $M_{Fe(III)}$ are moles of Fe(II) and Fe(III) in 0.5 M HCl extract, respectively. For each sample, the corresponding $\delta^{56}Fe_{struc\ Fe(II)}$ value is used to calculate $\delta^{56}Fe_{struc\ Fe(III)}$ in that sample.

If we assume that NaH_2PO_4 extraction caused a fractionation of ±0.5 ‰ for true edge plus structural Fe(II) or alternatively the structural Fe(II) in the interior octahedral sheet differed in $\delta^{56}Fe$ values with edge plus structural Fe(II) by ±0.5 ‰, the propagated error for calculated $\delta^{56}Fe$ for octahedral Fe(III) extracted by 0.5 M HCl will be within ±0.4 ‰ for all samples except one chemically reduced sample with high reduction extent (24%). This is due to the small proportion of Fe(II) in the 0.5 M HCl extracts (range: 1 to 46%, average: 24%) for all but one samples. The high reduction extent sample has 71% Fe(II) out of total Fe in the 0.5 M HCl extract, thus the propagated error for calculated $\delta^{56}Fe$ for octahedral Fe(III) was much larger (±1.2 ‰), which implies that the calculated fractionation factor between aqueous Fe(II) and structural Fe(III) for the 24% reduction sample will have a propagated error of ±1.2 ‰. The ±0.5 ‰ error for structural Fe(II) in the octahedral sheet is an estimated maximum error based on the differences between the surface atoms in iron oxides as compared to the interior of iron oxides (Crosby *et al.*, 2007; Wu *et al.*, 2009; Wu *et al.*, 2011).

A.2.3 Calculation of isotope composition for all produced Fe(II)

We calculated the isotope composition for all produced Fe(II) by the following mass balance equation:

$$M_{\text{all Fe(II)}} \bullet \delta^{56}Fe_{\text{all Fe(II)}} = M_{\text{aq Fe(II)}} \bullet \delta^{56}Fe_{\text{aq Fe(II)}} + M_{\text{basal Fe(II)}} \bullet \delta^{56}Fe_{\text{basal Fe(II)}} + M_{\text{edge plus struc Fe(II)}} \bullet \delta^{56}Fe_{\text{struc Fe(II)}} + M_{\text{struc Fe(II)}} \bullet \delta^{56}Fe_{\text{struc Fe(II)}} \quad \text{(A.2)}$$

where $M_{\text{all Fe(II)}}$ is the sum of moles of all Fe(II) phases, $\delta^{56}Fe_{\text{aq Fe(II)}}$, $\delta^{56}Fe_{\text{basal Fe(II)}}$, $\delta^{56}Fe_{\text{struc Fe(II)}}$ are measured isotope composition for aqueous, $CaCl_2$ extract, NaH_2PO_4 extract, respectively.

A.2.4 Calculation of isotope composition for residual Fe

We calculated the isotope composition for residual Fe (which could be obtained by HF dissolution) by the following mass balance equations:

$$(M_0 - M_{\text{ext}}) \bullet \delta^{56}Fe_{\text{residual}} + M_{\text{ext}} \bullet \delta^{56}Fe_{\text{ext}} = M_0 \bullet \delta^{56}Fe_{\text{NAu-1}} \quad \text{(A.3)}$$

$$M_{ext} = M_{aq\ Fe(II)} + M_{basal\ Fe(II)} + M_{struc\ Fe(II)} + M_{0.5M\ HCl} \quad (A.4)$$

$$M_{ext} \bullet \delta^{56}Fe_{ext} = M_{aq\ Fe(II)} \bullet \delta^{56}Fe_{aq\ Fe(II)} + M_{basal\ Fe(II)} \bullet \delta^{56}Fe_{basal\ Fe(II)} + M_{edge\ plus\ struc\ Fe(II)} \bullet \delta^{56}Fe_{struc\ Fe(II)} + M_{0.5M\ HCl\ ext} \bullet \delta^{56}Fe_{0.5M\ HCl\ ext} \quad (A.5)$$

where $\delta^{56}Fe_{residual}$ is the isotope composition for residual structural Fe(III) (unknown), M_0 is the initial moles of Fe in NAu-1 and $\delta^{56}Fe_{NAu-1}$ is the isotope composition of the starting bulk NAu-1, M_{ext} is the sum of moles of all extractable Fe phases including aqueous and three extracts and $\delta^{56}Fe_{ext}$ is the isotope composition of the total extractable Fe, $\delta^{56}Fe_{aq\ Fe(II)}$, $\delta^{56}Fe_{basal\ Fe(II)}$, $\delta^{56}Fe_{struc\ Fe(II)}$, $\delta^{56}Fe_{0.5M\ HCl\ ext}$ are measured isotope composition for aqueous, $CaCl_2$ extract, NaH_2PO_4 extract, 0.5 M HCl extract, respectively.

The results show that residual Fe has isotope compositions very close to the starting material (Table A.7). This is due to either the small amount of Fe extracted in initial data points and control experiments or the well balanced isotope compositions for all extracts for samples at later stage of reduction. In general, Fe isotope composition of all extractable Fe showed limited deviation relative to that of the starting material when natural abundance of Fe isotopes were investigated.

A.2.5 Calculation of structural Fe(III) at the edge sites

One unit cell (a = 4.99Å, b = 8.65Å) in NAu-1 contains 4 Fe atoms, as shown in Figure A.8A. In a 0.5 μm clay particle, there are 1002 and 578 Fe(III) atoms at the edge sites at a and b axes, respectively (Figure A.8B). As the total amount of Fe(III) atoms in one layer is 2.3×10^6, the proportion of Fe(III) at the edge sites is 0.3%. Similarly, Fe(III) at the edge sites accounts for 2.7% and 13.6% of total Fe(III) in 0.05 μm and 0.01 μm clay particles, respectively.

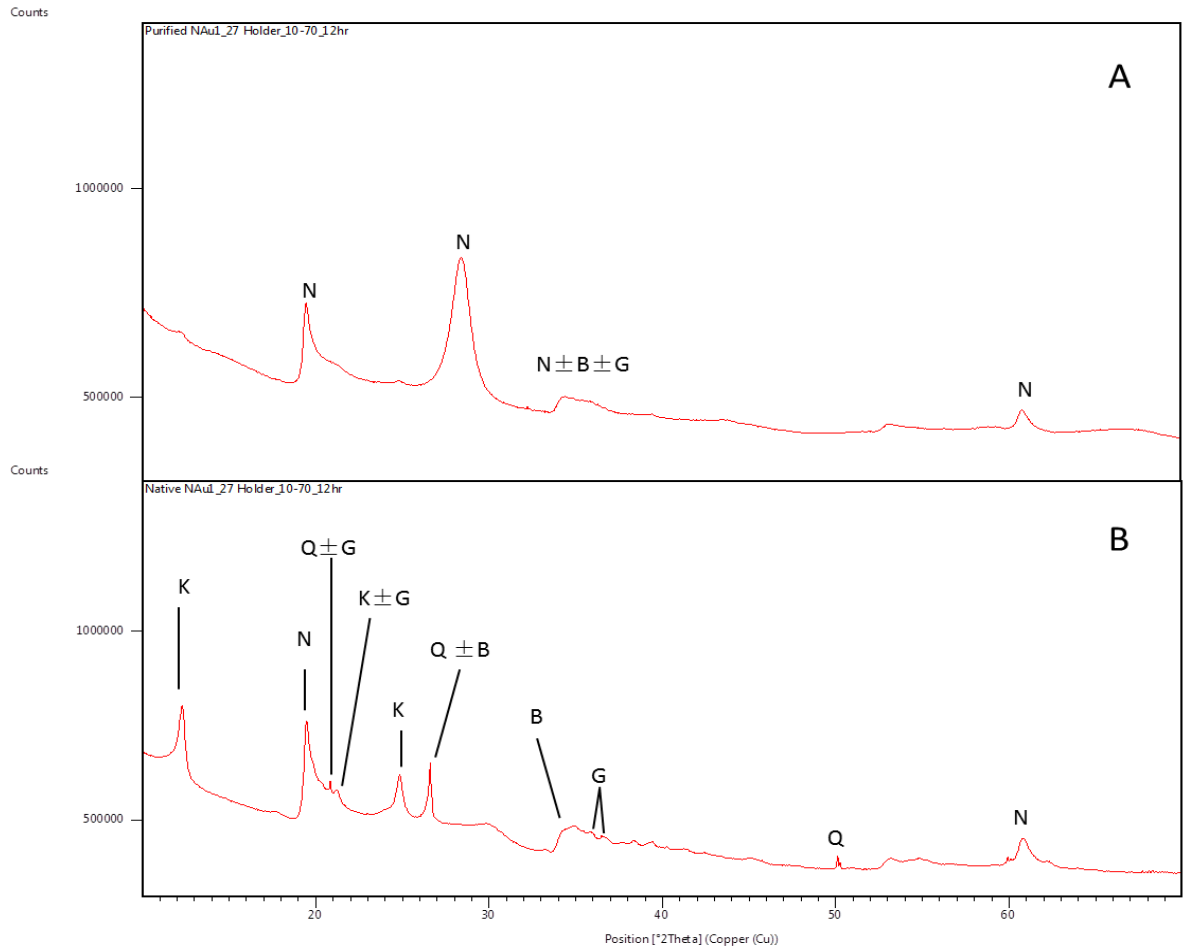

Figure A.1. XRD profiles of A) purified and B) native (unpurified) NAu-1. N = Nontronite, G = Goethite, K = Kaolinite, Q = Quartz, B = Biotite.

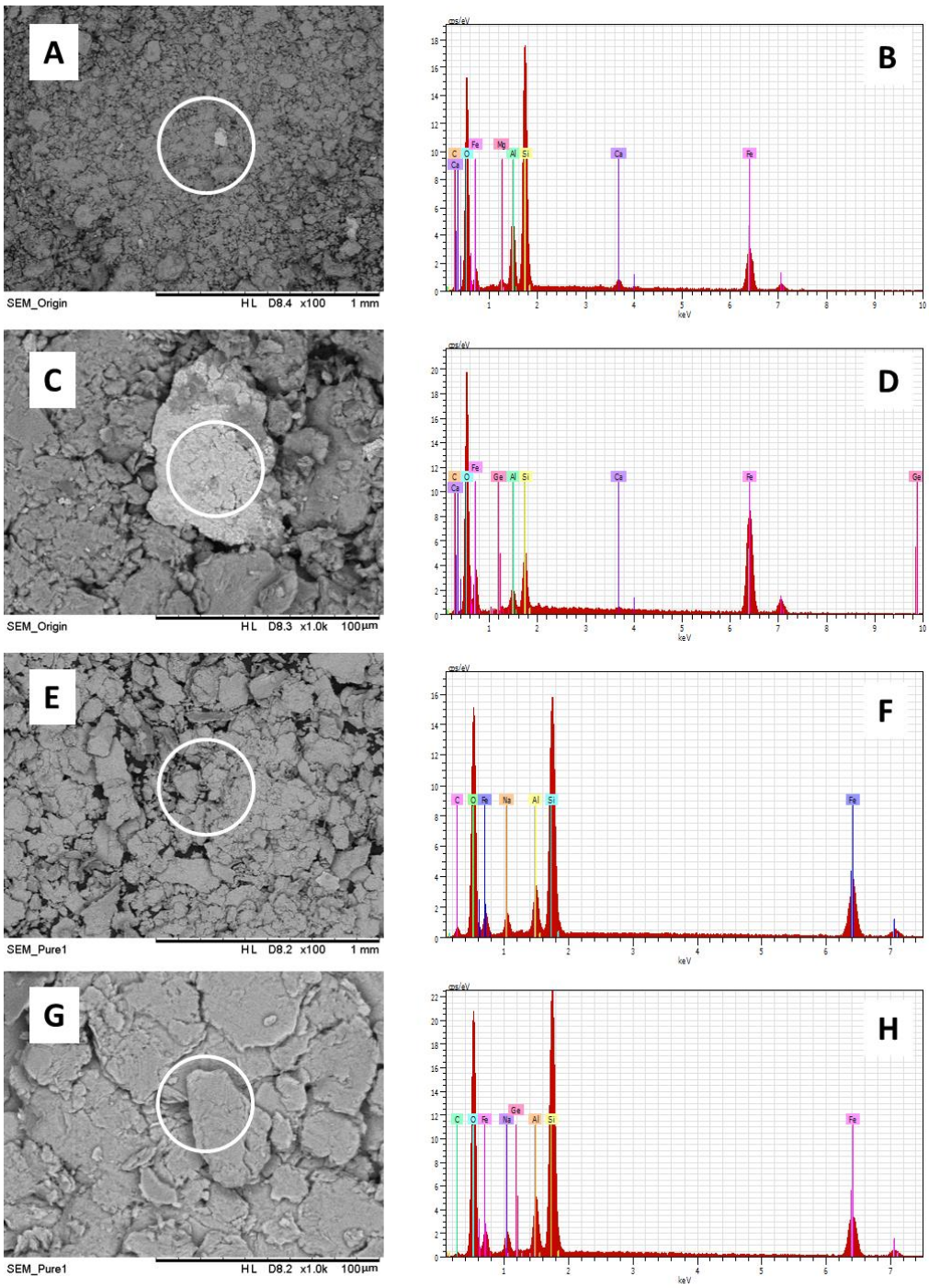

Figure A.2. Backscattered electron images of A, C) unpurified and E, G) purified NAu-1 with the corresponding relative elemental (EDS) compositions (B, D, F & H). White circles denote the area of EDS analysis.

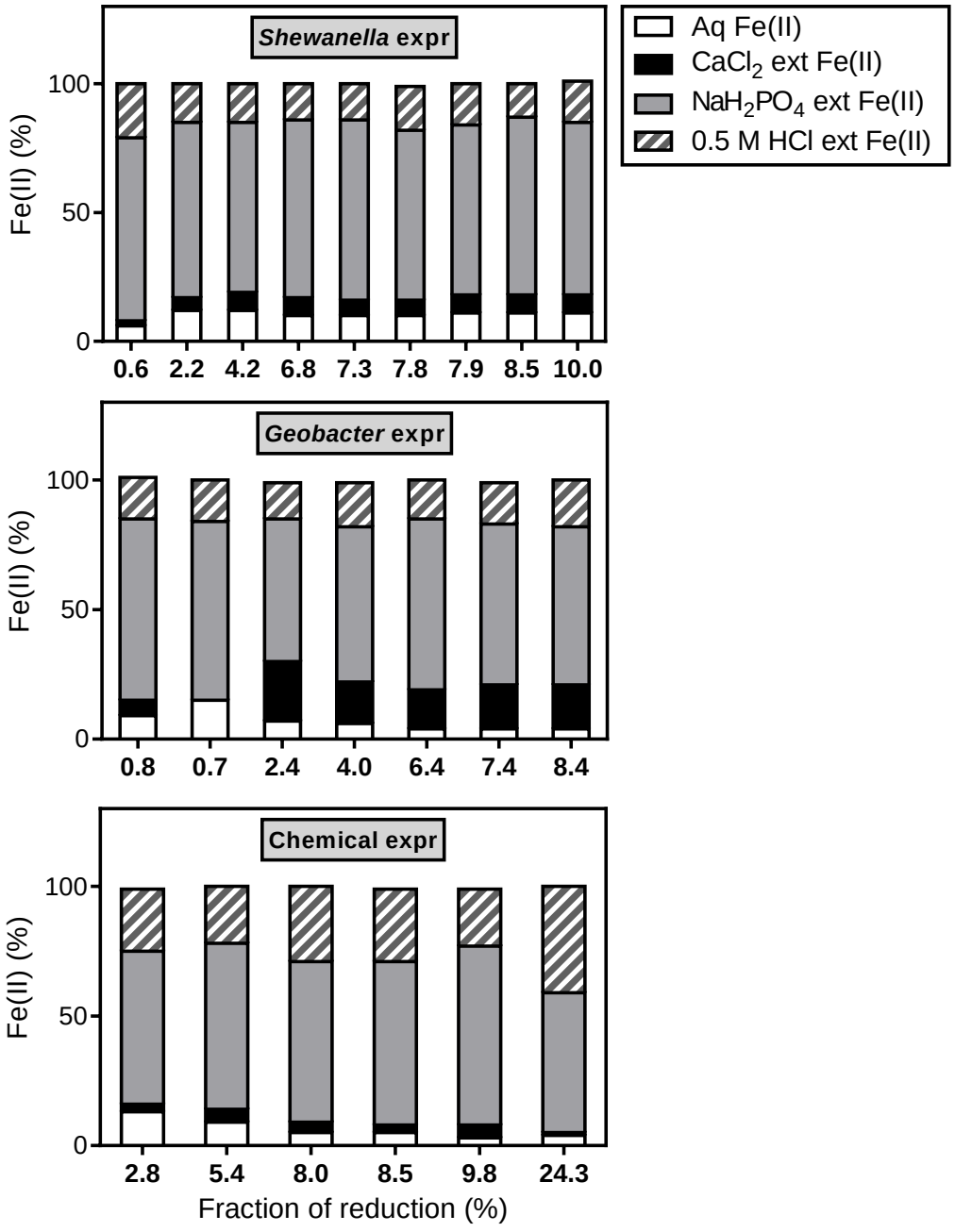

Figure A.3. Proportion of aqueous, $CaCl_2$ extracted (basal), NaH_2PO_4 extracted (edge plus structural), and 0.5 M HCl extracted [interior structural Fe(II)] out of total produced Fe(II) in *Shewanella* (A), *Geobacter* (B), and chemical (C) experiments versus fraction of reduction.

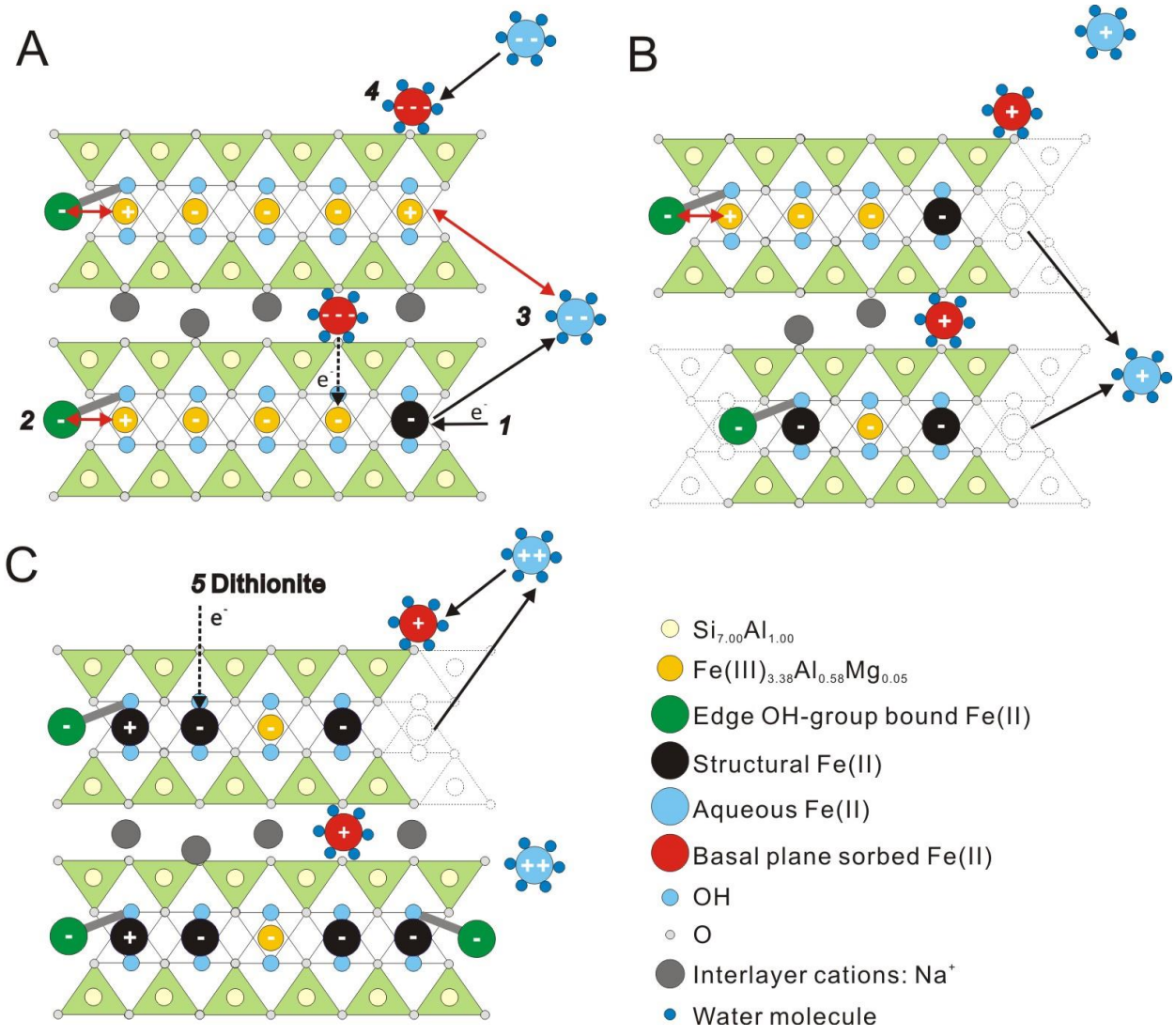

Figure A.4. Proposed reaction mechanisms in microbial and chemical reduction experiments: cross sections of NAu-1. (A) At low extent of reduction (i.e., ≤2%), electrons are supplied by the bacteria (*Shewanella* and *Geobacter*) or dithionite, to reduce structural Fe(III) on the edge sites (step 1). Fe(II) is released from the octahedral sheet and attaches to hydroxyl groups, producing edge-bound Fe(II) (step 2). Electron transfer and atom exchange (ETAE) occurs between edge-bound Fe(II) (low δ^{56}Fe indicated by "-") and structural Fe(III) (high δ^{56}Fe indicated by "+"), as shown by the red short arrows. A fraction of structural Fe is released to solution upon reduction and forms aqueous Fe(II), as indicated by the black

long arrow (step 3). ETAE between aqueous Fe(II) ("--" indicates lower δ^{56}Fe) and structural Fe(III) takes place, as indicated by the red long arrow. Aqueous phase Fe(II) can also adsorb onto basal planes ("---" indicates lowest δ^{56}Fe), as indicated by the black arrow (step 4). (B) At high extent of reduction (i.e., ~10%) in biological experiments, residual heavy structural Fe(III) is reduced and dissolved, producing isotopically heavy aqueous phase Fe(II) (indicated by "+"). Edge sites are saturated with interior structural Fe(II) ("-" indicates low δ^{56}Fe) and edge-bound Fe(II), inhibiting further reduction. ETAE between aqueous Fe(II) and structural Fe(III) is blocked, with only minor ETAE between edge-bound Fe(II) and structural Fe(III). (C) At ~24% reduction in chemical experiments, dithionite diffuses into the clay particles through basal planes (step 5) reducing interior structural Fe(III) in the absence of atom exchange.

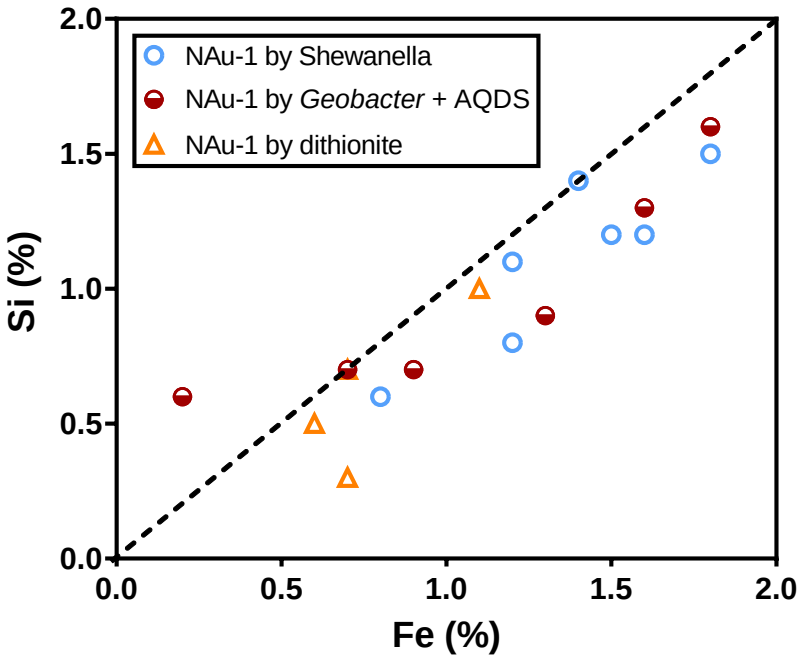

Figure A.5. Silicon vs. total Fe molar percentage dissolution (calculated by Si or total Fe concentrations in aqueous and basal plane-sorbed phases divided by initial Si or Fe concentrations in clays) for all reduction experiments. If reductive dissolution occurs, stoichiometric release of Si and Fe to aqueous and sorbed phases is expected and percentage dissolution of clay will be the same as calculated using either Si or Fe. Most data points lie close to the 1:1 dashed line, suggesting that reductive dissolution is within 2% for NAu-1.

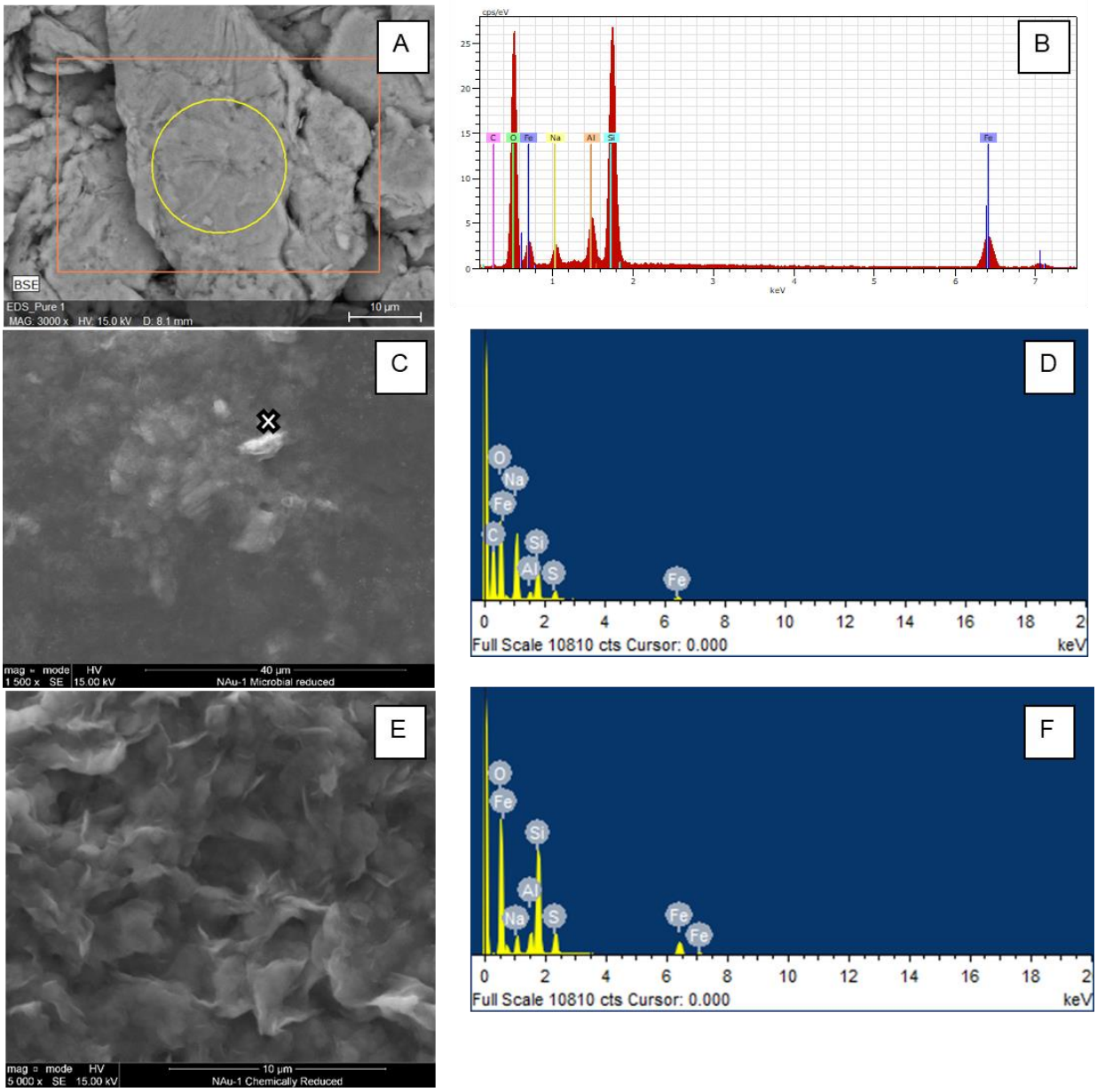

Figure A.6. SEM images of A) purified NAu-1, C) NAu-1 inoculated with *S. oneidensis* after 424 days and E) chemically reduced NAu-1. EDS spectra of B) purified NAu-1, D) NAu-1 inoculated with *S. oneidensis* after 424 days; and E) chemically reduced NAu-1. An "x" denotes the analysis location.

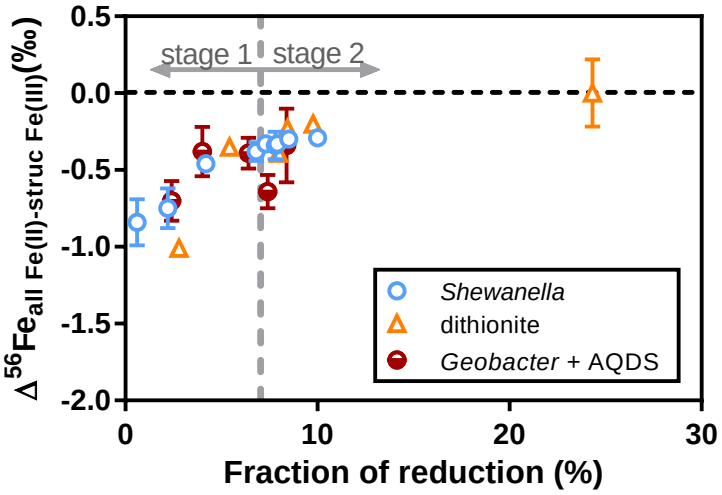

Figure A.7. Δ^{56}Fe between all Fe(II) and structural Fe(III). Dashed lines indicate Δ^{56}Fe = 0‰.

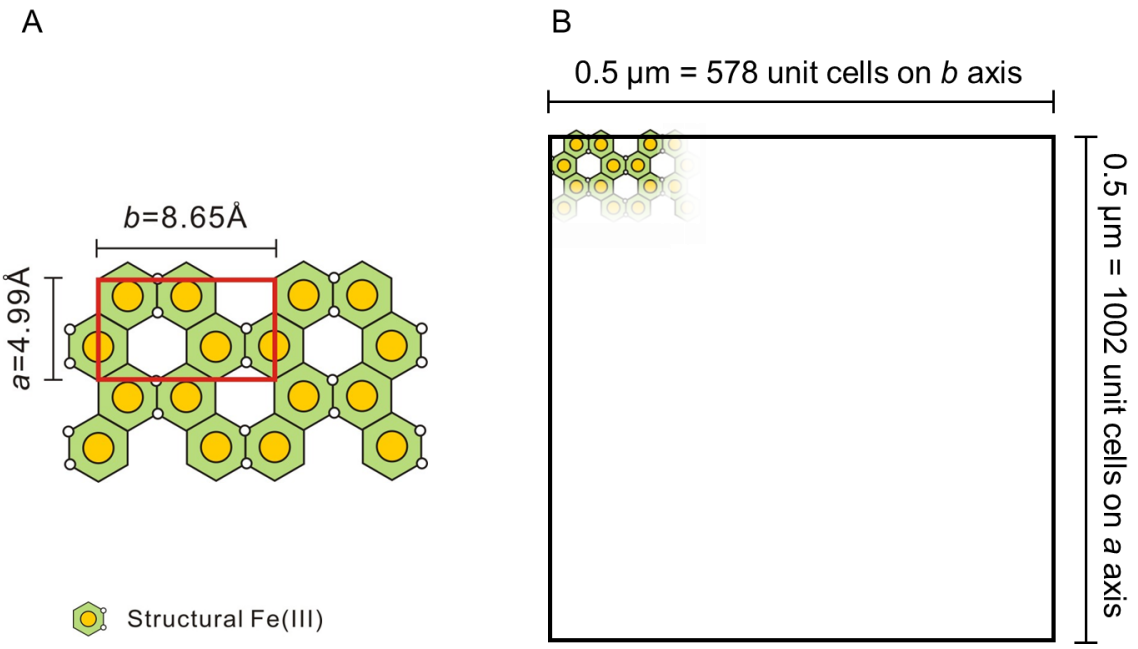

Figure A.8. Top view of NAu-1 showing (A) one unit cell contains four Fe(III) atoms, with the dimension of a = 4.99Å, b = 8.65Å, and (B) calculation of the number of structural Fe(III) on the edge sites in a sample of 0.5 µm clay particle (Neumann et al., 2015). Note that, the unit cell and the clay particle size in panel B are not to scale.

Table A.1. Experimental setup for chemical reduction reactors

Reactor No.	Temperature (℃)	Reaction time[a] (mins)	Amount of dithionite[b] (mg)	Reduction (%)
CR-1	20	0	15	2.8
CR-2	20	0	25	5.4
CR-3	70	5	25	8.0
CR-4	70	15	25	8.4
CR-5	20	360	200	9.8
CR-6	70	30	150	24.3

[a]Centrifuge time (15 mins) are not included in reaction time.
[b]Amount of dithionite was added to 10 mL 5 mg/mL NAu-1 suspension.

Table A.2. Iron concentrations for aqueous phase and three extractions in all microbial and chemical reduction experiments[a, b, c]

Days/I	Aqueous μM				$CaCl_2$ ext μM				NaH_2PO_4 ext μM				0.5 M HCl ext μM				Total Fe(II) μM		Total Fe μM		Reduction %	
D	Fe(II)	1SD	Fe(tot)	1SD	Fe(II)	1SD	Fe(tot)	1SD	Fe(II)	1SD	Fe(tot)	1SD	Fe(II)	1SD	Fe(tot)	1SD	Mean	1SD	Mean	1SD	Mean	1SD
	Shewanella biotic group																					
0	7.3	1.1	14.2	1.4	1.8	0.0	2.7	1.1	85.1	6.8	85.1	6.8	24.9	4.0	857	20	119	8.0	959	21	0.6%	0.1%
2	55.3	2.0	69.5	0.9	23.3	1.2	30.4	0.8	319	19	319	19	69.2	3.9	857	20	466	19	1276	27	2.2%	0.1%
4	103	6.0	110	4.7	61.7	5.2	65.8	3.1	582	18	582	18	135	9.1	741	2.9	882	22	1498	19	4.2%	0.2%
6	137	5.6	146	12	101	2.1	107	0.3	969	14	969	14	196	4.3	731	24	1403	16	1953	30	6.8%	0.1%
8	146	1.2	158	5.5	98.3	0.4	95.6	0.0	1063	17	1063	17	216	25	745	66	1523	30	2061	69	7.3%	0.0%
12	162	7.0	172	3.3	105	1.9	109	5.1	1069	38	1069	38	276	15	876	29	1612	42	2227	48	7.8%	0.3%
19	178	0.6	190	7.5	108	1.1	118	2.3	1079	3.2	1079	3.2	269	1.1	762	16	1633	3.6	2148	18	7.9%	0.0%
26	189	3.0	201	0.6	119	1.4	124	4.9	1211	26	1222	51.7	237	5.9	756	18	1755	27	2292	32	8.5%	0.1%
161	222	2.1	225	1.1	142	2.8	140	1.5	1375	12	1431	4.0	327	24	816	2.7	2066	27	2556	12	10.0%	0.2%
	Shewanella control group																					
0	1.6	1.0	12.3	3.8	1.6	1.3	4.2	1.4	NA	NA	48.5	0.6	9.4	0.8	886	2.9	12.6	1.8	951	5.0	0.1%	0.0%
2	2.4	1.8	14.3	2.6	1.1	1.6	3.0	2.0	NA	NA	65.0	1.2	12.5	1.8	886	2.9	16.0	3.0	968	4.5	0.1%	0.0%
4	0.0	2.1	13.9	5.0	0.0	0.6	5.3	2.6	NA	NA	65.0	1.2	11.5	0.8	866	7.2	11.5	2.3	950	9.2	0.1%	0.0%
6	7.8	4.8	20.5	0.6	2.7	2.6	5.5	1.8	NA	NA	77.3	0.9	13.0	2.3	876	3.0	23.5	5.9	979	3.6	0.1%	0.0%
8	8.6	1.5	26.5	2.2	0.0	0.6	1.6	1.2	NA	NA	76.5	1.0	12.5	1.9	906	21	21.1	2.5	1011	21	0.1%	0.0%
12	6.0	4.7	48.0	5.2	1.9	1.8	7.7	2.3	NA	NA	74.2	0.7	24.7	2.5	903	11	32.7	5.6	1033	12	0.2%	0.0%
19	8.2	0.9	116	4.2	0.3	1.5	7.5	2.2	NA	NA	105	0.4	23.0	1.4	844	8.0	31.5	2.2	1073	9.3	0.2%	0.0%
26	NA	NA	NA	NA	0.0	0.3	3.8	1.6	NA	NA	63.1	2.2	26.8	1.3	799	8.8	26.8	1.3	857	9.3	0.1%	0.0%
161	42.1	0.0	110	6.3	41.4	1.6	40.3	0.4	NA	NA	197	1.5	88.5	0.3	796	2.0	172	1.6	962	2.6	0.8%	0.0%

Geobacter biotic group																						
0	14.6	2.0	35.7	0.0	9.5	0.1	47.6	10.2	0.0	1.2	120	13	26.5	3.6	769	94	170	13	972	95	0.8%	0.1%
2	23.1	0.0	38.2	0.0	0.0	1.3	8.9	1.5	1.4	0.1	108	4.5	24.8	2.3	1115	72	156	5.2	1270	72	0.7%	0.0%
126	36.5	1.5	41.6	0.0	115	18	112	19	210	45	273	31	69.8	8.2	1074	88	495	37	1501	95	2.4%	0.3%
157	52.9	1.4	62.4	6.8	134	36	131	40	494	154	493	146	142	45	866	24	823	157	1553	154	4.0%	1.1%
162	57.9	2.6	64.8	2.1	200	26	209	21	806	101	872	61	192	33	857	24	1322	74	2002	69	6.4%	0.6%
177	67.6	1.8	75.9	3.0	265	5.5	259	12	988	43	944	15	249	17	1025	61	1526	23	2304	64	7.4%	0.2%
240	76.6	3.0	73.8	2.5	302	18	303	19	1012	5.9	1059	6.8	309	62	672	56	1746	65	2107	60	8.4%	0.2%
Geobacter control group																						
0	14.4	0.9	31.9	0.8	2.4	3.3	13.4	3.0	NA	NA	126	16	19.2	0.6	808	19	35.9	3.5	980	25	0.8%	0.1%
2	35.1	0.8	38.4	10	0.0	0.0	9.8	2.5	NA	NA	93.6	6.2	17.4	0.4	1197	41	52.5	0.9	1339	43	0.7%	0.0%
126	31.0	3.0	35.8	1.1	9.7	1.3	11.9	0.3	NA	NA	103	6.8	29.3	0.7	1202	25	70.0	3.3	1352	26	0.8%	0.1%
157	37.9	3.4	37.4	0.7	11.9	0.4	9.8	1.2	NA	NA	80.7	0.7	26.8	2.5	1122	19	76.6	4.2	1250	19	0.8%	0.0%
162	31.0	4.9	35.1	1.5	8.1	0.3	11.5	1.5	NA	NA	124	6.0	21.2	5.9	1061	55	60.3	7.7	1231	55	0.9%	0.1%
177	37.0	2.3	43.9	1.6	9.5	1.4	12.0	1.0	NA	NA	70.2	6.5	18.3	3.1	1163	53	64.8	4.1	1289	53	0.7%	0.0%
240	31.0	1.3	36.1	1.0	11.6	1.9	12.4	0.5	NA	NA	136	15	25.9	5.0	702	10	68.5	5.5	886	18	1.0%	0.0%
Chemical reduction [d]																						
CR-1	76.9	2.2	82.3	1.2	17.3	0.0	15.0	1.9	345	3.0	360	1.9	141	1.0	897	6.3	580	0.6	1354	9.2	2.8%	0.1%
CR-2	96.1	1.1	101	4.3	52.6	1.1	52.2	1.3	726	3.1	716	5.3	253	1.8	855	6.6	1128	5.9	1725	10	5.4%	0.3%
CR-3	85.2	2.0	82.2	1.1	61.3	0.9	59.2	1.0	1030	27	1010	9.1	478	2.3	1203	15	1655	31	2354	24	8.0%	0.4%
CR-4	87.9	8.6	73.1	1.5	58.1	2.1	52.8	2.8	1109	5.0	1054	9.2	499	3.0	1153	10	1753	5.3	2333	21	8.4%	0.4%
CR-5	66.8	2.1	65.5	0.6	99.6	1.7	114	0.7	1411	10	1481	11	453	3.1	1067	0.1	2031	10	2727	11	9.8%	0.5%
CR-6	208	1.7	195	7.7	47.2	2.1	40.0	0.4	2717	21	2828	9.0	2079	7.5	2921	18	5051	11	5984	16	24.3%	1.2%

[a]NA indicates data not available or not applicable.

[b]Initial Fe concentration of purified NAu-1 in reactors is 20.8 mM. The extent of reduction was calculated based on initial Fe content in the reactors and may be underestimated if total Fe recovery is less than 100%. However, this does not affect the conclusions.

[c]1 M $CaCl_2$ are used to remove sorbed Fe(II) at basal planes. 1 M NaH_2PO_4 are used to target edge OH-group bounded Fe(II), but also can extract some structural Fe(II).

[d]The residual solid of CR-6 after 0.5M HCl extraction was treated with 28 M HF to achieve complete dissolution. The measured Fe(II) concentration was 103.3 μM, less than 2.0% of total produced Fe(II).

[e]For microbial reduction, 1SD is one standard deviation based on analysis of two duplicate reactors; for chemical reduction, 1SD is calculated based on three measurement by Ferrozine method.

Table A.3. Fractions of Fe(II) in each phase out of total produced Fe(II) in all reduction experiments

Days/ID	% of total produced Fe(II)					Reduction %	
	Aqueous	Basal	Edge plus struc	Interior struc	Sum	Mean	1SD
Shewanella biotic group							
0	6%	2%	71%	21%	100%	0.6%	0.1%
2	12%	5%	68%	15%	100%	2.2%	0.1%
4	12%	7%	66%	15%	100%	4.2%	0.2%
6	10%	7%	69%	14%	100%	6.8%	0.1%
8	10%	6%	70%	14%	100%	7.3%	0.0%
12	10%	6%	66%	17%	100%	7.8%	0.3%
19	11%	7%	66%	16%	100%	7.9%	0.0%
26	11%	7%	69%	13%	100%	8.5%	0.1%
161	11%	7%	67%	16%	100%	10.0%	0.2%
Geobacter biotic group							
0	9%	6%	70%	16%	100%	0.8%	0.1%
2	15%	0%	69%	16%	100%	0.7%	0.0%
126	7%	23%	55%	14%	100%	2.4%	0.3%
157	6%	16%	60%	17%	100%	4.0%	1.1%
162	4%	15%	66%	15%	100%	6.4%	0.6%
177	4%	17%	62%	16%	100%	7.4%	0.2%
240	4%	17%	61%	18%	100%	8.4%	0.2%
Chemical reduction							
CR-1	13%	3%	59%	24%	100%	2.8%	0.1%
CR-2	9%	5%	64%	22%	100%	5.4%	0.3%
CR-3	5%	4%	62%	29%	100%	8.0%	0.4%
CR-4	5%	3%	63%	28%	100%	8.4%	0.4%
CR-5	3%	5%	69%	22%	100%	9.8%	0.5%
CR-6	4%	1%	54%	41%	100%	24.3%	1.2%

[b]1SD is one standard deviation based on either duplicate reactors (microbial reduction experiments) or propagated errors (chemical reduction experiments).

Table A.4. Iron isotope compositions and fractionations for aqueous phase and three extractions in all reduction experiments and exchange experiments[a].

	Aqueous		$CaCl_2$ ext		NaH_2PO_4 ext		0.5 M HCl ext		Struc Fe(III)		$\Delta^{56}Fe_{struc\ Fe(II)\text{-}struc\ Fe(III)}$		$\Delta^{56}Fe_{aq\ Fe(II)\text{-}struc\ Fe(II)}$		$\Delta^{56}Fe_{aq\ Fe(II)\text{-}struc\ Fe(III)}$		$\Delta^{56}Fe_{basal\ Fe(II)\text{-}aq\ Fe(II)}$		$\Delta^{56}Fe_{all\ Fe(II)\text{-}struc\ Fe(III)}$	
Days/ID	‰		‰		‰		‰		‰		‰		‰		‰		‰		‰	
	$\delta^{56}Fe$	1SD	$\delta^{56}Fe$	1SD	$\delta^{56}Fe$	1SD	$\delta^{56}Fe$	1SD	$\delta^{56}Fe$	1SD		1SD		1SD		1SD		1SD		1SD
Shewanella biotic group																				
0	0.15	0.06	0.01	0.01	-0.04	0.14	0.79	0.01	0.82	0.01	-0.85	0.15	0.19	0.08	-0.66	0.06	-0.15	0.07	-0.84	0.15
2	-0.19	0.05	-0.69	0.09	0.34	0.09	0.93	0.04	0.98	0.04	-0.63	0.13	-0.53	0.04	-1.17	0.07	-0.50	0.04	-0.75	0.13
4	0.20	0.04	0.08	0.01	0.53	0.01	0.85	0.03	0.93	0.05	-0.39	0.04	-0.34	0.03	-0.73	0.06	-0.11	0.03	-0.46	0.03
6	0.41	0.01	0.25	0.01	0.53	0.01	0.78	0.03	0.87	0.05	-0.34	0.06	-0.12	0.02	-0.46	0.05	-0.16	0.03	-0.38	0.06
8	0.54	0.03	0.43	0.01	0.49	0.01	0.73	0.00	0.83	0.01	-0.33	0.02	0.04	0.01	-0.29	0.03	-0.11	0.04	-0.33	0.02
12	0.61	0.02	0.51	0.01	0.44	0.00	0.69	0.07	0.80	0.09	-0.36	0.09	0.16	0.02	-0.19	0.10	-0.10	0.02	-0.34	0.09
19	0.65	0.03	0.57	0.01	0.44	0.00	0.68	0.03	0.81	0.05	-0.36	0.05	0.21	0.03	-0.15	0.06	-0.09	0.02	-0.33	0.05
26	0.69	0.03	0.60	0.00	0.48	0.00	0.71	0.01	0.81	0.02	-0.33	0.02	0.21	0.03	-0.12	0.04	-0.09	0.03	-0.30	0.02
161	0.78	0.03	0.73	0.02	0.40	0.03	0.60	0.01	0.73	0.02	-0.32	0.05	0.38	0.07	0.06	0.04	-0.08	0.02	-0.29	0.01
Shewanella control group																				
0	0.57	0.01	0.16	0.01	0.68	0.00	0.72	0.01	NA	NA	NA	NA	NA	NA	NA	NA	NA	NA	NA	NA
2	0.71	0.01	0.18	0.01	0.71	0.01	0.72	0.02	NA	NA	NA	NA	NA	NA	NA	NA	NA	NA	NA	NA
4	0.59	0.01	NA	NA	0.71	0.04	0.75	0.01	NA	NA	NA	NA	NA	NA	NA	NA	NA	NA	NA	NA
6	0.51	0.02	NA	NA	0.64	0.03	0.74	0.01	NA	NA	NA	NA	NA	NA	NA	NA	NA	NA	NA	NA
8	0.59	0.01	0.12	0.01	0.73	0.01	0.74	0.01	NA	NA	NA	NA	NA	NA	NA	NA	NA	NA	NA	NA
12	0.57	0.00	0.40	0.01	0.51	0.00	0.72	0.04	NA	NA	NA	NA	NA	NA	NA	NA	NA	NA	NA	NA
19	0.54	0.01	0.33	0.01	0.10	0.01	0.73	0.01	NA	NA	NA	NA	NA	NA	NA	NA	NA	NA	NA	NA
26	NA	NA	-0.11	0.03	0.17	0.00	0.83	0.03	NA	NA	NA	NA	NA	NA	NA	NA	NA	NA	NA	NA
161	NA	NA	NA	NA	0.46	0.02	0.87	0.01	NA	NA	NA	NA	NA	NA	NA	NA	NA	NA	NA	NA
Geobacter biotic group																				
0	NA	NA	0.16	0.02	0.58	0.01	0.76	0.02	0.77	0.14	-0.19	0.14	NA	NA	NA	NA	NA	NA	NA	NA
126	0.14	0.05	-0.44	0.02	0.38	0.02	0.97	0.03	1.01	0.12	-0.63	0.13	-0.23	0.05	-0.87	0.13	-0.59	0.05	-0.70	0.13
157	0.17	0.01	0.08	0.02	0.43	0.02	0.72	0.00	0.77	0.06	-0.34	0.06	-0.26	0.01	-0.60	0.06	-0.09	0.02	-0.38	0.16
162	0.31	0.03	0.38	0.02	0.48	0.02	0.77	0.03	0.85	0.08	-0.37	0.08	-0.17	0.04	-0.54	0.08	0.07	0.04	-0.39	0.10

177	0.38	0.00	0.56	0.01	0.35	0.05	0.86	0.00	1.02	0.10	-0.67	0.12	0.02	0.05	-0.64	0.10	0.19	0.01	-0.64	0.11
240	0.50	0.03	0.50	0.00	0.45	0.00	0.64	0.01	0.80	0.21	-0.35	0.21	0.05	0.03	-0.30	0.21	0.00	0.03	-0.34	0.24
Geobacter control group																				
0	NA	NA	NA	NA	NA	NA	NA	NA	NA	NA	NA	NA	NA	NA	NA	NA	NA	NA	NA	NA
126	NA	NA	0.21	0.05	0.50	0.02	0.73	0.02	NA	NA	NA	NA	NA	NA	NA	NA	NA	NA	NA	NA
157	NA	NA	0.14	0.02	0.31	0.02	0.71	0.02	NA	NA	NA	NA	NA	NA	NA	NA	NA	NA	NA	NA
162	NA	NA	0.19	0.01	0.58	0.05	NA	NA	NA	NA	NA	NA	NA	NA	NA	NA	NA	NA	NA	NA
177	NA	NA	NA	NA	0.38	0.02	0.70	0.00	NA	NA	NA	NA	NA	NA	NA	NA	NA	NA	NA	NA
Chemical reduction																				
CR-1	0.30	0.02	-0.27	0.02	0.08	0.01	0.95	0.02	1.11	0.03	-1.03	0.03	0.22	0.02	-0.81	0.03	-0.57	0.03	-1.01	0.03
CR-2	0.43	0.02	-0.03	0.01	0.61	0.01	0.82	0.01	0.91	0.02	-0.30	0.03	-0.18	0.02	-0.48	0.03	-0.46	0.02	-0.35	0.03
CR-3	0.67	0.04	NA	NA	0.50	0.05	0.73	0.01	0.88	0.04	-0.38	0.06	0.17	0.06	-0.21	0.06	-0.67	0.04	-0.39	0.05
CR-4	0.66	0.03	0.63	0.02	0.50	0.03	0.64	0.01	0.74	0.04	-0.25	0.04	0.16	0.04	-0.09	0.04	-0.03	0.03	-0.23	0.04
CR-5	0.76	0.00	0.71	0.00	0.48	0.00	0.61	0.00	0.70	0.01	-0.23	0.01	0.29	0.00	0.06	0.01	-0.06	0.00	-0.20	0.02
CR-6	1.18	0.00	0.96	0.07	0.36	0.01	0.37	0.06	0.40	0.20	-0.04	0.20	0.82	0.01	0.78	0.20	-0.22	0.07	0.00	0.22
Exchange experiments																				
30	-0.64	0.00	-0.75	0.01	-0.23	0.12	0.87	0.07	NA	NA	-1.09	0.14	-0.42	0.12	-1.51	0.07	-0.11	0.01	NA	NA
57	-0.65	0.00	-0.74	0.01	0.06	0.05	0.81	0.05	NA	NA	-0.76	0.07	-0.71	0.05	-1.47	0.05	-0.09	0.01	NA	NA

[a]Iron isotope compositions were measured directly for aqueous, $CaCl_2$ extract (basal-sorbed), NaH_2PO_4 extract [edge plus struc Fe(II)], and 0.5 M HCl extract [interior Fe(II) plus struc Fe(III)]. And the Fe isotope composition for structural Fe(III) was calculated according to the method in supplementary text. In control group, NaH_2PO_4 and 0.5 M HCl extract contains a very small amount of Fe(II). The δ^{56}Fe values for the original Fe in the purified NAu-1 and starting Fe(II) are 0.59‰ and −0.49‰, respectively.

[b]For δ^{56}Fe values, 1SD is one standard deviation based on two duplicate reactors for microbial reduction and exchange experiments or one standard deviation based on repeated analyses or one standard error for in-run statistics (40 1-second on peak integrations) for chemical reduction experiments. For fractionation factors, 1SD is based on propagated errors.

Table A.5. Iron isotope compositions of partially dissolved NAu-1 by HCl[a]

Sample	Time (h)	% dissolution	Accumulated % dissolution	^{56}Fe ‰	1SD ‰
Aliquot 1	5	1.5	1.5	0.74	0.01
Aliquot 2	24	1.2	3.7	0.64	0.01
Aliquot 3	29	1.8	5.5	0.70	0.00
Aliquot 4	53	2.5	8.0	0.67	0.02
Aliquot 5	57	0.5	8.5	0.73	0.00
Aliquot 6	101	2.9	11.4	0.64	0.08
Aliquot 7	125	1.4	12.8	0.58	0.00
Aliquot 8	199	4.9	17.7	0.58	0.01
Aliquot 9	295	3.4	21.1	0.56	0.01
Aliquot 10	365	3.4	24.5	0.53	0.02
Aliquot 11	438	3.3	27.8	0.52	0.00
Aliquot 12	576	5.3	33.1	0.54	0.00

[a] Partial dissolution experiment was performed by reacting 50 mg purified NAu-1 with 5 mL 0.5 M HCl for 5 hrs and then suspension was centrifuged and supernatant filtered through 0.2 μm filter to acquire aliquot 1. Another 5 mL 0.5 M HCl was added to the remaining solid and reacted for another 19 hrs. The suspension was centrifuged and supernatant filtered to acquire aliquot 2. The procedure was repeated until reaching a total of 33% dissolution after 576 hrs since starting of the experiment.

[b] 1SD is one standard deviation based on repeated isotopic analysis of a single aliquot or standard error for one analysis (in-run statistics, 40 1-second on peak integrations).

Table A.6. Relative elemental weight %, atomic % and elemental ratios of the purified NAu-1, inoculated NAu-1 and chemically reduced NAu-1 as measured by EDS.

	Starting Material		Biotic		Chemical	
Element	**Weight %**	**Atomic %**	**Weight %**	**Atomic %**	**Weight %**	**Atomic %**
C	6.33	6.18	35.55	46.66	NA	NA
O	83.68	61.32	40.02	39.43	49.74	67.61
Na	5.34	2.72	12.53	8.59	4.65	4.40
Al	5.06	2.20	0.88	0.51	3.27	2.64
Si	23.26	9.71	4.80	2.69	19.31	14.95
S	NA	NA	1.69	0.83	4.95	3.36
Fe	21.13	4.44	4.54	1.28	18.08	7.04
Ratios						
Fe:Si		0.46		0.48		0.47
Al:Si		0.23		0.19		0.18

Table A.7. Mass balance calculation for residual Fe in all reduction experiments.

Days/ID	% of total extractable Fe					Total extractable Fe		Residual Fe[a]	
						‰		‰	
	Aq	$CaCl_2$ ext	NaH_2PO_4 ext	0.5 M HCl ext	sum	$\delta^{56}Fe$	1SD	$\delta^{56}Fe$	1SD
Shewanella biotic group									
0	1%	0%	9%	89%	100%	0.71	0.01	0.58	0
2	5%	2%	25%	67%	100%	0.68	0.01	0.58	0
4	7%	4%	39%	49%	100%	0.65	0.02	0.58	0
6	7%	6%	50%	37%	100%	0.6	0	0.59	0
8	8%	5%	52%	36%	100%	0.58	0	0.59	0
12	8%	5%	48%	39%	100%	0.56	0.03	0.59	0
19	9%	5%	50%	35%	100%	0.55	0.01	0.59	0
26	9%	5%	53%	33%	100%	0.58	0	0.59	0
161	9%	5%	54%	32%	100%	0.49	0.01	0.6	0
Shewanella control group									
0	1%	0%	5%	93%	100%	0.72	0.01	0.58	0.02
2	1%	0%	7%	92%	100%	0.72	0.02	0.58	0.02
4	1%	1%	7%	91%	100%	0.74	0.01	0.58	0.02
6	2%	1%	8%	89%	100%	0.72	0.01	0.58	0.02
8	3%	0%	8%	90%	100%	0.73	0.02	0.58	0.02
12	5%	1%	7%	87%	100%	0.7	0.04	0.58	0.02
19	11%	1%	10%	79%	100%	0.64	0.01	0.59	0.02
26	0%	0%	6%	93%	100%	0.78	0.03	0.58	0.02
161	10%	4%	12%	74%	100%	0.7	0.01	0.58	0.02
Geobacter biotic group									
0	4%	5%	12%	79%	100%	0.68	0.1	0.58	0.02

126	3%	7%	18%	72%	100%	0.73	0.08	0.58	0.02
157	4%	8%	32%	56%	100%	0.55	0.06	0.59	0.02
162	3%	10%	44%	43%	100%	0.59	0.03	0.59	0.02
177	3%	11%	41%	44%	100%	0.6	0.03	0.59	0.02
240	4%	14%	50%	32%	100%	0.52	0.02	0.6	0.02
Geobacter control group									
0	3%	1%	13%	82%	100%	NA	NA	NA	NA
126	3%	1%	8%	89%	100%	0.68	0.02	0.58	0.02
157	3%	1%	6%	90%	100%	0.66	0.02	0.59	0.02
162	3%	1%	10%	86%	100%	NA	NA	NA	NA
177	3%	1%	5%	90%	100%	0.66	0.04	0.59	0.02
Chemical reduction									
CR-1	6%	1%	27%	66%	100%	0.66	0.01	0.58	0.02
CR-2	6%	3%	42%	50%	100%	0.69	0.01	0.58	0.02
CR-3	3%	3%	43%	51%	100%	0.61	0.02	0.59	0.02
CR-4	3%	2%	45%	49%	100%	0.58	0.01	0.59	0.02
CR-5	2%	4%	54%	39%	100%	0.54	0	0.6	0.02
CR-6	3%	1%	47%	49%	100%	0.39	0.03	0.64	0.03

[a]See supplementary text for calculation of δ^{56}Fe for residual Fe.

[b]1SD is one standard deviation based on either duplicate reactors (microbial reduction experiments) or propagated errors (chemical reduction experiments).

Appendix B

Supporting Information: Chapter 3

Bioavailable Fe in nontronite NAu-1 decreases during consecutive Fe redox cycles

B.1 Materials and methods

B.1.1 Redox cycle experiments

Table B.1. Volumes of MM or HEPES buffer added to each reactor at the beginning of each RP or OP

Redox period	Matrix[a]	B1E (mL)	B1L (mL)	B2E (mL)	B2L (mL)	Control (mL)
RP1	MM	120	120	120	120	100
OP1	HEPES	56	120	Broken during centrifugation after the RP1	120	84
RP2	MM	40	120		104	68
OP2	HEPES	8	88		56	52
RP3	MM	8	72		40	36
OP3	HEPES	8	8		0	12

[a]MM = minimal medium. The concentration of HEPES buffer was 10 mM (pH 6.8).

B.1.2 Iron isotope

Table B.2. Test solutions preparation and their Fe isotope values

Test solution ID	HPS Fe (μg)	Matrix		Fe isotope value	
		Content[a]	Amount (g)	δ^{56}Fe (‰)	1SD (‰)
T25	10	MM	1.0	0.09	0.05
T26	51	MM	2.0	0.10	0.01
T27	11	$CaCl_2$	1.1	-0.05	0.00
T28	51	$CaCl_2$	2.0	0.14	0.03
T29	10	NaH_2PO_4	2.1	-0.06	0.00
T30	48	NaH_2PO_4	1.0	0.09	0.00
T31	10	HCl	1.0	-0.04	0.00
T32	51	HCl	0.2	0.08	0.02
T33	11	MM	2.0	0.11	0.01
T34	10	$CaCl_2$	2.1	0.18	0.02
T35	51	HCl	1.0	0.08	0.00
T36	10	NaH_2PO_4	1.1	0.03	0.00

[a]MM = minimal medium.

B.2 Results

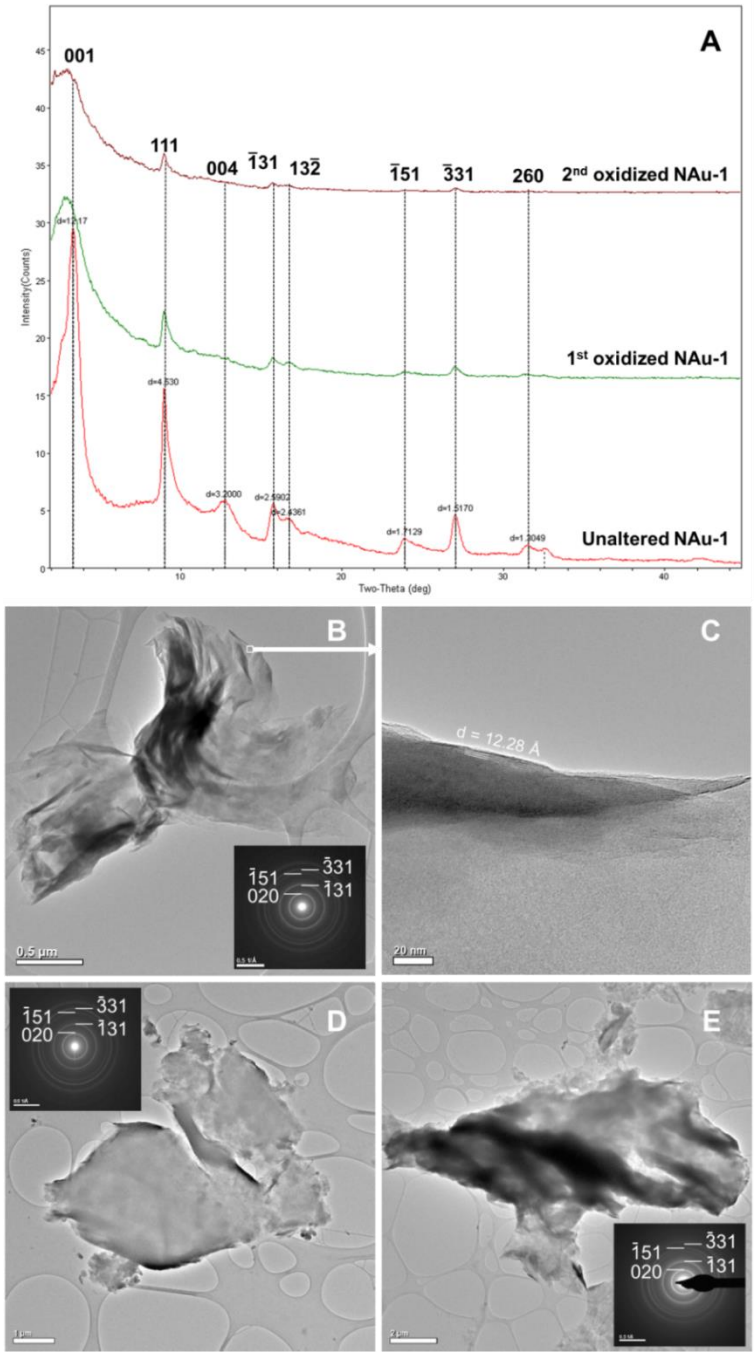

Figure B.1. A) XRD patterns of unaltered, 1st oxidized NAu-1, and 2nd oxidized NAu-1. Crystalline domain sizes were analyzed based on a pseudo-Voigt method by fitting the [111] and [060] (d-spacing =

1.517 Å) peaks positions and full width at half maximum (FWHM) using the JADE® 9.0 software package. Results indicate a 70% increase in domain size between unaltered NAu-1 and the 2nd oxidized NAu-1. B) TEM image of unaltered NAu-1. C) Magnified TEM image of the denoted area in B). TEM images of D) 1st oxidized NAu-1, and E) 2nd oxidized NAu-1. The corresponding SAED patterns are inserted.

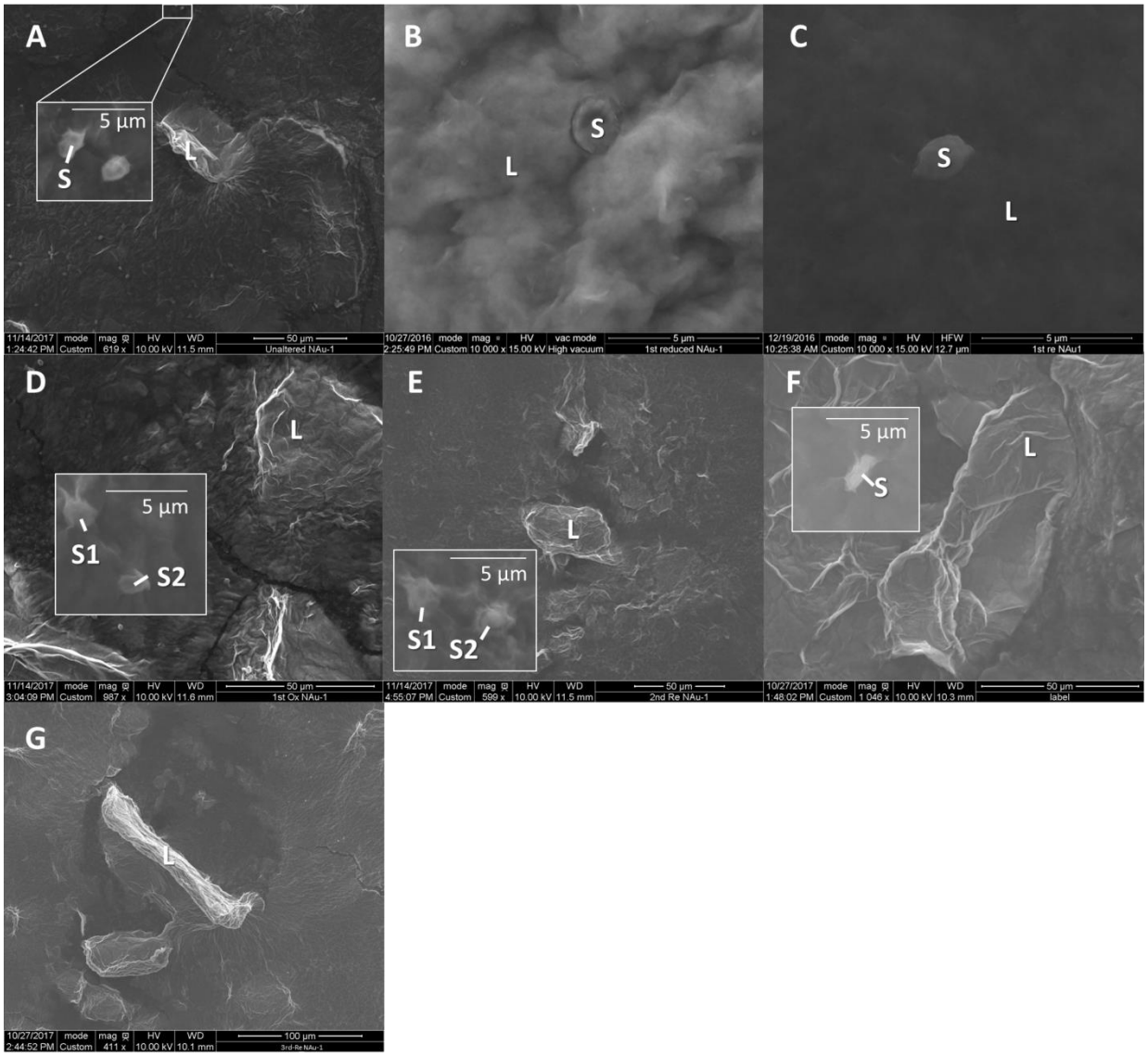

Figure B.2. SEM images of A) unaltered NAu-1, B) 1st reduced NAu-1 for 6 days, C) 1st reduced NAu-1 for 59 days, D) 1st oxidized NAu-1, E) 2nd reduced NAu-1, F) 2nd oxidized NAu-1, and G) 3rd reduced NAu-1. EDS spectra were taken at locations as denoted by "L", "S", "S1", and "S2". "L" denotes large particle and "S", "S1", "S2" denote small particles. The elemental compositions of corresponding locations during certain RP or OP are shown in Table B.6.

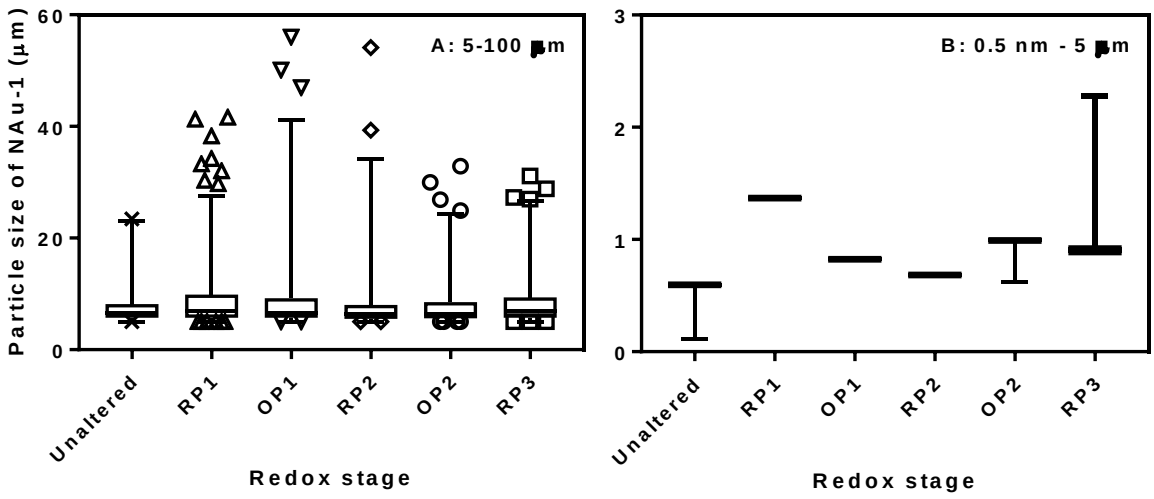

Figure B.3. Particle sizes of NAu-1 A) 5-100 µm and B) 0.5 nm - 5 µm that was unaltered or underwent three redox cycles. The low and high ends of the whiskers indicate A) the 1st and 99th percentiles of particle number and B) the 10th and 90th percentiles of sample volume. Scattered dots are outliers.

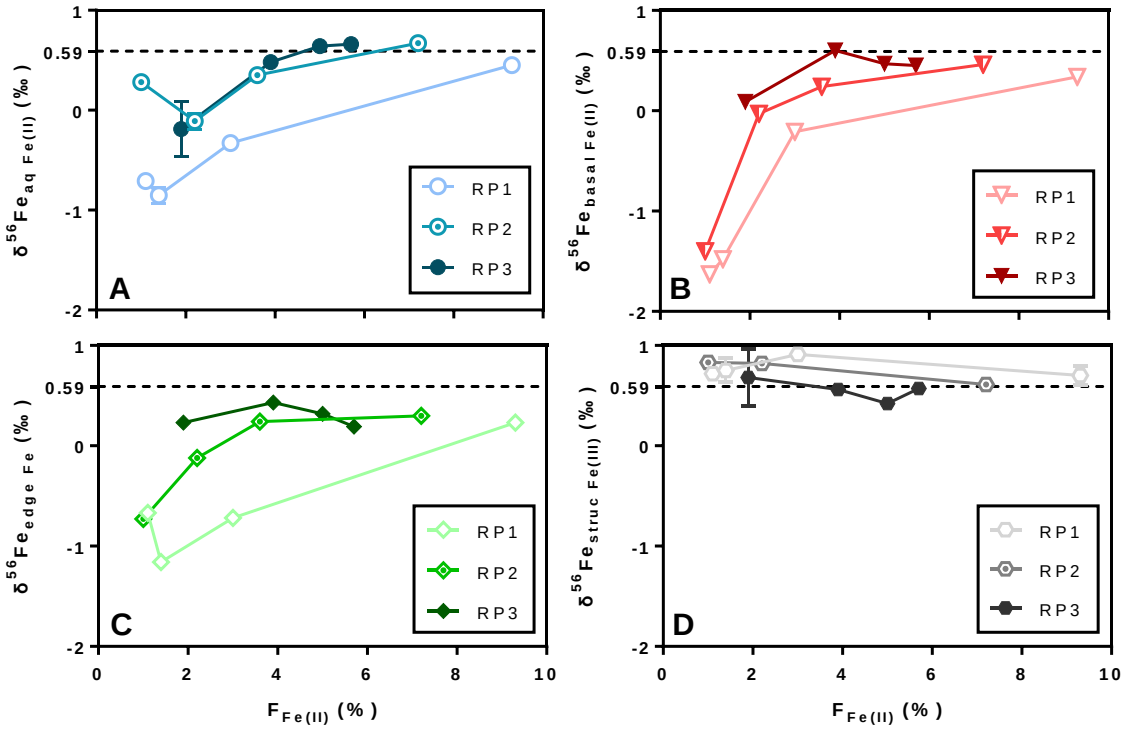

Figure B.4. Iron isotope compositions of A) aqueous Fe(II), B) basal-sorbed Fe(II), C) edge-bound Fe and D) structural Fe(III) vs. microbial Fe(III) reduction extent [$F_{Fe(II)}$]. The isotope value of structural Fe(III) is calculated according to Eq. (3.8). The dashed lines indicate that Fe isotope composition of the bulk NAu-1 is $\delta^{56}Fe_{bulk\ NAu\text{-}1}$ = 0.59‰. Error bars indicate ranges of duplicate measurement or observed in duplicate bioreactors.

Table B.3. Concentrations of Fe(II) and total Fe in the aqueous phase and the three extracts, fraction of total Fe(II) and rate of reaction from bioreactors and control during three redox cycles[a, b, c]

Redox period	Days	Aqueous (μM)				$CaCl_2$ ext (μM)				NaH_2PO_4 ext (μM)				HCl ext (μM)				Total Fe(II) (μM)		Total Fe (μM)		Fraction of total Fe(II) (%)		Rate of reaction (% day^{-1})	
		Fe(II)	1SD	Fe(tot)	1SD	Fe(II)	1SD	Fe(tot)	1SD	Fe(II)	1SD	Fe(tot)	1SD	Fe(II)	1SD	Fe(tot)	1SD	Mean	1SD	Mean	1SD	Mean	1SD	Mean	1SD
RP1 - bio	0	4.8	0.3	18.6	0.0	17.0	1.4	15.5	0.8	19.4	0.5	57.7	0.9	54.6	1.4	2289	6.9	95.9	2.0	2381	7.0	0.5	0.0	NA	NA
	1	45.6	3.0	70.5	1.2	46.8	0.9	42.5	0.8	59.0	1.6	96.1	1.6	79.4	1.1	2336	191.9	230.8	3.7	2545	191.9	1.1	0.0	1.1	0.0
	2	57.7	0.8	87.2	4.7	43.6	1.4	53.4	2.6	71.5	1.1	112.9	1.7	88.3	0.9	2232	68.3	261.1	2.1	2486	68.5	1.3	0.0	0.6	0.0
	3	71.1	3.1	93.2	1.9	56.7	1.3	76.3	18.9	86.2	3.9	125.7	3.8	84.5	3.6	2005	23.9	298.6	6.3	2300	30.7	1.4	0.0	0.5	0.0
	4	101.1	9.0	112.1	4.1	63.4	1.6	61.6	0.2	124.3	9.2	163.3	8.9	103.7	0.1	2056	65.1	392.5	12.9	2393	65.8	1.9	0.1	0.5	0.1
	6	168.8	15.7	179.9	15.3	99.7	8.1	99.2	10.2	330.0	59.8	366.4	51.9	130.8	12.7	1824	49.3	729.4	63.6	2469	73.9	3.5	0.3	0.6	0.3
	8	234.3	24.4	228.3	24.9	126.2	14.4	125.2	15.1	527.1	97.9	572.6	91.3	181.7	31.8	1836	136.8	1069	106.8	2762	167.0	5.2	0.5	0.6	0.5
	20	372.5	15.5	369.9	11.8	189.2	6.6	190.9	8.5	1121	63.4	1146	68.0	336.2	13.5	1790	41.5	2019	67.0	3496	81.0	9.7	0.3	0.5	0.3
OP1 - bio	21	0.0	0.9	0.0	0.7	100.4	7.6	100.9	7.5	106.2	8.7	198.1	24.5	63.0	7.4	1323	127.5	269.6	13.8	1622	130.0	1.3	0.1	168.6	0.1
	24	6.1	0.7	7.7	1.4	0.0	0.7	0.0	0.7	26.0	1.3	142.7	10.8	37.5	4.5	1380	70.8	69.6	4.8	1531	71.6	0.3	0.0	0.3	0.0
RP2 - bio	25	0.0	0.0	7.7	3.0	0.0	0.0	0.0	1.5	14.6	1.6	53.5	1.8	61.6	0.0	1341	6.9	76.2	1.6	1402	7.9	0.4	0.0	NA	NA
	26	0.0	2.2	23.7	0.0	13.6	2.1	17.1	1.1	75.2	0.0	130.2	0.0	112.0	2.4	1454	40.9	200.9	3.8	1625	41.0	1.0	0.0	1.0	0.0
	27	49.9	0.0	78.2	0.0	37.1	0.9	38.3	2.2	145.6	1.1	190.5	0.0	118.8	0.0	1297	15.5	351.4	1.4	1604	15.7	1.7	0.0	0.8	0.0
	28	95.9	0.0	102.1	0.0	53.9	0.0	68.2	0.5	178.7	1.8	218.5	3.4	131.5	3.4	1256	0.0	460.1	3.9	1645	3.5	2.2	0.0	0.7	0.0
	29	122.5	11.1	123.5	10.0	60.3	2.8	63.0	4.4	249.6	12.0	288.3	1.8	154.7	21.0	1208	16.1	587.1	26.7	1683	19.5	2.8	0.1	0.7	0.1
	31	178.2	17.2	169.9	14.8	72.9	5.3	72.3	5.6	404.3	68.9	418.6	59.4	210.1	22.2	1088	1.5	865.6	74.6	1748	61.5	4.2	0.4	0.7	0.4
	33	182.9	0.0	187.2	2.4	68.8	1.3	73.4	0.0	503.6	0.0	543.2	8.2	227.9	0.3	1131	0.0	983.2	1.3	1935	8.5	4.7	0.0	0.6	0.0
	45	236.4	6.8	230.7	6.0	91.6	0.8	87.4	2.0	880.9	46.1	864.4	54.1	322.3	9.3	1253	3.1	1531.2	47.5	2436	54.6	7.4	0.2	0.4	0.2
OP2 - bio	46	1.7	1.2	0.0	0.0	74.2	9.0	72.6	9.7	95.5	1.0	147.0	4.0	70.9	2.6	811.2	29.5	242.3	9.5	1031	31.3	1.2	0.0	124.2	0.0
	49	0.0	0.0	5.4	3.0	0.0	0.2	0.0	0.4	20.5	0.2	103.4	1.0	66.7	3.8	1172	23.8	87.2	3.8	1281	24.0	0.4	0.0	0.2	0.0
RP3 - bio	50	9.1	1.7	6.7	0.0	0.0	0.0	0.0	1.8	10.5	1.4	48.3	0.0	72.4	1.5	943.4	0.0	92.0	2.7	998.4	1.8	0.4	0.0	NA	NA
	51	0.0	0.0	9.3	1.6	0.0	0.8	0.0	1.2	20.5	8.0	67.0	6.2	80.7	11.8	1046	1.3	101.1	14.2	1122	6.7	0.5	0.1	0.5	0.1
	53	16.7	6.8	5.3	6.2	0.4	4.2	11.0	4.6	92.9	6.4	128.9	7.4	126.8	10.1	989.8	33.6	236.9	14.4	1135	35.3	1.1	0.1	0.4	0.1

	54	47.6	7.4	52.8	9.4	27.7	1.0	35.0	4.3	180.0	7.3	222.3	18.7	135.2	10.6	810.4	14.1	390.5	14.9	1121	25.6	1.9	0.1	0.5	0.1
	55	73.1	5.0	84.7	3.6	34.7	0.8	35.2	2.3	256.1	21.5	259.2	16.4	174.0	0.6	810.0	13.0	538.0	22.1	1189	21.4	2.6	0.1	0.5	0.1
	56	86.8	2.2	85.4	0.0	40.4	0.6	39.5	1.4	487.2	9.6	477.3	4.2	201.9	6.6	828.3	12.9	816.1	11.9	1431	13.7	3.9	0.1	0.7	0.1
	58	114.4	0.0	118.9	1.9	34.7	2.4	36.0	2.6	530.7	3.7	539.3	1.2	232.0	2.0	892.1	12.1	911.9	4.8	1586	12.6	4.4	0.0	0.5	0.0
	69	93.1	0.0	89.6	0.0	40.7	0.0	44.4	1.4	693.2	9.0	708.0	20.2	218.2	3.7	853.7	7.8	1045	9.7	1696	21.7	5.0	0.0	0.3	0.0
	105	116.2	2.2	119.0	2.4	35.8	0.0	38.0	0.0	745.9	7.7	747.3	15.2	276.5	1.6	925.8	11.1	1174	8.2	1830	19.0	5.7	0.0	0.1	0.0
OP3 - bio	106	0.5	2.2	2.3	0.0	0.0	0.0	0.0	0.0	133.0	4.2	192.9	18.6	143.2	5.2	834.3	11.1	276.8	7.0	1029	21.7	1.3	0.0	86.5	0.0
RP1 - control	0	0.0	2.3	0.0	2.9	0.0	1.7	0.0	0.0	2.5	1.5	53.2	2.8	12.6	1.8	1055.2	75.7	15.1	3.7	1108.4	75.8	0.1	0.0	NA	NA
	20	0.2	0.0	0.0	3.2	0.0	2.4	0.0	0.0	5.3	1.8	71.3	1.2	11.3	0.0	1357.5	61.0	16.7	3.0	1428.8	61.1	0.1	0.0	0.0	0.0
OP1 - control	21	0.0	0.0	0.0	0.0	0.0	2.8	0.0	1.7	3.6	1.7	50.4	1.6	8.4	0.9	462.2	15.1	11.9	3.4	512.6	15.3	0.1	0.0	0.5	0.0
	24	7.7	1.9	3.7	0.0	0.0	1.2	0.0	2.1	6.3	1.5	63.8	2.8	8.6	1.0	302.5	27.3	22.6	2.9	370.0	27.5	0.1	0.0	0.0	0.0
RP2 - control	25	0.0	3.8	6.7	2.4	0.0	0.0	0.0	1.3	4.7	1.1	41.7	2.0	10.5	1.8	335.9	14.5	15.2	4.3	384.2	14.8	0.1	0.0	NA	NA
	45	6.1	0.0	6.7	0.0	0.0	0.9	0.0	0.0	119.5	7.6	159.2	2.5	43.9	1.2	647.7	0.0	169.4	7.7	813.6	2.5	0.8	0.0	0.0	0.0
OP2 - control	46	1.8	2.3	0.7	2.3	15.6	1.2	14.3	1.7	27.2	0.0	97.9	0.0	18.0	0.0	477.8	0.0	62.7	2.6	590.7	2.8	0.3	0.0	10.3	0.0
	49	0.0	0.0	13.4	2.2	0.0	0.0	0.0	1.6	15.7	1.5	93.8	0.0	19.3	1.1	597.4	0.0	34.9	1.9	704.5	2.8	0.2	0.0	0.1	0.0
RP3 - control	50	3.0	0.0	9.5	0.0	0.0	0.0	0.0	0.0	8.5	1.9	37.3	0.0	23.4	2.8	459.0	24.4	34.8	3.4	505.9	24.4	0.2	0.0	NA	NA
	69	29.4	0.0	23.7	0.0	4.8	1.0	4.6	1.1	223.1	3.9	227.3	6.9	86.1	2.7	465.5	10.3	343.3	4.8	721.1	12.5	1.7	0.0	0.1	0.0
	105	72.3	0.0	71.6	3.8	13.8	1.1	17.6	5.5	417.5	0.8	419.2	2.9	125.4	2.2	510.8	0.0	629.2	2.6	1019.2	7.3	3.0	0.0	0.1	0.0
OP3 - control	106	0.0	0.0	12.7	14.3	0.0	0.0	0.9	1.9	81.5	2.2	97.0	3.3	61.9	0.0	344.4	11.7	143.5	2.2	455.0	18.9	0.7	0.0	46.8	0.0

[a]1SD represents ranges observed in duplicate bioreactors.

[b]NA indicates data not applicable.

[c]"- bio" and "- control" in the redox stage column indicate data from bioreactors and control reactor, respectively.

Table B.4. Proportions of Fe(II) in the aqueous phase and the three extracts out of total Fe(II) from bioreactors during three redox cycles [a, b]

Redox period	Days	Fraction of total Fe(II) (%)		Aqueous (%)		$CaCl_2$ ext (%)		NaH_2PO_4 ext (%)		HCl ext (%)	
		Mean	1SD	Fe(II)	1SD	Fe(II)	1SD	Fe(II)	1SD	Fe(II)	1SD
RP1	0	0.5	0.0	5.0	0.1	17.8	0.1	20.3	0.0	57.0	0.0
	1	1.1	0.0	19.8	0.1	20.3	0.0	25.6	0.0	34.4	0.0
	2	1.3	0.0	22.1	0.0	16.7	0.0	27.4	0.0	33.8	0.0
	3	1.4	0.0	23.8	0.0	19.0	0.0	28.9	0.1	28.3	0.0
	4	1.9	0.1	25.8	0.1	16.1	0.0	31.7	0.1	26.4	0.0
	6	3.5	0.3	23.1	0.1	13.7	0.1	45.2	0.2	17.9	0.1
	8	5.2	0.5	21.9	0.1	11.8	0.2	49.3	0.2	17.0	0.2
	20	9.7	0.3	18.4	0.1	9.4	0.0	55.5	0.1	16.6	0.1
OP1	21	1.3	0.1	0.0	NA	37.2	0.1	39.4	0.1	23.4	0.1
	24	0.3	0.0	8.8	0.1	0.0	NA	37.3	0.1	53.9	0.1
RP2	25	0.4	0.0	0.0	NA	0.0	NA	19.2	0.1	80.8	0.0
	26	1.0	0.0	0.0	NA	6.8	0.2	37.5	0.0	55.8	0.0
	27	1.7	0.0	14.2	0.0	10.5	0.0	41.4	0.0	33.8	0.0
	28	2.2	0.0	20.9	0.0	11.7	0.0	38.8	0.0	28.6	0.0
	29	2.8	0.1	20.9	0.1	10.3	0.1	42.5	0.1	26.4	0.1
	31	4.2	0.4	20.6	0.1	8.4	0.1	46.7	0.2	24.3	0.1
	33	4.7	0.0	18.6	0.0	7.0	0.0	51.2	0.0	23.2	0.0
	45	7.4	0.2	15.4	0.0	6.0	0.0	57.5	0.1	21.0	0.0
OP2	46	1.2	0.0	0.7	0.7	30.6	0.1	39.4	0.0	29.3	0.1

	49	0.4	0.0	0.0	NA	0.0	NA	23.5	0.0	76.5	0.1
	50	0.4	0.0	9.9	0.2	0.0	NA	11.5	0.1	78.7	0.0
	51	0.5	0.1	0.0	NA	0.0	NA	20.2	0.4	79.8	0.2
	53	1.1	0.1	7.1	0.4	0.2	9.7	39.2	0.1	53.5	0.1
	54	1.9	0.1	12.2	0.2	7.1	0.1	46.1	0.1	34.6	0.1
RP3	55	2.6	0.1	13.6	0.1	6.4	0.0	47.6	0.1	32.3	0.0
	56	3.9	0.1	10.6	0.0	4.9	0.0	59.7	0.0	24.7	0.0
	58	4.4	0.0	12.6	0.0	3.8	0.1	58.2	0.0	25.4	0.0
	69	5.0	0.0	8.9	0.0	3.9	0.0	66.3	0.0	20.9	0.0
	105	5.7	0.0	9.9	0.0	3.0	0.0	63.5	0.0	23.5	0.0
OP3	106	1.3	0.0	0.2	4.7	0.0	NA	48.1	0.0	51.8	0.0

[a]1SD indicates ranges observed in duplicate bioreactors.

[b]NA indicates data not applicable.

Table B.5. Concentrations of Si, Al and Mg in selected aqueous phase and extracts from bioreactors during the redox cycles and control during the RP1 and OP1[a, b, c, d]

Redox period	Days	Phase	Si (µM)		Al (µM)		Mg (µM)	
			Conc.	1SD	Conc.	1SD	Conc.	1SD
RP1 - bio	0	Aqueous	47.5	1.1	2.4	0.2	24.4	24.7
		$CaCl_2$ ext	54.9	0.4	4.0	0.1	84.7	5.6
		NaH_2PO_4 ext	1507.6	10.6	146.8	1.4	42.2	11.3
		HCl ext	1048.6	3.9	1508.2	4.6	196.4	4.3
	6	Aqueous	306.3	23.4	2.8	0.6	34.3	88.8
		$CaCl_2$ ext	53.9	0.9	3.3	1.2	161.3	16.1
		NaH_2PO_4 ext	NA	NA	NA	NA	NA	NA
		HCl ext	NA	NA	NA	NA	NA	NA
	20	Aqueous	688.9	11.6	4.7	0.1	38.5	38.3
		$CaCl_2$ ext	92.4	2.2	2.8	0.1	82.3	12.8
		NaH_2PO_4 ext	1073.9	6.4	343.7	1.6	35.7	7.3
		HCl ext	1110.8	1.6	1659.4	5.3	118.4	4.4
OP1 - bio	21	Aqueous	11.7	0.8	0.0	0.2	2.4	46.4
		$CaCl_2$ ext	14.1	0.4	3.0	0.0	76.2	7.1
		NaH_2PO_4 ext	377.1	4.2	156.0	0.2	38.2	8.5
		HCl ext	1576.1	5.2	921.4	0.9	173.6	3.8
	24	Aqueous	199.3	1.5	44.3	0.2	NA	NA

		$CaCl_2$ ext	11.1	0.6	3.5	0.2	NA	NA
RP2 - bio	25	Aqueous	14.0	0.4	0.0	0.0	NA	NA
		$CaCl_2$ ext	11.8	0.5	1.8	0.1	NA	NA
	31	Aqueous	72.2	1.7	6.1	0.1	NA	NA
		$CaCl_2$ ext	14.3	0.7	3.0	0.4	NA	NA
	45	Aqueous	162.4	2.3	1.2	0.1	NA	NA
		$CaCl_2$ ext	23.0	0.6	2.1	0.1	NA	NA
OP2 - bio	46	Aqueous	7.1	0.7	0.0	0.1	NA	NA
		$CaCl_2$ ext	5.2	1.0	3.0	0.0	NA	NA
	49	Aqueous	30.2	0.7	4.8	0.1	NA	NA
		$CaCl_2$ ext	3.3	1.4	2.1	0.0	NA	NA
RP3 - bio	50	Aqueous	5.8	0.9	0.0	0.0	NA	NA
		$CaCl_2$ ext	4.8	1.3	1.6	0.1	NA	NA
	56	Aqueous	19.2	1.0	1.4	0.4	NA	NA
		$CaCl_2$ ext	NA	NA	NA	NA	NA	NA
	69	Aqueous	57.9	0.2	2.9	0.9	NA	NA
		$CaCl_2$ ext	NA	NA	NA	NA	NA	NA
	105	Aqueous	93.2	2.6	0.3	0.1	NA	NA
		$CaCl_2$ ext	NA	NA	NA	NA	NA	NA
OP3 - bio	106	Aqueous	3.2	0.8	0.0	0.0	NA	NA
		$CaCl_2$ ext	4.0	0.3	1.5	0.0	NA	NA

RP1 - control	0	Aqueous	20.6	0.8	0.0	0.1	11.6	20.9
		$CaCl_2$ ext	19.5	0.9	3.0	0.0	75.0	1.5
		NaH_2PO_4 ext	327.6	3.7	74.8	0.5	48.6	1.2
		HCl ext	1324.6	17.8	966.1	3.1	260.0	0.6
	20	Aqueous	91.7	0.9	0.0	0.2	NA	NA
		$CaCl_2$ ext	9.2	1.1	1.9	0.0	NA	NA
		NaH_2PO_4 ext	338.9	3.1	90.7	0.6	NA	NA
		HCl ext	1194.8	2.7	1392.3	1.9	NA	NA
OP1 - control	21	Aqueous	NA	NA	NA	NA	1.0	23.9
		$CaCl_2$ ext	NA	NA	NA	NA	82.9	2.1
		NaH_2PO_4 ext	NA	NA	NA	NA	42.2	2.9
		HCl ext	NA	NA	NA	NA	239.8	0.9

[a]1SD indicates ranges observed in duplicate bioreactors.

[b]NA indicates data not available or applicable.

[c]"- bio" and "- control" in the redox period column indicate data from bioreactors and control.

[d]Concentrations of Si and Al were analyzed by ICP-OES, and their method detection limits are 0.33 and 0.02 μM, respectively. Mg was measured by ICP-MS, and its detection limit is 0.01 μM.

Table B.6. Atomic compositions of selected detecting area in SEM images of Figure B.2[a, b]

Elements	Unaltered NAu-1		RP1 (6 days)		RP1 (59 days)		OP1			RP2			OP2		RP3
	L	S	L	S	L	S	L	S1	S2	L	S1	S2	L	S	L
C	24.5	74.6	18.5	36.7	61.8	57.8	9.7	65.5	73.1	29.4	61.0	56.5	13.6	70.4	45.6
O	62.2	24.4	60.2	49.4	34.4	36.6	67.6	33.0	26.4	48.9	31.4	27.6	64.9	28.7	47.5
Na (Mg^{C})	0.6	0.2	1.6	1.9	1.8	3.8	0.5	0.0	0.0	7.6	5.6	13.8	0.3^{C}	0.2^{C}	1.8
Al	1.6	0.1	2.2	1.4	0.3	0.2	2.7	0.2	0.0	1.6	0.3	0.3	2.4	0.1	0.7
Si	8.1	0.5	11.9	7.4	1.3	1.3	13.5	0.9	0.5	8.3	1.4	1.8	12.8	0.5	3.2
Fe	3.0	0.3	5.4	3.2	0.5	0.4	5.9	0.4	0.0	4.2	0.4	0.0	6.0	0.0	1.3
Fe:Si	0.4	0.6	0.5	0.4	0.4	0.3	0.4	0.5	0.0	0.5	0.3	0.0	0.5	0.0	0.4

[a]"L", "S", "S1", "S2" indicate the locations for EDS analysis as shown in Figure B.3.

[b]Element carbon (C) was from the carbon tapes, solution precipitation (e.g., HEPES, lactate, HCO_3^-), and bacteria; oxygen (O) was from clay, solution precipitation, and bacteria.

[c]Values in the third row of under OP2 column are the atomic composition of magnesium (Mg), while other values in the third row are for sodium (Na).

Table B.7. Particle sizes of unaltered NAu-1 and NAu-1 that underwent redox cycles[a]

	Unaltered	RP1	OP1	RP2	OP2	RP3
Particles 5-100 μm[a]						
Number of particles	116	873	373	276	424	477
Minimum	5.0	5.0	5.0	5.0	5.0	5.0
1% Percentile	5.0	5.0	5.1	5.0	5.0	5.0
25% Percentile	5.7	5.7	5.7	5.5	5.6	5.7
Median	6.6	6.9	6.6	6.4	6.4	7.0
75% Percentile	8.2	9.9	9.2	8.0	8.5	9.4
99% Percentile	23.1	27.5	41.1	34.2	24.2	26.7
Maximum	23.4	41.6	56.1	54.1	32.9	31.1
Mean	7.5	8.7	8.7	8.0	7.8	8.7
Std. Deviation	2.9	4.7	6.1	5.4	3.6	4.6
Std. Error of Mean	0.3	0.2	0.3	0.3	0.2	0.2
Particles 0.5 nm - 5μm[b]						
10% Percentile	112.8	1369.5	823.5	684.5	624.0	903.28
50% Percentile	595.8	1369.5	823.5	684.5	990.8	903.28
90% Percentile	595.8	1369.5	823.5	684.5	990.8	2277.4

[a]Values are obtained by FlowCam® VS series and are in the unit of μm. Percentiles are based on numbers of particles.

[b]Values are obtained by VASCO nanoparticle size analyzer and are in the unit of nm. Percentiles are based on volumes of clay suspensions.

Table B.8. Iron isotope values ($\delta^{56}Fe$) of the aqueous phase and the three extracts and their Fe isotope fractionations from bioreactors during the redox cycles[a, b]

Redox period	Days		Fraction of total Fe(II) (%)	$\delta^{56}Fe_{aq\ Fe(II)}$		$\delta^{56}Fe_{basal\ Fe(II)}$		$\delta^{56}Fe_{edge\ Fe}$		$\delta^{56}Fe_{struc\ Fe}$		$\delta^{56}Fe_{struc\ Fe(III)}$		$\delta^{56}Fe_{all\ ext\ Fe}$		$\Delta^{56}Fe_{aq\ Fe(II)-edge\ Fe}$		$\Delta^{56}Fe_{aq\ Fe(II)-struc\ Fe(III)}$		$\Delta^{56}Fe_{edge\ Fe-struc\ Fe(III)}$		$\Delta^{56}Fe_{basal\ Fe(II)-aq\ Fe(II)}$	
	Since redox experiments started	Since corresponding RP/OP started		‰	1SD	‰	1SD	‰	1SD	‰	1SD	‰	1SD	‰	1SD	‰	1SD	‰	1SD	‰	1SD	‰	1SD
RP1	1	1	1.1	-0.71	0.00	-1.63	0.00	-0.67	0.00	0.68	0.02	0.72	0.03	0.56	0.08	-0.04	0.00	-1.43	0.03	-1.40	0.03	-0.92	0.00
	3	3	1.4	-0.85	0.08	-1.48	0.03	-1.16	0.05	0.67	0.00	0.75	0.12	0.47	0.09	0.31	0.09	-1.60	0.14	-1.91	0.13	-0.63	0.08
	6	6	3.5	-0.33	0.00	-0.21	0.00	-0.72	0.02	0.80	0.02	0.91	0.07	0.49	0.07	0.39	0.02	-1.23	0.07	-1.62	0.08	0.12	0.00
	20	20	9.7	0.45	0.01	0.34	0.00	0.23	0.00	0.62	0.00	0.70	0.09	0.46	0.08	0.22	0.01	-0.25	0.09	-0.47	0.09	-0.11	0.01
OP1	21	0	1.3	NA	NA	-0.65	0.00	0.40	0.00	0.64	0.00	0.65	0.02	0.52	0.02	NA	NA	NA	NA	-0.25	0.02	NA	NA
	24	3	0.3	NA	NA	NA	NA	0.44	0.00	0.56	0.00	0.57	0.06	0.55	0.02	NA	NA	NA	NA	-0.13	0.06	NA	NA
RP2	26	1	1.0	0.28	0.00	-1.40	0.00	-0.73	0.00	0.71	0.00	0.83	0.05	0.77	0.07	1.02	0.00	-0.55	0.05	-1.57	0.05	-1.69	0.00
	28	3	2.2	-0.11	0.08	-0.03	0.04	-0.12	0.00	0.72	0.00	0.82	0.05	0.68	0.06	0.01	0.08	-0.93	0.09	-0.94	0.05	0.08	0.09
	31	6	4.2	0.35	0.00	0.24	0.00	0.24	0.00	NA	NA	NA	NA	NA	NA	0.11	0.00	NA	NA	NA	NA	-0.11	0.00
	45	20	7.4	0.67	0.00	0.46	0.00	0.30	0.00	0.53	0.00	0.61	0.03	0.46	0.05	0.37	0.00	0.06	0.03	-0.31	0.03	-0.21	0.00
OP2	46	0	1.2	NA	NA	-0.43	0.03	0.61	0.00	0.61	0.00	0.61	0.03	0.54	0.07	NA	NA	NA	NA	0.00	0.03	NA	NA
	49	3	0.4	NA	NA	NA	NA	NA	NA	0.56	0.00	NA	NA	NA	NA	NA	NA	NA	NA	NA	NA	NA	NA
RP3	54	4	1.9	-0.19	0.28	0.09	0.06	0.23	0.06	0.61	0.00	0.68	0.28	0.49	0.04	-0.42	0.29	-0.87	0.40	-0.45	0.29	0.28	0.29
	56	6	3.9	0.48	0.02	0.60	0.00	0.43	0.01	0.52	0.02	0.56	0.07	0.49	0.07	0.06	0.02	-0.07	0.07	-0.13	0.07	0.12	0.02
	69	19	5.0	0.64	0.00	0.47	0.00	0.32	0.00	0.40	0.00	0.42	0.03	0.38	0.05	0.32	0.00	0.22	0.03	-0.10	0.03	-0.17	0.00
	105	55	5.7	0.66	0.00	0.45	0.00	0.19	0.00	0.45	0.00	0.57	0.02	0.36	0.03	0.47	0.00	0.10	0.02	-0.38	0.02	-0.21	0.00
OP3	106	0	1.3	NA	NA	NA	NA	0.14	0.00	0.65	0.00	0.76	0.05	0.56	0.10	NA	NA	NA	NA	-0.62	0.05	NA	NA

[a]NA indicates data not available or applicable.

[b]For δ^{56}Fe values, 1SD indicates ranges observed in duplicate bioreactors or repeated analyses or one standard error for in-run statistics (40 1-second on peak integrations). For fractionation factors, 1SD is based on propagated errors.

Appendix C

Supporting Information: Chapter 4

Importance of tetrahedral Fe during microbial reduction of nontronite NAu-2

C.1 Materials and methods

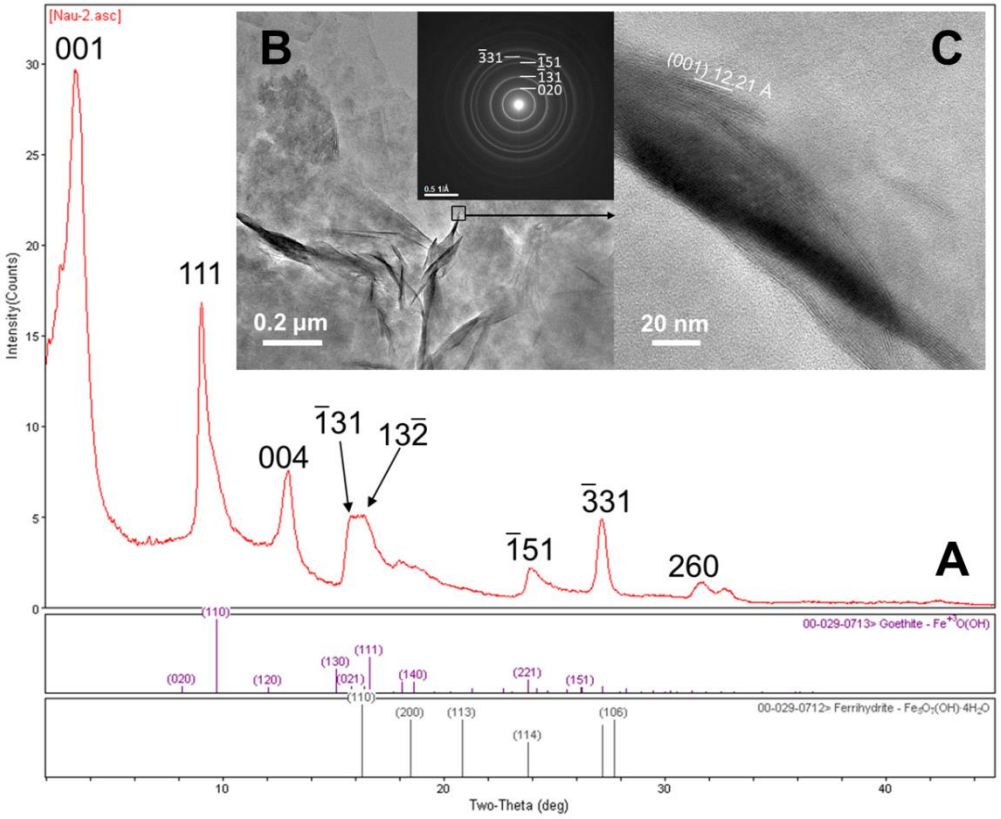

Figure C.1. A) XRD patterns (Mo radiation) and B) TEM image and the corresponding SAED (200 kV) (insert) of unaltered NAu-2. C) Magnified TEM image of the denoted area in B).

Table C.1. Experimental setup for the chemical reduction of NAu-2

Reactor ID	NAu-2 (g)	Dithionite (g)	Reacting time (h)	Reduction extent (%)
R-1	0.050	0.020	0.05	6.5
E-1	0.050	0.032	0.40	11.4
M-1	0.050	0.070	0.05	12.8
S-2	0.050	0.152	1.50	31.2
S-1	0.049	0.151	19.0	37.0

Table C.2. Iron isotope compositions of partially dissolved NAu-2[a]

Sample ID	Cumulative time (h)	Accumulated dissolution (%)	$\delta^{56}Fe_{each\ aliquot}$ (‰)	1SD[b] (‰)	$\delta^{56}Fe_{total\ ext\ Fe}$ (‰)
Aliquot 1	7.5	7.5	1.10	0.01	1.10
Aliquot 2	25.5	9.4	1.41	0.00	1.16
Aliquot 3	49.5	10.7	1.31	0.01	1.18
Aliquot 4	121.5	13.1	1.28	0.02	1.20
Aliquot 5	193.0	14.6	1.27	0.00	1.21
Aliquot 6	263.5	15.9	1.34	0.00	1.22
Aliquot 7	383.5	17.7	1.17	0.00	1.21
Aliquot 8	406.5	18.3	1.20	0.00	1.21

[a]Partial dissolution experiment was performed by reacting 50 mg unaltered NAu-2 with 5 mL 0.5 M HCl for 7.5 h followed by centrifugation of the suspension and supernatant filtered through 0.2 μm filter to acquire aliquot 1. Another 5 mL 0.5 M HCl was added to the remaining solid and reacted for another 18 h. The suspension was centrifuged and the supernatant filtered to acquire aliquot 2. The procedure was repeated until reaching a total of 22.3% dissolution after 711 h since starting of the experiment (Figure C.2A). This table only shows the samples with Fe isotope data.

[b]1SD is one standard deviation based on repeated isotope analyses of a single aliquot or standard error for one analysis (in-run statistics, 40 1-second on peak integrations).

C.2 Results and discussions

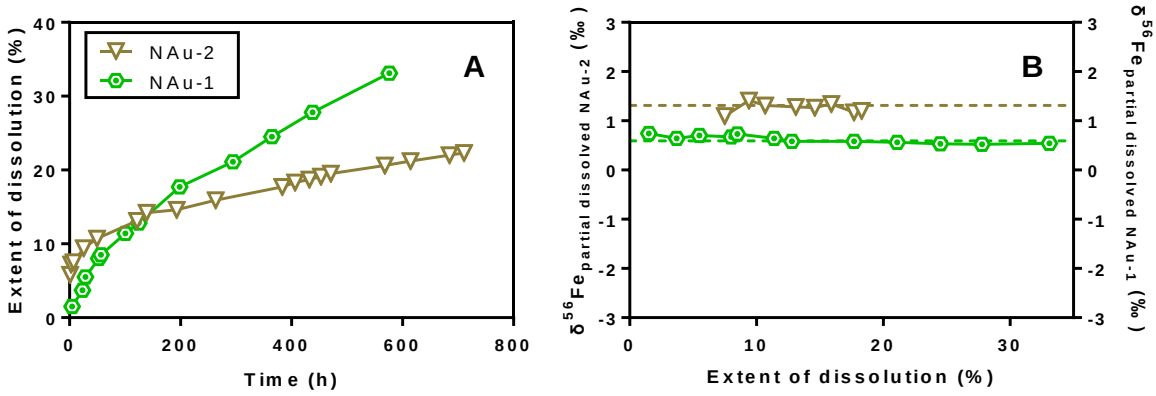

Figure C.2. A) Cumulative dissolution of NAu-2 and NAu-1 by 0.5 M HCl. B) Iron isotope compositions of partial dissolved aliquots of NAu-2 by 0.5 M HCl. Data of NAu-1 are from Shi *et al.* (2016).

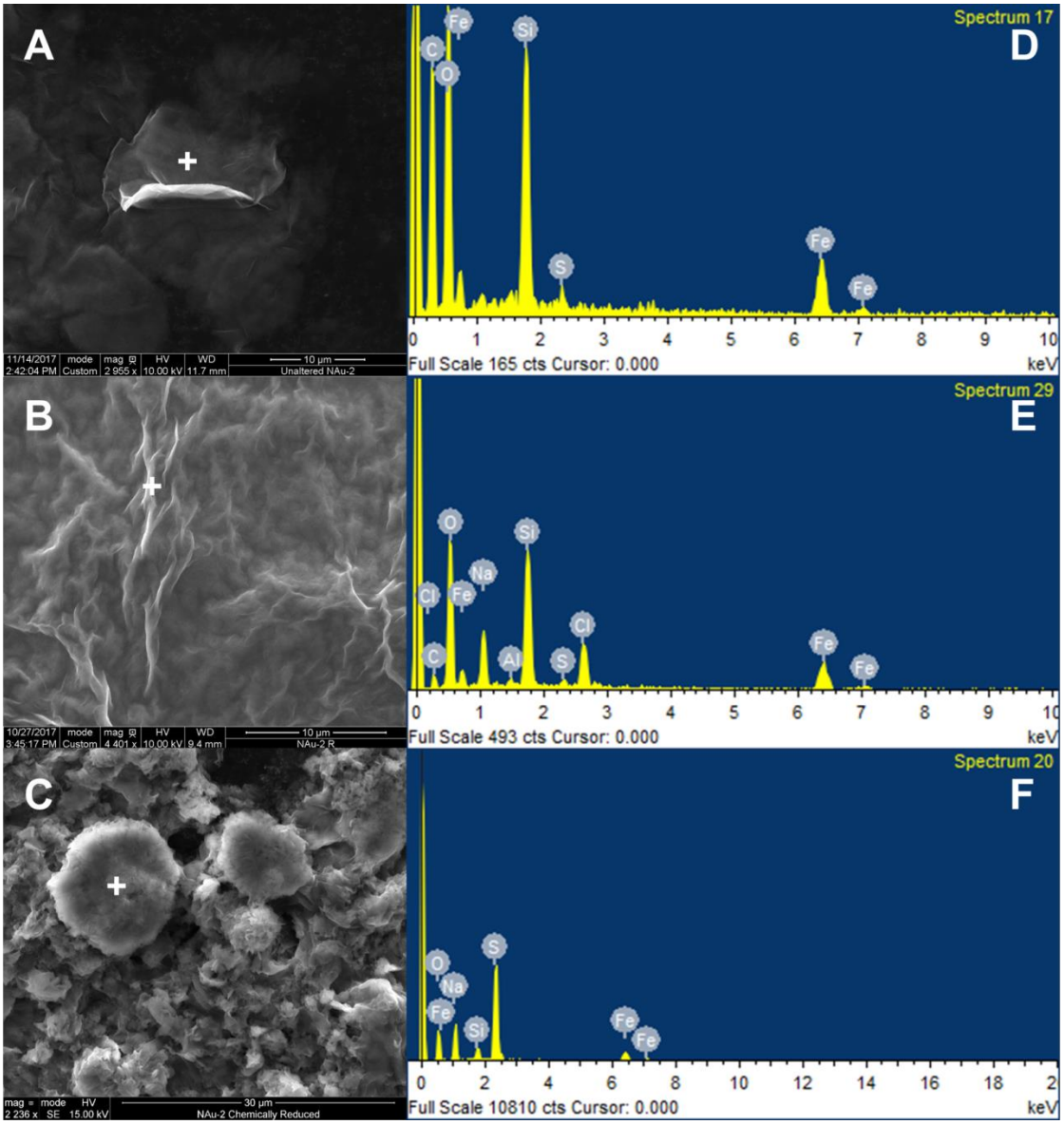

Figure C.3. SEM images of A) unaltered, B) bio-reduced, and C) chemically reduced NAu-2. EDS spectra of D) unaltered, E) bio-reduced, and F) chemically reduced NAu-2. The white crosses denote the analyzed locations.

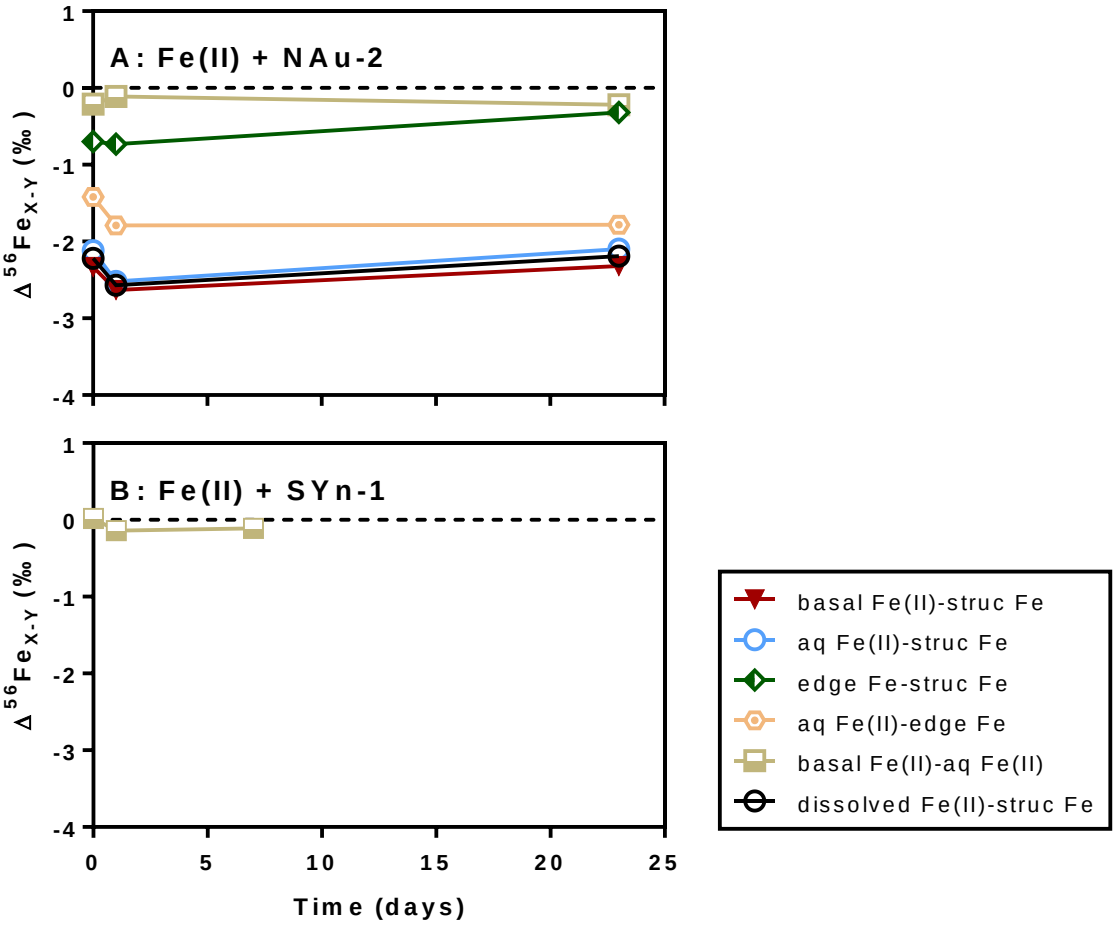

Figure C.4. Iron isotope fractionation factors between Fe phases X and Y vs. reduction extent of mixing experiments A) with NAu-2 and B) with SYn-1. See legend for the assigned X and Y from aqueous Fe(II), basal-sorbed Fe(II), edge-bound Fe, structural Fe, and dissolved Fe(II) [calculated according to Eq. (4.8)]. Error bars (smaller than data points) indicate one standard deviation of propagated errors.

Table C.3. Iron concentrations of aqueous phase and three extracts of biological reduction experiments (batch I and II), chemical reduction experiments, and the mixing experiments (with NAu-2 and SYn-1, respectively)[a]

Time[b]	Aqueous (μM)				1M $CaCl_2$ ext (μM)				1M NaH_2PO_4 ext (μM)				0.5M HCl ext (μM)				Total Fe(II) (μM)		Total Fe (μM)		Reduction extent[c]	
	Fe(II)	std	Fe(tot)	std	Fe(II)	std	Fe(tot)	std	Fe(II)	std	Fe(tot)	std	Fe(II)	std	Fe(tot)	std	Mean	std	Mean	std	%	std
	Batch I																					
1	18.7	9.0	31.2	5.1	2.4	0.6	5.6	0.6	26.0	9.3	158.3	6.9	387.9	9.4	1817	18.4	435.0	8.6	2012	17.3	1.9	0.0
2	40.2	1.0	48.3	11.3	0.0	0.0	2.8	2.8	26.0	10.5	158.3	1.7	693.5	2.1	1818	47.2	759.7	7.4	2027	57.4	3.3	0.0
3	44.4	3.8	29.3	1.4	5.5	2.8	6.4	1.0	32.5	1.8	162.1	2.6	965.3	23.4	1930	24.5	1048	22.6	2128	22.2	4.6	0.1
6	67.1	2.1	78.0	10.0	82.8	2.0	82.8	8.0	278.1	2.9	315.9	26.3	2457	98.5	3162	15.4	2885	99.7	3639	12.9	12.7	0.4
9	205.7	2.1	202.8	11.6	208.2	0.0	208.2	24.0	851.9	12.9	790.3	9.5	2362	37.0	3332	41.4	3628	26.2	4533	67.5	15.9	0.1
14	391.5	13.1	391.5	5.1	247.0	12.7	242.8	3.6	1494	74.8	1576	44.6	2316	79.2	2783	228.8	4449	179.8	4993	282.2	19.5	0.8
22	448.9	46.9	475.2	3.2	326.1	8.5	339.6	9.0	1680	58.4	1680	41.9	1970	72.0	2773	68.5	4425	168.8	5268	38.9	19.4	0.7
30	557.1	8.5	578.1	0.8	376.0	46.9	376.0	48.2	1812	26.2	1750	42.4	2329	38.3	2579	125.7	5074	50.6	5283	215.5	22.3	0.2
40	513.1	15.6	524.5	28.8	451.7	7.6	447.0	8.3	1792	4.2	1750	69.2	1900	9.9	2378	63.3	4657	6.1	5100	26.5	20.5	0.0
70	508.9	1.0	515.7	9.3	422.4	0.5	416.0	9.2	1932	28.1	1902	2.8	1876	64.8	2218	56.1	4740	94.4	5051	77.4	20.8	0.4
100	557.8	6.9	556.8	NA	422.1	10.7	419.0	NA	2074	34.1	1905	NA	1922	83.2	2337	NA	4975	90.8	5218	NA	21.9	0.4
	Batch II																					
0	0.0	1.4	0.0	0.1	0.0	1.4	0.0	0.0	0.9	0.8	74.6	7.6	45.7	0.5	1965	1.6	74.3	2.2	2046	7.8	0.3	0.0
1	0.0	7.8	0.0	0.1	0.0	0.0	0.0	0.0	4.8	1.6	86.4	7.8	185.1	1.4	2037	46.6	216.1	8.1	2136	47.3	1.0	0.0
2	22.7	1.3	32.2	0.5	0.0	0.0	0.0	1.5	2.8	2.8	110.6	1.1	465.3	4.1	2213	14.7	490.8	5.1	2359	14.8	2.2	0.0
3	4.6	1.2	32.9	0.0	0.0	0.0	0.0	0.0	18.5	0.5	99.4	10.0	815.5	33.7	2518	19.9	838.6	33.7	2651	22.3	3.7	0.1
4	29.6	1.6	15.5	0.9	0.0	0.0	0.0	0.0	25.1	2.3	133.1	11.2	1136	75.7	2466	27.3	1190	75.7	2614	29.6	5.2	0.3
5	40.3	3.7	32.3	1.1	3.0	3.0	13.3	4.4	82.0	32.9	225.1	28.4	1316	73.7	2709	18.1	1441	80.8	2980	34.0	6.3	0.4
6	36.8	6.4	29.8	0.2	13.7	0.8	14.1	5.9	167.8	74.2	283.7	78.5	1445	45.2	2826	51.4	1663	87.1	3154	94.0	7.3	0.4
7	47.1	8.8	57.3	8.3	22.4	8.9	27.6	6.0	345.4	91.6	512.6	101.6	1625	30.7	2785	34.4	2040	97.4	3382	107.8	9.0	0.4
8	63.3	8.2	85.3	5.3	36.7	8.2	41.3	11.6	361.6	75.6	465.8	81.4	1709	21.5	2898	24.4	2171	79.5	3490	85.9	9.6	0.4
9	80.3	13.0	83.0	11.7	47.3	12.9	48.1	11.5	485.1	63.3	647.6	60.4	1626	6.1	2692	15.2	2239	66.1	3471	64.4	9.9	0.3

10	84.3	7.1	89.0	10.9	64.6	14.5	54.6	13.8	537.0	72.2	662.4	77.2	1638	11.8	2724	69.9	2324	74.9	3530	105.6	10.2	0.3
11	100.6	15.5	100.1	9.9	62.7	21.9	74.6	17.0	590.5	55.1	726.9	49.1	1711	57.2	2787	22.8	2465	83.8	3688	57.6	10.9	0.4
13	122.2	24.2	121.3	21.8	95.9	20.7	98.9	22.9	688.6	62.6	783.2	32.9	1765	16.9	2816	22.8	2672	72.2	3819	51.0	11.8	0.3
15	120.5	31.4	155.1	23.3	120.7	25.6	123.5	22.3	742.8	84.9	862.5	65.2	1800	29.7	3000	20.9	2784	98.7	4141	75.7	12.3	0.4
17	154.2	25.4	171.7	30.5	135.1	23.6	136.9	27.0	869.5	106.5	1018	105.4	1826	29.8	2893	25.2	2984	115.9	4219	115.8	13.1	0.5
21	199.0	41.3	192.5	46.4	183.8	40.9	190.2	40.4	880.4	97.0	978.8	86.0	1890	36.0	2755	124.7	3153	118.7	4117	163.6	13.9	0.5
	Control group																					
1	27.1	11.4	55.5	46.6	0.0	0.0	0.7	1.2	20.0	13.0	147.5	3.0	72.5	6.2	1703.4	16.9	119.6	18.4	1907.1	49.7	0.5	0.0
2	31.8	1.6	26.6	6.5	0.0	0.0	0.0	0.0	8.6	5.1	153.7	0.0	70.0	2.3	1562.4	16.9	110.4	5.8	1742.7	18.1	0.5	0.0
3	40.0	9.2	24.0	11.9	0.0	0.0	0.0	0.0	35.8	3.5	139.0	0.0	44.2	5.2	1530.0	25.7	120.0	11.2	1693.1	28.3	0.5	0.0
6	31.5	2.9	50.2	17.5	2.8	1.2	50.9	24.7	15.9	0.0	19.8	2.6	102.6	6.0	2104.1	28.2	152.8	6.7	2224.9	41.5	0.7	0.0
9	30.9	1.6	26.9	18.0	7.9	5.4	39.5	28.0	19.3	1.6	54.8	31.9	65.8	2.9	2428.8	140.3	123.8	6.5	2550.0	147.6	0.5	0.0
14	0.0	0.0	0.0	0.0	13.1	22.7	0.0	0.0	20.6	14.8	85.7	0.0	45.5	10.9	2093.7	114.3	79.1	29.2	2179.4	114.3	0.3	0.0
22	0.0	0.0	0.0	0.0	0.0	0.0	0.1	0.2	40.7	5.7	101.1	6.4	3.5	0.0	1952.8	49.9	44.2	5.7	2054.1	50.3	0.2	0.0
30	0.0	0.0	0.0	0.0	0.0	0.0	0.7	1.3	27.8	3.2	72.5	2.1	58.6	8.7	1818.6	48.9	86.4	9.3	1891.8	49.0	0.4	0.0
40	34.3	5.2	26.4	NA	0.8	1.1	6.7	NA	23.6	4.7	91.2	NA	52.0	2.8	1926.8	NA	110.8	7.6	2051.1	0.0	0.5	0.0
70	25.5	5.3	29.4	NA	3.8	5.8	4.0	NA	14.3	0.9	74.5	NA	58.8	8.5	1503.3	50.5	102.5	11.6	1611.1	50.5	0.5	0.0
100	20.8	10.5	10.5	NA	0.0	1.6	0.0	NA	17.1	7.4	103.7	NA	NA	NA	NA	NA	NA	NA	NA	NA	NA	NA
	Chemical reduction																					
0.05	81.3	0.0	63.3	11.1	144.7	1.6	164.8	3.7	15.2	0.4	96.5	9.2	1230.7	37.6	3039.9	139.0	1472.0	37.6	3364.6	139.8	6.5	0.2
0.4	225.8	5.1	213.3	10.3	335.5	6.1	349.4	1.9	124.5	1.9	221.6	5.2	1897.6	29.0	3363.6	155.1	2583.2	30.1	4147.9	155.5	11.4	0.1
0.05	535.1	12.5	529.9	NA	304.1	6.8	319.4	NA	135.6	5.6	198.6	NA	1920.1	21.1	3177.0	NA	2895.0	26.0	4225.0	NA	12.8	0.1
1.5	1644.8	12.2	1593.1	27.6	483.6	2.9	493.7	5.3	2448.5	39.4	2712.0	141.4	2507.1	27.1	3148.5	89.8	7084.0	49.4	7947.2	169.8	31.2	0.2
19	1972.5	36.7	1915.3	28.9	444.0	5.1	455.6	3.5	3071.9	36.9	3181.7	107.0	2734.6	37.7	3342.7	74.9	8223.0	64.5	8895.3	133.8	37.0	0.3
	Mixing Fe(II) with NAu-2																					
0	880.4	13.2	871.8	15.3	767.3	7.7	743.8	4.0	5.7	0.6	53.9	1.0	342.8	0.6	1314.6	12.8	1996.2	15.4	2984.2	20.4	3.8	0.0
1	722.5	4.2	711.5	5.9	626.0	4.0	631.0	5.6	16.3	1.2	69.9	4.4	571.5	3.9	1533.5	25.7	1936.5	7.1	2945.9	27.3	6.3	0.0

3	650.3	2.0	672.5	1.9	601.3	4.2	579.8	13.6	12.0	1.2	54.9	0.9	663.6	12.3	1609.9	25.4	1927.0	13.2	2917.0	28.9	7.3	0.1
23	688.0	10.8	678.0	7.4	522.2	0.3	514.9	2.6	17.7	1.8	60.8	1.0	657.2	17.6	1582.8	16.1	1885.1	20.7	2836.5	18.0	7.2	0.2
	Mixing Fe(II) with SYn-1																					
0	1824.2	17.5	1772.3	25.1	132.0	3.3	122.1	2.7	33.6	0.6	38.2	1.6	15.4	1.5	25.5	0.5	2005.3	17.9	1958.1	25.3	NA	NA
1	1851.2	3.4	1776.0	21.5	113.2	1.4	121.0	1.8	28.8	0.1	24.5	3.8	16.5	1.3	28.7	3.1	2009.8	3.9	1950.2	22.1	NA	NA
7	1702.4	3.3	1837.0	15.1	110.0	3.2	115.1	4.3	25.7	0.9	31.9	1.4	12.5	2.5	33.0	4.0	1850.6	5.3	2016.9	16.2	NA	NA
17	1738.3	15.3	1712.3	5.8	97.6	3.0	101.3	1.3	5.4	0.4	48.1	0.5	16.6	1.7	48.7	1.9	1857.9	15.6	1910.4	6.3	NA	NA

[a]NA indicates data not available or not applicable.
[b]The unit of time for biological reduction and mixing experiments is “day”, for chemical reduction experiments is “hour”.
[c]Reduction extent for the mixing experiment is the HCl extractable Fe(II) out of the total Fe in NAu-2.

Table C.4. The proportions of dissolved Fe, Si, Al of batch I and II[a, b, c]

Days	Reduction extent (%)	Fe		Si		Al	
		(%)	1SD	(%)	1SD	(%)	1SD
Batch I							
1	1.9	0.20	0.02	0.41	0.00	NA	NA
3	4.6	0.20	0.01	0.41	0.00	NA	NA
9	15.9	1.80	0.12	1.16	0.00	NA	NA
14	19.5	2.80	0.03	2.86	0.17	NA	NA
40	20.5	4.30	0.13	4.26	0.33	NA	NA
70	20.8	4.10	0.06	4.96	0.02	NA	NA
Batch II							
0	0.3	0.03	0.00	0.18	0.01	0.07	0.00
3	3.7	0.14	0.00	0.36	0.00	0.10	0.00
9	9.9	0.68	0.02	0.61	0.00	0.37	0.01
21	13.9	1.30	0.04	1.12	0.02	0.06	0.01

[a]NA indicates data not available or not applicable.

[b]The proportion of dissolved Fe, Si, Al were calculated according to equations 4.5-4.7.

[c]Si concentrations of batch I were analyzed using a standard colorimetric method (DL = 0.83 μM) (Clesceri, 1989). Si and Al concentrations of batch II were analyzed by ICP-OES, and their method detection limits were 0.33 and 0.02 μM, respectively.

Table C.5. Iron isotope compositions of aqueous phase and three extracts and their Fe isotope fractionation factors for the biological reduction experiments (batch I and II), chemical reduction experiments, and the mixing experiments (with NAu-2 and SYn-1, respectively)[a]

Time[b]	Reduction extent[c] (%)	$\delta^{56}Fe_{aq\ Fe(II)}$		$\delta^{56}Fe_{basal\ Fe(II)}$		$\delta^{56}Fe_{edge\ Fe}$		$\delta^{56}Fe_{struc\ Fe}$		$\delta^{56}Fe_{struc\ Fe(III)}$		$\delta^{56}Fe_{all\ ext\ Fe}$		$\Delta^{56}Fe_{aq\ Fe(II)-edge\ Fe}$		$\Delta^{56}Fe_{aq\ Fe(II)-struc\ Fe}$		$\Delta^{56}Fe_{edge\ Fe-struc\ Fe}$		$\Delta^{56}Fe_{basal\ Fe(II)-aq\ Fe(II)}$		$\Delta^{56}Fe_{basal\ Fe(II)-struc\ Fe}$	
		‰	1SD	‰	1SD	‰	1SD	‰	1SD	‰	1SD	‰	1SD	‰	1SD	‰	1SD	‰	1SD	‰	1SD	‰	1SD
	Batch I																						
1	1.9	1.37	0.02	NA	NA	NA	NA	1.19	0.02	NA	NA	NA	NA	NA	NA	0.18	0.03	NA	NA	NA	NA	NA	NA
3	4.6	1.02	0.02	NA	NA	1.12	0.02	1.13	0.02	1.15	0.05	1.13	NA	-0.09	0.02	-0.11	0.02	-0.02	0.03	NA	NA	NA	NA
6	12.7	-0.65	0.00	-0.70	0.03	-0.89	0.01	1.39	0.02	9.34	0.06	1.10	0.19	0.25	0.01	-2.04	0.02	-2.28	0.02	-0.05	0.03	-2.09	0.04
9	15.9	-1.91	0.00	-2.09	0.01	0.77	0.00	1.57	0.02	3.51	0.03	1.11	0.13	-2.68	0.00	-3.48	0.02	-0.80	0.02	-0.18	0.01	-3.66	0.02
14	19.5	-1.29	0.00	-1.63	0.00	1.43	0.00	1.72	0.01	3.15	0.13	1.23	0.09	-2.72	0.00	-3.01	0.02	-0.29	0.02	-0.34	0.00	-3.35	0.02
40	20.5	-0.78	0.00	-0.91	0.01	1.65	0.03	1.56	0.02	1.21	0.04	1.13	0.08	-2.42	0.03	-2.34	0.02	0.09	0.04	-0.13	0.01	-2.47	0.02
70	20.8	-0.65	0.05	-0.73	0.01	1.63	0.02	1.52	0.00	0.93	0.06	1.15	0.09	-2.28	0.05	-2.17	0.05	0.11	0.02	-0.08	0.05	-2.25	0.01
100	21.9	-0.41	0.03	-0.54	0.03	1.61	0.00	1.44	0.01	0.63	0.06	1.15	0.10	-2.02	0.03	-1.85	0.03	0.17	0.01	-0.13	0.05	-1.98	0.03
	Batch II																						
0	0.3	NA	NA	NA	NA	0.43	0.00	1.29	0.01	1.31	0.18	1.26	NA	NA	NA	NA	NA	-0.87	0.01	NA	NA	NA	NA
1	0.9	NA	NA	NA	NA	0.46	0.00	1.28	0.00	1.36	0.03	1.24	NA	NA	NA	NA	NA	-0.82	0.00	NA	NA	NA	NA
2	2.2	-1.27	0.00	NA	NA	0.50	0.08	1.26	0.01	1.46	0.17	1.19	NA	-1.77	0.08	-2.53	0.01	-0.76	0.08	NA	NA	NA	NA
3	3.8	-1.17	0.03	NA	NA	1.06	0.00	1.25	0.00	1.36	0.06	1.22	NA	-2.23	0.03	-2.43	0.03	-0.20	0.00	NA	NA	NA	NA
4	5.6	-1.02	0.00	NA	NA	0.35	0.00	1.29	0.00	2.18	0.11	1.22	NA	-1.36	0.00	-2.31	0.00	-0.94	0.00	NA	NA	NA	NA
5	6.8	-1.21	0.00	NA	NA	-0.30	0.01	1.39	0.01	3.15	0.06	1.22	NA	-0.90	0.01	-2.60	0.01	-1.69	0.02	NA	NA	NA	NA
6	7.9	-1.15	0.00	-1.95	0.00	0.36	0.00	1.41	0.00	2.53	0.05	1.25	0.14	-1.51	0.00	-2.56	0.00	-1.05	0.00	-0.80	0.00	-3.36	0.00
7	9.6	-1.39	0.06	NA	NA	0.41	0.00	1.58	0.05	3.35	0.04	1.30	NA	-1.80	0.06	-2.97	0.08	-1.17	0.05	NA	NA	NA	NA
8	10.1	-1.33	0.00	-1.94	0.00	-0.13	0.00	1.54	0.02	4.07	0.04	1.16	0.16	-1.19	0.00	-2.86	0.02	-1.67	0.02	-0.62	0.00	-3.48	0.02
9	10.2	-1.41	0.00	-1.86	0.00	0.30	0.00	1.61	0.00	3.63	0.04	1.21	0.05	-1.71	0.00	-3.03	0.00	-1.31	0.00	-0.45	0.00	-3.48	0.00
10	10.6	NA	NA	-1.95	0.00	NA	NA	1.57	0.00	NA	NA	1.13	NA	NA	NA	NA	NA	NA	NA	NA	NA	-3.52	0.00
11	11.5	-1.48	0.00	-1.98	0.00	0.61	0.00	1.58	0.00	3.21	0.06	1.20	0.05	-2.09	0.00	-3.05	0.00	-0.96	0.00	-0.51	0.00	-3.56	0.00

13	12.3	-1.55	0.00	-1.99	0.00	0.43	0.00	1.69	0.09	3.82	0.06	1.20	0.07	-1.99	0.00	-3.25	0.09	-1.26	0.09	-0.43	0.00	-3.68	0.09
15	13.0	-1.53	0.01	NA	NA	0.34	0.00	1.66	0.00	3.69	0.03	1.18	NA	-1.87	0.01	-3.19	0.01	-1.32	0.00	NA	NA	NA	NA
17	13.7	NA	NA	-2.04	0.00	0.95	0.03	1.77	0.00	3.15	0.04	NA	NA	NA	NA	-3.32	0.00	-0.83	0.03	NA	NA	-3.81	0.00
21	14.5	NA	NA	-1.95	0.00	1.06	0.01	1.88	0.04	3.83	0.08	1.35	NA	NA	NA	NA	NA	-0.82	0.04	NA	NA	-3.83	0.04
	Chemical reduction																						
0.05	6.5	0.30	0.06	-1.36	0.00	0.92	0.00	1.31	0.00	1.58	0.08	1.15	0.28	-0.62	0.06	-1.02	0.06	-0.39	0.00	-1.66	0.06	-2.68	0.00
0.4	11.4	-0.43	0.00	-0.67	0.00	-0.23	0.00	1.59	0.01	3.95	0.07	1.20	0.07	-0.20	0.00	-2.02	0.01	-1.82	0.01	-0.24	0.00	-2.26	0.01
0.05	12.8	0.76	0.01	-1.13	0.01	NA	NA	1.58	0.00	NA	NA	NA	NA	NA	NA	-0.82	0.01	NA	NA	-1.89	0.02	-2.71	0.01
1.5	31.2	2.04	0.00	0.65	0.00	NA	NA	1.39	0.00	NA	NA	NA	NA	NA	NA	0.64	0.00	NA	NA	-1.39	0.00	-0.74	0.00
19	37	2.13	0.00	0.59	0.00	NA	NA	1.28	0.03	NA	NA	NA	NA	NA	NA	0.85	0.03	NA	NA	-1.54	0.00	-0.70	0.03
	Mixing Fe(II) with NAu-2																						
0	3.8	-0.69	0.03	-0.89	0.02	0.74	0.04	1.44	0.04	1.68	0.06	0.22	0.09	-1.42	0.05	-2.12	0.05	-0.70	0.06	-0.21	0.04	-2.33	0.05
1	6.3	-1.09	0.05	-1.21	0.04	0.70	0.06	1.43	0.03	1.85	0.09	0.24	0.11	-1.79	0.08	-2.52	0.06	-0.73	0.07	-0.11	0.06	-2.63	0.05
23	7.0	-0.95	0.00	-1.17	0.03	0.83	0.09	1.14	0.03	1.37	0.11	0.21	0.12	-1.78	0.09	-2.10	0.03	-0.32	0.10	-0.22	0.03	-2.32	0.04
	Mixing Fe(II) with SYn-1																						
0	NA	-0.33	0.00	-0.31	0.07	NA	NA	NA	NA	NA	NA	-0.33	0.22	NA	NA	NA	NA	NA	NA	0.02	0.07	NA	NA
1	NA	-0.29	0.01	-0.43	0.00	NA	NA	NA	NA	NA	NA	-0.30	0.03	NA	NA	NA	NA	NA	NA	-0.14	0.01	NA	NA
7	NA	-0.29	0.00	-0.39	0.00	NA	NA	NA	NA	NA	NA	-0.29	0.04	NA	NA	NA	NA	NA	NA	-0.11	0.01	NA	NA

[a]NA indicates data not available or not applicable.
[b]The unit of time for biological reduction and mixing experiments is “day”, for chemical reduction experiments is “hour”.
[c]Reduction extent for the mixing experiment is the HCl extractable Fe(II) out of the total Fe in NAu-2.